UCLA
UCLA Electronic Theses and Dissertations

Title
Surface Functionalization, Patterning, and in Situ Growth of Gold Nanoparticles

Permalink
https://escholarship.org/uc/item/4b4307rw

Author
Vinnacombe-Willson, Gail Anne

Publication Date
2022

Peer reviewed|Thesis/dissertation

eScholarship.org Powered by the California Digital Library
University of California

UNIVERSITY OF CALIFORNIA

Los Angeles

Surface Functionalization, Patterning, and *in Situ* Growth of Gold Nanoparticles

A dissertation submitted in partial satisfaction of the requirements for the degree Doctor of Philosophy in Chemistry

by

Gail Anne Vinnacombe-Willson

2022

© Copyright by

Gail Anne Vinnacombe-Willson

2022

ABSTRACT OF THE THESIS

Surface Functionalization, Patterning, and

in Situ Growth of Gold Nanoparticles

by

Gail Anne Vinnacombe-Willson

Doctor of Philosophy in Chemistry

University of California, Los Angeles, 2022

Prof. Steven J. Jonas, Co-Chair

Prof. Paul S. Weiss, Co-Chair

The primary focus of this thesis is the development of straightforward bottom-up methods for rationally incorporating gold nanoparticles (AuNPs) onto oxide materials, onto polymers, and within microfluidic devices. Plasmonic AuNPs strongly interact with light due to the localized surface plasmon resonance (LSPR) phenomenon. The position and quality of the LSPR peaks depend on the AuNP crystal structure, diameter, geometry, and local dielectric environment, which are easily modulated *via* wet-chemical synthesis. Beyond high optical extinction, the LSPR effect can also lead to efficient light-to-heat conversion, hot carrier generation, and intense localized electric fields. Moreover, when the individual particles are arranged into ordered arrays, even more complex optical responses and high-quality lattice plasmon resonances can be selected. Although wet-chemical synthesis yields individual plasmonic building blocks with superior qualities,

precisely engineering plasmonic substrates from colloidal AuNPs is often challenging. The fabrication strategies developed herein have led to advances regarding *in situ* control over AuNP size and shape, pattern scalability, translatability, and versatility. I employ self-assembly and scalable subtractive soft lithography to produce arbitrary patterns from pre-synthesized AuNPs. I establish wet-chemical approaches for direct nucleation, growth, and shape-control that avoid time-consuming ligand exchange, self-assembly, and the need for costly equipment. Lastly, I explored *in situ* shape control to integrate thermoplasmonic gold nanostars within microfluidic platforms to target biomedical applications, including liquid biopsies. Overall, this work has potential impact for the fabrication of plasmonic biomedical devices, sensors, optoelectronics, and heterogeneous catalysts.

The thesis of Gail Anne Vinnacombe-Willson is approved.

Xiangfeng Duan

Richard B. Kaner

Gerard C. L. Wong

Steven J. Jonas, Committee Co-Chair

Paul S. Weiss, Committee Co-Chair

University of California, Los Angeles

2022

To my mother, Rosalina Sonico Vinnacombe,

my very first teacher

and to Jake,

for his endless support, patience, and advice.

Table of Contents

List of Figures x
List of Tables xii
List of Acronyms xiv
Acknowledgments xvi
Co-Author Contributions xviii
VITA xx
Historical Overview 1
Modern-Day Implementation of Nanomaterials 3
Overview of the Thesis 4
References 5
Chapter 1. Introduction 8
Section 1.1. Plasmonic Properties of Metal Nanostructures 9
1.1.1. Plasmons 9
1.1.1.1. Bulk and surface plasmons 9
1.1.1.2. Localized surface plasmon resonance 11
1.1.2. Plasmonic nanoparticle dimers, lines, and arrays 16
Section 1.2. Colloidal Synthesis of Gold Nanoparticles 18
1.2.1. Early developments in colloidal synthesis 19
1.2.2. Seed-mediated growth 21
1.2.2.1. The role of the seed 22
1.2.2.2. The reductant 24
1.2.2.3. The surfactant and shape-directing reagents 25
1.2.2.4. Other factors and methods to adjust size and shape uniformity 27
1.2.3. Precision synthesis with microfluidics 27
Section 1.3. Engineering Plasmonic Substrates 30
1.3.1. Top-down engineering of plasmonic substrates 31
1.3.2. Plasmonic substrates from colloidal nanoparticles 32
Section 1.4. Summary 33
Section 1.5. References 34
Chapter 2. Large-Scale Soft-Lithographic Patterning of Plasmonic Nanoparticles 46

Section 2.1. Introduction 47
Section 2.2. Results and Discussion 48
Section 2.3. Conclusions and Prospects 65
Section 2.4. Materials and Methods 66
2.4.1. Materials 66
2.4.2. Instrumentation 67
2.4.3. Synthesis of 50 and 100 nm gold nanoparticles@(11-mercaptoundecyl)hexa(ethylene glycol) 68
2.4.4. Seeds@hexadecyltrimethylammonium chloride 68
2.4.5. 10 nm gold nanoparticles@hexadecyltrimethylammonium chloride 69
2.4.6. 50 nm gold nanoparticles@hexadecyltrimethylammonium chloride 69
2.4.7. 100 nm gold nanoparticles@hexadecyltrimethyl-ammonium chloride 70
2.4.8. Workup and storage 70
2.4.9. (11-mercaptoundecyl)hexa(ethylene glycol) coating 71
2.4.10. Self-Assembly of the gold nanoparticles into monolayers at the liquid-liquid interface 72
2.4.11. Monolayer transfer to desired substrates using a custom-built dip coater 72
2.4.12. Preparation of patterned gold nanoparticle monolayers *via* chemical lift-off lithography 73
2.4.13. Patterned gold nanoparticle monolayer microcontact printing on arbitrary substrates 73
Section 2.5. References 74
Chapter 3. Bottom-up *in Situ* Growth: A Paradigm Shift for Synthetic Studies of Gold Nanoparticles 78
Section 3.1. Introduction 79
3.1.1. Defining wet-chemical *in situ* growth 79
3.1.2. Rationale and motivation for *in situ* growth 81
3.1.3. Promoting substrate growth with chemical reductants 82
3.1.3.1. *In situ* growth *via* addition of external strong reductants 82
3.1.3.2. *In situ* growth on substrates with native strong reductants 84
Section 3.2. Patterning *in Situ* 87
3.2.1. Physical templates 87
3.2.2. Chemical templates 88
3.2.2.1. Substrate-native chemical templates 88

3.2.2.2. Chemical functionalization on generalized substrates 89
3.2.2.3. Block copolymer micelle lithography 91
3.2.3. Hybrid patterning approaches 91
3.2.3.1. Combination of colloidal synthesis and *in situ* overgrowth 92
3.2.3.2. Combination of top-down fabrication and *in situ* overgrowth 92
Section 3.3. Bottom-up Size and Shape Control 93
3.3.1. Nanorods 94
3.3.2. Triangles and other platelets 96
3.3.3. Branched structures 99
3.3.4. Vertical growth: Nanowires 102
Section 3.4. Summary and Prospects 104
Section 3.5. References 107
Chapter 4. Surface Lattice Plasmon Resonances by *in Situ* Growth of Gold Nanoparticle Arrays 113
Section 4.1. Introduction 114
Section 4.2. Results and Discussion 115
4.2.1. Stencil fabrication with thermal nanoimprint lithography 115
4.2.2. *In situ* size and shape modification 129
4.2.3. Lattice plasmon resonance characterization 137
Section 4.3. Conclusions and Prospects 142
Section 4.4. Materials and Methods 144
4.4.1. Materials 144
4.4.2. Methods 146
Section 4.5. References 153
Chapter 5. Gold Nanostars *in Situ* Shape Control on Oxide Substrates and in Microfluidic Channels 159
Section 5.1. Introduction 160
Section 5.2. Results and Discussion 161
5.2.1. Growth solution optimization for *in situ* shape control 161
5.2.2. *In situ* nanostars overgrowth on slides and in capillaries 165
5.2.3. *In situ* nanostars overgrowth in polydimethylsiloxane-microfluidics 173
Section 5.3. Conclusions and Prospects 185
Section 5.4. Materials and Methods 186

5.4.1. Materials 186
5.4.2. Colloidal gold nanostar synthesis 187
5.4.3. Preparation of functionalized glass capillaries 188
5.4.4. Preparation of polydimethylsiloxane channels 189
5.4.5. Microfluidic synthesis 190
5.4.6. Gold nanostar characterization 191
Section 5.5. References 192
Chapter 6. Plasmonic Response of *in Situ* Gold Nanostars and Hyperthermia-Mediated Cell Removal 196
Section 6.1. Introduction 197
6.1.1. Localized heating in gold nanostars 197
6.1.2. Surface-enhanced Raman scattering 197
6.1.3. Application of nanostars grown in microfluidic channels 200
Section 6.2. Results and Discussion 202
6.2.1. Nanostar plasmonic and photothermal response 202
6.2.2. Nanophotothermolysis of adherent cells 210
Section 6.3. Conclusions and Prospects 216
Section 6.4. Materials and Methods 217
6.4.1. Materials 217
6.4.2. Thermal imaging and surface-enhanced Raman scattering 217
6.4.3. Imaging cells on the gold nanostar films 218
6.4.4. Proof-of-concept cell release studies 218
Section 6.5. References 219
Chapter 7. Conclusions and Prospects 223
Section 7.1. Conclusions 224
7.1.1. Nanoparticle chemical lift-off lithography 224
7.1.2. *In situ* growth of gold nanoparticle arrays 225
7.1.3. *In situ* overgrowth of gold nanostars in microfluidics 225
7.1.4. Plasmonic response and point-and-shoot cell release in nanostar-coated microfluidic channels 226
Section 7.2. Prospects 227
Appendix A. Seeded-Growth Experiment Demonstrating Size- and Shape-Dependence on Gold Nanoparticle-Light Interactions 232

Section A.1. Introduction 233
Section A.2. Experimental 235
A.2.1. Experimental Turkevich synthesis of gold nanospheres 235
A.2.2. Seed-mediated growth of nanostars 236
A.2.3. Seed-mediated growth of 100 nm nanospheres 236
Section A.3. Hazards 237
Section A.4. Results and Discussion 238
Section A.5. Use and Assessment 245
Section A.6. Teacher Workshop Evaluation Sheet 248
Section A.7. Summer Program Homework Guidelines 249
Section A.8. Link to Student and Teacher Manuals 251
Section A.9. References 251

List of Figures

Figure 1.1. Plasmon schematics. 11
Figure 1.2. Plasmon resonances of nanorods. 14
Figure 1.3. Plasmon resonances of nanoparticles with different diameter.. 15
Figure 1.4. Nanoparticle coupling in dimers and chains. 17
Figure 1.5. Lattice plasmon resonances. 18
Figure 1.6. The LaMer model 20
Figure 1.7. Gold nanoparticles accessible *via* colloidal synthesis. 23
Figure 1.8. Micromixer examples. 28
Figure 1.9. Plasmonic assemblies with colloidal nanoparticles 32

Figure 2.1. Nanoparticle chemical lift-off lithgraphy process. 49
Figure 2.2. Gold nanoparticle monolayer self-assembly and substrate transfer. 50
Figure 2.3. Characterization of gold nanospheres. 51
Figure 2.4. Characterization of patterned polydimethylsiloxane stamps. 52
Figure 2.5. Scanning electron microscopy characterization of micrometer-scale patterns. 53
Figure 2.6. Control experiments. 55
Figure 2.7. Consecutive nanoparticle chemical lift-off lithography and microcontact printing... 55
Figure 2.8. Consecutive nanoparticle chemical lift-off lithography. 56
Figure 2.9. Microcontact printing. 56
Figure 2.10. Secondary chemical lift-off lithography electron microscopy images. 57
Figure 2.11. Microcontact printing electron microscopy images. 58
Figure 2.12. Microcontact printing on glass substrates. 59
Figure 2.13. Nanoparticle chemical lift-off lithography on pyramidal features 60
Figure 2.14. Pyramidal patterns after lift-off 61

Figure 2.15. Patterning chiral square spirals and lines. 62
Figure 2.16. Optical characterization of spiral patterns. 64

Figure 3.1. *In situ* shape control schematic 80
Figure 3.2. Schematics depicting the possible distribution of reductants in *in situ* growth 82
Figure 3.3. Synthesis of gold nanoparticles within responsive hydrogels 83
Figure 3.4. Plasmonic nanoparticles grown on polydimethylsiloxane 86
Figure 3.5. *In situ* nanoparticle patterning 89
Figure 3.6. Patterning and *in situ* overgrowth *via* dynamic templating 93
Figure 3.7. Nanorods synthesized by *in situ* overgrowth 95
Figure 3.8. *In situ* synthesis of triangles and platelets 98
Figure 3.9. Branched structures prepared by *in situ* growth or *in situ* overgrowth. 100
Figure 3.10. Schematic depicting heterogeneous and homogeneous nucleation. 101
Figure 3.11. Synthesis of vertical nanowires.. 104

Figure 4.1. Optimization of hydroxypropyl cellulose thermal nanoimprint lithography.. 116
Figure 4.2. Characterization of hydroxypropyl cellulose film patterning. 118
Figure 4.3. Patterned hydroxypropyl cellulose films on supported polydimethylsiloxane. 120
Figure 4.4. Ultraviolet-ozone treatment of hyxroxypropyl cellulose films. 122
Figure 4.5. Estimation of hydroyxypropyl cellulose etch rate. 123
Figure 4.6. Secondary nucleation evaluation and characterization of initial products 126
Figure 4.7. Ink application and array yield optimization 127
Figure 4.8. Control experiments. 128
Figure 4.9. Optimization of hydroxypropyl cellulose mask thickness 129
Figure 4.10. Wet-chemical modulation of nanoparticle diameter. 130
Figure 4.11. Scanning electron microscopy characterization of products. 132
Figure 4.12. Scanning electron microscopy estimation of patterning yield. 134
Figure 4.13. *In situ* shape control and overgrowth into nanostar arrays. 136
Figure 4.14. Additional scanning electron microscopy images of the Λ = 400 nm array. 138
Figure 4.15. Additional scanning electron microscopy images of the Λ = 500 nm array. 139
Figure 4.16. Additional scanning electron microscopy images of the Λ = 600 nm array. 140
Figure 4.17. Optical characterization of lattice plasmon resonances 141

Figure 5.1. Synthesis optimization of nanostars with different seeds 162
Figure 5.2. Addition of HCl to reduce secondary nucleation 163
Figure 5.3. Optimization of growth solution and yield of the final colloidal products. 164
Figure 5.4. Schematic and demonstration of *in situ* seed-mediated growth. 166
Figure 5.5. Effect of silver concentration on *in situ* products. 167
Figure 5.6. Comparison of colloidal and *in situ* products. 168
Figure 5.7. Detailed characterization of *in situ* synthesized gold nanostars. 169
Figure 5.8. Modulation of growth time and flow rate in glass microcapillaries. 170
Figure 5.9. Repetitions of growth at different flow rates. 171
Figure 5.10. Scanning electron microscopy comparison of products at the inlet and outlet 172
Figure 5.11. Additional scanning electron microscopy images. 173
Figure 5.12. Fabrication of polydimethylsiloxane microfluidic channels. 174

Figure 5.13. Optimization of polydimethylsiloxane channel binding to indium tin oxide..... 175
Figure 5.14. Characterization of nanostars in polydimethylsiloxane channels. 176
Figure 5.15. Wetting in herringbone channels after oxygen plasma treatment. 178
Figure 5.16. Flow profile simulations in the herringbone channels. 179
Figure 5.17. Nanostar gradients in microfluidics..... 181
Figure 5.18. Optimization of growth flow rate in featureless channels..... 182
Figure 5.19. Optimization of growth flow rate in herringbone channels..... 183
Figure 5.20. Evaluation of products at different flow rates and profiles. 183
Figure 5.21. Spectroscopic analysis of gold consumption in the channels..... 185

Figure 6.1. Jablonski diagrams for elastic and Raman scattering..... 198
Figure 6.2. Plasmon hybridization theory for a gold nanostar..... 199
Figure 6.3. Schematic for circulating tumor cell capture microfluidic device. 201
Figure 6.4. Thermal camera characterization of irradiated nanostars..... 203
Figure 6.5. Characterization of spot-to-spot variation in capillary heating. 203
Figure 6.6. Setup for thermal camera/surface enhanced Raman scattering measurements. 204
Figure 6.7. Surface enhanced Raman scattering spectroscopic characterization..... 206
Figure 6.8. Correlated study with thermal measurments and Raman scattering spectra. 207
Figure 6.9. Example of nanostar reshaping at high laser power..... 208
Figure 6.10. Method for estimating the steady state change in temperature. 208
Figure 6.11. Measured steady state temperature difference. 209
Figure 6.12. Correlated thermal and laser scanning confocal experimental setup.. 211
Figure 6.13. Probing grafted cell response to localized plasmonic heating..... 212
Figure 6.14. Cell adhesion to the nanostar-coated capillary over 1 h..... 213
Figure 6.15. Control experiment of temperature change in an unfunctionallized capillary. 214

Figure A.1. Schematics of Turkevich and seed-mediated synthesis..... 237
Figure A.2. Optical and electron microscopy characterization for Turkevich products..... 240
Figure A.3. Optical and electron microscopy characterization of gold nanostars. 242
Figure A.4. Transmitted and scattered light from nanoparticles with different diameters. 244

List of Tables

Table 4.1 Square pillar array hard polydimethylsiloxane stamp dimensions. 119
Table 4.2. Summary of products observed at different growth times..... 131
Table 4.3. Characterization of patterning yield across growth times 133

Table 5.1. Comparison of colloidal and *in situ* products. 168

Table 6.1. Measured power for continuous wave laser..... 214
Table 6.2. Extrapolated power for fs-pulsed laser. 214

List of Symbols

Chapter 1

$\epsilon(\omega)$	Complex dielectric function
ω_p	Plasma frequency
ω	External field frequency
γ	Damping constant
$\epsilon_1(\omega)$	Real part of the complex dielectric function
$\epsilon_2(\omega)$	Imaginary part of the complex dielectric function
a	Nanoparticle geometrical
α	Polarizability
ϵ_{in}	Permittivity inside the particle
ϵ_{out}	Permittivity outside the particle
α_{Drude}	Drude polarizability
σ_{abs}	Absorption cross section
ω_1	Plasmon resonance frequency
σ_{sca}	Scattering cross section
k	Wavenumber
a, b, c	Semi-axes of a nanoparticle
L	Geometrical factor for a nanoparticle
R_e	Reynold's number
υ	Characteristic fluid velocity
ρ	Fluid density
D_h	Hydraulic diameter of the microfluidic channel
μ	Fluid viscosity

Chapter 4

V_{final}	(Final) volume of the negative space around a pillar of a hard polydimethylsiloxane mold
V_1	Volume contained within a square region of a hard polydimethylsiloxane mold indicated in **Figure 4.2R**
V_2	Volume contained within the pillar region of a hard polydimethylsiloxane mold indicated in **Figure 4.2R**
$V_{initial}$	Volume of the initial hydroxypropyl cellulose film
A_1	Area covered by the square region of a hard polydimethylsiloxane mold indicated in **Figure 4.2R**
A_2	Area of a hard polydimethylsiloxane mold pillar indicated in **Figure 4.2R**
Λ	Lattice array spacing (from center to center of the pillars of a hard polydimethylsiloxane mold indicated in **Figure 4.2R**)
h_{pillar}	Height of the hard polydimethylsiloxane mold pillar

r	Radius of the hard polydimethylsiloxane mold pillar
h_{min}	Minimum height of the hydroxypropylcellulose film required to match the negative volume of the mold
λ	Irradiation wavelength
$\Lambda_{x,y}$	Lattice parameters in two orthagonal in-plane directions
n	Refractive index of the surrounding medium
$\sin\theta$	Illumination incidence angle
x,y	Geometrical parameters for a square array
n_{PDMS}	Refractive index of polydimethylsiloxane

Chapter 6

I_{SERS}	Surface enhanced Raman scattering intensity
a	Average size of field-enhancing features on the surface
r	Distance of adsorbate from feature surface
ΔT	Temperature change
q	Heat
$\dot{V}$	Volumetric flow rate
ρ	Water density
C_p	Specific heat of water
X	Power of the laser source

List of Acronyms

2/3D	Two/three dimensional
AA	Ascorbic acid
APTES	(3-Aminopropyl)triethoxysilane
APTMS	(3-Aminopropyl)trimethoxysilane
AR	Aspect ratio
AuNP	Gold nanoparticle
AuNST	Gold nanostar
Avg	Average
BCML	Block copolymer micelle lithography
CBAm	*N,N*-cystamine-bis-acrylamide
CCD	Charged-coupled device
CD	Circular dichroism
CNI	Compact nanoimprint tool
CPL	Circular polarized light
CTAB	Cetrimonium bromide; cetyltrimethylammonium bromide
CTAC	Cetrimonium chloride; cetyltrimethylammonium chloride
DCE	Dichloroethane
DMEM	Dulbecco's Modified Eagle Medium

DMF	*N, N*-dimethylformamide
(D)PBS	(Dubelco's) phosphate-buffered saline
EtOH	Ethanol
FTIR	Fourier-transform infrared
GFP	Green fluorescent protein
HB	Herringbone
HEPES	(4-(2-hydroxyethyl)-1-piperazineethanesulfonic acid)
HPC	Hydroxypropylcellulose
HPLC	High-performance liquid chromatography
(h)PDMS	(Hard) polydimethylsiloxane
PTFE	Polytetrafluoroethylene
ITO	Indium
Laser	Light amplification by stimulated emission of radiation
LPR	Lattice plasmon resonance
LSB	Laurylsulfobetaine: *N*-dodecyl-*N,N*-dimethyl-3-ammonio-1-propanesulfonate
LSPR	Localized surface plasmon resonance
Max	Maximum
MBA	Mercaptobenzoic acid
MBAm	*N,N*-methylene-bis-acrylamide
Min	Minimum
MPTMS	(3-Mercaptopropyl)trimethoxysilane
MUHEG	(11-mercaptoundecyl)hexa(ethylene glycol)
MW	Molecular weight
N.A.	Numerical aperture
(N)IR	(Near) infrared
(NP-)CLL	(Nanoparticle-)chemical lift-off lithography
PEG-SH	Polyethylene glycol-thiol
PMHS	Polymethylhydrosiloxane
PMMA	Poly(methyl methacrylate)
PNIPAm	Poly(*N*-isopropylacrylamide)
PVP	Polyvinylpyrrolidone
SEM	Scanning electron microscopy
SERS	Surface enhanced Raman scattering
SPR	Surface plasmon resonance
TBA-TBP	Tetrabutylammonium tetraphenylborate
TEM	Transmission electron microscopy
(t-)NIL	(Thermal-)nanoimprint lithography
UV	Ultraviolet
VdW	van der Waals

Acknowledgments

To my husband, I thank you for growing with me and for helping me push through the countless challenges in academia. I thank my mother for encouraging me throughout my education and for her hard work to provide me with opportunities to go further in life. I also thank my family, especially my cousins and all members of the "Willson 8 Ranch." I would not be where I am today without your love and support.

I would first like to thank my dissertation mentors, Prof. Paul S. Weiss and Prof. Steven J. Jonas, for giving me the opportunity to join UCLA and to work with top scientists and experts locally and globally. I also thank the Weiss and Jonas groups for all their feedback and advice. From the group, I especially thank Derek, Xi, and Joy for their talent and dedication as my mentees. I would also like to thank Dr. Kris Barr for his assistance, know-how, and *persistent* optimism while we worked together in the PEERS program and as TAs.

In addition to the teams at UCLA, I also thank the groups of Prof. V. C. Tung (KAUST) and Dr. A. Mihi and Dr. L. Scarabelli (ICMAB) for sharing their time, laboratory space, and equipment during my stays as a visiting researcher, where I explored new projects, techniques, ideas and places. Ylli, Jose, Pau, Martí, Minghua, David, Serni, Miquel, Oriol, Luis, Osnat, and all the many current and former members of the NANOPTO team who helped with our project, thank you all for welcoming me and for making every day in the lab fun and exciting!

Aside from my advisors, I have been fortunate to encounter so many mentors who supported me both in and outside of the lab. I would like to thank Prof. Mary E. Anderson for her advice and guidance as one of my earliest mentors in graduate school. I also thank Prof. Sarah H. Tolbert for her advisement as part of the California NanoSystems Institute outreach program, which taught me invaluable lessons regarding education and nanoscience communication.

Now to my lab parents, Naihao and Leo. First, thank you both for always believing in me. In times where I made mistakes or felt unsure of my capabilities, neither of you gave up on my ability to learn and progress. Thank you for the long days and late nights spent working with me in the lab and for reading and editing all of my papers, abstracts, emails, *etc.* Your efforts ultimately helped shape me into my role as "nanoparticle girl." Even more, I am thankful for all the lessons you taught me outside of lab, which have helped me become a better cook, a harsher movie critic, a more effective troll, and a person who goes up rocks. I have learned so much from you in research and in life, and I am so happy to know you, both as mentors and friends.

Fidel, you have been there for me since the beginning at UCLA, and I will really miss our game nights, dinners, movie nights, and concerts. You added a lot of joy to my grad school experience and I am so thankful to have met you. Dr. Luo, even before I joined PhD, you challenged me to be my best. Thank you for your friendship and for the competition!

Finally, I gratefully acknowledge research funding from the Alex's Lemonade Stand Foundation for Childhood Cancer Research, the Hyundai Hope on Wheels Foundation for Pediatric Cancer Research, the UCLA Clinical and Translational Science Institute Core Voucher Program (UL1TR001881), and the Spanish National Research Council I-LINK 2020 international travel grant. I also acknowledge the UCLA graduate division of the University of California Office of the President Dissertation Year Fellowship.

Over the course of the 6 years of my PhD studies, I have learned so much from so many and am truly grateful to everyone who supported me along the way.

Gail A. Vinnacombe-Willson, 2022

Co-Author Contributions

Chapter 2 is a version of: Scarabelli, L., Chiang, N., Vinnacombe-Willson, G. A., Pérez, L. A., Dore, C., Mihi, A., Weiss, P. S., Jonas S. J. "Patterning of Plasmonic Nanoparticles Through Chemical Lift-Off Lithography." *ACS Mater. Lett.* 2021, 3 (3), 282-289.

N.C. and L.S. contributed equally. The manuscript was written through contributions of all authors. L.S., N.C., and G.A.V.W. designed and performed the synthesis and self-assembly of the colloids and developed and optimized the NP-CLL technique. Experiments were designed by L.S., N.C., and G.A.V.W. Circular dichroism spectra were collected by L.S. with the assistance of L.A.P. and A.M. The hydroxypropyl cellulose transfer was optimized and performed by C.D. Figures were prepared by L.S., N.C., and G.A.V.W. The manuscript was written by L.S., N.C., G.A.V.W., A.M., S.J.J., and P.S.W. with assistance from all other authors.

Chapter 4 is a version of: Vinnacombe-Willson, G. A., Conti, Y., Jonas S. J, Weiss, P. S., Mihi, A., Scarabelli, L. "Surface Lattice Plasmon Resonances by Direct Surface Growth of Gold Nanoparticles in Ordered Arrays." *Submitted.*

Experiments were designed by G.A.V.W. and L.S. G.A.V.W. and L.S. led the optimization of the HPC stencil fabrication. G.A.V.W., L.S., and Y.C. performed the synthesis optimization of the AuNPs into arrays. Morphological characterization of the AuNPs was performed by G.A.V.W. and L.S. Optical characterization was carried out by L.S. and Y.C. The manuscript was written by G.A.V.W., L.S., S.J.J., P.S.W., A.M., with assistance from all other authors.

Chapter 5,6 are a version of: Vinnacombe-Willson, G. A., Chiang, N., Scarabelli, L., Hu, Y., Heidenreich, L., Xi, L, Gong, Y., Inouye, D. T., Fisher, T., Weiss, P. S., Jonas, S. J. "*in Situ* Growth

of Gold Nanostars in Flow for Controlled Hyperthermia-Mediated Cell Release," *ACS Cent. Sci.* 6 (11), 2105-2116.

The experiments were designed by G.A.V.W., L.S., N.C., P.S.W., and S.J.J. G.A.V.W. and L.S. led the colloidal and *in situ* growth optimization. N.C. led the concurrent Raman/thermal imaging and laser scanning confocal/thermal imaging. Data were collected by G.A.V.W., L.S., N.C., L.K.H., X.L., Y.G., and D.T.I. Thermal analyses were performed by Y.H. and T.S.F. Figures were prepared by G.A.V.W., L.S., N.C., and Y.H. The manuscript was written by G.A.V.W., L.S., N.C., P.S.W., and S.J.J., with assistance from all other authors. The experiments relating to the polydimethylsiloxane microfluidic channels were led and designed by G.A.V.W. The synthesis and device fabrication optimization was led by G.A.V.W., with assistance from Joy Lee, who led the spectroscopic analysis of gold consumption in the herringbone micromixer. The COMSOL simulations were performed by Isa M. Frost.

Appendix A is a version of: Vinnacombe-Willson, G. A., Chiang, N., Weiss, P. S., Tolbert, S. H., Scarabelli, L. "Seeded-Growth Experiment Demonstrating Size- and Shape-Dependence on Gold Nanoparticle–Light Interactions," *J. Chem. Ed.* 2020, 98 (2), 546-552.

G.A.V.W. and L.S. led the development of the laboratory experiment with assistance from N.C. G.A.V.W, N.C., L.S., and S.T. led the implementation of the experiment in middle and high school teacher workshops and with high school students as part of the California NanoSystems Institute high school summer camp. G.A.V.W and L.S. prepared the figures. The manuscript was written by G.A.V.W., N.C., and L.S., with support from P.S.W. and S.T.

VITA

Gail A. Vinnacombe-Willson

EDUCATION

Contra Costa Community College	**University of San Francisco**	**University of California, Los Angeles**
A.A. Liberal Arts, Emphasis in Mathematics & Science	B.S. Chemistry – ACS certified Minor: Mathematics	M.S. Materials Chemistry
Sept. 2008- May 2012	*Aug. 2012-May 2016*	*June 2016-May 2018*

RESEARCH EXPERIENCE

University of California, Los Angeles | Graduate Student Researcher

June 2016 – July 2022 | Los Angeles, CA | Advisors: Prof. Paul S. Weiss & Prof. Steven J. Jonas

- Led a project integrating plasmonic nanoparticles in microfluidic platforms and on polymers for biomedical applications.
- Connected with groups outside my area of expertise and formed new collaborations with groups outside my field and engaged with a diverse team of engineers, physicians, and chemists.
- Produced one 1st-author paper (*ACS Cent. Sci.*) and one 3rd-author paper (*ACS Mater. Lett.*), a patent, an oral presentation, two national and one international poster presentations, and one poster award.
- Mentored bioengineering students in a project designing a 3D-printed fitting for uniform distribution of aerosols into cell-culture plates (invention disclosure submitted) for applications in therapeutics for cystic fibrosis.

Institute of Materials Science of Barcelona | Visiting Graduate Student Researcher

May 2021 – Nov. 2021 | | Barcelona, Spain | Hosts: Dr. Agustín Mihi & Dr. Leonardo Scarabelli

- Advanced the understanding of how bottom-up wet chemical synthesis, soft lithography, and surface chemical functionalization of polymers can be combined to create nanopatterned plasmonic substrates.
- Established methods for scalable fabrication of plasmonic substrates and provided data key for securing a two-year international collaboration grant.

King Abdullah University of Science and Technology |Visiting Graduate Student Researcher

Nov. 2019 | Thuwal, Saudi Arabia | Host: Dr. Vincent Tung

- Two-week research visit integrating my patterned plasmonic substrates with two-dimensional materials.
- Established a collaboration between my thesis advisor (Prof. Jonas) and Prof. Tung's group, and the two groups are continuing to pursue joint research lines.

University of San Francisco | Undergraduate Researcher

March 2014 – May 2016 | San Francisco, CA | Advisors: Prof. Claire Castro & Prof. William Karney

- Elucidated key mechanisms which increased understanding of the role of curvature in annulene carbon-carbon rearrangements, leading to a 3rd author publication in *J. Org. Chem.,* two oral and four poster presentations, and one oral presentation award.

PUBLICATIONS

1. **Vinnacombe-Willson, G. A**., Stefancu, A., Cortés, E. Weiss, P. S., Scarabelli, L. "Direct Bottom-Up *in Situ* Growth: A Paradigm Shift for Studies in Wet-Chemical Synthesis of Gold Nanoparticles." *In preparation.*

2. **Vinnacombe-Willson, G. A**., Conti, Y., Jonas S. J, Weiss, P. S., Mihi, A., Scarabelli, L. "Surface Lattice Plasmon Resonances by Direct Surface Growth of Gold Nanoparticles in Ordered Arrays." *Submitted.*
3. Scarabelli, L., Chiang, N., **Vinnacombe-Willson, G. A**., Pérez, L. A., Dore, C., Mihi, A., Weiss, P. S., Jonas S. J. "Patterning of Plasmonic Nanoparticles through Chemical Lift-Off Lithography." *ACS Mater. Lett.* 2021, 3 (3), 282-289.
4. **Vinnacombe-Willson, G. A.**, Chiang, N., Weiss, P. S., Tolbert, S. H., Scarabelli, L. "Seeded-Growth Experiment Demonstrating Size- and Shape-Dependence on Gold Nanoparticle–Light Interactions," *J. Chem. Ed.* 2020, 98 (2), 546-552.
5. **Vinnacombe-Willson, G. A.**, Chiang, N., Scarabelli, L., Hu, Y., Heidenreich, L., Xi, L, Gong, Y., Inouye, D. T., Fisher, T., Weiss, P. S., Jonas, S. J. "*in Situ* Growth of Gold Nanostars in Flow for Controlled Hyperthermia-Mediated Cell Release," *ACS Cent. Sci.* 6 (11), 2105-2116.
6. Irace, E. E., Brayfindley, E., **Vinnacombe, G. A.**, Castro, C. & Karney, W. L. Stone-Wales Rearrangements in Hydrocarbons: From Planar to Bowl-Shaped Substrates. J. Org. Chem. 2015, 80 (23), 11718–11725.

PATENTS

Systems and methods of using anisotropic nanostructures in microfluidic devices for binding and optional release of molecules and cells. *International Patent Appl. No.* WO2020037238A1 – Feb 20, 2020

COMMUNICATION & PRESENTATIONS

1. Bruins Fighting Pediatric Cancer Education Fair, Los Angeles, CA, May 2022 Talk.
2. ACS National Meeting, San Diego, CA, March 2022 Talk.
3. NANOPTO meeting, Barcelona, Spain, September 2021 Talk.
4. ACS National Meeting, San Diego, CA, Aug. 2019 Talk & Poster. **Selected for Sci-Mix**
5. 47th IUPAC World Chemistry Congress, Paris, France July 2019 Poster.
6. APS Far West Meeting, Fullerton, CA, Oct. 2018 Poster; **Graduate Award**
7. ACS National Meeting, Boston, MA, Aug. 2018 Poster.
8. Northern California Undergraduate Research Symposium, Moraga, CA, Apr. 2016 Talk.
9. ACS National Meeting, Denver, CO, Apr. 2016 Poster.
10. Creative Activity and Research Day, San Francisco, CA, Oct. 2015 Talk. **Undergraduate Award**
11. USF ACS Student Chapter Meeting, San Francisco, CA, Mar. 2015 Poster.
12. Northern California Undergraduate Research Symposium, Santa Cruz, CA, May 2015 Poster.
13. Creative Activity and Research Day, San Francisco, CA, Apr. 2015 Poster.

AWARDS & HONORS

1. University of California Office of the President Graduate Dissertation Year Fellowship
2. I-LINK+ 2020 International Collaboration Grant
3. UCLA Brain Research Institute Annual Calendar Image Contest Winner
4. American Chemical Society Travel Showcase Award
5. American Physical Society Far West Graduate Student Poster Award, American Physical Society
6. Hanson-Dow Excellence in Teaching Award, University of California, Los Angeles
7. NSF Graduate Research Fellowship Honorable Mention, National Science Foundation
8. The American Institute of Chemists Student Award, American Institute of Chemists
9. The American Chemical Society Inorganic Chemistry Award, American Chemical Society
10. Oral Presentation Award at Creative Activity and Research Day, University of San Francisco
11. Ron Najafi Award for Innovations and Entrepreneurship in Chemistry, University of San Francisco
12. Award for Overall Achievement in Physical Chemistry, University of San Francisco

Historical Overview

Nanotechnology involves the fabrication and manipulation of materials at the nanoscale, with the purpose of creating and studying novel systems with properties that differ from bulk materials.[1–3] Although the term "nanotechnology" was first coined by Taniguchi in 1974,[4] the nanotechnology boom is often attributed to the famous 1959 lecture "*There's Plenty of Room at the Bottom: An Invitation to Enter a New Field of Physics*" by Richard Feynman.[5] In his talk, Feynman contemplated building up new materials atom-by-atom to produce precisely tailored nanoscale systems with exceptional properties. He contemplated how this approach could push the miniaturization of computers, machines, and medical technologies for the greater benefit of society. In line with this idea, modern nanoscience has broadly expanded to incorporate many disciplines, including physics, chemistry, biology, and engineering, and targets the development of novel medical treatments, electronics, and technologies for a cleaner more sustainable future.[3]

The work presented in this thesis focuses on a specific branch of nanoscience concerning the study of plasmonic metal nanoparticles, which are of great research interest due to their exciting and tunable size-related characteristics.[6] When copper, silver, and gold are miniaturized to the nanometer scale, they exhibit vibrant colors that starkly differ from the characteristic metallic appearance of their bulk counterparts. This property is a direct consequence of their small dimensions, which lead to great enhancement of ultraviolet (UV)-visible-near infrared (NIR) light absorption and scattering.[6] Moreover, plasmonic nanoparticles are characterized by high local field enhancements,[7] high surface area-to-volume ratio,[8] increased chemical reactivity,[8] low melting point,[9] and other unique chemical, physical, and biological characteristics that differ from bulk metals.[6] Research on this topic focuses on improving control over these size-dependent

properties and improving the understanding how they can be leveraged to engineer nanoparticles for select applications in chemistry,[8,10] physics,[11–13] and biology.[2,14]

Although the study of plasmonic nanoparticles remains an active field of research, the first colloidal and *in situ* syntheses of plasmonic nanoparticles dates back to long before mentions of nanotechnology and plasmons.[6,15] One of the most famous historical objects incorporating nanoparticles is the 5th century CE Roman artifact, the Lycurgus cup, a chalice depicting the death of King Lycurgus of Thrace in dichroic glass.[16] Different colorations can be observed depending on illumination and viewing angles, which was finally attributed to the impregnation of the glass with silver, gold, and copper nanoparticles in 1990.[17] Although the idea of nanoparticles was a foreign concept to glass makers during this time, silver and copper nanoparticles were used in lustrous ceramic glass as early as 1400-1300 BCE in Mesopotamia.[18,19] By the 17th century, it was routine to prepare brightly colored glass by dissolving bulk gold in *aqua regia* (royal water) and incorporating the resulting gold salt during the glass-making process with appropriately added reductants.[16] In the 1685 work *De Auro,* Andreas Cassisus famously described the preparation of purple glass through the incorporation of gold salts, which came to be known as the "purple of Cassisus."[20]* Another early implementation of plasmonic particles included the invention of Daguerreotype photographs in 1839, which relied on *in situ* photooxidation of silver ions on a copper sheet to capture images.[21] In 1857, an important breakthrough was made when Michael Faraday performed the first systematic synthetic study of colloidal gold nanoparticles, which led him to make the first connection between the color of the solution and the size of the metal,

*There are mentions of ceramic glass with faint pink to purple coloration due to the use of gold salts as much as 25 years earlier than the publication of *De Auro*. However, *De Auro* is most famously credited for this process.

describing the gold as being "reduced in exceedingly fine particles."†[22,23] Ultimately, the wine-red coloration of gold nanoparticle colloids would not be explained fully until more than 50 years later, in 1908, when Gustav Mie provided solutions to Maxwell's equations for spherical metal nanoparticles.[24] Additionally, the first capabilities to "see" and to measure nanoparticles with diameters as low as 10 nm was realized by with the 1898 development of the ultramicroscope by Richard Zsigmondy, who won a Nobel prize for this discovery in 1925.[25,26] At the time of Feynman's famous talk, the limit of resolution for electron microscopies advanced to 10 Å. Today, sub-Angstrom resolution is routine.[27–29]

Modern-Day Implementation of Nanomaterials

With modern capabilities that enable researchers to characterize and to manipulate materials at the nano- and atomic scales, the nanotechnology research boom has produced a plethora of commercial products that take advantage of nanomaterials. For example, carbon nanotubes have structural and optical properties that facilitate implementation in lightweight and durable sports equipment,[30] batteries,[31] and ultrablack satellite coatings.[32] Inorganic nanoparticles find commercial use in sunscreens (titanium dioxide and zinc oxide)[33] and cosmetics (silica and gold).[34] For energy applications, nanostructured silicon is found in commercial solar cells and transistors.[35,36] High-quality displays take advantage of the optical properties of quantum dots (cadmium selenide and indium phosphide).[37] The antibacterial properties of nanosilver motivate its implementation in bandages and active wear.[38,39] In December 2019, the global pandemic caused by the SARS-CoV-2 virus profoundly impacted

†Faraday's colloidal "ruby gold" solutions remain stable and retain their optical properties 150 years later. They are housed at The Royal Institution in London.

society and consequently garnered even more attention for applied nanomaterials. Specifically, early strategies to mitigate the spread of the virus relied on lipid nanoparticle-mRNA vaccines and silver nanoparticle rapid diagnostic tests.[40–43] Although commercial nanotechnologies do not (yet) include the nano-cars, nano-surgeons or self-replicating nanobots as imagined by Feynmann[5] and others,[44] nanoscience remains an exciting frontier for researchers in all fields and important works in this area continue to unfold.

Overview of the Thesis

The introductory chapter begins with a brief description of plasmons in metals from bulk systems down to the nanoscale and factors that affect the plasmonic properties of individual nanoparticle. Then, factors affecting size and shape in the colloidal synthesis of gold nanoparticles and the engineering of plasmonic substrates and devices are discussed. In **Chapter 2**, a study of the synthesis, self-assembly, and patterning of colloidally made gold nanospheres *via* soft-lithography is presented. In **Chapter 3**, I will provide background on the developments of *in situ* growth methods, where instead of using pre-made colloidal particles, the nanostructures are grown directly on the solid material of interest. In **Chapter 4** and **5**, I describe how I have applied *in situ* growth and *in situ* shape control to fabricate gold nanoparticle arrays and thermoplasmonic nanostar-functionalized microfluidic devices, respectively. A summary of the conclusions and a brief outlook on the field will follow. Lastly, once can recall that the closing remarks in Feynman's famous lecture were reserved to express his hope that the new and exciting field of nanoscience would encourage more involvement of students and young people in science. With this same spirit, the **Appendix** of this thesis will present an educational laboratory experiment where high-school or undergraduate students synthesize gold nanoparticles with different sizes and shapes.

References

[1] P. K. Jain, X. Huang, I. H. El-Sayed, M. A. El-Sayed, *Acc. Chem. Res.* **2008**, *41*, 1578.

[2] E. C. Dreaden, A. M. Alkilany, X. Huang, C. J. Murphy, M. A. El-Sayed, *Chem. Soc. Rev.* **2012**, *41*, 2740.

[3] L. Pokrajac, A. Abbas, W. Chrzanowski, G. M. Dias, B. J. Eggleton, S. Maguire, E. Maine, T. Malloy, J. Nathwani, L. Nazar, A. Sips, J. Sone, A. van den Berg, P. S. Weiss, S. Mitra, *ACS Nano* **2021**, *15*, 18608.

[4] N. Taniguchi, **1974**.

[5] R. Feynman, *J. Eng. Sci.* **1960**, *4*, 23.

[6] M. Pelton, G. Bryant, *Introduction to Metal-Nanoparticle Plasmonics*, John Wiley & Sons Inc., And Science Wise Publishing, **2013**.

[7] K. A. Willets, R. P. Van Duyne, *Annu. Rev. Phys. Chem.* **2007**, *58*, 267.

[8] E. Cortés, P. H. Camargo, *Plasmonic Catalysis: From Fundamentals to Applications*, John Wiley & Sons, **2021**.

[9] J.-H. Shim, B.-J. Lee, Y. W. Cho, *Surf. Sci.* **2002**, *512*, 262.

[10] P. Ilgin, O. Ozay, H. Ozay, *Appl. Catal. B Environ.* **2019**, *241*, 415.

[11] J. Henzie, M. H. Lee, T. W. Odom, *Nat. Nanotechnol.* **2007**, *2*, 549.

[12] W. Zhou, M. Dridi, J. Y. Suh, C. H. Kim, D. T. Co, M. R. Wasielewski, G. C. Schatz, T. W. Odom, *Nat. Nanotechnol.* **2013**, *8*, 506.

[13] V. A. Turek, Y. Francescato, P. Cadinu, C. R. Crick, L. Elliott, Y. Chen, V. Urland, A. P. Ivanov, L. Velleman, M. Hong, R. Vilar, S. A. Maier, V. Giannini, J. B. Edel, *ACS Photonics* **2016**, *3*, 35.

[14] Y. Chen, Y. Xianyu, X. Jiang, *Acc. Chem. Res.* **2017**, *50*, 310.

[15] P. Sciau, in *Deliv. Nanoparticles*, IntechOpen, Rijeka, **2012**, p. 554.

[16] I. Freestone, N. Meeks, M. Sax, C. Higgitt, *Gold Bull.* **2007**, *40*, 270.

[17] D. J. Barber, I. C. Freestone, *Archaeometry* **1990**, *32*, 33.

[18] F. J. Heiligtag, M. Niederberger, *Mater. Today* **2013**, *16*, 262.

[19] C. Louis, O. Pluchery (eds.), *Gold Nanoparticles for Physics, Chemistry and Biology*. World Scientific, **2017**.

[20] L. B. Hunt, *Gold Bull.* **1976**, *9*, 134.

[21] A. E. Schlather, P. Gieri, M. Robinson, S. A. Centeno, A. Manjavacas, *Proc. Natl. Acad. Sci.* **2019**, *116*, 13791.

[22] M. Faraday, *Philos. Trans. R. Soc. Lond.* **1857**, *147*, 145.

[23] D. Thompson, *Gold Bull.* **2007**, *40*, 267.

[24] G. Mie, *Ann. Phys.* **1908**, *330*, 377.

[25] R. Zsigmondy, *Justus Liebigs Ann. Chem.* **1898**, *301*, 29.

[26] T. Mappes, N. Jahr, A. Csaki, N. Vogler, J. Popp, W. Fritzsche, *Angew. Chem. Int. Ed.* **2012**, *51*, 11208.

[27] H. Gawronski, M. Mehlhorn, K. Morgenstern, *Science* **2008**, *319*, 930.

[28] A. N. Chaika, O. V. Molodtsova, A. A. Zakharov, D. Marchenko, J. Sánchez-Barriga, A. Varykhalov, I. V. Shvets, V. Yu. Aristov, *Nano Res.* **2013**, *6*, 562.

[29] S. J. Pennycook, *MRS Bull.* **2015**, *40*, 71.

[30] A. M. K. Esawi, M. M. Farag, *Mater. Des.* **2007**, *28*, 2394.

[31] P. Simon, Y. Gogotsi, *Nat. Mater.* **2008**, *7*, 845.

[32] F. De Nicola, P. Hines, M. De Crescenzi, N. Motta, *Phys. Rev. B* **2017**, *96*, 045409.

[33] R. G. de Sá, T. M. Arantes, E. F. de Macedo, L. M. Dona', J. C. F. Pereira, C. R. Hurtado, R. J. Varghese, O. S. Oluwafemi, D. B. Tada, *Colloids Surf. B* **2021**, *202*, 111636.

[34] G. Fytianos, A. Rahdar, G. Z. Kyzas, *Nanomater. Basel Switz.* **2020**, *10*, 979.

[35] R. Martins, L. Raniero, L. Pereira, D. Costa†, H. Águas, S. Pereira, L. Silva, A. Gonçalves, I. Ferreira, E. Fortunato, *Philos. Mag.* **2009**, *89*, 2699.

[36] S. E. Han, G. Chen, *Nano Lett.* **2010**, *10*, 4692.

[37] Y. Shirasaki, G. J. Supran, M. G. Bawendi, V. Bulović, *Nat. Photonics* **2013**, *7*, 13.

[38] L. J. Wilkinson, R. J. White, J. K. Chipman, *J. Wound Care* **2011**, *20*, 543.

[39] H. E. Emam, A. P. Manian, B. Široká, H. Duelli, B. Redl, A. Pipal, T. Bechtold, *J. Clean. Prod.* **2013**, *39*, 17.

[40] W. W.-W. Hsiao, T.-N. Le, D. M. Pham, H.-H. Ko, H.-C. Chang, C.-C. Lee, N. Sharma, C.-K. Lee, W.-H. Chiang, *Biosensors* **2021**, *11*, 295.

[41] E. J. Anderson, N. G. Rouphael, A. T. Widge, L. A. Jackson, P. C. Roberts, M. Makhene, J. D. Chappell, M. R. Denison, L. J. Stevens, A. J. Pruijssers, A. B. McDermott, B. Flach, B. C. Lin, N. A. Doria-Rose, S. O'Dell, S. D. Schmidt, K. S. Corbett, P. A. Swanson, M. Padilla, K. M. Neuzil, H. Bennett, B. Leav, M. Makowski, J. Albert, K. Cross, V. V. Edara, K. Floyd, M. S. Suthar, D. R. Martinez, R. Baric, W. Buchanan, C. J. Luke, V. K. Phadke, C. A. Rostad, J. E. Ledgerwood, B. S. Graham, J. H. Beigel, *N. Engl. J. Med.* **2020**, *383*, 2427.

[42] L. R. Baden, H. M. El Sahly, B. Essink, K. Kotloff, S. Frey, R. Novak, D. Diemert, S. A. Spector, N. Rouphael, C. B. Creech, J. McGettigan, S. Khetan, N. Segall, J. Solis, A. Brosz, C. Fierro, H. Schwartz, K. Neuzil, L. Corey, P. Gilbert, H. Janes, D. Follmann, M. Marovich, J. Mascola, L. Polakowski, J. Ledgerwood, B. S. Graham, H. Bennett, R. Pajon, C. Knightly, B. Leav, W. Deng, H. Zhou, S. Han, M. Ivarsson, J. Miller, T. Zaks, *N. Engl. J. Med.* **2021**, *384*, 403.

[43] M. Sarsfield, A. Roberts, K. A. Streletzky, P. S. Fodor, C. R. Kothapalli, *Chem. Eng. Technol.* **2021**, *44*, 622.

[44] Kolbe, Winrich, *Star Trek: The Next Generation,* Season 3, Episode 1. **1989**.

Chapter 1. Introduction

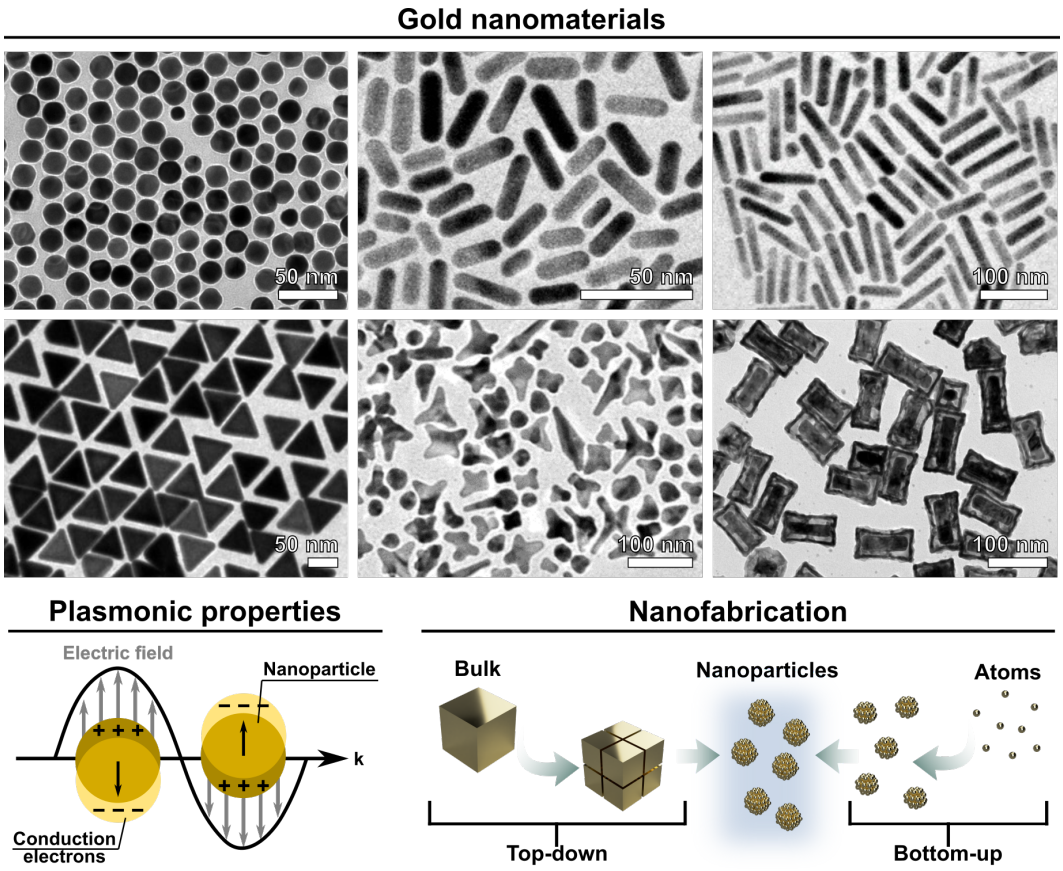

Compared to bulk gold, plasmonic gold nanoparticles have unique size-related properties, including high surface area, low melting point, and strong interaction with light. Their optical properties depend on the local dielectric environment as well as their geometrical characteristics, which can be controlled by bottom-up or top-down nanofabrication.

Section 1.1. Plasmonic Properties of Metal Nanostructures

Over the past few decades, significant research emphasis has been placed on plasmonic nanomaterials, as they possess intriguing physical, electronic, and chemical properties.[1–3] The term "plasmon" was first introduced to describe high frequency collective oscillations in metals by David Pines in the 1950s.[4] Plasmons in metals earned their name due to their similarity to electron density oscillations in gaseous plasmas, with the difference being that metals have much higher electron densities, resulting in considerably higher frequencies.[5] In this section, we will briefly discuss the plasmonic properties of bulk metals, metal-dielectric interfaces, and nanoparticles.

1.1.1. Plasmons

1.1.1.1. Bulk and surface plasmons

In bulk materials, an incident electromagnetic field can induce "volume" plasmons, which manifest as longitudinal propagating charge-density waves as depicted in **Figure 1.1A**.[5] In a metal-dielectric interface as shown in **Figure 1.1B**, highly localized "surface plasmons" that propagate parallel to the surface and decay exponentially away from the interface emerge.[5–9] As for the bulk case, regions with alternating positive and negative charge densities are generated by the external electromagnetic field. At the interface, this effect results in the generation of transverse electromagnetic fields induced by the oscillating conduction electrons of the metal. The resulting hybrid propagating wave can be described as a surface plasmon polariton.[5] Unlike bulk systems, surface plasmons can be excited with light as long as the momentum mismatch between the incoming light and the surface plasmon is compensated *via* a grating, local surface modification, and/or coupling through a high refractive index prism. The resonant amplification of the surface

plasmon by light is called the surface plasmon resonance (SPR).[5] This highly surface-localized effect is sensitive to changes at the boundary of the metal and the dielectric, and so, SPR shifts are applied to monitor adsorption of molecules or other materials onto metal surfaces.[6]

The Drude-Lorentz model provides a simple approximation for describing the dynamics of a metal's conduction electrons inside an external electric field. In this model, the conduction electrons are treated as a sea of non-interacting electrons moving about periodic, fixed, positively charged cores. The complex dielectric function of the metal in the Drude-Lorentz model, the frequency dependent permittivity of metals, is written as:[10]

$$\epsilon(\omega) = 1 - \frac{\omega_p^2}{\omega^2 + i\omega\gamma} \quad \textbf{[Eq. 1.1]}$$

Here, ω_p is the bulk plasma frequency and γ is a constant representing damping effects. In the first order approximation, the complex dielectric function is expressed as the sum of the real ($\epsilon_1(\omega)$) and imaginary parts ($\epsilon_2(\omega)$):[5,11,12]

$$\epsilon(\omega) = \epsilon_1(\omega) + i\epsilon_2(\omega) \qquad \textbf{[Eq. 1.2]}$$

The real part describes the degree to which the material is polarizable in response to the external field without absorbing energy, where the imaginary part describes energy absorption. Materials capable of supporting a SPR should have a large real and small imaginary permittivity, meaning they can generate a large alternating field on their surface and have negligible absorbance. Some metals exhibiting SPRs include silver, gold, copper, aluminum, sodium, and indium.[13] However, among these materials, silver, gold, and copper are more widely used due to practical requirements for metals with low damping rates that are stable under the appropriate experimental conditions. The overall interaction of metals with light is described by both free- and bound-electron effects. Lower energy excitations of electrons occur within the conduction band (intraband transitions). Electrons in the metal are excited from the valence band to the Fermi level at higher energies, and

the optical response is dominated by these interband transitions, resulting in low or no plasmon resonances.[11] Silver, gold, and copper have interband transition thresholds beginning at *ca.* 3.6 (344 nm), 2.4 (516 nm), and 2.1 eV (590 nm), respectively, making them suitable for applications requiring SPRs in the visible and near-infrared region.[11,14,15] Silver is the only metal of the three that can support stronger SPRs over the entire visible region (1.8-3.1 eV), however, the stability and biocompatibility of gold make it the preferred choice for many applications.[2]

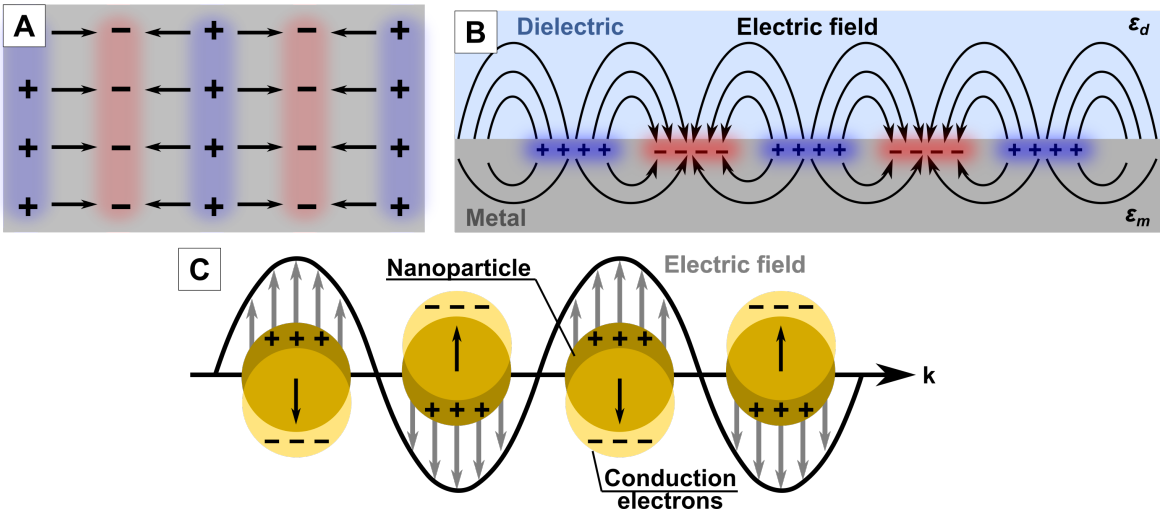

Figure 1.1. Schematic depicting a **A:** volume plasmon (black arrows indicate the electric field), **B:** surface plasmon, and **C:** localized surface plasmon.

1.1.1.2. Localized surface plasmon resonance

When these metals capable of supporting SPRs are instead confined to the nanoscale, they take on dimensions smaller than the wavelengths of the applied field. Instead of the propagating waves seen in the nanoscale metal thin film case, plasmons in nanoparticles form standing waves, and can be described classically as radiating dipoles (**Figure 1.1C**): Impinging light causes the conduction electrons to accumulate at one end of the particle. In response, Coulombic attraction towards the positively charged nanoparticle cores leads to a restoring force, which defines the characteristic oscillation frequency. The introduction of a periodic driving force (light) meeting

the characteristic frequency effectively leads to resonant amplification. This effect is known as the localized surface plasmon resonance (LSPR).[5,6] In this description, the nanoparticle is in the quasistatic limit, where the applied field is spatially constant over the entire structure. Here, the polarizability (α) of the particle is given as:[5]

$$\alpha = \frac{a^3(\epsilon_{in}-\epsilon_{out})\epsilon_{out}}{\epsilon_{in}+2\epsilon_{out}} \quad \textbf{[Eq. 1.3]}$$

where ϵ_{in} represents the dielectric properties of the metal and ϵ_{out} represents the medium surrounding the particle. These expressions are simplified in terms of the plasmon resonance frequency ω_1 and the frequency of the external field ω, when damping is ignored and the particles are considered in vacuum or air, with ϵ_{out} = 1:

$$\alpha_{Drude} = \frac{-\omega_1^2 a^3}{\omega^2-\omega_1^2} \quad \textbf{[Eq. 1.4]}$$

where the particle response to the external field becomes resonant as $\omega \rightarrow \omega_1$.

The LSPR effect gives high optical extinction for nanoparticles with dimension a, where the extinction cross section is the sum of the absorption (σ_{abs}) and scattering cross sections (σ_{sca}), which can be expressed using the polarizability as:[5]

$$\sigma_{abs} = 4\pi k a^3 Im\left[\frac{\epsilon_{in}-\epsilon_{out}}{\epsilon_{in}+2\epsilon_{out}}\right] \quad \textbf{[Eq. 1.5]}$$

$$\sigma_{sca} = \frac{8}{3}\pi k^4 a^6 \left[\frac{\epsilon_{in}-\epsilon_{out}}{\epsilon_{in}+2\epsilon_{out}}\right]^2 \quad \textbf{[Eq. 1.6]}$$

Note that the absorption cross section is proportional to the volume of the particle, and the scattering cross section, which involves absorption and instantaneous elastic reemission of the light, and scales as the square of the particle volume. From these expressions the optical cross sections are maximized when $\epsilon_{in} = -2\epsilon_{out}$.

The near- and far-field optical response also changes for nanoparticles with non-spherical shape. Once again, the Drude model can be used to describe the geometrically dependent

polarizability for the simplest non-spherically symmetric nanoparticle with semi-axes a, b, and c, in the quasistatic limit:

$$\alpha = \frac{abc(\epsilon_{in}-\epsilon_{out})\epsilon_{out}}{3(\epsilon_{out}+L(\epsilon_{in}-\epsilon_{out}))} \textbf{ [Eq. 1.7]}$$

The effect of the geometry is given by the geometrical factor L (still without considering particle size). This expression can once again be simplified similarly to **Equation 1.4**:

$$\alpha_{Drude} = \frac{-\omega_1^2 abc}{\omega^2 - L\omega_p^2} \qquad \textbf{[Eq. 1.8]}$$

Here, the particle response is resonant when $\omega \rightarrow \omega_p\sqrt{L}$, and the resonant frequency of the particle can be directly calculated with $\omega_1 = \omega_p\sqrt{L}$. For a sphere, the L value along all axes is 1/3 (since $a = b = c$. For an ellipsoid where $a = b \neq c$, a trend where increasing c ($L \rightarrow 0$ in the elongation direction) gives lower ω_1. Overall, the shift to lower frequencies can be qualitatively understood to be caused by a reduced restoring force between the charges that accumulate on opposite sides of the long axis of the ellipsoid.

To emphasize the effect of shape on the plasmonic response, we consider gold nanorods as an example. Like the case of the simpler ellipsoid, nanorods support new ω_1 at higher wavelengths due to their longitudinal plasmon mode as shown in **Figure 1.2A,B**. Extinction peaks for the transverse plasmon mode at ~ 520 nm (corresponding to oscillation in the x-y plane as defined in **Figure 1.2A**) and the longitudinal mode, tuned from ~650-875 nm, are shown in **Figure 1.2B**. Increasing the aspect ratio (AR, the ratio of rod length to width) leads to a red-shift in the longitudinal mode peak. The shape-dependent far-field response is further highlighted in the calculated spectra shown in **Figure 1.2C**. Incident light polarized parallel to the long axis of the rod drives the longitudinal plasmon oscillation and shifts to higher wavelengths occur as rod length

L is increased. **Figure 1.2D** shows a similar geometrical effect in the near-field, where rods with increasing *L* exhibit higher local near-field amplification when irradiated at longer wavelengths.[16]

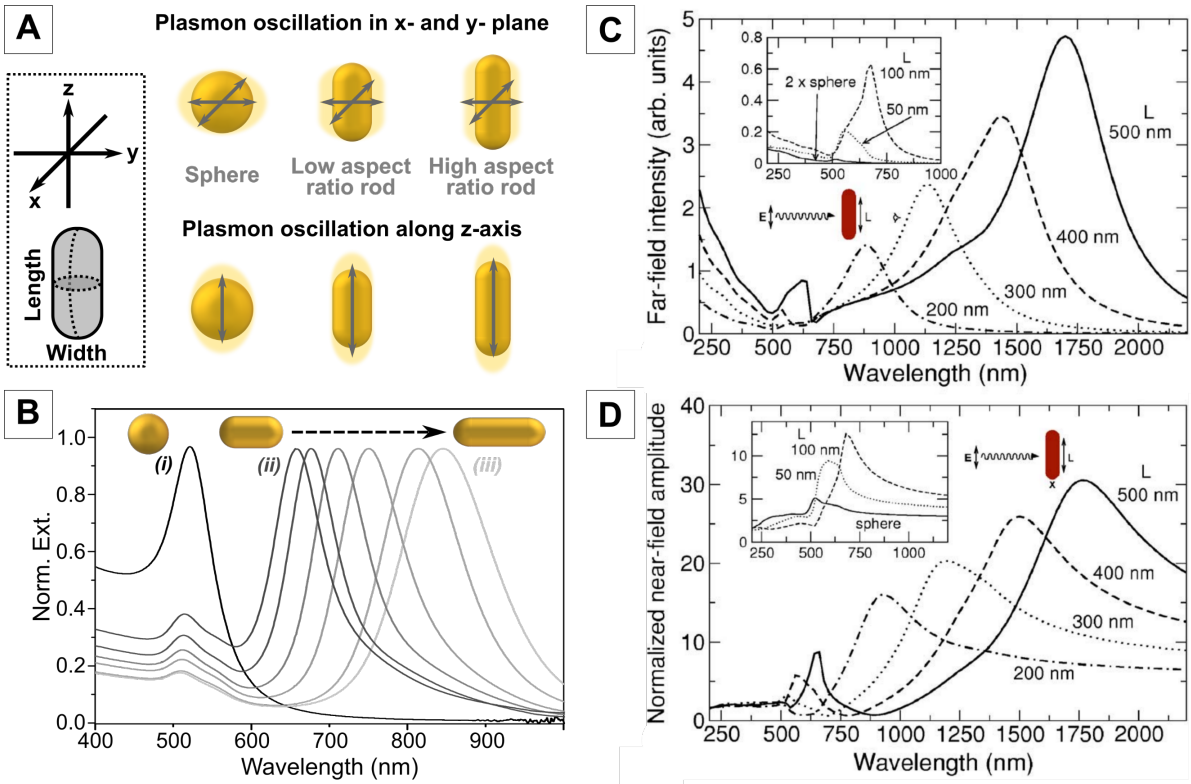

Figure 1.2: A: Schematic showing plasmon oscillations in a metal sphere and in nanorods with different aspect ratios. For nanorods, the oscillation in the x-y plane is called the transverse plasmon resonance (*i*) and the oscillation along the z-axis is the longitudinal mode (*ii-iii*). Increasing the aspect ratio (AR) red shifts the longitudinal mode. **B:** Ultraviolet-visible spectra for a gold nanosphere and for different AR gold nanorods. **C:** Far-field intensity as a function of wavelength for an electromagnetic plane wave incident on a gold nanorod with length *L* and radius (R) of 40 nm. The polarization is parallel to the rod. **D:** Normalized near-field amplitude for the same system as **C**. The near field is evaluated 1 nm from the nanorod. Results for small *L* and spheres are shown in the insets [adapted with permission from ref. 16].

Thus far, we have provided expressions for nanoparticles in the quasistatic limit, which only includes particles with sizes below 10% of the wavelength of light, roughly 20 nm and lower. For larger particles, higher order modes (quadrupole, octupole *etc*.) become non-negligible. Indeed, the latter case applies to many nanoparticle systems of interest. Mie's solutions for local

and far-field scattering by metal nanoparticles describe the trend of red-shifting LSPR wavelength with increasing size, shown for ~10-100 nm diameter nanospheres in **Figure 1.3**. For more complex systems and geometries, Mie scattering can be evaluated numerically, which is discussed in detail elsewhere.[5]

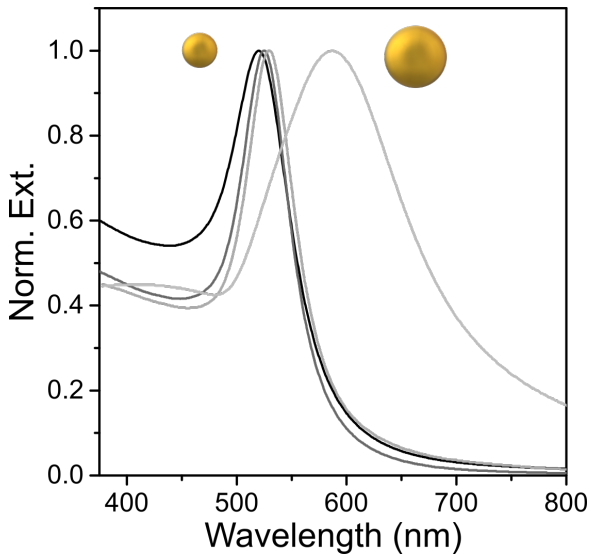

Figure 1.3. Ultraviolet-visible spectroscopic characterization of aqueous solutions of gold nanoparticles with ~10, 25, 50, and 100 nm diameters.

In addition to high optical extinction and local near-field enhancement, plasmonic excitation presents other interesting consequences. For example, individual electrons can take on the energy lost to the collective oscillation of the conduction electrons during dephasing. So-called "hot electrons" with energies higher than the thermal energy of the system can then be transferred to molecules to promote chemical reactions or be applied in photochemistry and photovoltaics.[17] In addition, light absorption by the particle can lead to intense heating close to the particle's surface through plasmon-phonon coupling.[18] Plasmonic heating is more common in branched particles, nanorods, and nanoshells, and prior work has explored the application of thermoplasmonic particles in cancer therapeutics, where localized heating is used to kill nearby cancer cells.[19–21]

In summary, the spectral position of plasmon resonances in individual nanoparticles depends on the local dielectric environment, metal identity, particle geometry and size. Of these, the manipulation of the particle shape is especially powerful. Altering the shape to include small sharp features produces strong local field enhancements,[22,23] and overall introduction of shape anisotropy produces new LSPR modes, with the plasmons in certain particle geometries favoring different decay pathways. Thus, the control of nanoparticle morphology through bottom-up colloidal synthesis poses great research interest and will be discussed in **Section 1.2**.

1.1.2. Plasmonic nanoparticle dimers, lines, and arrays

More than just tuning the plasmonic responses of individual nanoparticles, controlling their positions relative to one another can also be used to engineer more complex plasmonic responses. When two or more nanoparticles are placed in close proximity, the interaction of their plasmon modes can be described using a model similar to molecular orbital hybridization. The nanoparticle's individual plasmon modes hybridize with one another to produce low-energy bonding plasmon modes and higher-energy antibonding modes.[24–27] The spatial distribution of the "bonding" plasmon modes similarly resembles bonding molecular orbitals, exhibiting higher localization in between the nanoparticles, creating regions with intense local field enhancements, so-called "hotspots," relevant for sensing applications.[28–32] Confinement of the electric fields to the interparticle gaps can produce significant field enhancements as shown in **Figure 1.4**.[33–36]

Moreover, arrangement of particles into chains or periodic arrays with set spacings can lead to hybridization between the individual plasmon modes with the diffraction modes of the array, compensating the optical losses and producing lattice plasmon resonances (LPRs) with narrow profiles (few nm) (**Figure 1.5A,B**).[37–40] Because LPRs occur at wavelengths where the

plasmonic oscillations of the particles in the array are in phase with one another, their spectral position depends on the geometrical parameters of the array as shown in **Figure 1.5C,D**.[41] The spectral position of the LPR is also influenced by the illumination angle, which we will discuss further in **Chapter 4**. Beyond LPRs, even more interesting magnetic, electronic, and optical responses can be engineered *via* fabrication of different patterns,[42–46] such as gratings,[47] lines for waveguides[44,48–50] and chiral superstructures.[51–55]

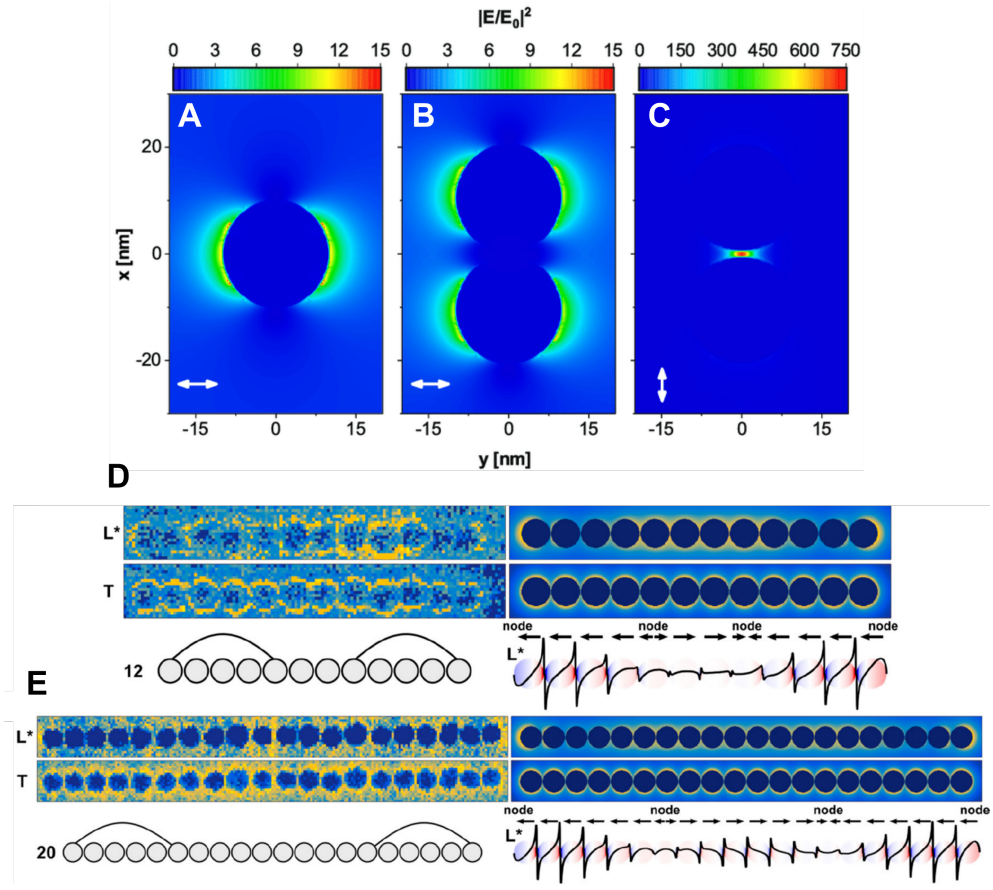

Figure 1.4. A-C: Near field distributions under different incident light polarizations (indicated by the white arrows) for (**A**) a single metal nanoparticle and (**B,C**) a nanoparticle dimer [reproduced from ref. 34]. **D,E:** Experimental electron energy loss spectroscopy data showing the longitudinal (L*) and transverse (T) plasmon modes in coupled gold nanoparticle chains (*left*) and simulated plasmon modes (*right*) [reproduced from ref. 36].

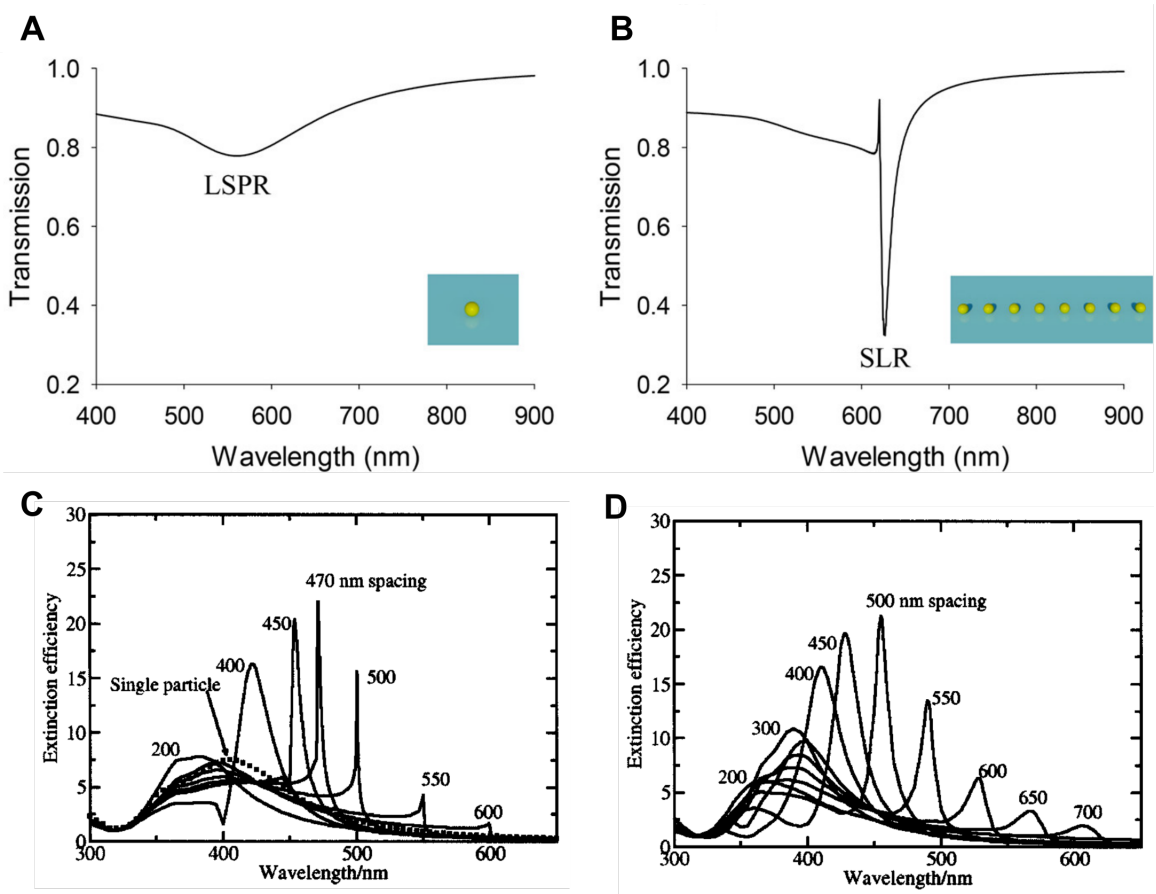

Figure 1.5. A,B: Simulated transmission spectra for (**A**) a single 60 nm gold nanosphere in air and (**B**) a linear arrangement of spheres with periodicity of 620 nm [reproduced from ref. 37]. LSPR: localized surface plasmon resonance; SLR: surface lattice resonance (referred to as a lattice plasmon resonance). **C,D**: Extinction spectra of 400 50 nm silver nanoparticles arranged in (**C**) a one-dimensional chain and (**D**) a two-dimensional hexagonal array [reproduced from ref. 41 with permission from AIP publishing].

Section 1.2. Colloidal Synthesis of Gold Nanoparticles

The most common strategy for tuning the plasmonic properties of nanoparticles is to do so in colloidal suspensions *via* bottom-up synthesis. The work presented in this thesis focuses on gold plasmonic nanoparticles in particular, and so this section will primarily focus on the colloidal synthetic developments in this area. There are three basic elements in the wet-chemical synthesis of gold nanoparticles: (*i)* the gold salt, the source of gold ions, usually $HAuCl_4$, $NaHAuCl_4$, or $KAuCl_4$, (*ii*) a capping ligand, usually a surfactant, to stabilize the particles in colloidal suspension

via coulombic and/or steric repulsion, and (*iii*) a reducing agent, to reduce the Au^{3+} ions. Although electrochemical reduction[56,57] or light can be used in place of a chemical reductant, we will not focus on these strategies here and direct the reader to recent comprehensive reviews.[58–61]

1.2.1. Early developments in colloidal synthesis

Early synthetic protocols for spherical gold nanoparticles served as a jumping off points for understanding how to tune the size, shape, and surface chemistry of nanoparticles using growth reagents and conditions. Many of these techniques continue to be used today. In 1951 and 1973, Turkevich and Frens developed a robust synthetic method where the introduction of sodium citrate into a boiling aqueous solution of gold salt promoted the formation and growth of nanospheres.[62,63] The sphere diameters could be tuned between 5-150 nm simply by changing the concentrations of the reagents present in solution. In 1989, "polyol synthesis" involving the reduction of metal salts by multivalent alcohols, or polyols, under microwave irradiation or reflux conditions was described.[64] Although initial extensions of this technique were described for the synthesis of cobalt, nickel, copper, and platinum nanoparticles, it has since been translated to silver and gold.[65–68] In this technique, the high boiling points of the polyols enable broad tunability of the reaction temperature to optimize particle uniformity and crystallinity.[69] In 1994, the synthesis of small (1.5-6 nm), hydrophobic, alkanethiol-stabilized gold particles at room temperature was realized by Brust and co-workers using a biphasic system.[70] Each of these foundational methods and other one-pot synthetic methods follows a homogeneous nucleation and growth process that proceeds according to the LaMer model (**Figure 1.6)**.

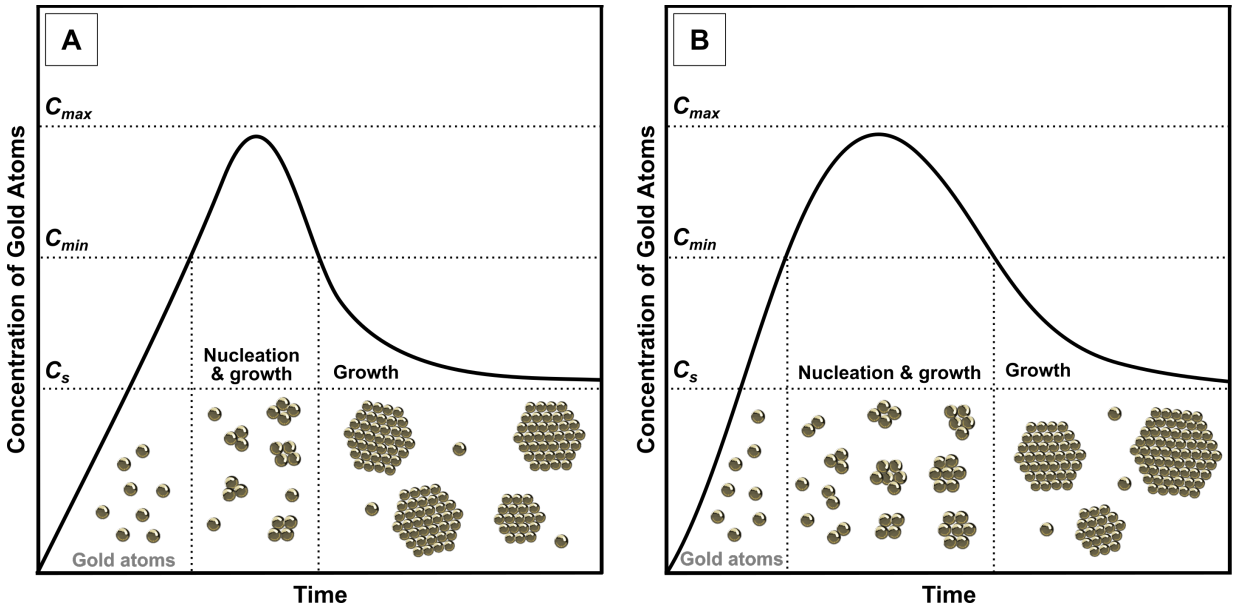

Figure 1.6. A,B: The LaMer model showing the homogeneous process of nuclei formation and growth. C_{max} = critical limiting supersaturation concentration of gold atoms, C_{min} = minimum supersaturation concentration of the gold atoms, C_s = solubility concentration of the nanocrystals. When the solution first reaches C_{min}, nucleation begins, and nucleation events continue until the concentration dips below C_{min} once again. Here, we compare growth for a system with a **A:** shorter and **B:** longer nucleation periods to depict how extended nucleation times can increase size dispersity.

In the LaMer model, as the concentration of gold atoms increases above the minimum supersaturation concentration (C_{min}), nanoparticle nucleation begins and small clusters form.[71] The clusters continue to form until the gold concentration returns below C_{min}. At this point, no more nuclei form, and the existing nuclei increase in size. The particle growth levels off once the maximum solubility concentration for the nanocrystals (C_s) is reached. In this growth scheme, nucleation and growth occur in the same solution and the uniformity of the products is improved by reducing the window of time in which nuclei are allowed to form. Moreover, the size of the products can be tuned by changing the number of formed nuclei relative to the total concentration of gold. For example, modulating the relative amount of Au^{3+} compared to citrate solution in the Turkevich-Frens synthesis changes the number of formed nuclei relative to the total available gold.[63] This small change is what enables modulation of particle diameter, although particles

larger than 30 nm synthesized with the Turkevich-Frens method exhibit fairly broad size distributions and irregular shape.[72] Next, we will discuss a different growth mechanism, heterogeneous nucleation through seed-mediated growth, which is capable of improved product uniformity compared to homogeneous nucleation.

1.2.2. Seed-mediated growth

Although nanoobjects of various dimensions and geometries can be synthesized with one-pot methods,[73–77] seed-mediated growth is probably one of the most prevalent and well-developed approaches for tuning the size and shape of gold nanoparticles with high yield. The idea for seed-mediated growth dates back as early as 1925 and proceeds by heterogeneous nucleation using small "seed" nanoparticles as templates for later overgrowth.[78] This approach leads to improvement in the size distributions of the products due to the control of the chemical environment separately and precisely during the nucleation and growth stages. In this scheme, the chemical environment of the seed solution is optimized so that nuclei are rapidly formed (quasi-simultaneously) *via* homogeneous nucleation. The uniform seeds are then introduced into a second "growth solution" containing a different composition of gold salt, capping ligand, and reducing agents. Natan and co-workers performed initial explorations into seed-mediated growth for gold nanospheres.[72] Here, seeds were prepared by rapid reduction of Au^{3+} to Au^{0} by sodium borohydride and boiling aqueous citrate. On the other hand, the growth solution exhibited a mild reducing environment, promoting final reduction from Au^{1+} to Au^{0} to occur directly on the preformed seeds. The implementation of only weak reductants (rather than strong reductants capable of completely reducing Au^{3+} to zero valent gold) in the growth solution is key for effectively disfavoring additional homogeneous nucleation during the growth step significantly

improving size-yield.[3] Interestingly, oblate spheroid products were produced for certain compositions of the growth solution.[72] The possibility to select for such anisotropic objects through seed-mediated growth was subsequently explored in great detail. The size and shape of the seed,[80–82] reductant,[83,84] pH,[85,86] temperature,[29,87] and the presence of "shape-directing reagents"[88–94] serve to direct the anisotropic growth of gold nanoparticles.[68,89–91,93–98]

1.2.2.1. The role of the seed

The quality, size, crystal habit, and surface chemistry of the seeds greatly affect the size distribution and shape of the final products. Although in reality many particle geometries, (including anisotropic ones) can be used as seeds, the most common are citrate-capped seeds made with the Turkevich-Frens method[79,86] and cetrimonium bromide/chloride (CTAB/C)-capped seeds made by sodium borohydride reduction.[81,84,85] Sodium borohydride reduction can be used to make seeds capped with other surfactants as well.[83,99] Regardless of which seeds are selected, in each case, the size and crystal habit of the seeds, *e.g.,* single-crystal, mono- and penta-twinned, influence the growth kinetics and crystal structure of the final products.[80–83,87,89,99–101] The faster growth rates of small clusters compared to larger ones leads to size distribution narrowing over time during seed growth in a phenomenon called size focusing.[72,102] More actively, the uniformity of the seeds in both size and crystal structure can be controlled through thermal[87] and oxidative chemical etching treatments.[82,103] The crystal defects present in the seeds are especially important, because while additional twin defects can be introduced during growth, they generally cannot be removed.[81,89] Twin defects in the seed are thought to arise depending on numerous factors, *i.e.,*

[3] Homogeneous nucleation during the growth step is also often referred to as secondary nucleation to distinguish this phenomenon from the initial homogeneous nucleation of the seeds.[79]

preferential surfactant binding to certain facets, presence of halides, properties of the solvent, and temperature. Note that common methods produce a mixture of seed products and the presence of seeds with different crystal habits is a source for lower shape yield. For example, in the synthesis of gold nanostars in the presence of zwitterionic surfactant laurylsulfobetaine (LSB), the optimized yield of penta-branched stars is dependent on the initial yield of penta-twinned LSB seeds.[83] The remaining seed population (30%) are monocrystalline, producing low aspect ratio tetrapods.

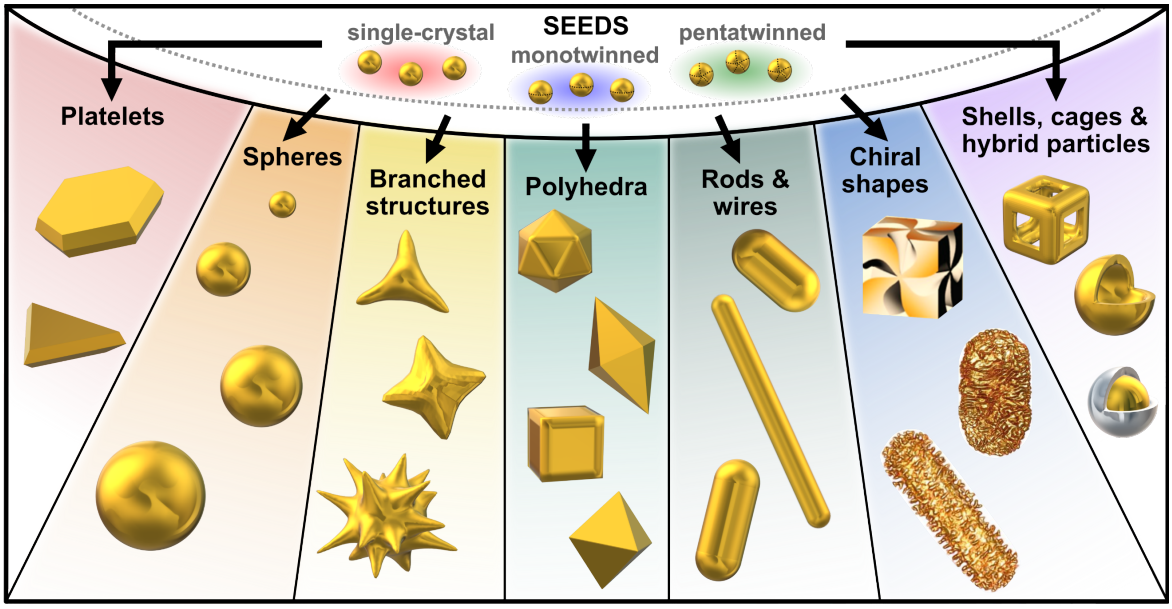

Figure 1.7: Schematic showing some examples of gold nanoparticle seeds and some geometries accessible with bottom-up seed-mediated growth.

Thus far, synthesis of rods[104] and stars[83,105] from single crystalline seeds, platelets and triangles from mono-twinned seeds,[81,106] and nanorods,[84] bipyramids, dodecahedra,[87,107] penta-branched stars[83,100] from penta-twinned seeds under the appropriate growth environments. Particles presenting polycrystalline features[108] and more complex facets (*e.g.*, chiral shapes)[109,110] have also been demonstrated with the seeded growth method. In **Figure 1.7**, we provide a summary of some of the possible geometries that can be accessed. In the growth solution,

as with seed synthesis, the selected reductant, pH, surfactant, halides, solvent, and silver salts all act to promote growth along specific crystal facets.[98] Undoubtedly there are many "handles" for controlling shape-directed growth and a comprehensive review of each of these aspects is not feasible here. Therefore, important aspects to consider regarding the reductant, shape directing surfactants, and ions will be briefly outlined.

1.2.2.2. The reductant

In seed-mediated growth, it is important to implement reductants capable of reducing the gold precursor only from Au^{3+} to Au^{1+}, favoring the final reduction to Au^0 to occur mainly on the seed itself.[78] Prior work applies polyvinylpyrrolidone (PVP), hydroxylamine,[72] 2-mercaptosuccinic acid,[111] and ascorbic acid (AA) as growth solution reductants,[98] with AA being the most popular outside of polyol synthetic protocols. In a standard synthesis, the reductant is first added to a growth solution containing the other shape-directing reagents, then seeds are subsequently introduced. The addition of the reductant is performed in this fashion to avoid dissolution of the seeds *via* oxidation by the Au^{3+} in the growth solution following the comproportion reaction of gold shown in **Eq. 1.9**.

$$Au^{3+}\,(aq) + 2Au^{0}\,(s) \rightarrow 3Au^{1+}\,(aq) \quad \textbf{[Eq. 1.9]}$$

Increasing the concentration of AA generally speeds up gold precursor reduction, promoting the growth of kinetically favored high-aspect ratio branched structures.[83,99] However, shape control is a complex task, since side-reactions can occur between the many components in the growth solution.[83] Furthermore, in synthetic recipes using AA as a weak reductant, it has been shown that the ascorbate ion is responsible for efficient reduction of the gold precursor. Thus, higher pH creates stronger reducing environments whereas lower pH solutions are more mildly reducing.[112]

For example, Murphy showed that the aspect ratio of rods synthesized in the presence of silver and CTAB with AA as a reductant can be tuned between 4 and 18 simply by changing the pH from 2.8 to 5.6 (first pK_a of AA = 4.1).[85] Mirkin also used NaOH to promote the anisotropic growth of nanoprisms with AA reduction.[107] The upper pH limit for tuning AA strength is ~8-9 pH, because, at this point, the AA becomes strong enough that it can complete the reduction from Au^{3+} to Au^0, which is undesirable.[84]

1.2.2.3. The surfactant and shape-directing reagents

More than just stabilizing the colloid, many works have shown that the concentration, charge, counterion, and chain length of the ligand are important for shape control during seeding and growth.[68] Quaternary ammonium salts, CTAX, are common surfactants used in seed-mediated gold nanoparticle synthesis. In these systems, the CTA^+ ion's affinity for high energy {100} and {110} facets reduce the rate of growth along those directions, and can be used to fabricate rods through elongation by addition of atoms on the {111} face.[113,114] Stabilization of certain crystal facets with different ligands is a powerful tool affecting the final shape of the products overall. In fact, simply replacing CTAB with ligands that have specific affinity for gold {111}, such as PVP,[108] Triton-X,[99] or LSB,[83] under kinetically favored reduction conditions alternatively produces nanostars. Recently, amino acids and peptides have been demonstrated to promote the formation of twisted structures stemming from certain crystalline facets of nanocubes enantioselectively.[109] The resulting helicoid nanocubes synthesized with glutathione and cysteine exhibit tunable chiral optical activity, presenting an exciting synthetic direction for creating nanostructures with interesting and complex properties.[115]

Recent work focused on the roles of the ligand includes studies on the addition of co-surfactants (aromatic species, fatty acids, long chain alkanols) to promote or to diminish adsorption and interrogate factors affecting facet accessibility and shape direction.[116–119] Another central idea that has been proposed regarding the roles of the ligand is the capability of the surfactant micelles to act as soft templates for directing shape. This idea was initially proposed for rods, although the consensus is that CTAB micelles do not play as major a role as the previously discussed effects.[84] Nonetheless, the idea of a micellar template has since been applied to achieve the synthesis of chiral nanorods.[110] In this work, González-Rubio *et al.* apply helical micellar templates created using CTAX and 1,1′-bi(2-naphthol) (which naturally forms elongated coiled micelles) as a co-surfactant to induce the formation of twisted chiral wrinkles on pre-made rods.[110][4]

The counterions of the ligand, usually halides, are also important to consider and have been suggested to affect particle shape *via* altering the ligand layer organization, acting as oxidative etchants and/or changing the availability of gold and silver salts depending on concentration. For instance, although CTAC and CTAB both produce CTA^+, high yields of rods are generally achieved with CTAB, with Br^- apparently playing a necessary role in anisotropic growth.[114] One explanation for this effect is that the Cl^- and Br^- counterions affect the ordering of the ligand layer, and the absence of Br^- produces a less compact surface coating. Accordingly, CTAC is better put to use for the synthesis of different size nanospheres.[29,120] In addition, high concentrations of CTAB lead to oxidative etching along the edge of the {111} crystal plane.[94,121,113] Thus far, we have discussed major roles of surfactants and counterions in directing anisotropic growth and have provided some examples. There are additional factors, such as concentration, charge, chain length, that we will not discuss in detail here, however, these elements are also important to consider and

[4] This work is also an example where an anisotropic nanoobject is later overgrown into other complex shapes.

can all serve as handles for tuning shape control during seeding, growth, and/or overgrowth steps.[68]

1.2.2.4. Other factors and methods to adjust size and shape uniformity

In addition to the capping ligands, reducing agents, and seeds, other shape-directing reagents can be added to the seeding and/or growth. Silver nitrate, for example, is a common shape-directing reagent for nanostars and nanorods.[83,84,99] There have been a few proposed mechanisms for the roles of silver in the growth of different anisotropic shapes (*i*) underpotential deposition of Ag^{1+} on certain crystal facets, (*ii*) silver bromide binding to certain facets, and (*iii*) disruption of the surfactant "soft template" by the silver ions.[122–124] Beyond the silver ions themselves, the interactions of nitrate counterions with oxygen may contribute to the reproducibility and to directing anisotropic growth.[124] However, nitrate has been shown to have minimal or no effect on the synthesis of some pentabranched nanostructures.[100] Aside from silver salts, iodide is another common shape-directing reagent. In the growth of nanorods, Mirkin[91] proposed that iodide adsorbs selectively to the {111} facets of the nanorod tips to prevent binding of CTAB, promoting growth in that direction. In the synthesis of gold nanotriangles, Scarabelli *et al.* showed that the addition of iodide in the seed solution was key for the formation of triangular shapes, where simply decreasing the concentration of iodide in solution produced triangles with longer edge lengths.[81,125]

1.2.3. Precision synthesis with microfluidics

In standard colloidal syntheses, certain protocols require rapid and/or simultaneous addition of reagents to the growth solution and vigorous stirring to ensure their uniform

distribution.[83,97,126] As an alternative, gold nanoparticle synthesis can be carried out in systems with controlled reagent and thermal mixing and fluid flows, called microfluidic devices.[45,127,128] Microfluidic flow systems contain one or more channels with dimensions lower than 1 mm. Typically, the channels are fabricated with glass, silicon, or polymers, most commonly polydimethylsiloxane (PDMS or silicone), and can incorporate junctions linked with tubing made of polyetheretherketone, polytetrafluoroethylene, polyethylene, or other polymers.[129,130] The precise control of the flow of small volumes of liquids by microfluidics leads to their application in flow cytometry, immunoassays, particle or cell separation, cell patterning, and the fabrication of organic and inorganic nanoparticles.[129–133] Next, we focus on the microfluidic synthesis of gold nanoparticles, which is achieved by combining two or more solutions containing growth reagents.

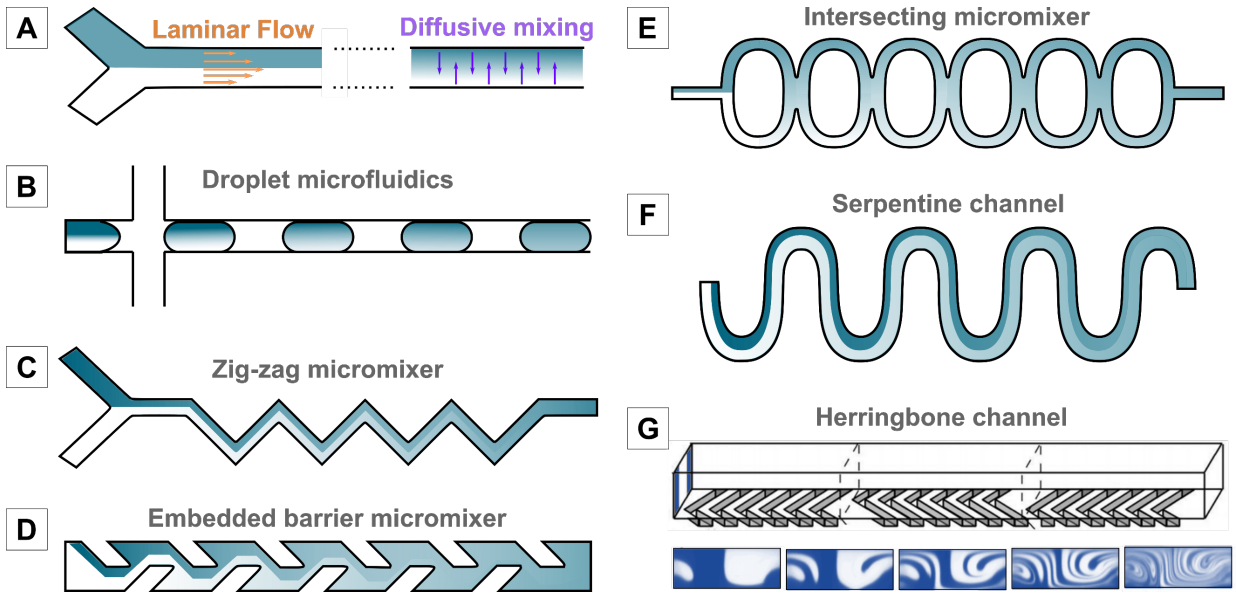

Figure 1.8. A-F: Schematics showing some examples mixing in microfluidic channels, with all flows proceeding from left to right. **A:** Co-flow of two solutions in a featureless channel with a laminar flow profile, where diffusion dominates mixing. **B:** Droplet microfluidics where diffusion more effectively leads to mixing in the small volume. **C-F:** Various examples of channels with features inducing exchange of the two introduced solutions by changing the flow profile. **G:** A herringbone micromixer and the resulting flow profile cross sections (*below*) as the solutions progress through the channel [adapted from ref. 136 with permission from AAAS].

In microfluidic devices, fluid flow in the channels is characterized by the Reynold's number (R_e), which expresses the ratio of force associated with momentum to the force associated with viscous shear and is defined as:

$$R_e = \frac{\upsilon D_h \rho}{\mu} \qquad \textbf{[Eq. 1.10]}$$

where υ is the characteristic fluid velocity, ρ is fluid density, D_h is the hydraulic diameter, and μ is the viscosity of the fluid.[129] Flows with R_e below 2000 and above 3500 are considered laminar and turbulent flow, respectively, and transitional flows constitute intermediate values. In laminar flows, mass exchange between two or more streams flowing in constant contact with one another will occur by diffusion, rather than advection.

In microfluidic devices, R_e stays well below 100 (often going below 1) due to small features and low flow velocities, placing them in the laminar flow regime. For uniform metal nanoparticle synthesis, it is important to ensure that the timescale of mass transfer by diffusion occurs faster than the nucleation or growth. Reducing the size of the channels so that $R_e \ll 1$ facilitates molecular diffusion and enhances the effect of Taylor-Aris dispersion, where shear flow disperses the molecular species along the flow direction.[130,134] Another strategy is to modify the microfluidic device to induce different flow profiles that promote reagent exchange *via* active[135] or passive mixing. Common passive mixers for systems with moderate and low R_e include herringbone,[136] zig-zag,[137] intersecting,[132] and serpentine channels,[132] and channels with embedded barriers (**Figure 1.8**).[138]

So far, uniform gold nanospheres,[139] gold-coated particles[140] and shaped goldparticles[137,141] have been synthesized in microfluidic reactors. In the work of Khöler, intersecting geometries were used to mix the growth solution uniformly *via* repeated splitting and recombination of the solution in the channel.[139] As previously discussed, the uniform local

distribution of heat and reactants can be improved by reducing the dimensions of the microfluidic device (**Figure 1.8A**). This effect is more pronounced when the reactant volume is further reduced into individual "microdroplets" *via* controlled co-flow with immiscible solvents or gasses (**Figure 1.8B**).[137,142,143] Malmstadt demonstrated this strategy by synthesizing narrower size distributions of gold nanospheres by flowing ionic liquid droplets through serpentine channels.[142] Later, Abell applied a similar method using zig-zag micromixers (similar to **Figure 1.8C,F**) conjointly with droplet microfluidics to confine the growth reagents to picoliter volumes and synthesize uniform gold nanostars capped with citrate and PVP.[137]

Section 1.3. Engineering Plasmonic Substrates

While some of the complex plasmonic responses discussed in **Section 1.1** can be engineered with colloidal systems,[46,144–150] many devices, sensors, heterogeneous catalysts, and biomedical platforms benefit from incorporating plasmonic nanostructures on or within solid supports, such as polymers,[151–153] glass,[133,154–158] hydrogels,[159,160] semiconductors,[161–165] two-dimensional materials,[166–168] and metals.[169] There are two general approaches to the fabrication of nanostructures: top-down and bottom-up. In top-down plasmonic gold nanofabrication, the nanomaterials are fabricated by breaking down a starting bulk material, which contrasts bottom-up methods, where the nanomaterials are formed from gold atoms. Next, we will provide background summarizing the implementations of these approaches for plasmonic substrate fabrication.

1.3.1. Top-down engineering of plasmonic substrates

Top-down nanofabrication relies on either maskless or through-mask approaches for creating nanoscale features.[54,170–172] Direct write methods include electron beam lithography, focused ion beam, scanning probe lithography, and direct laser writing. In some cases, the nanoscale features can be directly etched into a gold thin film.[173] However, many approaches first create the nanopatterns in a sacrificial material, such as a photo-linkable polymer, called a photoresist.[172,174] In through-mask techniques, such as photolithography[175,176] or phase-shift lithography,[177,178] the photoresist is exposed to light through masks made by direct-write methods. The exposed areas of the photoresist either become more or less soluble in a developer solvent (which is used to remove the more permeable material) depending on whether a negative or positive resist is used, respectively. A following lift-off or dry-etching step is then used to create the final nanoscale plasmonic features. There are also through-mask methods that do not rely on photolithography, using masks made from self-assembled monolayers of polystyrene or silica nanoparticles[179,180] or chemical-etch resistant layers (*e.g.,* molecular monolayers).[181–184] To date, maskless and through-mask patterning approaches have undergone further development regarding improved pattern resolution, reduced processing time, and engineering unique plasmonic structures.[52,54,55,172,174] Despite these developments, the limitations of top-down methods include the cost, requirement for specialized equipment, and the polycrystallinity of the nanostructures.[171,185] The latter factor is especially important for fabricating high-quality plasmonic substrates since it leads to damping of the plasmonic response due to nonradiative loss pathways.[171]

1.3.2. Plasmonic substrates from colloidal nanoparticles

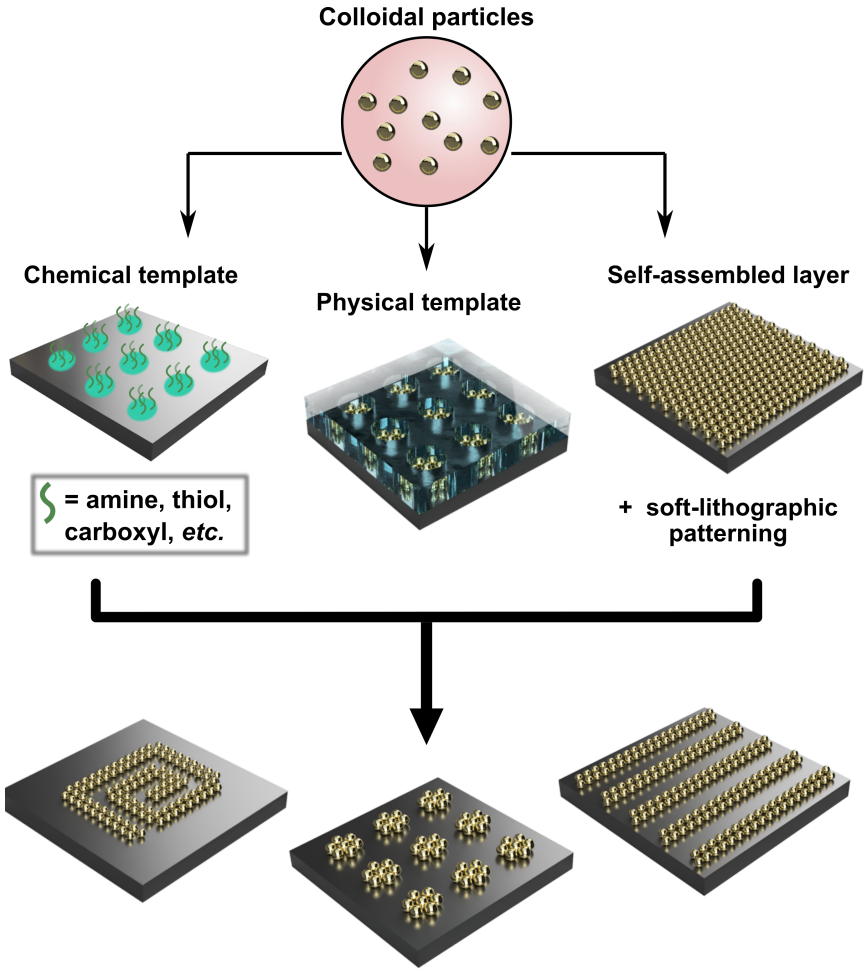

Figure 1.9. Schematic showing examples of plasmonic substrates fabrication strategies using colloidally synthesized particles (*top*), and potential arrangements (*bottom*).

In contrast to top-down methods, bottom-up wet chemical synthesis makes it possible to fabricate higher quality single-crystal nanoparticles and rationally tune morphology, as can be concluded from the discussion in **Section 1.2.2**. Therefore, if precise control over the crystal structure, size, shape, and surface chemistry for each individual plasmonic unit is desired, bottom-up synthesis should be applied (**Figure 1.9**). Integrating colloidal particles with substrates usually

begins with nanoparticle pre-synthesis, followed by ligand exchange/modification of the particle surface chemistry and self-assembly. Uniform films of pre-synthesized gold nanoparticles can be prepared following ligand exchange and self-assembly *via* centrifugation,[186] controlled solvent evaporation,[187–190] or assembly at a liquid-liquid,[191,192] or a liquid-air interface.[81,187,193–195] This self-assembly process can be combined with chemically[161,196,197] or physically patterned[29,38,40,42,51,198] substrates, or soft-lithography with nanoparticle inks[159,162,199,200] to produce patterns. The application of physically patterned stamps and substrates to assist in directing the site-specific attachment of particles is especially popular and includes templated,[29,38,40,42,51] capillary-assisted,[201,202] optically printed,[203,204] and electrophoretic self-assembly processes.[205,206]

Section 1.4. Summary

The LSPR effect gives rise to unique physical and chemical properties in metal nanoparticles. Of the metals capable of supporting plasmon resonances, gold, in particular, is especially useful for applications in biology and medicine and for those requiring irradiation in the visible-NIR range. The LSPR peak can be tuned from ~500 nm to 1800 nm through modification of the nanoparticle geometry, size, and local environment.[97–99,207] Furthermore, more complex optical responses can be engineered when particles are rationally arranged.[36–38,42–44,49–51] In the colloidal synthesis of anisotropic nanoparticles, pH, temperature, chosen seed, surfactants, reductants, and other shape-directing reagents are used as handles for tuning the products.[97–99,207] The realization of intrinsically chiral gold nanoparticles achieved solely by controlling the chemical environment constitutes a major interesting direction for future developments in colloidal synthesis that has important implications especially in biology and sensing.[110,115]

Another interesting body of research regarding gold nanoparticle synthesis is the application of microfluidic devices for the precision synthesis of colloids. Although there have been notable developments in this area, there remain limitations to these techniques, such as scalability, time-consuming design and fabrication, and the physical and chemical limitations of the microchannel material.[129,130] As an example, PDMS is common in microfluidic cannels containing lithographically produced features. In PDMS devices, the channels must be mounted to a glass or oxide substrate following UV-ozone, air, hydrogen, or oxygen plasma treatments and the binding strength between the two materials is sometimes insufficient for high pressure flows. Moreover, PDMS is incompatible with corrosive solvents, high temperatures, and can significantly swell in the presence of organic solvents.[208] These aspects aside, microfluidics offers high size and shape yield and opens up the possibility for fully automated and programmable reactors. Even more, these systems provide unique environments to study factors affecting particle morphology.[137,140,209,210] Owing to the unmatched versatility of bottom-up synthesis, the implementation of colloidal particles for the fabrication of plasmonic substrates is widely popular.[29,38,40,42,46,51,161] In the next chapter, we will provide a focused discussion on a method utilizing subtractive soft-lithography and colloidal self-assembly to fabricate plasmonic substrates.

Section 1.5. References

[1] P. K. Jain, X. Huang, I. H. El-Sayed, M. A. El-Sayed, *Acc. Chem. Res.* **2008**, *41*, 1578.

[2] E. C. Dreaden, A. M. Alkilany, X. Huang, C. J. Murphy, M. A. El-Sayed, *Chem. Soc. Rev.* **2012**, *41*, 2740.

[3] D. J. de Aberasturi, A. B. Serrano-Montes, L. M. Liz-Marzán, *Adv. Opt. Mater.* **2015**, *3*, 602.

[4] D. Bohm, D. Pines, *Phys. Rev.* **1953**, *92*, 609.

[5] M. Pelton, G. Bryant, *Introduction to Metal-Nanoparticle Plasmonics*, John Wiley & Sons, **2013**.

[6] K. A. Willets, R. P. Van Duyne, *Annu. Rev. Phys. Chem.* **2007**, *58*, 267.

[7] W. Knoll, *Annu. Rev. Phys. Chem.* **1998**, *49*, 569.

[8] J. M. Brockman, B. P. Nelson, R. M. Corn, *Annu. Rev. Phys. Chem.* **2000**, *51*, 41.

[9] R. P. Van Duyne, *Science* **2004**, *306*, 985.

[10] Y. Li, *Plasmonic Optics: Theory and Applications*, SPIE Press, **2017**.

[11] H. Wang, F. Tam, N. K. Grady, N. J. Halas, *J. Phys. Chem. B* **2005**, *109*, 18218.

[12] M. G. Blaber, M. D. Arnold, M. J. Ford, *J Condens Matter Phys* **2010**, *22*, 095501.

[13] M. G. Blaber, M. D. Arnold, N. Harris, M. J. Ford, M. B. Cortie, *Phys. B Condens. Matter* **2007**, *394*, 184.

[14] K. Kolwas, A. Derkachova, *Nanomaterials* **2020**, *10*, 1411.

[15] R. Rosei, F. Antonangeli, U. M. Grassano, *Surf. Sci.* **1973**, *37*, 689.

[16] J. Aizpurua, G. W. Bryant, L. J. Richter, F. J. García de Abajo, B. K. Kelley, T. Mallouk, *Phys. Rev. B* **2005**, *71*, 235420.

[17] A. Manjavacas, J. G. Liu, V. Kulkarni, P. Nordlander, *ACS Nano* **2014**, *8*, 7630.

[18] M. L. Brongersma, N. J. Halas, P. Nordlander, *Nat. Nanotechnol.* **2015**, *10*, 25.

[19] A. M. Gobin, M. H. Lee, N. J. Halas, W. D. James, R. A. Drezek, J. L. West, *Nano Lett.* **2007**, *7*, 1929.

[20] Y. Wang, K. C. L. Black, H. Luehmann, W. Li, Y. Zhang, X. Cai, D. Wan, S.-Y. Liu, M. Li, P. Kim, Z.-Y. Li, L. V. Wang, Y. Liu, Y. Xia, *ACS Nano* **2013**, *7*, 2068.

[21] X. Huang, M. A. El-Sayed, *Alex. J. Med.* **2011**, *47*, 1.

[22] A. Guerrero-Martínez, S. Barbosa, I. Pastoriza-Santos, L. M. Liz-Marzán, *Curr. Opin. Colloid Interface Sci.* **2011**, *16*, 118.

[23] K. Chandra, K. S. B. Culver, S. E. Werner, R. C. Lee, T. W. Odom, *Chem. Mater.* **2016**, *28*, 6763.

[24] P. Nordlander, C. Oubre, E. Prodan, K. Li, M. I. Stockman, *Nano Lett.* **2004**, *4*, 899.

[25] F. Hao, C. L. Nehl, J. H. Hafner, P. Nordlander, *Nano Lett.* **2007**, *7*, 729.

[26] B. Willingham, D. W. Brandl, P. Nordlander, *Appl. Phys. B* **2008**, *93*, 209.

[27] D. W. Brandl, C. Oubre, P. Nordlander, *J. Chem. Phys.* **2005**, *123*, 024701.

[28] C. Fernández-López, L. Polavarapu, D. M. Solís, J. M. Taboada, F. Obelleiro, R. Contreras-Cáceres, I. Pastoriza-Santos, J. Pérez-Juste, *ACS Appl. Mater. Interfaces* **2015**, *7*, 12530.

[29] C. Hanske, G. González-Rubio, C. Hamon, P. Formentín, E. Modin, A. Chuvilin, A. Guerrero-Martínez, L. F. Marsal, L. M. Liz-Marzán, *J. Phys. Chem. C* **2017**, *121*, 10899.

[30] H.-H. Jeong, M. C. Adams, J.-P. Günther, M. Alarcón-Correa, I. Kim, E. Choi, C. Miksch, A. F. Mark, A. G. Mark, P. Fischer, *ACS Nano* **2019**, *13*, 11453.

[31] Z. Wang, K. Cai, Y. Lu, H. Wu, Y. Li, Q. Zhou, *Nanotechnol. Rev.* **2019**, *8*, 24.

[32] L. Tian, C. Wang, H. Zhao, F. Sun, H. Dong, K. Feng, P. Wang, G. He, G. Li, *J. Am. Chem. Soc.* **2021**, *143*, 8631.

[33] R. Alvarez-Puebla, L. M. Liz-Marzán, F. J. García de Abajo, *J. Phys. Chem. Lett.* **2010**, *1*, 2428.

[34] C. Heck, Gold and Silver Nanolenses Self-Assembled by DNA Origami, **2018**.

[35] J. Langer, D. Jimenez de Aberasturi, J. Aizpurua, R. A. Alvarez-Puebla, B. Auguié, J. J. Baumberg, G. C. Bazan, S. E. J. Bell, A. Boisen, A. G. Brolo, J. Choo, D. Cialla-May, V. Deckert, L. Fabris, K. Faulds, F. J. García de Abajo, R. Goodacre, D. Graham, A. J. Haes, C. L. Haynes, C. Huck, T. Itoh, M. Käll, J. Kneipp, N. A. Kotov, H. Kuang, E. C. Le Ru, H. K. Lee, J.-F. Li, X. Y. Ling, S. A. Maier, T. Mayerhöfer, M. Moskovits, K. Murakoshi, J.-M. Nam, S. Nie, Y. Ozaki, I. Pastoriza-Santos, J. Perez-Juste, J. Popp, A. Pucci, S. Reich, B. Ren, G. C. Schatz, T. Shegai, S. Schlücker, L.-L. Tay, K. G. Thomas, Z.-Q. Tian, R. P. Van Duyne, T. Vo-Dinh, Y. Wang, K. A. Willets, C. Xu, H. Xu, Y. Xu, Y. S. Yamamoto, B. Zhao, L. M. Liz-Marzán, *ACS Nano* **2020**, *14*, 28.

[36] M. Mayer, P. L. Potapov, D. Pohl, A. M. Steiner, J. Schultz, B. Rellinghaus, A. Lubk, T. A. F. König, A. Fery, *Nano Lett.* **2019**, *19*, 3854.

[37] V. G. Kravets, A. V. Kabashin, W. L. Barnes, A. N. Grigorenko, *Chem. Rev.* **2018**, *118*, 5912.

[38] P. Molet, N. Passarelli, L. A. Pérez, L. Scarabelli, A. Mihi, *Adv. Opt. Mater.* **2021**, *9*, 2100761.

[39] C. Matricardi, C. Hanske, J. L. Garcia-Pomar, J. Langer, A. Mihi, L. M. Liz-Marzán, *ACS Nano* **2018**, *12*, 8531.

[40] L. Scarabelli, D. Vila-Liarte, A. Mihi, L. M. Liz-Marzán, *Acc. Mater. Res.* **2021**, *2*, 816.

[41] S. Zou, N. Janel, G. C. Schatz, *J. Chem. Phys.* **2004**, *120*, 10871.

[42] M. Mayer, M. Tebbe, C. Kuttner, M. J. Schnepf, T. A. F. König, A. Fery, *Faraday Discuss.* **2016**, *191*, 159.

[43] E. S. A. Goerlitzer, R. Mohammadi, S. Nechayev, K. Volk, M. Rey, P. Banzer, M. Karg, N. Vogel, *Adv. Mater.* **2020**, *32*, 2001330.

[44] M. Hoffmann, D. Schletz, A. M. Steiner, D. Wolf, M. Mayer, A. Fery, *J. Phys. Chem. C* **2022**, *126*, 2475.

[45] A. Alvarez-Fernandez, C. Cummins, M. Saba, U. Steiner, G. Fleury, V. Ponsinet, S. Guldin, *Adv. Opt. Mater.* **2021**, *9*, 2100175.

[46] D. Vila-Liarte, N. A. Kotov, L. M. Liz-Marzán, *Chem. Sci.* **2022**, *13*, 595.

[47] A. K. Ghosh, S. Sarkar, L. J. Nebel, O. Aftenieva, V. Gupta, O. Sander, A. Das, J. Joseph, S. Wießner, T. A. F. König, A. Fery, *Adv. Funct. Mater.* **2021**, *31*, 2101959.

[48] K. Vogele, J. List, G. Pardatscher, N. B. Holland, F. C. Simmel, T. Pirzer, *ACS Nano* **2016**, *10*, 11377.

[49] F. N. Gür, C. P. T. McPolin, S. Raza, M. Mayer, D. J. Roth, A. M. Steiner, M. Löffler, A. Fery, M. L. Brongersma, A. V. Zayats, T. A. F. König, T. L. Schmidt, *Nano Lett.* **2018**, *18*, 7323.

[50] S. Sarkar, V. Gupta, T. Tsuda, J. Gour, A. Singh, O. Aftenieva, A. M. Steiner, M. Hoffmann, S. Kumar, A. Fery, J. Joseph, T. A. F. König, *Adv. Funct. Mater.* **2021**, *31*, 2011099.

[51] P. T. Probst, M. Mayer, V. Gupta, A. M. Steiner, Z. Zhou, G. K. Auernhammer, T. A. F. König, A. Fery, *Nat. Mater.* **2021**, *20*, 1024.

[52] W. Ma, L. Xu, A. F. de Moura, X. Wu, H. Kuang, C. Xu, N. A. Kotov, *Chem. Rev.* **2017**, *117*, 8041.

[53] J.-Y. Kim, J. Yeom, G. Zhao, H. Calcaterra, J. Munn, P. Zhang, N. Kotov, *J. Am. Chem. Soc.* **2019**, *141*, 11739.

[54] G. Klös, M. Miola, D. S. Sutherland, *J. Phys. Chem. C* **2019**, *123*, 7347.

[55] G. Klös, A. Andersen, M. Miola, H. Birkedal, D. S. Sutherland, *Nano Res.* **2019**, *12*, 1635.

[56] Yu, S.-S. Chang, C.-L. Lee, C. R. C. Wang, *J. Phys. Chem. B* **1997**, *101*, 6661.

[57] S. Link, Z. L. Wang, M. A. El-Sayed, *J. Phys. Chem. B* **2000**, *104*, 7867.

[58] I. Saldan, O. Dobrovetska, L. Sus, O. Makota, O. Pereviznyk, O. Kuntyi, O. Reshetnyak, *J. Solid State Electrochem.* **2018**, *22*, 637.

[59] N. Jara, N. S. Milán, A. Rahman, L. Mouheb, D. C. Boffito, C. Jeffryes, S. A. Dahoumane, *Molecules* **2021**, *26*, 4585.

[60] S. P. McDarby, M. L. Personick, *ChemNanoMat* **2022**, *8*, e202100472.

[61] J. Piaskowski, G. R. Bourret, *Molecules* **2022**, *27*, 2485.

[62] J. Turkevich, P. C. Stevenson, J. Hillier, *Discuss. Faraday Soc.* **1951**, *11*, 55.

[63] G. Frens, *Nat. Phys. Sci.* **1973**, *241*, 20.

[64] F. Fievet, J. P. Lagier, B. Blin, B. Beaudoin, M. Figlarz, *Solid State Ion.* **1989**, *32–33*, 198.

[65] Y. Sun, Y. Xia, *Adv. Mater.* **2002**, *14*, 833.

[66] I. Pastoriza-Santos, L. M. Liz-Marzán, *Langmuir* **2002**, *18*, 2888.

[67] Y. Sun, B. Mayers, T. Herricks, Y. Xia, *Nano Lett.* **2003**, *3*, 955.

[68] A. R. Tao, S. Habas, P. Yang, *Small* **2008**, *4*, 310.

[69] H. Dong, Y.-C. Chen, C. Feldmann, *Green Chem.* **2015**, *17*, 4107.

[70] M. Brust, M. Walker, D. Bethell, D. J. Schiffrin, R. Whyman, *J. Chem. Soc. Chem. Commun.* **1994**, 801.

[71] V. K. LaMer, R. H. Dinegar, *J. Am. Chem. Soc.* **1950**, *72*, 4847.

[72] K. R. Brown, D. G. Walter, M. J. Natan, *Chem. Mater.* **2000**, *12*, 306.

[73] K. K. Caswell, C. M. Bender, C. J. Murphy, *Nano Lett.* **2003**, *3*, 667.

[74] J. Xie, J. Y. Lee, D. I. C. Wang, *Chem. Mater.* **2007**, *19*, 2823.

[75] P. C. Angelomé, H. Heidari Mezerji, B. Goris, I. Pastoriza-Santos, J. Pérez-Juste, S. Bals, L. M. Liz-Marzán, *Chem. Mater.* **2012**, *24*, 1393.

[76] P. J. Straney, C. M. Andolina, J. E. Millstone, *Langmuir* **2013**, *29*, 4396.

[77] A. Umar, J. Lee, J. Dey, S.-M. Choi, *Chem. Mater.* **2016**, *28*, 4962.

[78] R. Zsigmondy, Thiessen, Peter Adolf, *Akkademische Verlagsgesellschaft* **1925**.

[79] N. G. Bastús, J. Comenge, V. Puntes, *Langmuir* **2011**, *27*, 11098.

[80] A. Gole, C. J. Murphy, *Chem. Mater.* **2004**, *16*, 3633.

[81] L. Scarabelli, M. Coronado-Puchau, J. J. Giner-Casares, J. Langer, L. M. Liz-Marzán, *ACS Nano* **2014**, *8*, 5833.

[82] G. González-Rubio, T. M. de Oliveira, T. Altantzis, A. L. Porta, A. Guerrero-Martínez, S. Bals, L. Scarabelli, L. M. Liz-Marzán, *Chem. Commun.* **2017**, *53*, 11360.

[83] A. Casu, E. Cabrini, A. Donà, A. Falqui, Y. Diaz-Fernandez, C. Milanese, A. Taglietti, P. Pallavicini, *Chem. - Eur. J.* **2012**, *18*, 9381.

[84] L. Scarabelli, A. Sánchez-Iglesias, J. Pérez-Juste, L. M. Liz-Marzán, *J. Phys. Chem. Lett.* **2015**, *6*, 4270.

[85] B. D. Busbee, S. O. Obare, C. J. Murphy, *Adv. Mater.* **2003**, *15*, 414.

[86] X. Ji, X. Song, J. Li, Y. Bai, W. Yang, X. Peng, *J. Am. Chem. Soc.* **2007**, *129*, 13939.

[87] A. Sánchez-Iglesias, N. Winckelmans, T. Altantzis, S. Bals, M. Grzelczak, L. M. Liz-Marzán, *J. Am. Chem. Soc.* **2017**, *139*, 107.

[88] H.-Y. Wu, H.-C. Chu, T.-J. Kuo, C.-L. Kuo, M. H. Huang, *Chem. Mater.* **2005**, *17*, 6447.

[89] M. Grzelczak, A. Sánchez-Iglesias, H. Heidari, S. Bals, I. Pastoriza-Santos, J. Pérez-Juste, L. M. Liz-Marzán, *ACS Omega* **2016**, *1*, 177.

[90] M. L. Personick, M. R. Langille, J. Zhang, C. A. Mirkin, *Nano Lett.* **2011**, *11*, 3394.

[91] J. E. Millstone, W. Wei, M. R. Jones, H. Yoo, C. A. Mirkin, *Nano Lett.* **2008**, *8*, 2526.

[92] M. R. Langille, M. L. Personick, J. Zhang, C. A. Mirkin, *J. Am. Chem. Soc.* **2012**, *134*, 14542.

[93] S. E. Lohse, N. D. Burrows, L. Scarabelli, L. M. Liz-Marzán, C. J. Murphy, *Chem. Mater.* **2014**, *26*, 34.

[94] G. Weng, X. Dong, J. Li, J. Zhao, *J. Mater. Sci.* **2016**, *51*, 7678.

[95] M. Grzelczak, J. Pérez-Juste, P. Mulvaney, L. M. Liz-Marzán, *Chem. Soc. Rev.* **2008**, *37*, 1783.

[96] M. L. Personick, C. A. Mirkin, *J. Am. Chem. Soc.* **2013**, *135*, 18238.

[97] L. Scarabelli, *Pure Appl. Chem.* **2018**, *90*, 1393.

[98] L. Liz-Marzán, *Colloidal Synthesis of Plasmonic Nanometals*, CRC Press, **2020**.

[99] P. Pallavicini, A. Donà, A. Casu, G. Chirico, M. Collini, G. Dacarro, A. Falqui, C. Milanese, L. Sironi, A. Taglietti, *Chem. Commun.* **2013**, *49*, 6265.

[100] H.-L. Wu, C.-H. Chen, M. H. Huang, *Chem. Mater.* **2009**, *21*, 110.

[101] P. Choo, D. Arenas-Esteban, I. Jung, W. J. Chang, E. A. Weiss, S. Bals, T. W. Odom, *ACS Nano* **2022**, *16*, 4408.

[102] N. R. Jana, L. Gearheart, C. J. Murphy, *Langmuir* **2001**, *17*, 6782.

[103] M. N. O'Brien, M. R. Jones, K. A. Brown, C. A. Mirkin, *J. Am. Chem. Soc.* **2014**, *136*, 7603.

[104] K. Park, M.-S. Hsiao, H. Koerner, A. Jawaid, J. Che, R. A. Vaia, *J. Phys. Chem. C* **2016**, *120*, 28235.

[105] A. Kedia, P. Senthil Kumar, *J. Phys. Chem. C* **2012**, *116*, 1679.

[106] E. Krauss, R. Kullock, X. Wu, P. Geisler, N. Lundt, M. Kamp, B. Hecht, *Cryst. Growth Des.* **2018**, *18*, 1297.

[107] J. E. Millstone, S. Park, K. L. Shuford, L. Qin, G. C. Schatz, C. A. Mirkin, *J. Am. Chem. Soc.* **2005**, *127*, 5312.

[108] P. S. Kumar, I. Pastoriza-Santos, B. Rodríguez-González, F. J. G. de Abajo, L. M. Liz-Marzán, *Nanotechnology* **2007**, *19*, 015606.

[109] H.-E. Lee, H.-Y. Ahn, J. Mun, Y. Y. Lee, M. Kim, N. H. Cho, K. Chang, W. S. Kim, J. Rho, K. T. Nam, *Nature* **2018**, *556*, 360.

[110] G. González-Rubio, J. Mosquera, V. Kumar, A. Pedrazo-Tardajos, P. Llombart, D. M. Solís, I. Lobato, E. G. Noya, A. Guerrero-Martínez, J. M. Taboada, F. Obelleiro, L. G. MacDowell, S. Bals, L. M. Liz-Marzán, *Science* **2020**, *368*, 1472.

[111] J. Niu, T. Zhu, Z. Liu, *Nanotechnology* **2007**, *18*, 325607.

[112] G. Gramlich, J. Zhang, W. M. Nau, *J. Am. Chem. Soc.* **2002**, *124*, 11252.

[113] C. Bullen, P. Zijlstra, E. Bakker, M. Gu, C. Raston, *Cryst. Growth Des.* **2011**, *11*, 3375.

[114] N. R. Jana, L. Gearheart, C. J. Murphy, *Adv. Mater.* **2001**, *13*, 1389.

[115] H.-E. Lee, H.-Y. Ahn, J. Mun, Y. Y. Lee, M. Kim, N. H. Cho, K. Chang, W. S. Kim, J. Rho, K. T. Nam, *Nature* **2018**, *556*, 360.

[116] L. Scarabelli, M. Grzelczak, L. M. Liz-Marzán, *Chem. Mater.* **2013**, *25*, 4232.

[117] X. Ye, C. Zheng, J. Chen, Y. Gao, C. B. Murray, *Nano Lett.* **2013**, *13*, 765.

[118] G. González-Rubio, V. Kumar, P. Llombart, P. Díaz-Núñez, E. Bladt, T. Altantzis, S. Bals, O. Peña-Rodríguez, E. G. Noya, L. G. MacDowell, A. Guerrero-Martínez, L. M. Liz-Marzán, *ACS Nano* **2019**, *13*, 4424.

[119] R. Ye, M. Zhao, X. Mao, Z. Wang, D. A. Garzón, H. Pu, Z. Zhao, P. Chen, *Nat. Commun.* **2021**, *12*, 4287.

[120] S. K. Meena, S. Celiksoy, P. Schäfer, A. Henkel, C. Sönnichsen, M. Sulpizi, *Phys. Chem. Chem. Phys.* **2016**, *18*, 13246.

[121] B. J. Wiley, Y. Chen, J. M. McLellan, Y. Xiong, Z.-Y. Li, D. Ginger, Y. Xia, *Nano Lett.* **2007**, *7*, 1032.

[122] M. Liu, P. Guyot-Sionnest, *J. Phys. Chem. B* **2005**, *109*, 22192.

[123] M. L. Personick, M. R. Langille, J. Zhang, C. A. Mirkin, *Nano Lett.* **2011**, *11*, 3394.

[124] N. D. Burrows, S. Harvey, F. A. Idesis, C. J. Murphy, *Langmuir* **2017**, *33*, 1891.

[125] L. Scarabelli, L. M. Liz-Marzán, *ACS Nano* **2021**, *15*, 18600.

[126] H. Yuan, C. G. Khoury, H. Hwang, C. M. Wilson, G. A. Grant, T. Vo-Dinh, *Nanotechnology* **2012**, *23*, 075102.

[127] C. V. Navin, K. S. Krishna, C. S. Theegala, C. S. S. R. Kumar, *Nanotechnol. Rev.* **2014**, *3*, 39.

[128] J. R. Adleman, D. A. Boyd, D. G. Goodwin, D. Psaltis, *Nano Lett.* **2009**, *9*, 4417.

[129] D. J. Beebe, G. A. Mensing, G. M. Walker, *Annu. Rev. Biomed. Eng.* **2002**, *4*, 261.

[130] P. Tabeling, *Introduction to Microfluidics*, Oxford University Press Inc., New York, **2005**.

[131] S. L. Stott, C.-H. Hsu, D. I. Tsukrov, M. Yu, D. T. Miyamoto, B. A. Waltman, S. M. Rothenberg, A. M. Shah, M. E. Smas, G. K. Korir, F. P. Floyd, A. J. Gilman, J. B. Lord, D. Winokur, S. Springer, D. Irimia, S. Nagrath, L. V. Sequist, R. J. Lee, K. J. Isselbacher, S. Maheswaran, D. A. Haber, M. Toner, *Proc. Natl. Acad. Sci.* **2010**, *107*, 18392.

[132] C.-Y. Lee, C.-L. Chang, Y.-N. Wang, L.-M. Fu, *Int. J. Mol. Sci.* **2011**, *12*, 3263.

[133] M.-H. Park, E. Reátegui, W. Li, S. N. Tessier, K. H. K. Wong, A. E. Jensen, V. Thapar, D. Ting, M. Toner, S. L. Stott, P. T. Hammond, *J. Am. Chem. Soc.* **2017**, *139*, 2741.

[134] E. Y. Westerbeek, J. G. Bomer, W. Olthuis, J. C. T. Eijkel, W. De Malsche, *Lab. Chip* **2020**, *20*, 3938.

[135] K. Sugano, Y. Uchida, O. Ichihashi, H. Yamada, T. Tsuchiya, O. Tabata, *Microfluid. Nanofluidics* **2010**, *9*, 1165.

[136] A. D. Stroock, S. K. W. Dertinger, A. Ajdari, I. Mezić, H. A. Stone, G. M. Whitesides, *Science* **2002**, *295*, 647.

[137] S. Abalde-Cela, P. Taladriz-Blanco, M. G. de Oliveira, C. Abell, *Sci. Rep.* **2018**, *8*, 2440.

[138] M. Antognoli, D. Stoecklein, C. Galletti, E. Brunazzi, D. Di Carlo, *Lab. Chip* **2021**, *21*, 3910.

[139] J. Wagner, J. M. Köhler, *Nano Lett.* **2005**, *5*, 685.

[140] S. Duraiswamy, S. A. Khan, *Nano Lett.* **2010**, *10*, 3757.

[141] J. Boleininger, A. Kurz, V. Reuss, C. Sönnichsen, *Phys. Chem. Chem. Phys.* **2006**, *8*, 3824.

[142] L. L. Lazarus, A. S.-J. Yang, S. Chu, R. L. Brutchey, N. Malmstadt, *Lab. Chip* **2010**, *10*, 3377.

[143] L. Zhang, Y. Wang, L. Tong, Y. Xia, *Langmuir* **2013**, *29*, 15719.

[144] R. Schreiber, N. Luong, Z. Fan, A. Kuzyk, P. C. Nickels, T. Zhang, D. M. Smith, B. Yurke, W. Kuang, A. O. Govorov, T. Liedl, *Nat. Commun.* **2013**, *4*, 2948.

[145] G. Dai, X. Lu, Z. Chen, C. Meng, W. Ni, Q. Wang, *ACS Appl. Mater. Interfaces* **2014**, *6*, 5388.

[146] R. P. M. Höller, M. Dulle, S. Thomä, M. Mayer, A. M. Steiner, S. Förster, A. Fery, C. Kuttner, M. Chanana, *ACS Nano* **2016**, *10*, 5740.

[147] A. Kuzyk, R. Jungmann, G. P. Acuna, N. Liu, *ACS Photonics* **2018**, *5*, 1151.

[148] K. Martens, F. Binkowski, L. Nguyen, L. Hu, A. O. Govorov, S. Burger, T. Liedl, *Nat. Commun.* **2021**, *12*, 2025.

[149] J. Dong, Y. Zhou, J. Pan, C. Zhou, Q. Wang, *Chem. Commun.* **2021**, *57*, 6201.

[150] M. Dass, F. N. Gür, K. Kołątaj, M. J. Urban, T. Liedl, *J. Phys. Chem. C* **2021**, *125*, 5969.

[151] N. Wu, Y. Tian, X. Zou, V. Silva, A. Chery, X. Wang, *J. Opt. Soc. Am. B* **2012**, *29*, 2016.

[152] A. Shiohara, J. Langer, L. Polavarapu, L. M. Liz-Marzán, *Nanoscale* **2014**, *6*, 9817.

[153] B. Fortuni, Y. Fujita, M. Ricci, T. Inose, R. Aubert, G. Lu, J. A. Hutchison, J. Hofkens, L. Latterini, H. Uji-i, *Chem. Commun.* **2017**, *53*, 5121.

[154] T. Schumacher, K. Kratzer, D. Molnar, M. Hentschel, H. Giessen, M. Lippitz, *Nat. Commun.* **2011**, *2*, 333.

[155] M. Zhu, G. Baffou, N. Meyerbröker, J. Polleux, *ACS Nano* **2012**, *6*, 7227.

[156] J. J. Giner-Casares, M. Henriksen-Lacey, I. García, L. M. Liz-Marzán, *Angew. Chem. Int. Ed.* **2016**, *55*, 974.

[157] G. Palermo, M. Rippa, Y. Conti, A. Vestri, R. Castagna, G. Fusco, E. Suffredini, J. Zhou, J. Zyss, A. De Luca, L. Petti, *ACS Appl. Mater. Interfaces* **2021**, *13*, 43715.

[158] G. A. Vinnacombe-Willson, N. Chiang, L. Scarabelli, Y. Hu, L. K. Heidenreich, X. Li, Y. Gong, D. T. Inouye, T. S. Fisher, P. S. Weiss, S. J. Jonas, *ACS Cent. Sci.* **2020**, *6*, 2105.

[159] F. Ren, C. Yesildag, Z. Zhang, M. C. Lensen, *Polymers* **2017**, *9*, 154.

[160] B. Molina-Martínez, L. M. Liz-Marzán, *Biomater. Biosyst.* **2022**, *6*, 100044.

[161] T. Liu, T. D. Keiper, X. Wang, G. Yang, D. T. Hallinan, J. Zhao, P. Xiong, *ACS Appl. Mater. Interfaces* **2017**, *9 49*, 43363.

[162] C. M. Platnich, A. Banerjee, V. Ozhukil Kollath, K. Karan, S. Trudel, *Can. J. Chem.* **2018**, *96*, 190.

[163] J. Zhang, M. Kambayashi, M. Oyama, *Electroanalysis* **2005**, *17*, 408.

[164] M. Ben Haddada, J. Blanchard, S. Casale, J.-M. Krafft, A. Vallée, C. Méthivier, S. Boujday, *Gold Bull.* **2013**, *46*, 335.

[165] A. Sobhani, M. W. Knight, Y. Wang, B. Zheng, N. S. King, L. V. Brown, Z. Fang, P. Nordlander, N. J. Halas, *Nat. Commun.* **2013**, *4*, 1643.

[166] B. Song, K. He, Y. Yuan, S. Sharifi-Asl, M. Cheng, J. Lu, W. A. Saidi, R. Shahbazian-Yassar, *Nanoscale* **2018**, *10*, 15809.

[167] Y.-K. Kim, H.-K. Na, Y. W. Lee, H. Jang, S. W. Han, D.-H. Min, *Chem. Commun.* **2010**, *46*, 3185.

[168] U. J. Kim, S. Yoo, Y. Park, M. Shin, J. Kim, H. Jeong, C.-W. Baik, Y.-G. Roh, J. Lee, K. Im, H. Son, S. Hwang, C.-W. Lee, S. Park, *ACS Photonics* **2015**, *2*, 506.

[169] G.-C. Li, Y.-L. Zhang, J. Jiang, Y. Luo, D. Y. Lei, *ACS Nano* **2017**, *11*, 3067.

[170] T. J. Merkel, K. P. Herlihy, J. Nunes, R. M. Orgel, J. P. Rolland, J. M. DeSimone, *Langmuir* **2010**, *26*, 13086.

[171] S. Kasani, K. Curtin, N. Wu, *Nanophotonics* **2019**, *8*, 2065.

[172] T. Lee, C. Lee, D. K. Oh, T. Badloe, J. G. Ok, J. Rho, *Sensors* **2020**, *20*, 4108.

[173] Y. Chen, K. Bi, Q. Wang, M. Zheng, Q. Liu, Y. Han, J. Yang, S. Chang, G. Zhang, H. Duan, *ACS Nano* **2016**, *10*, 11228.

[174] J. Henzie, M. H. Lee, T. W. Odom, *Nat. Nanotechnol.* **2007**, *2*, 549.

[175] C. Zhao, T. Man, X. Xu, Q. Yang, W. Liu, S. J. Jonas, M. A. Teitell, P.-Y. Chiou, P. S. Weiss, *ACS Mater. Lett.* **2020**, *2*, 1475.

[176] W. Liu, J. Wang, X. Xu, C. Zhao, X. Xu, P. S. Weiss, *ACS Nano* **2021**, *15*, 12180.

[177] C. Lu, R. H. Lipson, *Laser Photonics Rev.* **2010**, *4*, 568.

[178] N. Gisbert Quilis, M. Lequeux, P. Venugopalan, I. Khan, W. Knoll, S. Boujday, M. Lamy de la Chapelle, J. Dostalek, *Nanoscale* **2018**, *10*, 10268.

[179] T. R. Jensen, G. C. Schatz, R. P. Van Duyne, *J. Phys. Chem. B* **1999**, *103*, 2394.

[180] C. L. Haynes, R. P. Van Duyne, *J. Phys. Chem. B* **2001**, *105*, 5599.

[181] F. Huo, Z. Zheng, G. Zheng, L. R. Giam, H. Zhang, C. A. Mirkin, *Science* **2008**, *321*, 1658.

[182] Liao Wei-Ssu, Cheunkar Sarawut, Cao Huan H., Bednar Heidi R., Weiss Paul S., Andrews Anne M., *Science* **2012**, *337*, 1517.

[183] X. Xu, Q. Yang, K. M. Cheung, C. Zhao, N. Wattanatorn, J. N. Belling, J. M. Abendroth, L. S. Slaughter, C. A. Mirkin, A. M. Andrews, P. S. Weiss, *Nano Lett.* **2017**, *17*, 3302.

[184] C. Zhao, Q. Liu, K. M. Cheung, W. Liu, Q. Yang, X. Xu, T. Man, P. S. Weiss, C. Zhou, A. M. Andrews, *ACS Nano* **2021**, *15*, 904.

[185] G. Tagliabue, A. S. Jermyn, R. Sundararaman, A. J. Welch, J. S. DuChene, R. Pala, A. R. Davoyan, P. Narang, H. A. Atwater, *Nat. Commun.* **2018**, *9*, 3394.

[186] I.-C. Ni, S.-C. Yang, C.-W. Jiang, C.-S. Luo, W. Kuo, K.-J. Lin, S.-D. Tzeng, *J. Phys. Chem. C* **2012**, *116*, 8095.

[187] A. Sánchez-Iglesias, B. Rivas-Murias, M. Grzelczak, J. Pérez-Juste, L. M. Liz-Marzán, F. Rivadulla, M. A. Correa-Duarte, *Nano Lett.* **2012**, *12*, 6066.

[188] J. W. Boley, S.-H. Hyun, E. L. White, D. H. Thompson, R. K. Kramer, *ACS Appl. Mater. Interfaces* **2016**, *8*, 34171.

[189] J. Kim, X. Song, F. Ji, B. Luo, N. F. Ice, Q. Liu, Q. Zhang, Q. Chen, *Nano Lett.* **2017**, *17*, 3270.

[190] W. Ahmed, Ö. Demirtaş, İ. M. Öztürk, A. Bek, *ACS Appl. Nano Mater.* **2020**, *3*, 6766.

[191] P.-P. Fang, S. Chen, H. Deng, M. D. Scanlon, F. Gumy, H. J. Lee, D. Momotenko, V. Amstutz, F. Cortés-Salazar, C. M. Pereira, Z. Yang, H. H. Girault, *ACS Nano* **2013**, *7*, 9241.

[192] L. Velleman, D. Sikdar, V. A. Turek, A. R. Kucernak, S. J. Roser, A. A. Kornyshev, J. B. Edel, *Nanoscale* **2016**, *8*, 19229.

[193] H. Min, J. Zhou, X. Bai, L. Li, K. Zhang, T. Wang, X. Zhang, Y. Li, Y. Jiao, X. Qi, Y. Fu, *Langmuir* **2017**, *33*, 6732.

[194] J. Mitchell, J. J. Weimer, *Langmuir* **2021**, *37*, 5139.

[195] T. Wen, S. A. Majetich, *ACS Nano* **2011**, *5*, 8868.

[196] S. Gilles, C. Kaulen, M. Pabst, U. Simon, A. Offenhäusser, D. Mayer, *Nanotechnology* **2011**, *22*, 295301.

[197] H. L. Huang, J.-K. Chen, M. P. Houng, *Thin Solid Films* **2012**, *524*, 304.

[198] N. J. Greybush, I. Liberal, L. Malassis, J. M. Kikkawa, N. Engheta, C. B. Murray, C. R. Kagan, *ACS Nano* **2017**, *11*, 2917.

[199] N. Chiang, L. Scarabelli, G. A. Vinnacombe-Willson, L. A. Pérez, C. Dore, A. Mihi, S. J. Jonas, P. S. Weiss, *ACS Mater. Lett.* **2021**, *3*, 282.

[200] V. Santhanam, R. P. Andres, *Nano Lett.* **2004**, *4*, 41.

[201] M. Mayer, M. J. Schnepf, T. A. F. König, A. Fery, *Adv. Opt. Mater.* **2019**, *7*, 1800564.

[202] R. D. Neal, R. A. Hughes, A. S. Preston, S. D. Golze, T. B. Demille, S. Neretina, *J. Mater. Chem. C* **2021**, *9*, 12974.

[203] J. Gargiulo, I. L. Violi, S. Cerrota, L. Chvátal, E. Cortés, E. M. Perassi, F. Diaz, P. Zemánek, F. D. Stefani, *ACS Nano* **2017**, *11*, 9678.

[204] I. L. Violi, J. Gargiulo, C. von Bilderling, E. Cortés, F. D. Stefani, *Nano Lett.* **2016**, *16*, 6529.

[205] S. Siavoshi, C. Yilmaz, S. Somu, T. Musacchio, J. R. Upponi, V. P. Torchilin, A. Busnaina, *Langmuir* **2011**, *27*, 7301.

[206] H. Zhang, J. Cadusch, C. Kinnear, T. James, A. Roberts, P. Mulvaney, *ACS Nano* **2018**, *12*, 7529.

[207] Y. Tian, S. Qiang, L. Wang, *Front. Bioeng. Biotechnol.* **2019**, *7*, 398.

[208] J. N. Lee, C. Park, G. M. Whitesides, *Anal. Chem.* **2003**, *75*, 6544.

[209] V. Sebastian Cabeza, S. Kuhn, A. A. Kulkarni, K. F. Jensen, *Langmuir* **2012**, *28*, 7007.

[210] G. Tofighi, H. Lichtenberg, J. Pesek, T. L. Sheppard, W. Wang, L. Schöttner, G. Rinke, R. Dittmeyer, J.-D. Grunwaldt, *React. Chem. Eng.* **2017**, *2*, 876.

Chapter 2. Large-Scale Soft-Lithographic Patterning of Plasmonic Nanoparticles

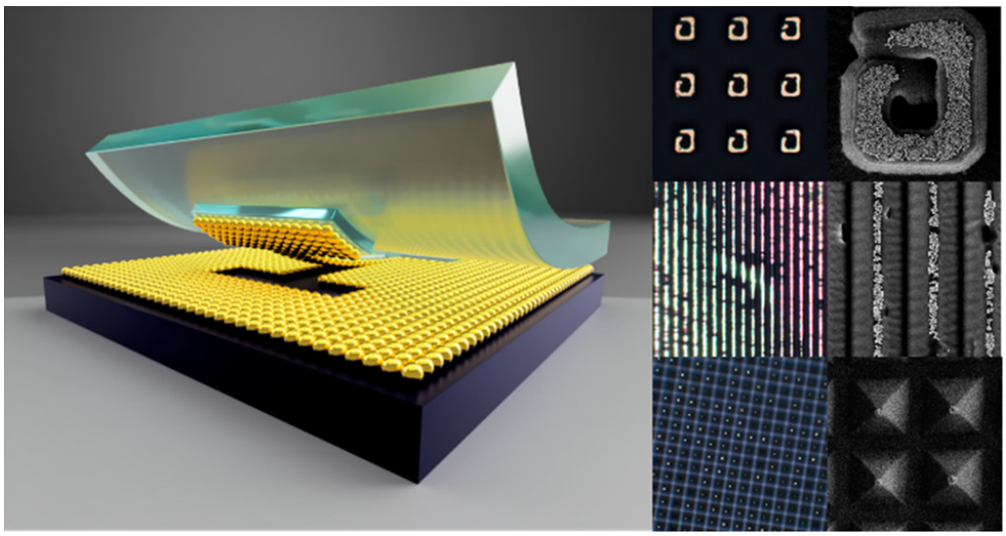

A chemically driven subtractive soft lithographic patterning technique was used to fabricate plasmonic substrates from colloidal plasmonic gold nanoparticles. The developed method is highly versatile, offering tunability with the diameter of the individual plasmonic units, pattern geometry, and receiving substrate. Overall, this nanoparticle chemical lift-off lithographic method constitutes a facile, scalable approach, applicable for the fabrication of plasmonic sensors and optoelectronics.

Section 2.1. Introduction

As discussed in **Chapter 1**, plasmon resonances confine light in sub-diffraction volumes, which can lead to enhancement of light-matter interactions and drive a variety of nanoscale phenomena, including amplification of linear[1,2] and non-linear[3,4] optical processes, photothermal conversion,[5,6] hot-carrier generation,[7] and strong-coupling interactions.[8,9] These capabilities place plasmonics at the intersection of nanophotonics and nanoelectronics, offering solutions for ultra-small light sources, quantum-computing, and opto-electronic devices.[10] From **Section 1.2**, it is apparent that colloidal noble metal nanoparticles are one of the most versatile platforms for engineering plasmonic resonances given the remarkable control over their crystallographic structure and optical properties offered by wet-chemistry synthesis.[11,12] When plasmonic nanostructures made by bottom-up synthesis are organized in periodic patterns (*i.e.,* in one, two, or three dimensions), new interesting plasmonic responses can be engineered (**Section 1.3**).[13–15] As summarized in **Section 1.3.2**, various approaches have been pursued for the fabrication of plasmonic substrates from nanoparticles prepared with batch synthesis. In particular, the combination of colloidal self-assembly with soft-lithography has led to the fabrication of large-area micro- and nanoscale hierarchical structures and periodic arrays from colloidal nanoparticles.[16–19] However, a generalized approach that could adapt to different plasmonic building-block sizes, shapes and compositions, and different substrate materials has not yet been realized.[20] Moreover, accessing nanoscale features with high fidelity over large areas remains a challenge.[21–23] In this chapter, we present a gold nanoparticle patterning method based on chemical lift-off lithography (CLL), a subtractive patterning technique originally introduced for generating metal patterns *via* self-assembly monolayer patterning and etching.[24–27] Unlike additive microcontact printing, CLL uses chemical interactions between the ink and the stamp to

push the resolution limit down to tens of nanometers or lower.[28] The versatile nanoparticle patterning approach based on this method, nanoparticle chemical lift-off lithography (NP-CLL), combines colloidal nanochemistry and lithographic patterning. This technique takes advantage of condensation chemistry for organizing pre-synthetized plasmonic nanoparticles into arbitrary micro- and nanoscale patterns, including islands, lines, and square spirals.

Section 2.2. Results and Discussion

The advance at the core of NP-CLL lies in the application of pre-synthetized mercaptoalkanol-capped gold nanoparticles (AuNPs), which are organized into monolayers and later undergo a condensation reaction with a patterned elastomeric stamp. The AuNPs are first self-assembled into monolayers at a liquid-liquid interface, exploiting fine control over three effects:[29,30] *i)* spontaneous migration of nanoparticles towards the interface to reduce the surface tension between two immiscible liquids; *ii)* colloidal instability triggered by high ionic strength resulting from the addition of tetrabutylammonium tetraphenylborate (TBA-TPB); and *iii)* nanoparticle resistance towards aggregation conferred by the thiol ligand. Gold nanoparticle monolayers are then transferred to desired substrates using a custom-built automated dip coater (**Figure 2.1A**, **Figure 2.2**). This self-assembly approach has the benefit of being extremely versatile and straightforward to adapt for particles with different sizes, shapes, and compositions.[29] Moreover, it is easily scalable to tens of centimeters, enabling the use of the described patterning technique for the preparation of wafer-scale devices. As for the thiol ligand, we used (11-mercaptoundecyl)hexa(ethylene glycol) (MUHEG), which is capable of stabilizing colloids up to 100 nm in aqueous media (**Figure 2.3**).

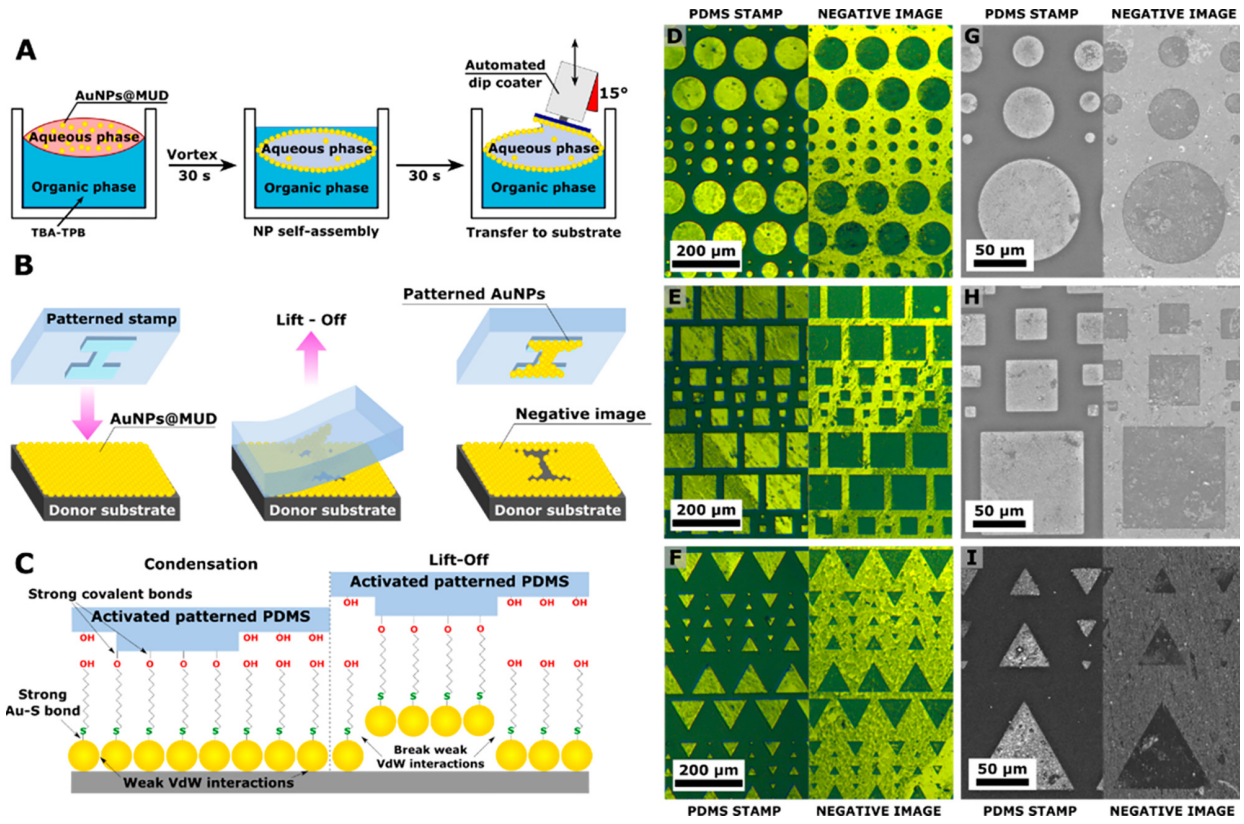

Figure 2.1. A,B: Schematic of (**A**) gold nanoparticle (AuNP) self-assembly at the liquid-liquid interface, and (**B**) the chemical lift-off lithography (CLL) process on the assembled AuNP monolayer. **C:** Schematic of the interactions that occur during CLL. **D-F:** Optical images and **G-I:** scanning electron microscopy images of a polydimethylsiloxane (PDMS) patterned stamp after lift-off (*left*) and the corresponding complementary negative image imprinted in the AuNP monolayer donor substrate (*right*).

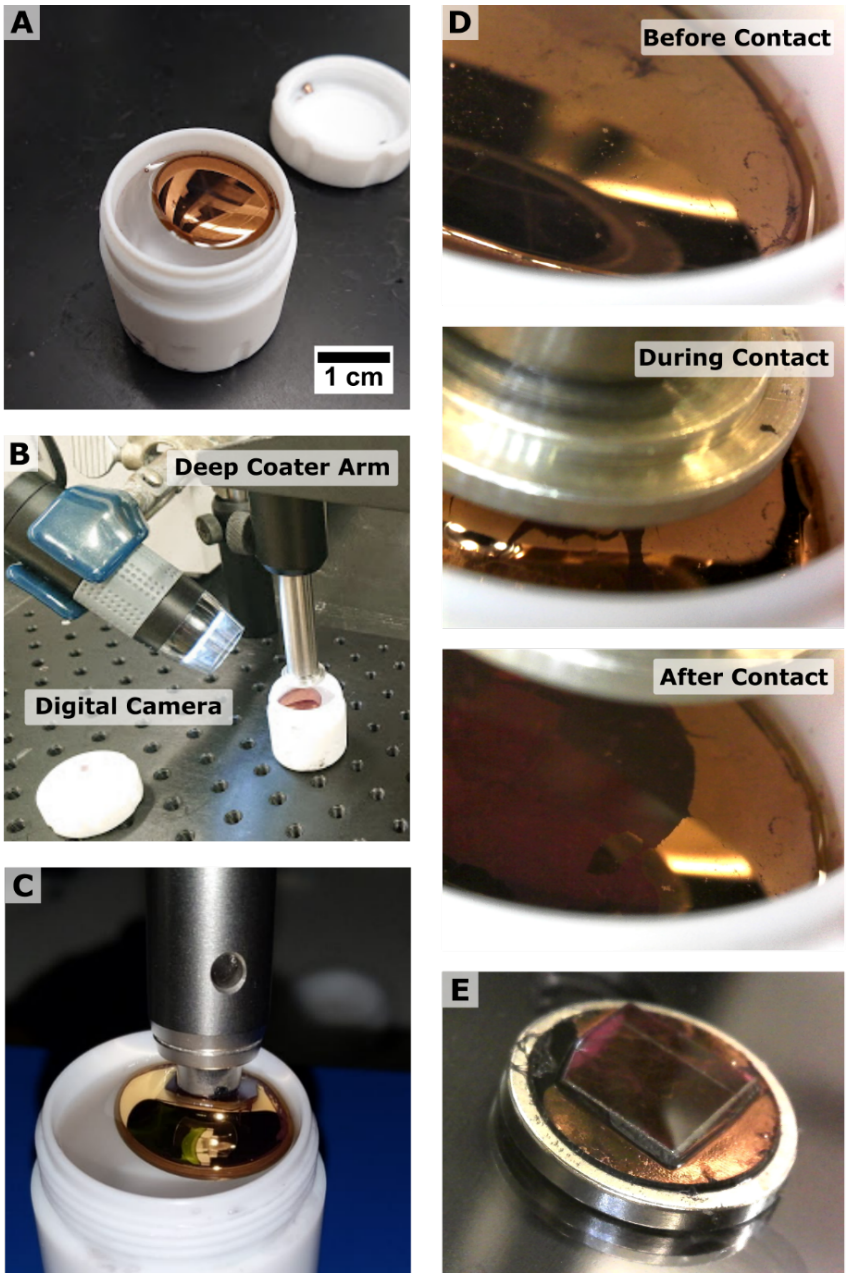

Figure 2.2. **A:** Digital photograph of the self-assembled nanoparticles at the liquid-liquid interface. **B:** Digital photograph of the dip coater setup. **C:** Digital photograph of the monolayer in contact with the substrate. **D:** Higher magnification optical images of the Au nanoparticle monolayer being transferred to a substrate taken with the digital camera shown in **B**. The pictures show the monolayer (*top*) during the approach of the dip coater arm, (*middle*) once contact has been established, and (*bottom*) after the arm has been retracted. **E:** Digital photograph of the monolayer produced on the substrate.

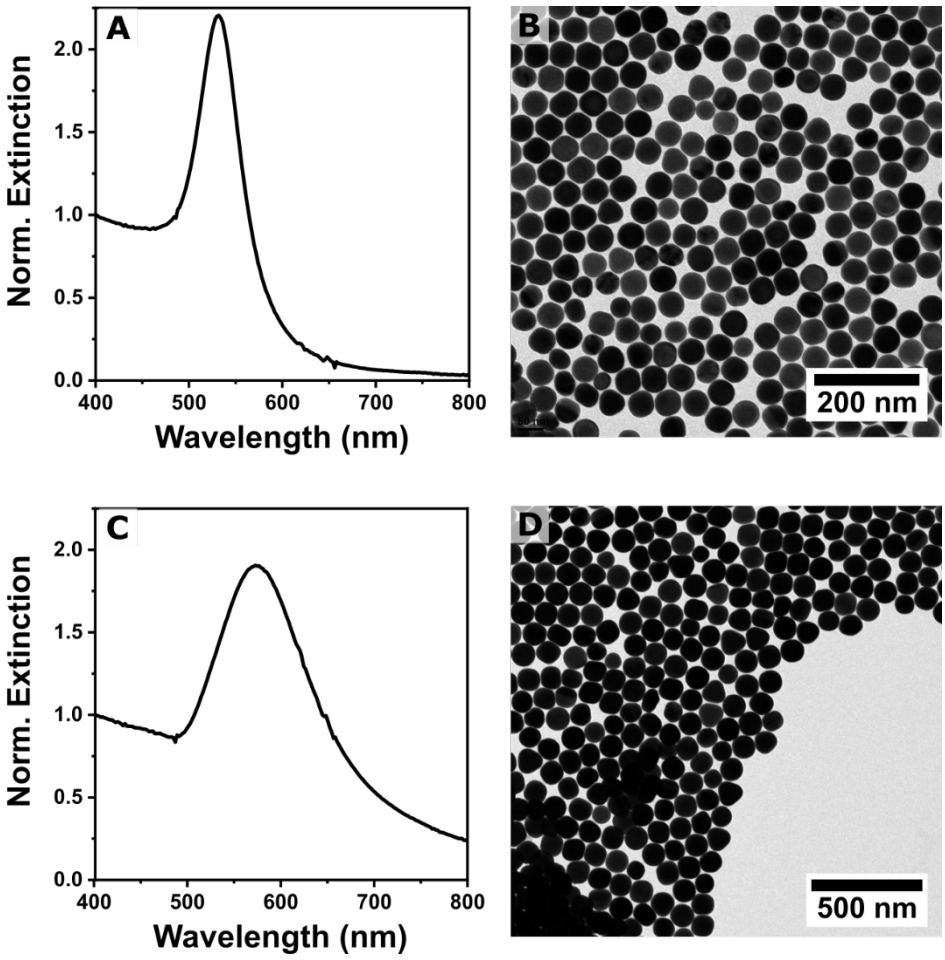

Figure 2.3. **Left:** Extinction ultraviolet (UV)-visible spectra of the synthesized colloids. **Right:** Transmission electron microscopy images of the colloids used in the manuscript after the ligand exchange reaction. **A,B:** 50 ± 3 nm (11-mercaptoundecyl)hexa(ethylene glycol) (MUHEG)-coated gold nanoparticles. **C,D:** 100 ± 9 nm MUHEG-coated gold nanoparticles.

The NP-CLL patterning process consists of conformally contacting an activated, patterned polydimethylsiloxane (PDMS) stamp directly onto the AuNP monolayer donor substrate (**Figure 2.1B**) at 60 °C for 3 h in an oven. During this time, the hydroxyl termini on both the activated PDMS and the mercaptoalkanol-coated AuNPs undergo condensation reactions yielding strong covalent bonds in the contact regions. **Figure 2.1C** illustrates the three main interactions in the

system: *i)* the covalent ether bonds formed between the mercaptoalkanol ligand and the PDMS; *ii)* the sulfur-gold bonds between the thiols and the AuNP surface; and *iii)* the AuNP-AuNP and AuNP-substrate van der Waals (VdW) interactions. The interplay of these forces was exploited to generate patterned monolayers of AuNPs, *i.e.,* when the PDMS stamp is removed, the weak VdW interactions are more readily broken. Therefore, the AuNPs in contact with the patterned regions of the stamp are "lifted-off" with the PDMS, leaving a complementary negative image of the pattern on the donor substrate (**Figure 2.1B**). **Figure 2.1** shows optical and scanning electron microscopy (SEM) images of patterned substrates obtained by lifting-off 50 ± 3 nm MUHEG-capped AuNPs (**Figure 2.3**) using stamps with 10-100 μm features (**Figure 2.4**).

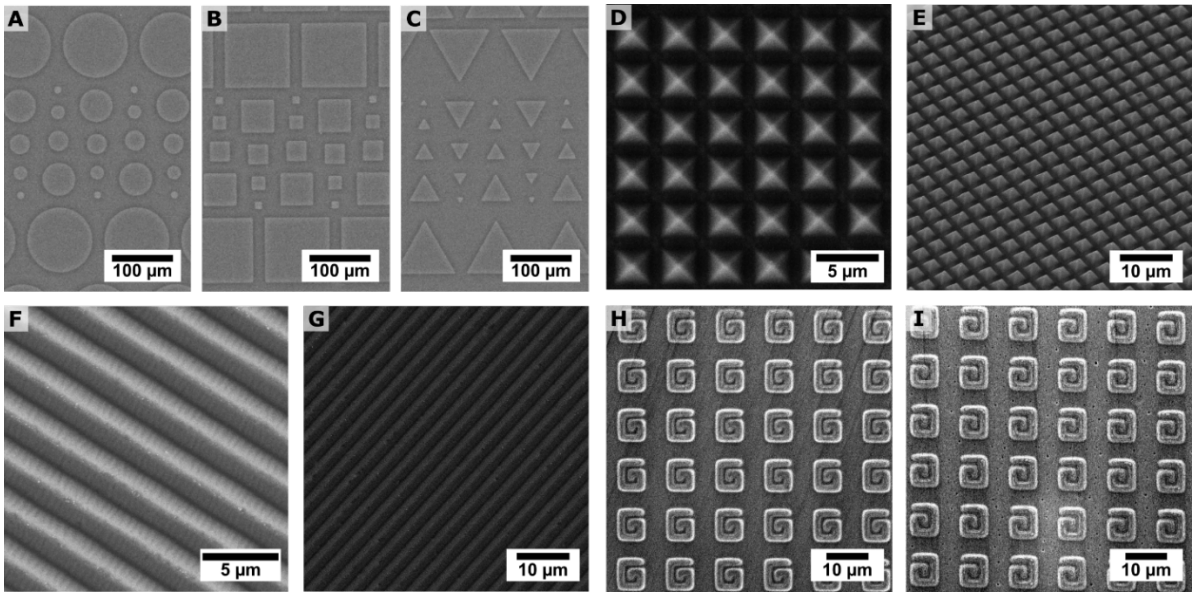

Figure 2.4. **A-I:** Scanning electron microscopy images of the polydimethylsiloxane patterns used for nanoparticle chemical lift-off lithography. (**A-C**) Large geometric shapes, (**D,E**) pyramids, (**F,G)** gratings, and (**H,I**) spirals (counterclockwise and clockwise).

Continuous smooth curved lines and straight edges were both reproduced with high fidelity using NP-CLL (**Figure 2.5**). However, particle vacancies and clusters can be observed in the lifted-off

regions. We believe that these imperfections largely originate in the original gold nanoparticle monolayer. The application of positive pressure before lift-off would improve the uniformity of contact with the PDMS stamp but would induce deformation of the stamp itself.[28,31] Another possible approach would be to accelerate the condensation reaction by performing the CLL process at higher temperature, although the range would be limited by gold colloid and PDMS stability.

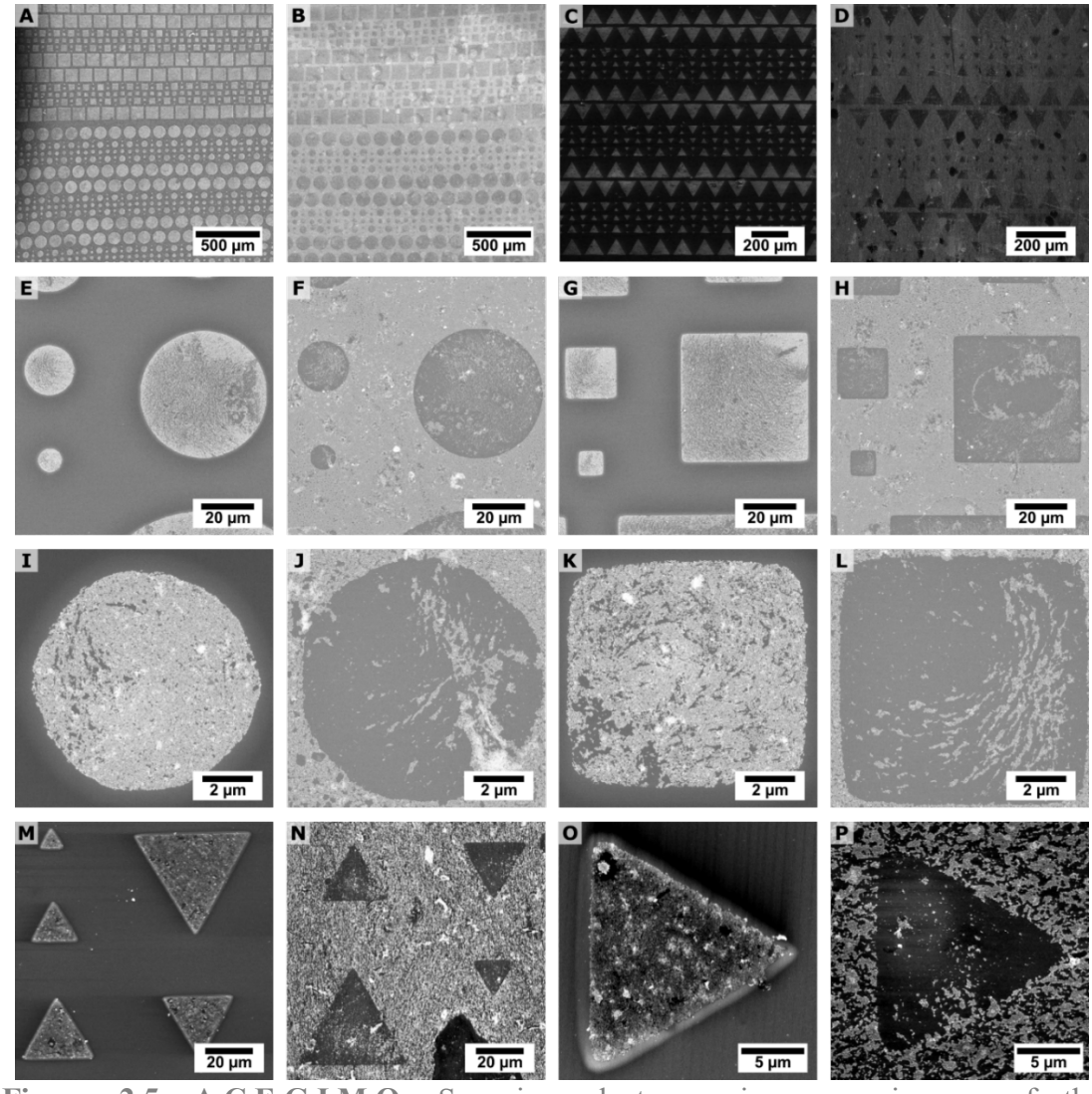

Figure 2.5. **A,C,E,G,I,M,O:** Scanning electron microscopy images of the polydimethylsiloxane patterns after lift-off. **B,D,F,H,J,L,N,P:** Complementary negative image imprinted into the original monolayer at different magnifications.

The NP-CLL mechanism was tested further in a control experiment where the same procedure was repeated without activation of the patterned PDMS. In this case, no particles were observed to be transferred from the donor substrate to the stamp (**Figure 2.6**), consistent with the condensation reaction being the driving mechanism for lift-off. During the preparation of the initial nanoparticle monolayers, an increment in the concentration of AuNPs in the aqueous phase during assembly of the liquid-liquid interface can result in nanoparticle multilayers. However, this result does *not* affect lift-off and still yields patterned monolayers on the PDMS stamp, because the AuNP-AuNP and AuNP-substrate interactions are governed by similar VdW interactions. Based on this observation, we noted the possibility for engineering interparticle and substrate-particle interactions to fabricate patterned stacks of plasmonic nanostructures *via* NP-CLL.[32] This strategy will be the subject of future implementations of the technique.

One of the advantages of NP-CLL (and all CLL processes) is the simultaneous production of two patterned plasmonic substrates: the PDMS stamp with the lifted-off nanoparticles and the complementary negative image remaining on the AuNP monolayer.[25,33] To this end, we demonstrated both consecutive NP-CLL as well as nanoparticle microcontact transfer printing using the prepared PDMS substrates (**Figure 2.7**). In the former case, the complementary negative image is reused for secondary NP-CLL using an activated flat PDMS stamp and repeating the same procedure (**Figure 2.8**). In the latter case, the patterned AuNP monolayer is released from the PDMS stamp and transferred onto a receiving surface (**Figure 2.9**). High magnification electron microscopy images after transfer of the negative image from the pre-patterned monolayer onto a flat PDMS substrate following secondary NP-CLL show good pattern reproducibility, similar to the initial NP-CLL step (**Figure 2.10**).

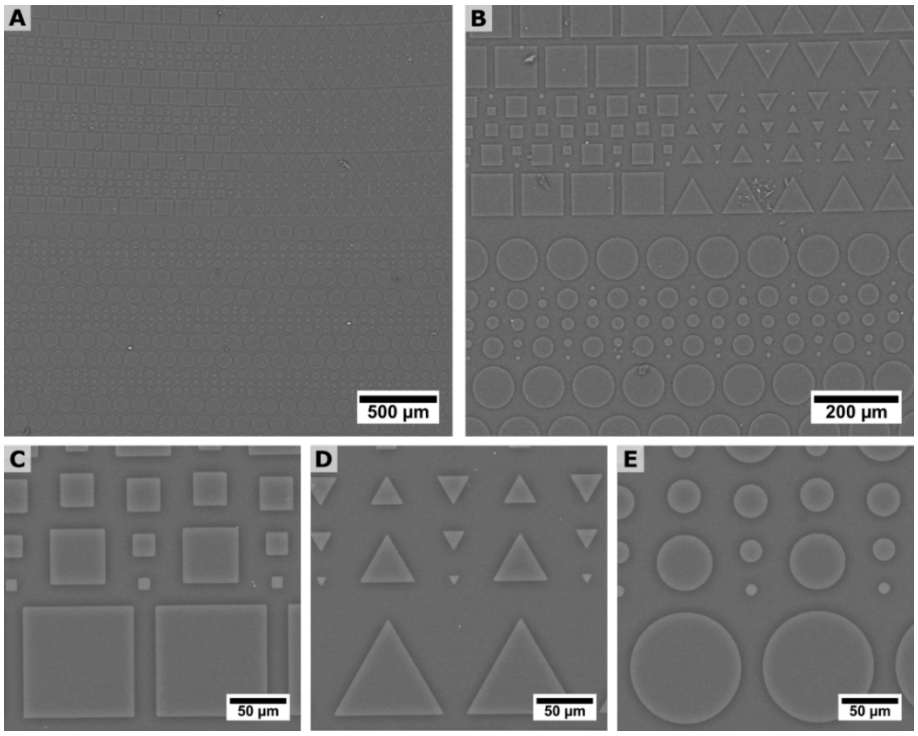

Figure 2.6. A-E: Scanning electron microscopy characterization at different magnifications of the polydimethylsiloxane (PDMS) pattern after lift-off when no UV-ozone activation was performed on the PDMS. The observation that no gold nanoparticles were bound to the stamp is consistent with the chemistry-based mechanism proposed in the text.

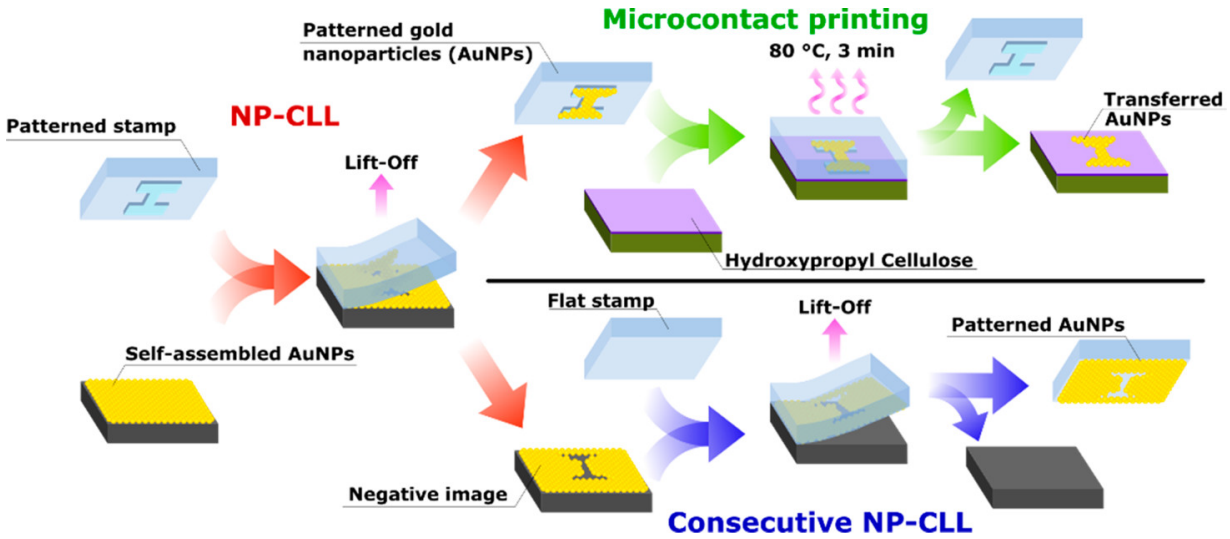

Figure 2.7. Overview of the three lithographic procedures: nanoparticle chemical lift-off lithography (NP-CLL, red), microcontact printing (green), and consecutive NP-CLL (blue). AuNPs: Au nanoparticles.

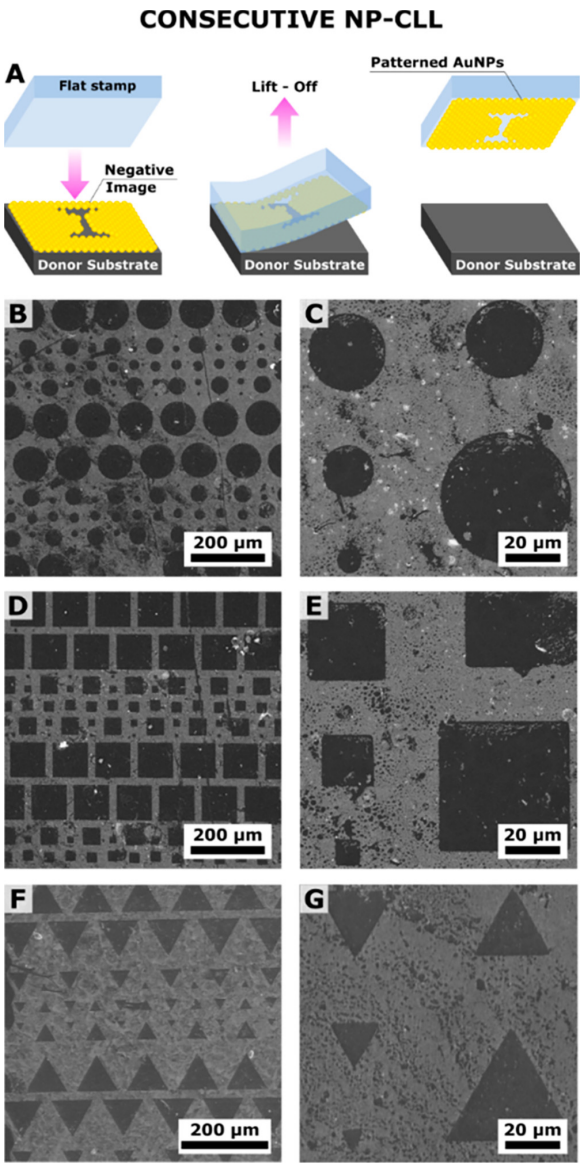

Figure 2.8. Consecutive nanoparticle chemical lift-off lithography (NP-CLL). A: Schematic illustration and **B-E**: scanning electron microscopy images at different magnifications of the lift-off of a complementary negative image imprinted into the original gold nanoparticle (Au NPs) monolayer using a flat PDMS stamp.

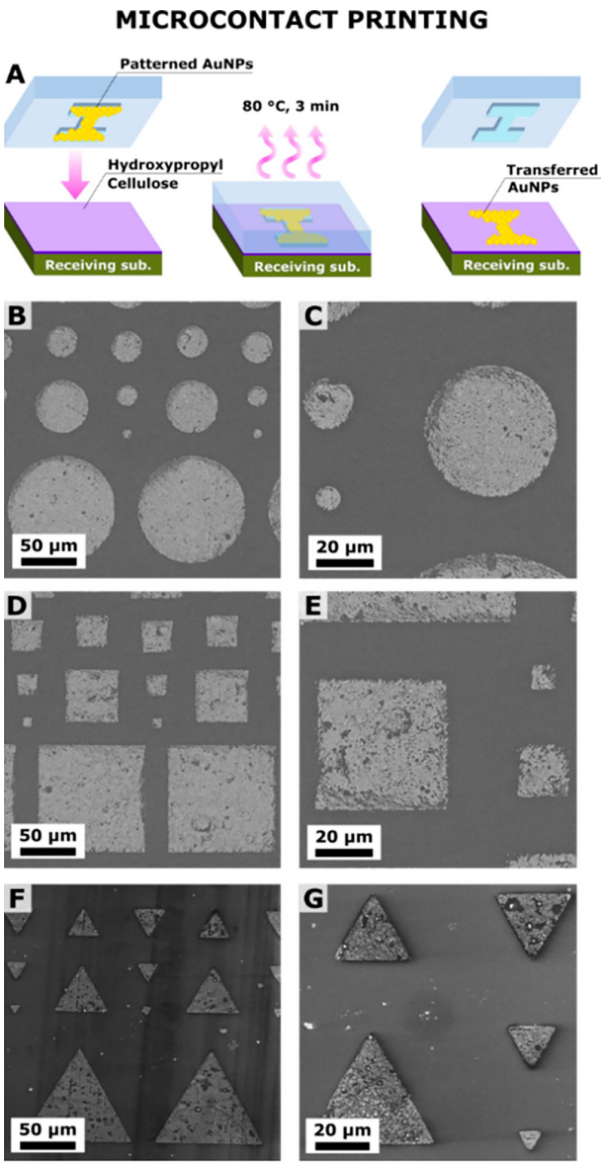

Figure 2.9. Microcontact printing. A: Schematic illustration and **B-G**: scanning electron microscopy at different magnifications of the patterns of gold nanoparticles (AuNPs) transferred from a patterned stamp to a clean glass substrate via contact printing mediated by hydroxypropyl cellulose.

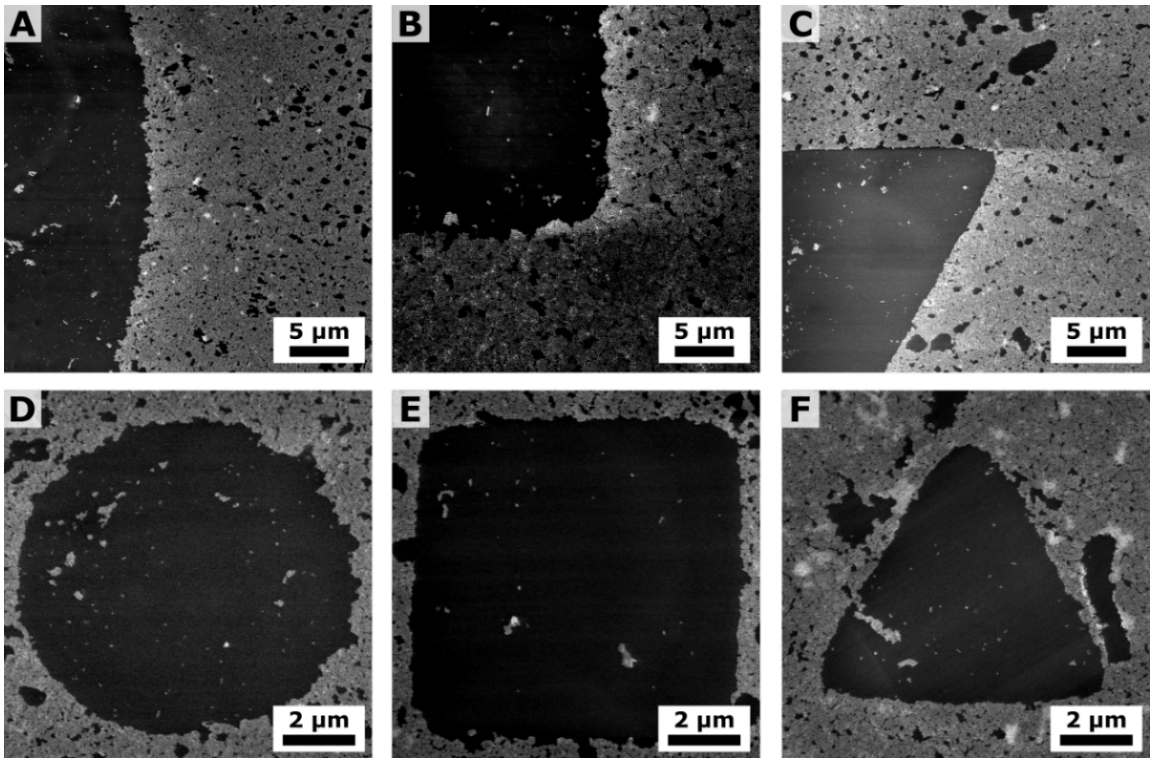

Figure 2.10. A-F: High-magnification scanning electron microscopy images of the featureless flat polydimethylsiloxane stamp used for a consecutive secondary chemical lift-off lithography (CLL) of the complementary negative pattern, highlighting how smaller features such as corners and edges match the stamp resolution (which is limited by the microwriter resolution).

In the microcontact printing procedure, we exploited the thermoplastic behavior of dry hydroxypropyl cellulose (HPC) films.[34] Additionally, HPC is water soluble and thus can be used as a sacrificial layer, potentially expanding the versatility of this approach for integrating plasmonic building blocks with a variety of different substrate materials such as graphene, transition metal dichalcogenides, and semiconducting materials.[34] The procedure is straightforward. In brief, a thin layer (~50 nm) of HPC is spin coated onto a clean glass slide and placed in contact with the patterned stamp. Transfer of the nanoparticle layer is achieved by raising the temperature to 80 °C for 3 min. From electron microscopy inspection of the receiving substrate, we confirmed that patterned features are maintained. Moreover, we did not observe signs of

coalescence of neighboring nanoparticles. Note that the transferred pattern presents more vacancies, indicating that the transfer is only semi-quantitative (**Figure 2.11-12**). The yield of the transfer could be improved by exposing the patterned AuNP stamp to UV-ozone treatment prior to the microcontact printing step. This treatment breaks the thiol-Au bonds that anchor the particles to the PDMS stamp,[35] facilitating the transfer upon contact with the receiving substrate. However, this procedure can damage AuNPs if non-spherical structures are used, due to removal of the capping ligands and consequent reshaping that minimizes the surface energy of the nanocrystals.[36]

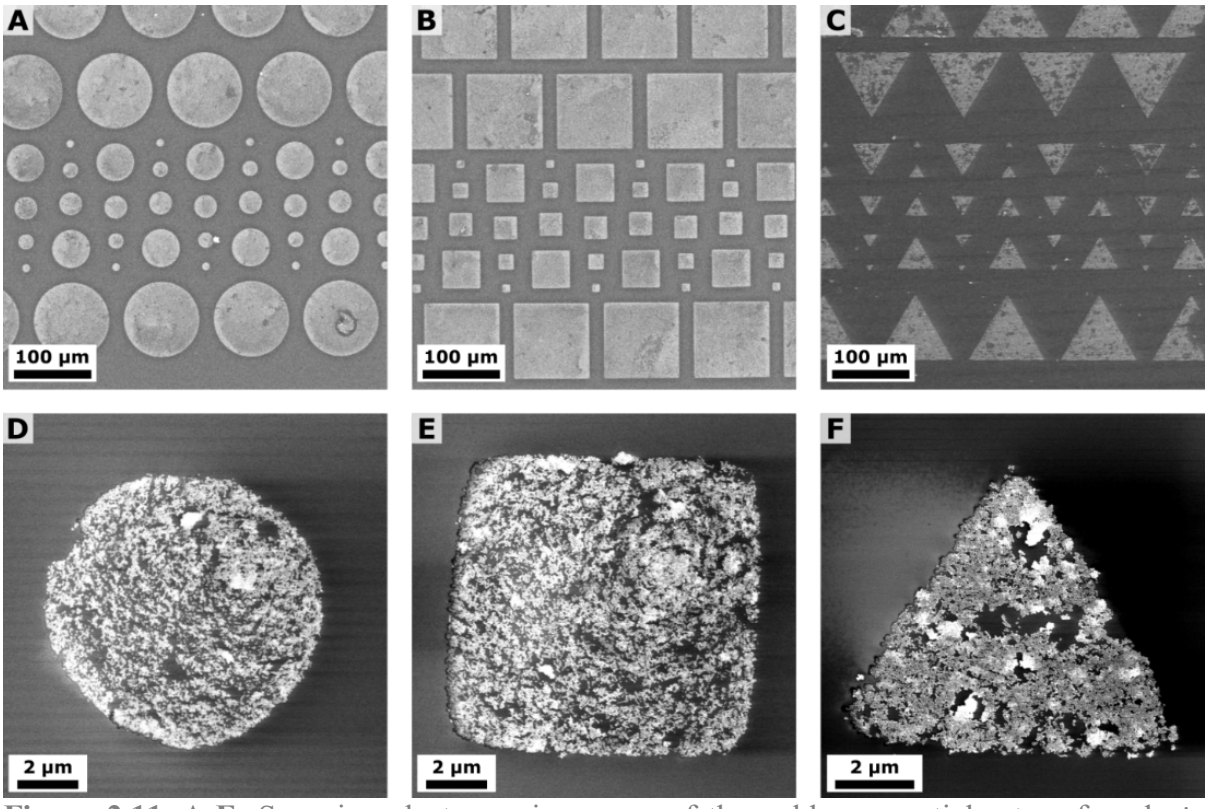

Figure 2.11. **A-F:** Scanning electron microscopy of the gold nanoparticles transferred *via* hydroxypropylcellulose-mediated microcontact printing, showing (**A-C**) long-range transfer and (**D-F**) small features.

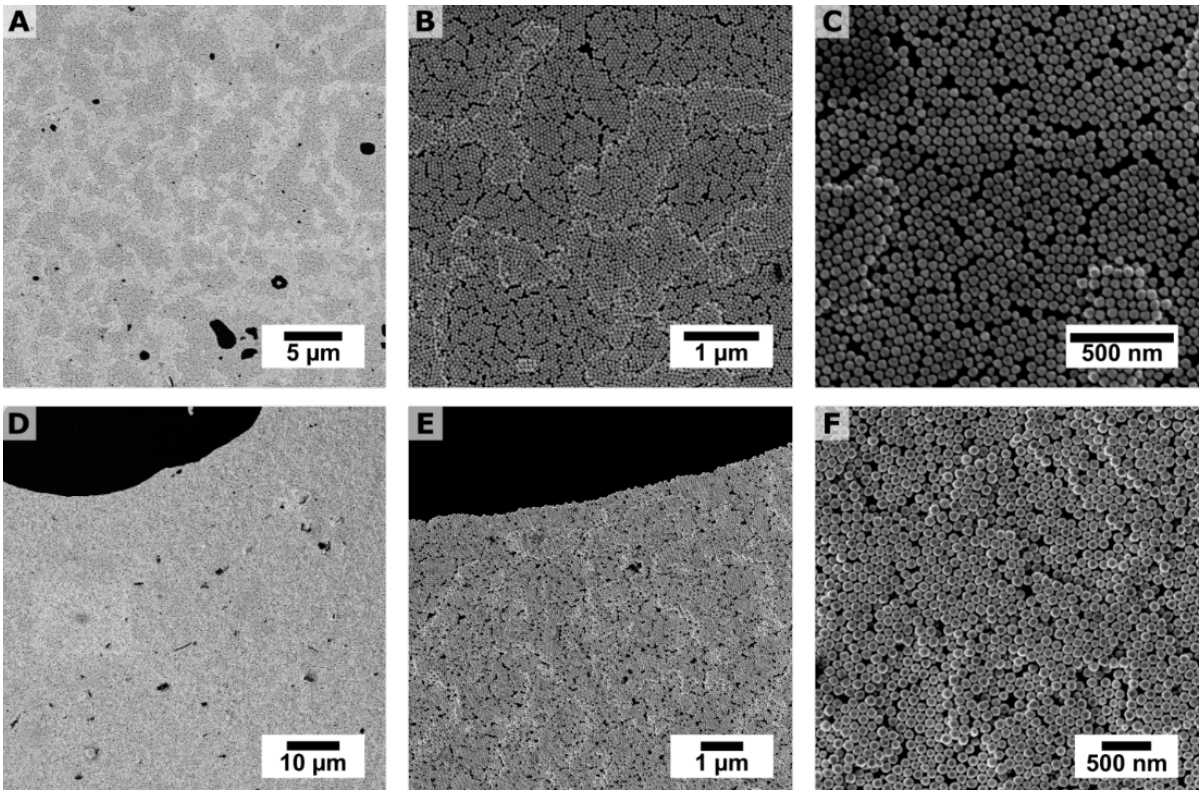

Figure 2.12. A-F: Scanning electron microscopy at different magnifications of the nanoparticle monolayers obtained using (**A-C**) 50 ± 3 nm, and (**D-F**) 100 ± 9 nm particles after transfer to glass substrates.

We have achieved high-fidelity micron-sized patterns with feature dimensions 300 times larger than single particles. However, NP-CLL offers the opportunity to push the resolution further by including features similar in size even to single particles. To demonstrate this capability, we used PDMS stamps comprised of pyramidal features with contact areas of ~200 nm × ~200 nm (**Figure 2.13** and **Figure 2.4**) and compared lift-off from monolayers of two different particle sizes (**Figure 2.13**): 50 ± 3 nm, and 100 ± 9 nm (**Figure 2.3**). Successful NP-CLL was confirmed by optical and electron microscopy (**Figure 2.13**). As expected, the combination of pyramidal stamps with particles >50 nm led to lower numbers of lifted-off objects per contact area. In particular, SEM analysis confirms that small clusters of AuNPs can be lifted-off onto the tips of each pyramid feature over 5 mm × 5 mm areas (**Figure 2.13D-F**), giving lift-off yields of 79%, calculated as

"occupied" over ~300 pyramids. Interestingly, the use of larger particles results in higher fidelity reproduction of the pattern compared to smaller ones. We hypothesize that the presence of defects in the original monolayer has little effect on the fidelity when fewer particles are lifted-off. Moreover, pressure applied onto the PDMS stamp could be used as another way to modulate the contact area, and thus the quantity of AuNPs per pyramid, through stamp deformation, as in our prior work.[28]

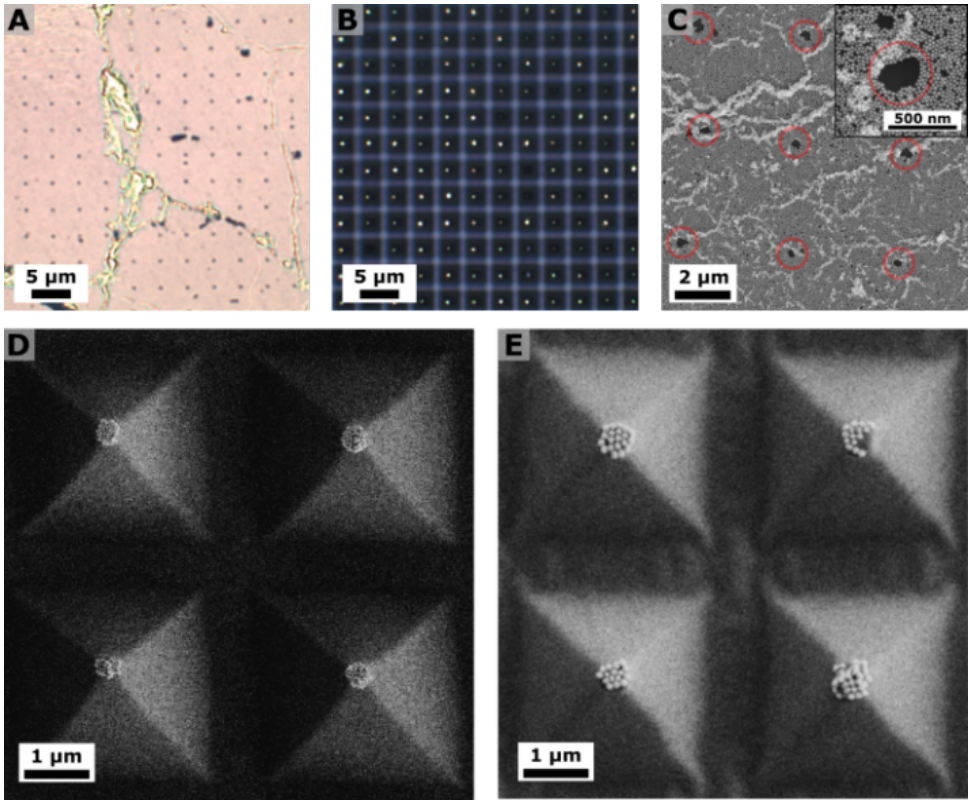

Figure 2.13. A,B: Bright-field microscopy images of (**A**) the complementary negative image with the imprinted pyramid pattern into the nanoparticle monolayer and (**B**) the patterned polydimethylsiloxane (PDMS) after lift-off. **C:** Scanning electron microscopy (SEM) analysis of the complementary negative image. **Inset**: higher magnification image of one circled area. **D-F:** Scanning electron microscopy image of the patterned PDMS after lift-off using different nanoparticle dimensions: (**D**) 50 ± 3 nm and (**E**) 100 ± 9 nm.

Overall, these results suggest the possibility for NP-CLL to reach single-particle manipulation. In fact, when attention was taken to apply only minimum pressure over the stamp, we occasionally observed the lift-off of either a few and/or single building blocks in small regions of the patterned PDMS (**Figure 2.14**). We note that applying weight evenly over large-scale stamps is challenging without specialized equipment.[28,37] However, this limitation could be addressed using polymers with higher elastic moduli.[38]

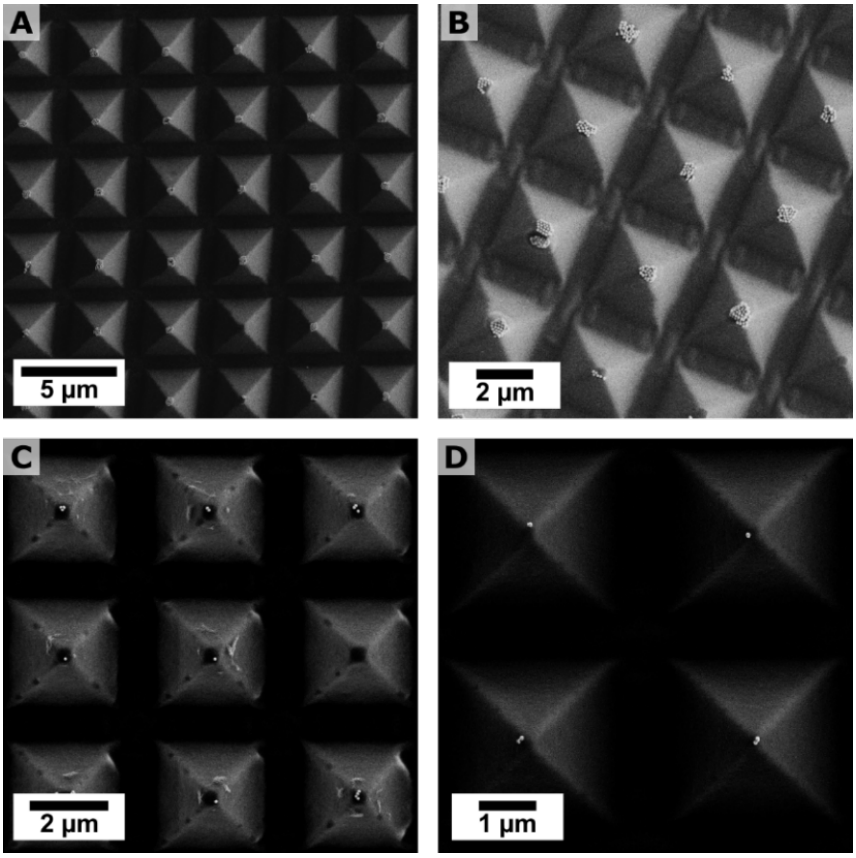

Figure 2.14. A-B: Scanning electron microscopy characterization of pyramidal polydimethylsiloxane patterns after lift-off. **A,B:** low magnification images showing the possibility of fabricating large-scale patterns. **C,D:** high-magnification images of pyramidal patterns where lower pressure was applied during lift-off, demonstrating few and single particle lift-off. AuNP dimensions: **A,C:** 50 ± 3 nm; **B,D:** 100 ± 9 nm.

Moreover, NP-CLL can be extended to patterns presenting corners and turns. This capability was demonstrated using square spiral patterns in both clockwise and counterclockwise orientations (**Figure 2.15A-C**). We also prepared substrates with patterns capable of long-range plasmon energy transfer (**Figure 2.15D-F**) consisting of continuous lines with ~500 nm linewidths, corresponding to an average of 10 nanoparticles placed side-to-side. As reported by Fery and coworkers, these substrates are expected to sustain long-range plasmon propagation.[39] Both the patterned PDMS and the complementary negative image imprinted on the nanoparticle monolayer were reproduced with high-fidelity and yield (**Figure 2.15**).

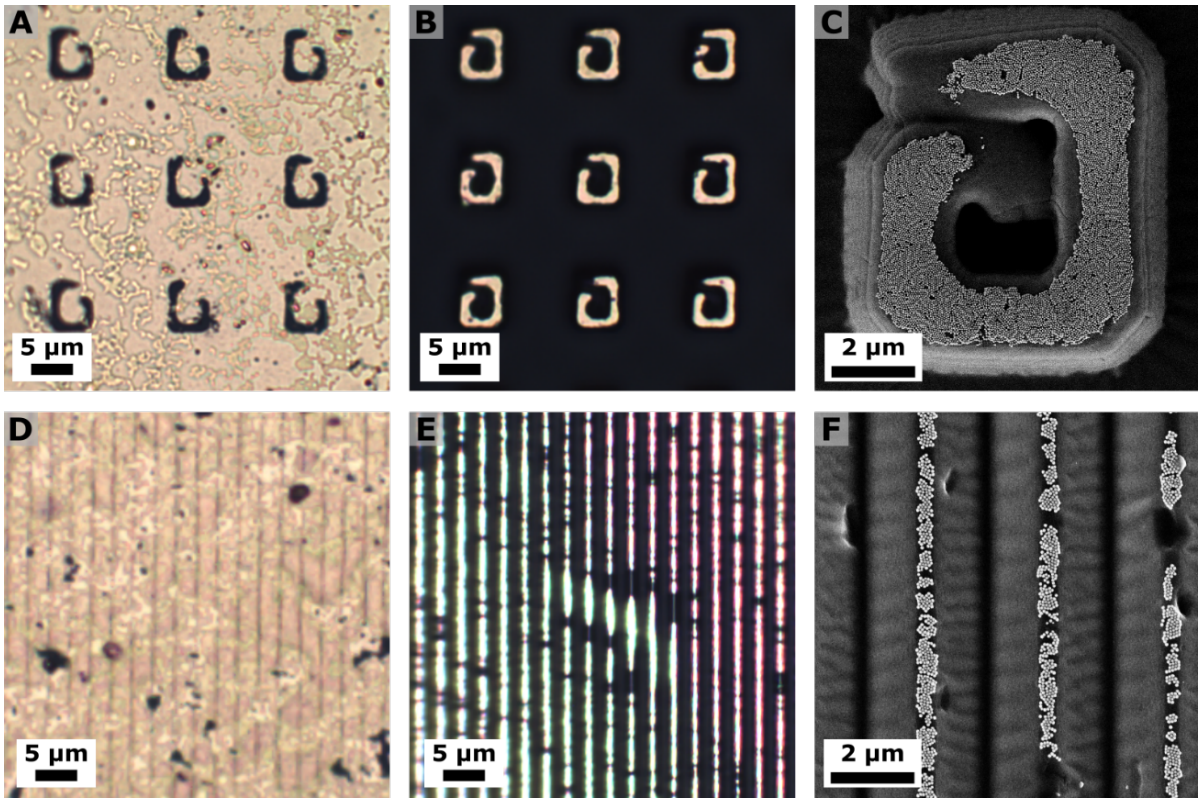

Figure 2.15. A,B: Bright-field microscopy images. **C:** Scanning electron microscopy (SEM) of patterned spiral features comprised of gold nanoparticles produced as the complementary negative image on (**A**) the substrate and (**B,C**) lifted-off onto the patterned PDMS. **D,E:** Bright-field and (**F**) SEM images of gratings produced as complementary negative images on the (**D**) substrate and (**E,F**) lifted-off onto the PDMS stamp.

The optical extinction of spiral structures was characterized in the entire visible-near-infrared (vis-NIR) range with randomized polarization. We measured a single broad plasmon band centered at *ca*. 800 nm (**Figure 2.16A**) that resembles the optical properties of the close-packed AuNP monolayer. The observed extinction spectrum suggests that the particle assembly is continuous along the dimensions of the spirals and thus enables long-range plasmon propagation.[40] Despite the intense scattering contribution from the micron-scale design of the pattern to the overall optical response, we attempt to characterize the chiral activity of the prepared patterns using a custom-built far-field circular dichroism setup in order to test the near-field plasmon propagation along the spirals. First, patterned nanoparticles were transferred on a glass slide using the HPC-mediated transfer strategy described in **Figure 2.9**.

Scanning electron microscopy confirmed that the transfer maintained the structures intact and the AuNPs closely packed over the entire spiral structure (**Figure 2.16B**). Then, circular dichroism (CD) was measured in the vis-NIR region. The high fidelity of the spiral pattern enabled us to interrogate different regions of interest for each sample, as shown by optical images recorded from the CD setup (field of view ~ 0.07 mm^2, **Figure 2.16C**). Extinction spectra of an L spiral sample, recorded with linearly, and left and right circularly polarized light are shown in **Figure 2.16D**. Differences between left and right circular polarization can be appreciated in the NIR region of the extinction spectra without need for further data processing. The CD was measured as the difference between the two extinction spectra, showing mirrored activity for the clockwise (L sample, in red) and the counterclockwise (R sample, in blue) square spirals (**Figure 2.16E**; see Instrumentation **Section 2.4.2** for more details regarding data acquisition and processing). We interpret the relatively weak CD signal and small signal-to-noise ratio by the micrometer-scale dimensions of the prepared chiral patterns. Specifically, the broad excitation band formed by the

sub-radiant propagating plasmon modes[41] are dominated by the far-field scattering.[40] We hypothesize that by reducing the dimensions of the spirals to submicron scales, and/or with the implementation of near-field techniques,[42] the scattering could be decreased. As a result, the detectable optical activity could be significantly enhanced to target a broader range of applications. Overall, the reported data support the possibility of engineering chiral plasmonic assemblies using NP-CLL with colloidal nanoparticles, and we are currently pursuing studies in this direction.

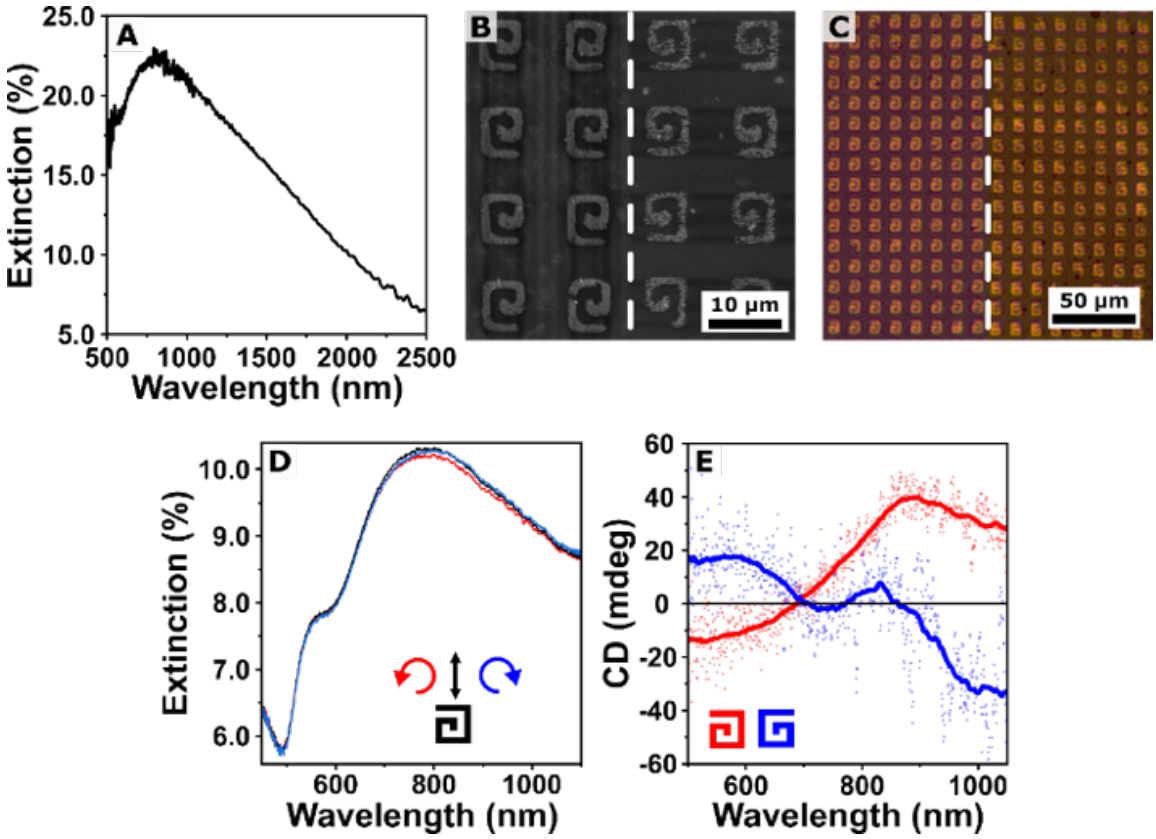

Figure 2.16. **A:** Extinction spectra measured in the visible-near infrared (vis-NIR) range showing a single broad plasmonic band. **B:** Scanning electron microscopy and **C:** optical bright field images of both clockwise (*left*) and counterclockwise (*right*) spirals, confirm that the close-packed particles form continuous structures. **D:** Extinction spectra obtained illuminating a clockwise (L) sample with left circularly polarized light (**red line**), linearly polarized (**black line**), and right circularly polarized light (**blue line**). **E:** Circular dichroism of a clockwise (L sample, **red**) and counterclockwise (R sample, **blue**) spiral structure.

Savitky-Golay filtered signals (solid traces) are superimposed over the raw data (scattered dots). The inset drawings show the pattern orientation for the plotted spectra.

Section 2.3. Conclusions and Prospects

In this chapter we provide a specific example combining colloidal nanochemistry with a soft-lithographic patterning technique (NP-CLL) for the organization of plasmonic nanoparticles into micro- and nanoscale patterns as an alternative approach for the fabrication of functional photonic materials. The capability of NP-CLL to work with arbitrary patterns, including pyramids, lines, and square spirals was demonstrated, achieving, in the last case, chiral activity in the visible and near-infrared range. The potential to access nanoscale patterns using NP-CLL paves the way for targeting plasmonic arrays with lattice parameters compatible with sharp lattice plasmonic resonances in the vis-NIR region. Moreover, our results suggest the possibility of achieving single plasmonic object manipulation in two dimensions. Reaching this goal would enable preparation of plasmonic arrays similar to those prepared by standard lithographic methodologies but characterized by improved quality factors.[15] Future pattern designs can be optimized to match the symmetry of the underlying AuNP assembly better in order to favor single particle lift-off. We anticipate that interparticle interactions can also be tuned *via* surface chemistry, adding another level of control over the lift-off process.[43] Another possible advance with NP-CLL would be the implementation of anisotropic colloids. Although their self-assembly at the liquid-liquid interface has already been demonstrated,[29] the use of anisotropic shapes would require a degree of control over their orientations in the original monolayer. Overall, NP-CLL could lead to the rational application of both in- and out-of-plane plasmonic modes, the exploitation of polarized resonances, and the introduction of chiral properties for the fabrication of meta-materials. Moreover, in

combination with control over the surface chemistry of the plasmonic building blocks, our method opens opportunities for the construction of more complex, dynamic/reversible three-dimensional nanoscale architectures.[44] Ultimately, despite the benefits of the NP-CLL approach, the batch pre-synthesis, ligand exchange, and self-assembly processes are quite time consuming. This limitation is also observed in other methods that similarly rely on soft lithography (*i.e.,* microcontact printing).[21,45] Moreover, although some works applying colloidal self-assembly achieve patterned premade anisotropic particles like nanorods[46–48] and triangles,[49] it is still challenging to orient and to arrange anisotropic particles specifically on a substrate starting from colloidal particles. These limitations inspire alternative approaches, where instead of using pre-made colloids, the nanoparticles are reduced directly on the surface and bottom-up chemistry is used to control their shape *in situ*. These *in situ* growth methods will be discussed in **Chapter 3**.

Section 2.4. Materials and Methods

2.4.1. Materials

Hexadecyltrimethylammonium chloride (CTAC, 25 wt% in water), hydrogen tetrachloroaurate trihydrate ($HAuCl_4 \cdot H_2O$, ≥99.9%), L-ascorbic acid (AA, ≥99%), sodium bromide (NaBr, ≥99.0%), sodium borohydride ($NaBH_4$, 99%), (11-mercaptoundecyl)hexa(ethylene glycol) (MUHEG, 90%), sodium citrate tribasic dihydrate (≥98%), sodium hydroxide (NaOH, ≥98%), tetraphenylboron tetrabutylammonium (TBA-TPB, 99%), 1,2-dichloroethane (DCE, 99%), hydrogen peroxide (H_2O_2, 30% wt%), ammonium hydroxide solution (NH_4OH, 28% NH_3 in H_2O, ≥99.99%), and ethanol (>99.9%, absolute grade) were purchased from Millipore-Sigma (Massachusetts, USA). Hydroxypropyl cellulose (HPC),

with average MW ~100,000, powder, 20 mesh particle size (99% through) and degree of substitution = 3, was purchased from Millipore-Sigma. Polydimethylsiloxane (PDMS, Sylgard 184) was purchased from Dow Corning (Michigan, USA). All chemicals were used as received. Milli-Q water (resistivity 18.2 MΩ·cm at 25 ºC) was used in all experiments. All glassware was washed with *aqua regia*, rinsed with Milli-Q water, sonicated three times for 3 min, and dried before use. (Warning: *aqua regia* is an extremely corrosive liquid and strong oxidizer and require proper personal protective equipment to be handled safely).

2.4.2. Instrumentation

Transmission electron microscopy (TEM) images were collected with a FEI Titan 80-300 kV S/TEM instrument (Oregon, USA) operating at 300 kV using carbon-coated 400 square mesh copper grids. All samples were centrifuged twice before drop casting onto the TEM grid. Scanning electron microscopy (SEM) images were collected with a Zeiss SUPRA 40VP Field Emission Gun (Oberkochen, Germany), a FEI QUANTA 200 Field Emission Gun, and a FEI QUANTA 650 Field Emission Gun, operating between 5 and 30 kV. Optical images were taken S-4 using a WiTEC Alpha300 (Ulm. Germany) equipped with Zeiss objectives. Extinction spectra of the gold colloids were recorded using an Agilent 8453 ultraviolet (UV)-visible diode-array spectrophotometer (California, USA) using quartz cuvettes. A Fourier transform infrared (FTIR) spectrometer (Vertex 70 Bruker, Massachusetts, USA) attached to an optical microscope (Hyperion, Bruker) was used for far-field reflection and transmission measurements in the 400 to 3000 nm range. The background reflection spectrum was set with a silver mirror with 96% reflectivity in the tested range of wavelengths and the transmission background was taken in air.

The spectra were collected with a 4× objective (NA: 0.10). Spiral masters were prepared using a Micro-Writer ML3 (resolution: 600 nm) from Durham Magneto Optics Ltd. (Durham, UK).

Circular dichroism (CD) spectra were measured using a custom-built set-up. A Tungsten Halogen Lamp (Ocean Optics, HL-2000-HP, Florida, USA) was used as the light source; the unpolarized light passes through a Glan-Thompson linear polarizer, followed by a superachromatic quarter-wave plate (Thorlabs, SAQWP05M-700, 325-1100 nm, New Jersey, USA) oriented ±45º with respect to the fast axis in order to obtain circular polarized light (CPL). The CPL was focused on the sample using a 10× Olympus objective (NA: 0.25). The transmitted light was then collected using a fiber coupled spectrophotometer (Ocean Optics, QEPro-FL). Transmission spectra were collected over different spots (three per sample), averaged, and converted into extinction. The extinction difference between right and left circular polarized light: ΔExt=ExtR-ExtL, is used to extrapolate the samples' CD, which is finally converted into mdeg.

2.4.3. Synthesis of 50 and 100 nm gold nanoparticles@(11-mercaptoundecyl)hexa(ethylene glycol)

A CTAC/AA-based synthesis originally developed by G. González-Rubio *et al.* was used to prepare AuNPs.[50] This seeded-growth method combines selective bromine-induced oxidative etching and subsequent overgrowth to decrease size dispersity and improve roundness.

2.4.4. Seeds@hexadecyltrimethylammonium chloride

Seeds were prepared by standard $NaBH_4$ reduction. Specifically, 50 μL of a 50 mM $HAuCl_4$ solution was added to 5 mL of 0.1 M CTAC solution; 200 μL of a freshly prepared 20 mM

$NaBH_4$ solution was then injected under vigorous stirring. After 3 min, the mixture was diluted ten times in 100 mM CTAC.

2.4.5. 10 nm gold nanoparticles@hexadecyltrimethylammonium chloride

These intermediate seeds can be prepared in large batches and remain stable for over 6 months. A 900 µL aliquot of the small seeds@CTAC is added to 10 mL of 25 mM CTAC solution, followed by 40 µL of a 0.1 M AA solution. Then, 50 µL of a 50 mM HAuCl4 solution was added under vigorous stirring. The mixture was left undisturbed at room temperature for at least 10 min. The resulting AuNPs presented a localized surface plasmon resonance (LSPR) at 520 nm.

2.4.6. 50 nm gold nanoparticles@hexadecyltrimethylammonium chloride

The final growth is a three-step process. The amounts given here are for 100 mL of product but the synthesis can be scaled up to produce batches of 1 L or more.

Step 1: First, 750 µL of 10 nm AuNPs and 250 µL of a 0.1 M AA solution was added to 100 mL of 25 mM CTAC solution, followed by the addition of 250 µL of a 0.05 M $HAuCl_4$ under vigorous stirring. The mixture was left undisturbed at room temperature until growth was complete (45– 60 min). The status of the growth was monitored using the absorbance at 400 nm *via* UV-visible spectroscopy.[51]

Step 2: The growth solution is heated to 40 ºC and another aliquot of 250 µL of the 50 mM $HAuCl_4$ is added. A comproportionation reaction will partially oxidize the nanoparticles. Progress can be monitored using UV-visible spectroscopy (*i.e.*, monitoring the absorbance at 400 nm). In a typical synthesis, the oxidation will be completed in 20–30 min. At this point, the solution is heated to

75 ºC and kept at that temperature for 30 min. The higher temperature forces the equilibrium back towards the reduction of the precursor, achieving more uniform particles.

Step 3: Finally, the solution is cooled down to 40 ºC, and a final oxidative etch is performed to improve the spherical shape of the particles. This etch is achieved by adding 100 mg of NaBr and 250 µL 50 mM $HAuCl_4$ solution to the growth mixture. This step takes 45–60 min and can be monitored by UV-visible spectroscopy, as in the previous steps.[51]

2.4.7. 100 nm gold nanoparticles@hexadecyltrimethyl-ammonium chloride

The procedure is identical to the one used for 50 nm particles. The only difference is a ten-fold reduction in the amount of 10 nm seeds used for the first growth step, 75 µL for 100 mL of final product.

2.4.8. Workup and storage

In order to keep the colloids stable for storage, the batches are centrifuged, and the particles are resuspended in 1 mM CTAC using the following protocols depending on the nanoparticle size:

50 nm: A total of three centrifugation steps are performed: (1) 6500 rpm for 15 min and resuspend in ~1/10th of the initial volume. (2-3) 5500 rpm for 5 min; after the second centrifugation step resuspend the particles in Milli-Q water. Following the final centrifugation, the AuNPs are resuspended in a 1 mM CTAC solution, reducing the volume fivefold.

100 nm: A total of three centrifugation steps are performed: (1) 2500 rpm for 15 min and resuspend in ~1/10th of the initial volume. (2-3) 2000 rpm for 5 min. After the second centrifugation step, resuspend in Milli-Q water and then in a 1 mM CTAC solution following the last centrifugation,

reducing again the volume five times. After the three centrifugation steps, the final solution should be 1/20th of the original volume at 1 mM CTAC with an approximate concentration of Au^0 of 2 mM, corresponding to an absorbance intensity at 400 nm of 5.[51]

2.4.9. (11-mercaptoundecyl)hexa(ethylene glycol) coating

The ligand exchange reaction is performed on small aliquots of the AuNP batch, which are used directly for monolayer formation (*N.B.*,— the product must be used within 1 week from the ligand exchange reaction). The aliquot (typically 5 mL) is centrifuged twice and resuspended in water. This process brings the concentration of CTAC below the critical micellar concentration, enabling the nanoparticles to cross the isoelectric point immediately after thiol functionalization begins. The ligand exchange reaction is initiated by adding MUHEG, under vigorous stirring, to the colloidal suspension to achieve a final concentration of 0.5 mg/mL. The reaction was left undisturbed for at least 24 h to ensure complete thiol surface passivation. *N.B.*,— Even though MUHEG is quite water soluble, nanoparticles larger than 50 nm will tend to pack together in aqueous media. Therefore, the colloidal suspension will appear purple/bluish and present a broad band in UV-vis spectra. This color and this absorption peak are normal and will not affect the monolayer formation. Finally, the nanoparticles were washed by centrifugation to remove any unbound ligands. In particular, the product was centrifuged three times at either 5000 rpm for 10 min for 50 nm colloids or 2000 rpm for 5 min for 100 nm colloids.

2.4.10. Self-assembly of the gold nanoparticles into monolayers at the liquid-liquid interface

The nanoparticles were assembled inside a 15 mL polytetrafluoroethylene (PTFE) jar (34 mm height, 34 mm in diameter, purchased from Fisher Scientific). The jar was filled with 12.5 mL of DCE, 150 µL of a TBA-TPB 1 mM solution in DCE, 500 µL of AuNPs, and 1 mL of Milli-Q water.

N.B.,– The amount of TBA-TPB needed for monolayer formation can vary over time due to the formation of hydrochloric acid in DCE (*i.e.*, higher hydrochloric acid concentrations will require lower amounts of TBA-TPB). The jar was then capped and vortexed for 30 s. The formation of an emulsion accelerates the assembly process. After 1 min, the PTFE jar is opened, revealing the gold monolayer formed at the liquid-liquid interface.

N.B.,– The "coverage" of the liquid-liquid interface by the AuNP monolayer can be modified either by injecting or extracting water from the aqueous phase using a micropipette effectively changing the surface area available for the monolayer to form.

2.4.11. Monolayer transfer to desired substrates using a custom-built dip coater

A custom-built dip coater was assembled consisting of a function generator connected to a piezoelectric translator stage moving an optical post linearly with an inclination of 15° over the z-direction (vertical). Glass or silicon substrates were cleaned with piranha solution for 30 min, rinsed thoroughly with water, sonicated for 15 min in a 5:1:1 v/v mixture of H_2O:H_2O_2:NH_4OH, rinsed again with water, and stored in water for up to one month. *Warning: piranha solutions are extremely corrosive liquid and strong oxidizer and requires proper personal protective equipment*

to be handled safely. Before use, the substrates were rinsed with water and isopropyl alcohol, blown dry under a stream of nitrogen and fixed to the optical post using a setscrew and double-sided tape. The substrate was brought in contact with the monolayer, moving the post downward at roughly 50 μm/s. Once contact was established, the substrate was retracted at 1 μm/s, facilitating transfer of the monolayer. Once separation is completed, the substrate is retrieved from the post, covered, and left to dry for 1 h.

2.4.12. Preparation of patterned gold nanoparticle monolayers *via* chemical lift-off lithography

The patterned PDMS stamps were prepared using the standard 10:1 precursor to cross-linker ratio.[52] Stamps were then activated by exposure to UV-ozone for 15 min (Jelight, Model 42, California, USA). Immediately after activation, the stamps were placed in contact with the AuNP monolayers, making sure to avoid trapping of air bubbles, and applying a gentle pressure to the stamp. At this point, the substrates were placed overnight in an oven at 60 °C. Demolding is performed after the substrates are allowed to cool to room temperature, whereby the PDMS is separated from the substrate slowly and in one single motion.

2.4.13. Patterned gold nanoparticle monolayer microcontact printing on arbitrary substrates

Nanoparticle transfer is achieved using a simple dry-transfer procedure mediated by HPC. Here a 22 mg/mL HPC solution in water is poured on a glass slide and spin coated at 3000 rpm for 30 s, obtaining films ~50 nm thick. The patterned PDMS decorated with the AuNP monolayer was placed into contact with the HPC thin film and heated to 80 °C on a hotplate for 3 min while

manually applying a gentle pressure. Upon removal, the nanoparticles are transferred from the PDMS to the substrate within areas defined by the stamp's features.

Section 2.5. References

[1] S. Bagheri, H. Giessen, F. Neubrech, *Adv. Opt. Mater.* **2014**, *2*, 1050.

[2] E. Fort, S. Grésillon, *J. Phys. D: Appl. Phys.* **2007**, *41*, 013001.

[3] L. J. Sherry, R. Jin, C. A. Mirkin, G. C. Schatz, R. P. Van Duyne, *Nano Lett.* **2006**, *6*, 2060.

[4] A. B. Zrimsek, N. Chiang, M. Mattei, S. Zaleski, M. O. McAnally, C. T. Chapman, A.-I. Henry, G. C. Schatz, R. P. Van Duyne, *Chem. Rev.* **2017**, *117*, 7583.

[5] U. Bhattacharjee, C. A. West, S. A. Hosseini Jebeli, H. J. Goldwyn, X.-T. Kong, Z. Hu, E. K. Beutler, W.-S. Chang, K. A. Willets, S. Link, D. J. Masiello, *ACS Nano* **2019**, *13*, 9655.

[6] C. Bi, J. Chen, Y. Chen, Y. Song, A. Li, S. Li, Z. Mao, C. Gao, D. Wang, H. Möhwald, H. Xia, *Chem. Mater.* **2018**, *30*, 2709.

[7] S. K. Cushing, N. Wu, *J. Phys. Chem. Lett.* **2016**, *7*, 666.

[8] A. I. Väkeväinen, R. J. Moerland, H. T. Rekola, A.-P. Eskelinen, J.-P. Martikainen, D.-H. Kim, P. Törmä, *Nano Lett.* **2014**, *14*, 1721.

[9] T. W. Ebbesen, *Acc. Chem. Res.* **2016**, *49*, 2403.

[10] M. I. Stockman, K. Kneipp, S. I. Bozhevolnyi, S. Saha, A. Dutta, J. Ndukaife, N. Kinsey, H. Reddy, U. Guler, V. M. Shalaev, A. Boltasseva, B. Gholipour, H. N. S. Krishnamoorthy, K. F. MacDonald, C. Soci, N. I. Zheludev, V. Savinov, R. Singh, P. G. s, C. Lienau, M. Vadai, M. L. Solomon, D. R. Barton, M. Lawrence, J. A. Dionne, S. V. Boriskina, R. Esteban, J. Aizpurua, X. Zhang, S. Yang, D. Wang, W. Wang, T. W. Odom, N. Accanto, P. M. de Roque, I. M. Hancu, L. Piatkowski, N. F. van Hulst, M. F. Kling, *J. Opt.* **2018**, *20*, 043001.

[11] L. Scarabelli, *Pure Appl. Chem.* **2018**, *90*, 1393.

[12] G. González-Rubio, T. M. de Oliveira, T. Altantzis, A. L. Porta, A. Guerrero-Martínez, S. Bals, L. Scarabelli, L. M. Liz-Marzán, *Chem. Commun.* **2017**, *53*, 11360.

[13] V. G. Kravets, A. V. Kabashin, W. L. Barnes, A. N. Grigorenko, *Chem. Rev.* **2018**, *118*, 5912.

[14] W. Wang, N. Watkins, A. Yang, R. D. Schaller, G. C. Schatz, T. W. Odom, *J. Phys. Chem. Lett.* **2019**, *10*, 3301.

[15] Z. Li, S. Butun, K. Aydin, *ACS Nano* **2014**, *8*, 8242.

[16] C. Hamon, S. Novikov, L. Scarabelli, L. Basabe-Desmonts, L. M. Liz-Marzán, *ACS Nano* **2014**, *8*, 10694.

[17] M. Tebbe, M. Mayer, B. A. Glatz, C. Hanske, P. T. Probst, M. B. Müller, M. Karg, M. Chanana, T. A. F. König, C. Kuttner, A. Fery, *Faraday Discuss* **2015**, *181*, 243.

[18] C. Matricardi, C. Hanske, J. L. Garcia-Pomar, J. Langer, A. Mihi, L. M. Liz-Marzán, *ACS Nano* **2018**, *12*, 8531.

[19] C.-Y. Chen, C.-H. Chang, C.-M. Wang, Y.-J. Li, H.-Y. Chu, H.-H. Chan, Y.-W. Huang, W.-S. Liao, *Nanomaterials* **2018**, *8*, 71.

[20] H. Zhang, C. Kinnear, P. Mulvaney, *Adv. Mater.* **2020**, *32*, 1904551.

[21] V. Santhanam, R. P. Andres, *Nano Lett.* **2004**, *4*, 41.

[22] D. S. Ginger, H. Zhang, C. A. Mirkin, *Angew. Chem. Int. Ed.* **2004**, *43*, 30.

[23] Y. Wu, Y. Jiang, X. Zheng, S. Jia, Z. Zhu, B. Ren, H. Ma, *R. Soc. Open Sci.* **2018**, *5*, 172034.

[24] W.-S. Liao, S. Cheunkar, H. H. Cao, H. R. Bednar, P. S. Weiss, A. M. Andrews, *Science* **2012**, *337*, 1517.

[25] A. M. Andrews, W.-S. Liao, P. S. Weiss, *Acc. Chem. Res.* **2016**, *49*, 1449.

[26] K. M. Cheung, D. M. Stemer, C. Zhao, T. D. Young, J. N. Belling, A. M. Andrews, P. S. Weiss, *ACS Mater. Lett.* **2020**, *2*, 76.

[27] J. N. Belling, L. K. Heidenreich, J. H. Park, L. M. Kawakami, J. Takahashi, I. M. Frost, Y. Gong, T. D. Young, J. A. Jackman, S. J. Jonas, N.-J. Cho, P. S. Weiss, *ACS Appl. Mater. Interfaces* **2020**, *12*, 45744.

[28] X. Xu, Q. Yang, K. M. Cheung, C. Zhao, N. Wattanatorn, J. N. Belling, J. M. Abendroth, L. S. Slaughter, C. A. Mirkin, A. M. Andrews, P. S. Weiss, *Nano Lett.* **2017**, *17*, 3302.

[29] L. Velleman, L. Scarabelli, D. Sikdar, A. A. Kornyshev, L. M. Liz-Marzán, J. B. Edel, *Faraday Discuss.* **2017**, *205*, 67.

[30] L. Velleman, D. Sikdar, V. A. Turek, A. R. Kucernak, S. J. Roser, A. A. Kornyshev, J. B. Edel, *Nanoscale* **2016**, *8*, 19229.

[31] C. Zhao, X. Xu, Q. Yang, T. Man, S. J. Jonas, J. J. Schwartz, A. M. Andrews, P. S. Weiss, *Nano Lett.* **2017**, *17*, 5035.

[32] D. Nepal, M. S. Onses, K. Park, M. Jespersen, C. J. Thode, P. F. Nealey, R. A. Vaia, *ACS Nano* **2012**, *6*, 5693.

[33] Liao Wei-Ssu, Cheunkar Sarawut, Cao Huan H., Bednar Heidi R., Weiss Paul S., Andrews Anne M., *Science* **2012**, *337*, 1517.

[34] C. Dore, B. Dörling, J. L. Garcia-Pomar, M. Campoy-Quiles, A. Mihi, *Small* **2020**, *16*, 2004795.

[35] C. G. Worley, R. W. Linton, *J. Vac. Sci. Technol. A* **1995**, *13*, 2281.

[36] C. Hamon, S. M. Novikov, L. Scarabelli, D. M. Solís, T. Altantzis, S. Bals, J. M. Taboada, F. Obelleiro, L. M. Liz-Marzan, *ACS Photonics* **2015**, *2*, 1482.

[37] F. Huo, Z. Zheng, G. Zheng, L. R. Giam, H. Zhang, C. A. Mirkin, *Science* **2008**, *321*, 1658.

[38] T. W. Odom, J. C. Love, D. B. Wolfe, K. E. Paul, G. M. Whitesides, *Langmuir* **2002**, *18*, 5314.

[39] M. Mayer, P. L. Potapov, D. Pohl, A. M. Steiner, J. Schultz, B. Rellinghaus, A. Lubk, T. A. F. König, A. Fery, *Nano Lett.* **2019**, *19*, 3854.

[40] B. Willingham, S. Link, *Opt. Express* **2011**, *19*, 6450.

[41] Y. Zhao, A. N. Askarpour, L. Sun, J. Shi, X. Li, A. Alù, *Nat. Commun.* **2017**, *8*, 14180.

[42] P. Schattschneider, S. Rubino, C. Hébert, J. Rusz, J. Kuneš, P. Novák, E. Carlino, M. Fabrizioli, G. Panaccione, G. Rossi, *Nature* **2006**, *441*, 486.

[43] E. Moaseri, J. A. Bollinger, B. Changalvaie, L. Johnson, J. Schroer, K. P. Johnston, T. M. Truskett, *Langmuir* **2017**, *33*, 12244.

[44] B. A. Grzybowski, K. Fitzner, J. Paczesny, S. Granick, *Chem. Soc. Rev.* **2017**, *46*, 5647.

[45] J. Chen, P. Mela, M. Möller, M. C. Lensen, *ACS Nano* **2009**, *3*, 1451.

[46] M. Mayer, M. Tebbe, C. Kuttner, M. J. Schnepf, T. A. F. König, A. Fery, *Faraday Discuss.* **2016**, *191*, 159.

[47] C. Hamon, S. M. Novikov, L. Scarabelli, D. M. Solís, T. Altantzis, S. Bals, J. M. Taboada, F. Obelleiro, L. M. Liz-Marzán, *ACS Photonics* **2015**, *2*, 1482.

[48] H. Zhang, Y. Liu, M. F. S. Shahidan, C. Kinnear, F. Maasoumi, J. Cadusch, E. M. Akinoglu, T. D. James, A. Widmer-Cooper, A. Roberts, P. Mulvaney, *Adv. Funct. Mater.* **2021**, *31*, 2006753.

[49] Y. Zhou, X. Zhou, D. J. Park, K. Torabi, K. A. Brown, M. R. Jones, C. Zhang, G. C. Schatz, C. A. Mirkin, *Nano Lett.* **2014**, *14*, 2157.

[50] C. Hanske, G. González-Rubio, C. Hamon, P. Formentín, E. Modin, A. Chuvilin, A. Guerrero-Martínez, L. F. Marsal, L. M. Liz-Marzán, *J. Phys. Chem. C* **2017**, *121*, 10899.

[51] L. Scarabelli, A. Sánchez-Iglesias, J. Pérez-Juste, L. M. Liz-Marzán, *J. Phys. Chem. Lett.* **2015**, *6*, 4270.

[52] D. Qin, Y. Xia, G. M. Whitesides, *Nat. Protoc.* **2010**, *5*, 491.

Chapter 3. Bottom-up *in Situ* Growth: A Paradigm Shift for Synthetic Studies of Gold Nanoparticles

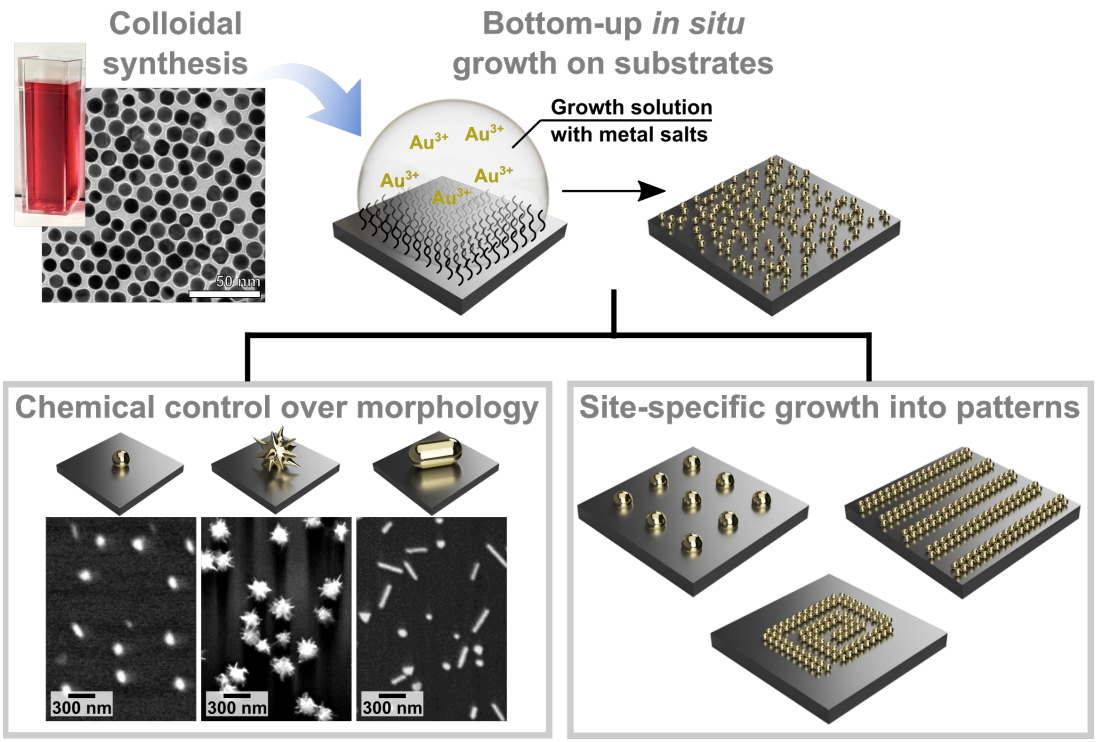

***In situ* bottom-up synthesis on substrates** offers a cost effective and straightforward alternative to colloidal synthesis and self-assembly and top-down nanofabrication. *In situ* growth leverages the versatility of bottom-up chemistry to modify the morphology of the nanostructures and has broad potential impacts for the fabrication of plasmonic substrates for catalysis, sensing, medicine, and optoelectronics.

Section 3.1. Introduction

3.1.1. Defining wet-chemical *in situ* growth

The discussion at the end of **Chapter 1** and the example provided in **Chapter 2** highlight developments applying colloidal nanoparticles for the fabrication of plasmonic substrates with methods based on self-assembly. Despite the significant progress made in this area, there are various challenges associated with techniques that use colloids as building blocks. For instance, it remains a considerable challenge to position anisotropic particles on substrates precisely.[1–4] Moreover, while the soft-lithography methods applied in conjunction with these procedures (*i.e.* microcontact printing, chemical lift-off lithography, nanoimprint lithography, *etc.*) are potentially scalable, the pre-synthesis, ligand exchange, and self-assembly of the colloids are less so.[5–10] The latter processing steps are usually limited by mixing/uneven distribution of reagents in large volumes and the requirement of multiple centrifugation steps.[9,11,12] This chapter reviews solutions that address these limitations, where instead of using pre-made colloids, the metal precursors are reduced directly on surfaces and bottom-up chemistry is used to control their shape *in situ*.

We define wet-chemical *in situ* growth as the bottom-up formation of nanoparticles directly on a solid substrate *via* chemical reduction of gold salts (**Figure 3.1**). This process is sometimes referred to as electroless nanomaterial fabrication or electroless deposition.[13] Additional relevant publications can be found using these terms if the reader would like to discover more literature regarding *in situ* nanoparticles fabrication. However, here, we find it important to use the terminology "*in situ* surface growth" because our specific interest is to create nanoparticles with controlled morphologies on substrates, akin to colloidal size and shape control, but in a new environment. In contrast, electroless deposition is more general in scope and primarily refers to

metal thin film fabrication.[14] Thus, we find it appropriate to differentiate the two approaches based on their ultimate goals.

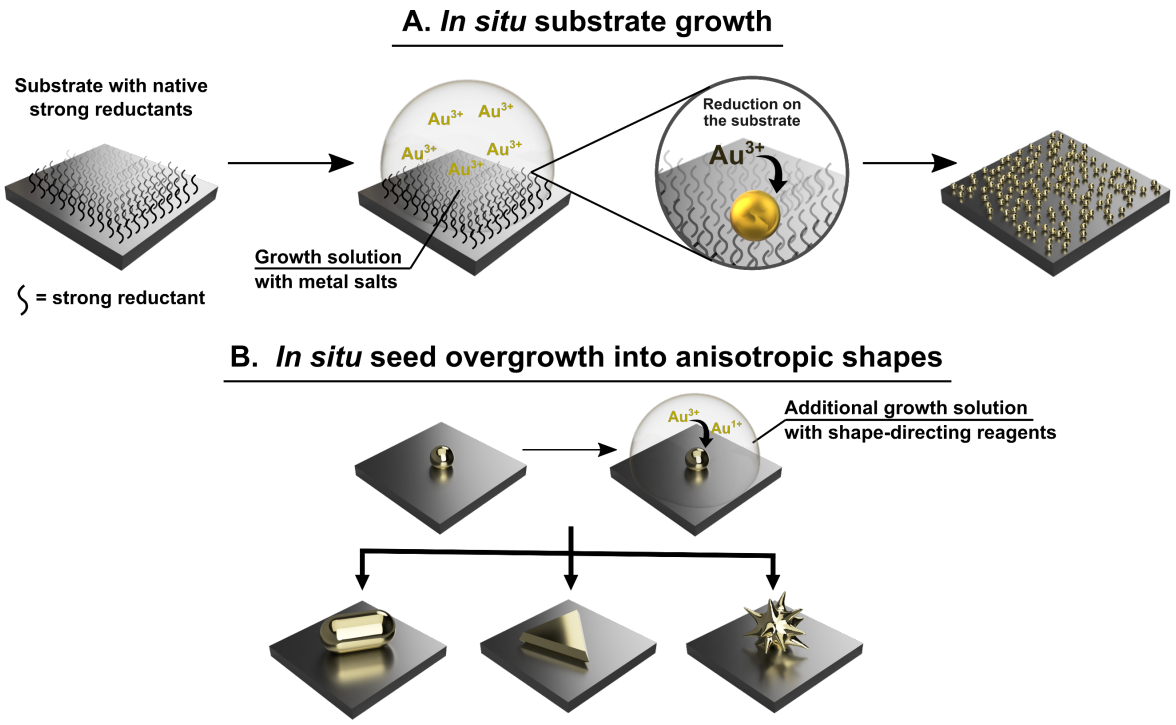

Figure 3.1. Routes for direct *in situ* chemical surface growth of gold nanoparticle nuclei **A:** without and **B:** with patterning. **C:** Controlled overgrowth of the nuclei, or seeds, on the substrate (*in situ* shape control).

Nonetheless, the formation of nanoparticles directly on a material by chemical approaches is not a new idea or practice. In fact, *in situ* formation of gold and other plasmonic metal nanoparticles in colored ceramic glass was routinely performed as early as the 17th century, before there was any idea of the existence of nanoscale particles.[15] During the glass-making process, gold salts and reductant additives such as tin (in the form of stannous chloride) or antimony would be added, leading to the formation of gold nanoparticles within the glass substrate.[15–17] The particle sizes could be tuned *in situ* by modifying the amount of salt, treatment temperature, and time until the desired intensity and hue were obtained.[17] Nowadays, *in situ* growth is being tested and

developed for materials beyond glass (**Figure 3.1A**). The potential to use colloidal synthetic principles to modify the particle geometry has also been validated by demonstrations of shape-controlled overgrowth, where subsequent incubation of substrate-formed nuclei in a separate growth solution containing shape-directing reagents is used to create anisotropic shpaes (**Figure 3.1B**).[18–22]

3.1.2. Rationale and motivation for *in situ* growth

There are numerous potential benefits to *in situ* synthesis, including: (*i*) the capability to modify size and shape directly on the substrate,[18–22] (*ii*) chemical control over the particle position and its orientation relative to the substrate,[23–26] (*iii*) tunability of the particle-substrate interaction,[27,28] and (*iv*) the avoidance of time-consuming and complex pre-synthesis, ligand exchange, and self-assembly. Notwithstanding, there are many aspects of *in situ* growth that require further study. Namely, although fundamental synthetic principles from colloidal systems can serve as a starting point for approaching *in situ* growth, *in situ* size and shape control is not nearly as well-developed or understood. While some works have taken inspiration from colloidal synthesis to modify particle morphology, there are significant differences between *in situ* and colloidal environments that affect anisotropic growth, which we will discuss in detail below. In addition, the development of robust, versatile, and scalable schemes for directing nucleation and growth to occur at specific regions (*i.e.,* patterns) on the target material with nanometer resolution remains a challenge for *in situ* systems.

3.1.3. Promoting substrate growth with chemical reductants

As for colloidal synthesis, pure *in situ* growth begins with the initial single-step homogeneous nucleation of gold nanoparticles from gold salts in a controlled chemical environment. In both approaches, the type, strength, and quantity of chemical reductants greatly influences the uniformity and morphology of the final products.[13,29] Moreover, the timing and conditions under which reductants are introduced (slowly or rapidly, at room temperature or low temperature, under vigorous stirring, *etc*.) is also important.[30–34] With *in situ* growth, the goal is to create nucleation sites selectively on the substrate.

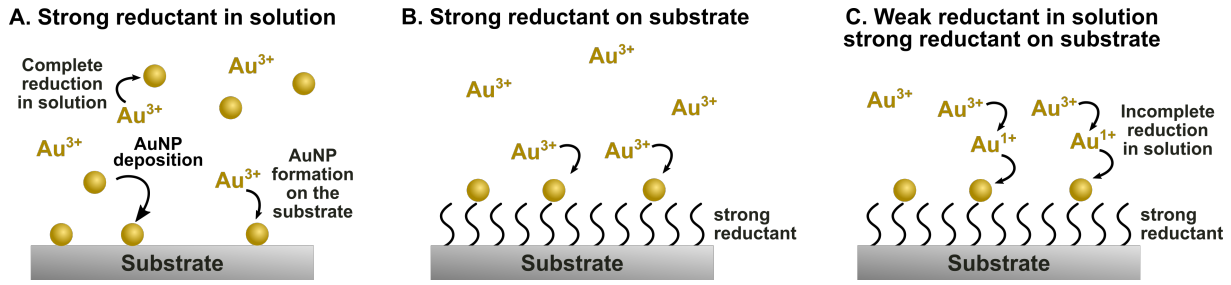

Figure 3.2. A-C: Schematics depicting *in situ* growth with (**A**) an externally added strong reductant, (**B**) on a substrate with functionalities capable of completely reducing Au^{3+} to Au^{0}, and (**C**) on a substrate with strong reductants and weak reductants added to the growth solution.

Selective nucleation can be accomplished by externally adding strong reductants into the growth solution or by taking advantage of native reducing groups on the substrate as depicted in **Figure 3.2**. We reserve the following section on reductants to summarize studies where both nucleation and growth were performed chemically (**Figure 3.2**).

3.1.3.1. *In situ* growth *via* addition of external strong reductants

In some studies, strong reductants capable of reducing Au^{3+} to Au^{0} (such as $NaBH_4$) are added to the growth solution to create gold nanoparticles on a variety of substrates, including

biocompatible or conductive polymers[35] and hydrogels.[36] One of the early examples of this approach was demonstrated in 2004 by Langer and colleagues.[36] In this work, gold nanoparticle-hydrogel composites were made by swelling thermoresponsive poly(*N*-isopropylacrylamide) (PNIPAm) hydrogels with gold salts, followed by swelling in an aqueous solution of $NaBH_4$ (**Figure 3.3**).

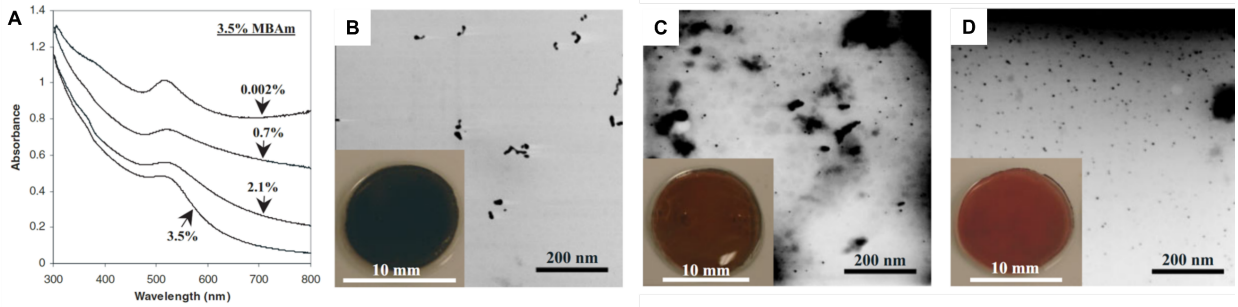

Figure 3.3. A: Extinction spectra of gold nanoparticles grown in poly(N-isopropylacrylamide) with $NaBH_4$ with 3.5% N,N-methylene-bis-acrylamide (MBAm) and different quantities of N,N-cystamine-bis-acrylamide (CBAm) – the source of disulfide bridges that serve as Au binding sites. **B-D:** Gold nanoparticle products synthesized with 0.002/2.1/3.5 % CBAm. *Insets*: Digital photographs of the gels [reproduced with permission from ref. 36].

It was found that the thiol-containing groups in the gel were capable of acting as sites promoting gold nanoparticle nucleation. Scanning transmission electron microscopy (SEM) characterization showed that as more thiol moieties were introduced, the particles became more uniform and their average size decreased. In addition, the formation of the gold nanoparticles internally within the gel altered the material properties. Large increases in the swelling ratio were observed, which was attributed to the surface charge of the gold nanoparticles. These results show that the density of nucleation sites significantly affects the morphology and uniformity of the gold nanoparticles. Moreover, these data highlight the importance of considering how changing material compositions to increase nucleation site density or particle density affect the properties of the substrate.

3.1.3.2. *In situ* growth on substrates with native strong reductants

Strong reductants are not always needed in the growth solution to achieve nanoparticle formation on the substrate. In fact, in many cases, Au^{3+} can be completely be reduced to Au^0 owing to the presence of strongly reducing groups on the substrate (**Figure 3.2B**). The implementation of a substrate with strong reductants presents an advantage compared to adding external strong reductants, because this way it is less likely that particles will form in solution away from the target substrate (**Figure 3.2A,B**). Solution nucleation of particles leads to consumption of the gold precursor and can produce polycrystalline structures that can later deposit onto the surface, increasing polydispersity of the final products.[24,37–39] There are many materials on which direct growth of gold and silver nanoparticles can be directly performed. A few examples include graphene/graphene oxide,[40,41] MoS_2,[42,43] cellulose,[44,45] silicon,[46] polydimethylsiloxane (PDMS),[47–51] polyelectrolyte multilayers,[52] and conductive polymers including polypyrrole[53] and polyaniline.[54]

In particular, many studies providing important synthetic insights take advantage of Si-H groups in organosilica, hydridosilica, and other silicone-based polymers.[55–57] Among these materials, PDMS is common for testing *in situ* synthesis of nanomaterials due to its low cost, tunability of its physical properties, and suitability for biological applications.[58–60] The synthesis of gold nanoparticles on PDMS has, thus far, provided important insights into how growth time, temperature, reagent concentrations, and nucleation site density effect nanoparticle morphology.[47–51] A standard commercial kit for PDMS contains two components, the base and curing agent. After thoroughly mixing the reagents together, thermal treatments are applied to obtain the final polymer. During the heating process, oligosilanes in the base react with polymethylhydrosiloxane, a cross-linker found in the curing agent solution, in the presence of a

platinum catalyst. The strongly reducing Si-H groups responsible for reducing metal salts in native PDMS result from incomplete consumption of polymethylhydrosiloxane.[49,55,57,58]

Therefore, changing the curing-agent-to-base ratio (η) modifies the density of Si-H and the nucleation site density. This process can be envisioned as the colloidal synthesis analogue to changing the seed to gold salt ratio. Zhang and co-workers showed that altering the amount of unreacted Si-H determined whether particle growth was directed to occur within the polymer matrix or localized on the surface.[48] Moreover, the quantity of Si-H groups was used to modify the shape and geometry of the prepared nanostructures (**Figure 3.4A-E**). A similar result was observed in the work of Bonyár *et al.* who tested the effects of growth time and temperature by performing the growth at 22-80 °C with incubation times of 2 h to 7 days.[61] Higher growth temperature and longer incubation time yielded products with higher extinction, indicative of more growth. One limitation of relying on the native Si-H groups is that their concentration varies with the curing time, temperature, humidity, and age of the sample.[58] Moreover, there is a limit to how far the η value can be pushed, as having little curing agent ($\eta < \sim 0.5:10$) and/or too much curing agent ($\eta \geq 5:10$) produce PDMS films that are no longer structurally robust.[59] Furthermore, as with PNIPAm, there is an upper limit to the quantity of nanoparticles that can be incorporated into silicone-based systems before their presence starts to damage or change the physical properties of the substrate**.** In one example, Tsuge *et al.* observed that high concentrations of *in situ* silver nanoparticles led to a significant increase in the water sliding angle of PDMS-based slippery-liquid coatings incorporating polymethylhydrosiloxane as a lubricant.[55]

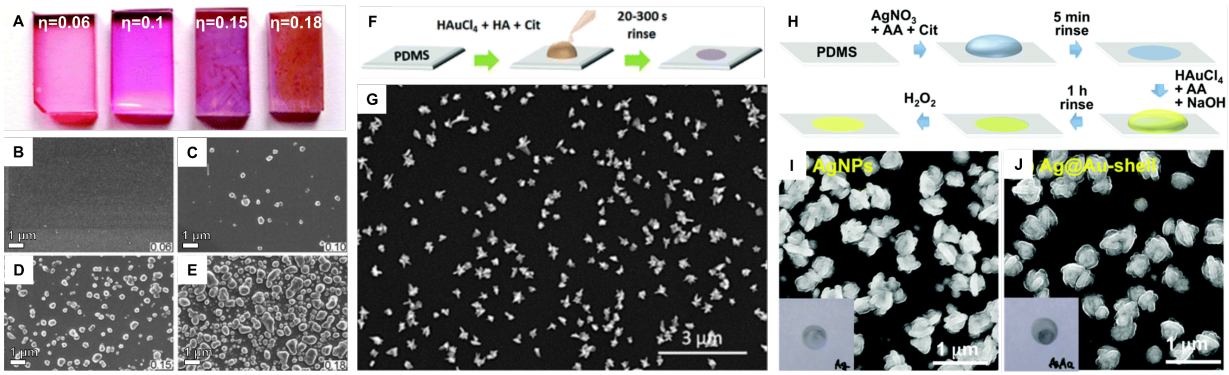

Figure 3.4. A: Digital photographs of polydimethylsiloxane (PDMS) substrates with different curing-agent-to-base mass ratios (η) following gold nanoparticle growth. **B-E:** Scanning electron microscopy images of the products [reproduced with permission from ref. 48]. **F:** Schematic of the growth process for *in situ* synthesis of citrate-capped nanostars and **G:** an electron microscopy image of the products [reproduced with permission from ref. 62]. **H:** Schematic of growth process for Ag@Au shell particles and **I-J:** images of the synthesized particles [reproduced with permission from ref. 47].

In colloidal seed-mediated growth, weak and strong reductants are applied in separate stages of the synthesis, with the seed solution containing strong reductants and the growth solution containing weak reductants.[29,62] Similarly, strong and weak reductants can be spatially separated for *in situ* growth, with the strong reductants confined to the substrate and weak reductants applied in the growth solution as depicted in **Figure 3.2C**. Applying weak reductants along with other shape-directing reagents to the growth solution *in situ* should improve the size and shape yield of the nanoparticle product and facilitate the synthesis of anisotropic shapes. Fortuni *et al.* tested the separation of strong and weak reductants and the addition of other shape-directing reagents *in situ*, *via* substrate growth of gold nanostars and Ag@Au-shells (**Figure 3.4F-J**).[47,63] The *in situ* synthesis of gold nanostars on 1:10 PDMS with weak reductant hydroxylammonium chloride and citrate was explored. Within 60 s particles with diameters of 200 nm were formed and ~300-400 nm nanostars were obtained after 2 min (**Figure 3.4F-G**). Hydroxylammonium chloride was essential for the rapid growth of AuNSTs. Furthermore, no nanostars were produced within the 2 min timeframe when neither citrate or hydroxylammonium chloride were added. Compared

to relying on the native Si-H groups alone without added weak reductant or ligands, much lower concentrations of gold salt were used here and with shorter synthesis times (2 min vs. 2 h to several days; 5 mM vs. 14.7 mM $HAuCl_4$). Overall, Fortuni *et al.* demonstrated that selective formation of nuclei on the substrate can be promoted by incorporating strong reductants on the surface of the target material. Similar to colloidal systems, the temperature, reagent concentration, and the presence of shape-directing agents chemically direct the growth process. Next, we will discuss strategies incorporating *in situ* growth that involve patterning.

Section 3.2. Patterning *in Situ*

There is significant motivation to apply patterning methodologies to engineer the plasmonic properties of the system as described in **Chapter 1**. Moreover, patterning provides a means to control the number and density of nuclei on the substrate, which is beneficial for performing detailed synthetic investigations. Next, general approaches for incorporating region-selective *in situ* growth will be discussed along with some highlighted examples.

3.2.1. Physical templates

Microfluidic devices have been used to physically constrain nanoparticle growth to the internal walls of channels, *e.g.*, those made of PDMS or $SnCl_2$-sensitized glass.[48,64,65] Although the growth is only selectively performed within micron/millimeter-scale features (defined by the size of the channel), these systems demonstrate the potential for *in situ* growth to access complex three-dimensional (3D) substrate geometries, such as curved surfaces or 3D spiral channels.[64] There is, of course, interest in pursuing site-specific growth with nanometer or single-particle resolution, which can be achieved using polystyrene nanosphere self-assemblies (from nanosphere

lithography) as a sacrificial mask directing *in situ* growth to exposed areas.[46] However, nanosphere lithography is limited by the kinds of patterns that can be accessed, producing only hexagonal arrays with variable spacings. Top-down lithographic fabrication can be used to improve reproducibility and precision, as demonstrated by Odom and co-workers, who performed selective metal precursor reduction in nanohole arrays fabricated *via* solvent-assisted nanoscale embossing.[66] The nanohole arrays acted as physical templates in which the metal precursor could be deposited, so that, following *in situ* reduction, precisely positioned nanoparticle arrays could be obtained, especially when pyramidal holes were used.[66]

3.2.2. Chemical templates

3.2.2.1. Substrate-native chemical templates

With chemical templates, the substrate is modified to expose/inhibit strongly reducing groups only at specific regions using patterned chemical functionality. In some cases, the chemical specificity for growth in sub-micron areas can be attained using the characteristic properties of the material. In PDMS, for example, treatment with ultraviolet (UV)-ozone or oxygen/air plasma treatment produces a brittle silica layer on the surface. This silica layer prevents exposure of the growth-active Si-H groups to the metal precursor, inhibiting growth (**Figure 3.5A,B**). Cracks in the silica layer can be formed by bending the substrate over a curved surface following oxygen-plasma treatment, or by performing the plasma activation while the substrate is stretched.[50,51] Directional deformation of the PDMS has been used to grow ~100 nm particle arrays on 800 nm wide and 120 nm amplitude cracks.[50] Directional wrinkling gives a similar result, producing line arrays 400 nm wide and 30 nm deep (**Figure 3.5A,B**).[51]

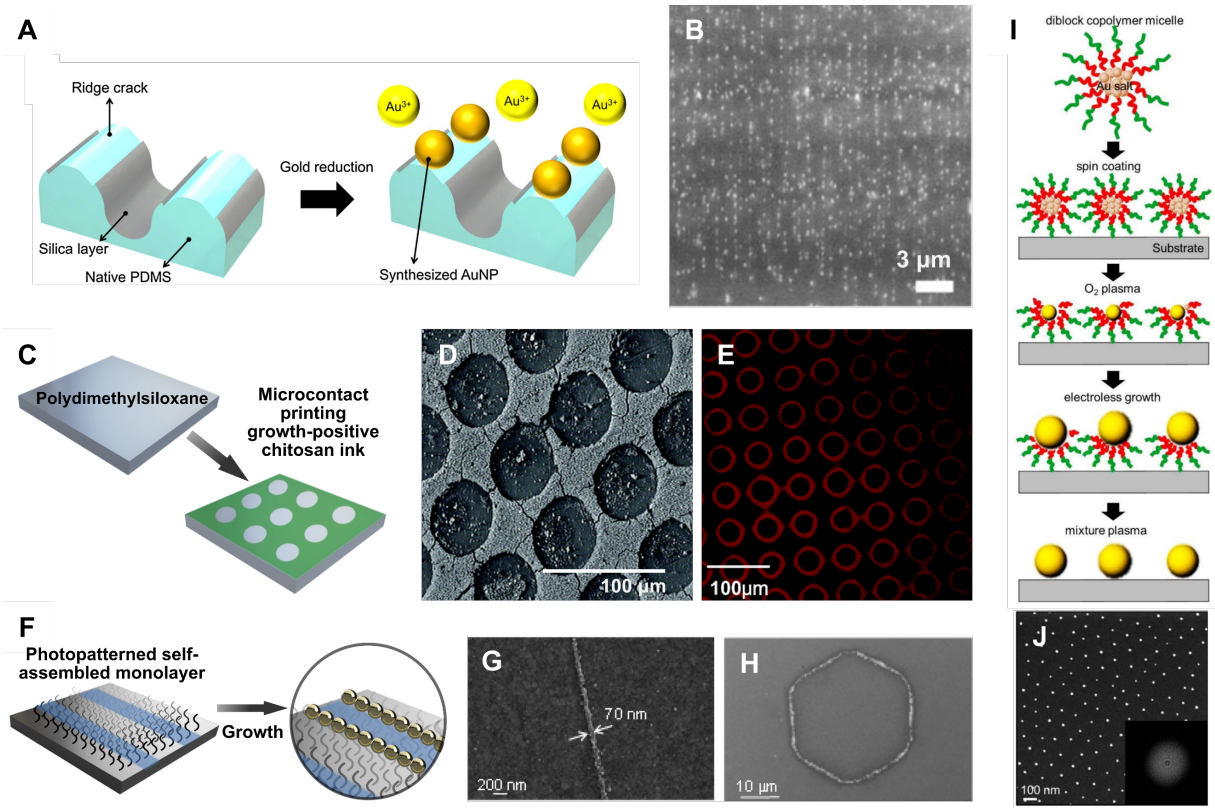

Figure 3.5. A: Schematic showing nanoparticle growth on polydimethylsiloxane "ridgecracks" and **B:** the resulting linear arrays [reproduced with permission from ref. 51]. **C:** Schematic showing chemical patterning with microcontact printing. **D:** Scanning electron microscopy images of the inverted hole arrays following gold nanoparticle growth and **E:** confocal laser scanning microscopy images of chemically patterned rings made by the same method [reproduced with permission from ref. 67. Copyright 2006 American Chemical Society]. **F:** Schematic of photolithographically patterned chemical substrates and scanning electron microscopy images of **G:** nanowires and **H:** nanorings following in situ gold reduction [reproduced with permission from ref. 68. Copyright 2016 American Chemical Society]. **I:** Schematic of block copolymer micelle lithography gold nanoparticle patterning and **J:** the resulting arrays [reproduced with permission from ref. 38. Copyright 2020 American Chemical Society].

3.2.2.2. Chemical functionalization on generalized substrates

Aside from utilizing material-specific chemical functionality, patterning nanoparticle growth on general substrates can be achieved through the application of molecular patterns that inhibit or promote growth in certain regions (**Figure 3.5C-H**). Self-assembled monolayers are often used as chemical inks or masks, which can be patterned straightforwardly *via* top-down or

soft lithography.[67,68] For instance, Wang *et al.*[67] patterned a growth-active ink *via* microcontact printing (**Figure 3.3C-E**) while Ellsworth and Walker applied top-down lithography to promote nanoparticle growth at the interface of two chemically different regions (**Figure 3.5F-H**).[68]

In general, secondary homogeneous and off-pattern nucleation is an ever present concern. Therefore, regardless of what kind of mask is used, it is much easier to control nanoparticle formation using a substrate that does not promote nucleation in combination with a growth-positive ink. However, if it is not possible to apply a growth-inert material, increasing the chemical contrast between the ink and the substrate to promote patterned nanoparticle formation (*i.e.,* kinetically favoring the reduction of the metal precursor on the ink compared to other areas) proves to be effective. In a specific example, Wang patterned growth-positive chitosan on polyester, polystyrene, polyethylene, and PDMS. Chitosan accumulated into ring arrangements on topologically patterned PDMS and was also contact printed onto PDMS substrates presenting circular wells (**Figure 3.5C-E**). The nanoparticles nucleated selectively in areas where chitosan was present only for the PDMS substrates. The authors ascribed this result to the orientation of amine groups away from the hydrophobic surface. The amine groups could then attract gold ions and perform the reduction. Although the roles of the Si-H moieties in the PDMS are not addressed, preferential growth appeared to occur. There are different explanations for this result: (1) PDMS presents fewer nucleation sites than chitosan-covered regions, and we are observing differences in particle density (also considering the resolution of SEM. (2) Hydrophilicity of the two growth-active areas, with PDMS being more hydrophobic, disfavors growth in those regions. (3) Chitosan more rapidly reduces gold ions, and continued growth of the quickly formed nuclei leads to rapid consumption of gold precursor preventing gold nanoparticle formation on the less strongly reducing Si-H groups. It is possible all of these factors play a role, and understanding how they

contribute will be important for optimizing *in situ* growth strategies on PDMS-based systems and other substrates.

3.2.2.3. Block copolymer micelle lithography

One of the most popular and reliable *in situ* growth patterning methods is block-copolymer micelle lithography (BCML, **Figure 3.5I,J**).[69–72] In this technique, the block copolymer micelles containing gold seed precursors are self-assembled into hexagonal arrays on the substrate *via* spin coating or dip coating onto the substrate. The array spacings with this technique can be controlled by changing the assembly time, temperature, and the components of the block copolymer, with polystyrene-b-poly(2-vinylpyridine) and polystyrene-b-poly(4-vinylpyridine) being common.[69-71] One limitation of standard BCML self-assembly is that only hexagonal arrays between ~3 nm and 200 nm can be readily fabricated.[69–71] Modifications to the technique applying co-assembly of different block copolymers can create *in situ* gold nanoparticles following wave-like patterns.[72] Performing sequential BCML steps combining assemblies with different spacings can also be used to fabricate Moiré patterns.[72] Otherwise, accessing more complex patterns (even just line arrays) with BCML requires combinations of top-down metal deposition,[72] photolithography,[69] and/or soft-lithography.[6] One such example is the scanning probe BCML method, which uses a cantilever to place the micelles into select regions.[73] However, this direct write printing method requires appropriate equipment and lengthy processing times.

3.2.3. Hybrid patterning approaches

There are markedly few studies that apply only *in situ* growth and provide detailed interrogation of anisotropic nanoparticle growth and/or patterning. Therefore, our discussion will

next include studies that implement hybrid *in situ* methods, which involve *in situ* overgrowth of substrate-anchored colloidal seeds or seeds made by top-down methods.

3.2.3.1. Combination of colloidal synthesis and *in situ* overgrowth

The colloidal seeds can also be patterned on substrates, *i.e.,* by soft lithography.[40,41,74] The seeds play the same role as they do in colloidal synthesis, acting as sites for preferred gold deposition. The affinity for gold to amine, thiol, carboxylic acid groups, *etc.* can be applied to attach colloidally prepared seeds to substrates so that subsequent *in situ* overgrowth into larger diameters or anisotropic shapes can be performed. On oxides, like glass, silicon oxide, or indium tin oxide, amine-presenting poly-L-lysine,[75] (3-aminopropyl)triethoxysilane (APTES),[23] (3-aminopropyl)trimethoxysilane (APTMS), and (3-mercaptopropyl)trimethoxysilane (MPTMS)[76] are common seed anchoring layers. We note reports of more uniform particle substrate attachment with APTES/APTMS mixed coatings.[77] This method has been applied for *in situ* overgrowth into multimetallic cubes,[22] concave structures,[21] and rods.[27] Ultimately, one reported benefit of performing *in situ* growth in this way is that it can improve the density of the overgrown nanostructures, which is useful for fabricating sensors.[21]

3.2.3.2. Combination of top-down fabrication and *in situ* overgrowth

One of the main challenges associated with BCML and the other *in situ* patterning is the limited tunability with regard to the kinds of patterns that can be fabricated. One approach towards addressing this limitation in the combination of *in* situ overgrowth with seeds made by top-down nanofabrication, which enables access to arbitrary patterns and higher resolution. Neretina and co-

workers demonstrate this possibility using top-down dynamic metal templating in combination with physical shadow masks (**Figure 3.6**).[78]

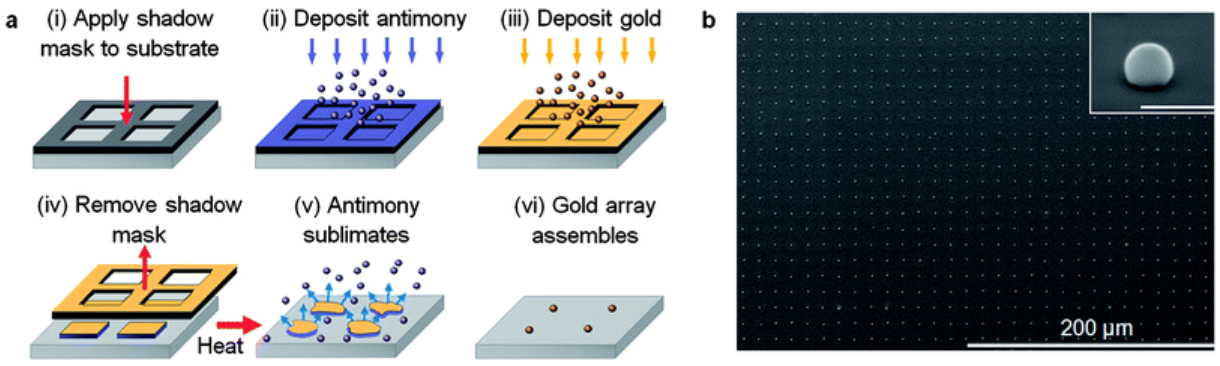

Figure 3.6. A: Schematic of the dynamic templating procedure: (i) a shadow mask is applied to the substrate. Next, (ii) antimony is deposited to the exposed areas, (iii) followed by gold deposition. Finally, (iv) the mask is removed and (v) the sample is heated to induce gold agglomeration and antimony sublimation until (vi) the seed array is formed. **B:** An electron microscopy image of the seed array prepared on a (0001)- oriented sapphire substrate. The inset shows a high magnification image of an individual seed at a 65 tilt side-view (scale bar = 1 mm) [reproduced with permission from ref. 78].

First, the deposition of Sb, then Au through the shadow mask is performed, the mask is lifted off, and the Sb-Au disks are heated to sublimate the Sb, creating gold seeds. Rather than a shadow mask fabricated *via* top-down lithography, a moldable polymer can be made into a mask using nanoimprint lithography (NIL), which also provides greater geometrical tunability compared to BCML.[24,79,80] These methods have been thus far applied to study the overgrowth of stars,[39] platelets,[24,81] chiral structures,[82] and even complex cage geometries.[83]

Section 3.3. Bottom-up Size and Shape Control

Next, we describe some examples of anisotropic growth *in situ,* and include work applying patterning (*i.e.,* BCML),[19,20,38] non-patterned *in situ* growth,[13,84] and those where *in situ* overgrowth was performed on seeds prepared from colloidal solution.[21,26,27] Thus far, some

examples of shapes accessible with *in situ* shape control include spheres of different sizes,[38,85] polyhedra/triangular plates,[20,24,81] branched structures,[19,25,39,84,86] nanorods,[27,28,87] concave structures,[21] and standing nanowires.[26,88] In the next sections, we discuss selected research focused on the synthesis of various anisotropic structures *in situ*, beginning with nanorods, then continuing to platelets, stars, and nanowires.

3.3.1. Nanorods

Gold nanorods are popular anisotropic particles used for thermoplasmonic applications and sensing.[33,89,90] Colloidal synthesis recipes are often used as starting points for the synthesis of nanorods *in situ*. In the colloidal synthesis method by Murphy, cetrimonium bromide (CTAB) and $AgNO_3$ are used as shape-directing reagents.[91] However, certain factors differentiate bottom-up synthesis on a substrate and in colloidal solutions. For example, surface-nuclei or surface-particle interactions can affect anisotropic growth. Oyama, for one, explored nanorod growth from colloidal 4 nm citrate-capped seeds attached to ITO substrates with APTES and MPTMS (**Figure 3.7A-B**).[27] The substrates were immersed in an overgrowth solution containing the shape-directing reagents over 24 h, producing high aspect ratio nanorods, but with fairly low yield. It was found that fewer rods were produced when the seeds were more strongly bound to the substrate with MPTMS compared to seeds bound weakly with APTES. The substrate was also found to affect growth of nanorods on polymethylmethacrylate (PMMA) by Abyaneh and co-workers, with low molecular weight PMMA yielding more rods, however the mechanism behind to this result is not clear (**Figure 3.7C-D**).[28]

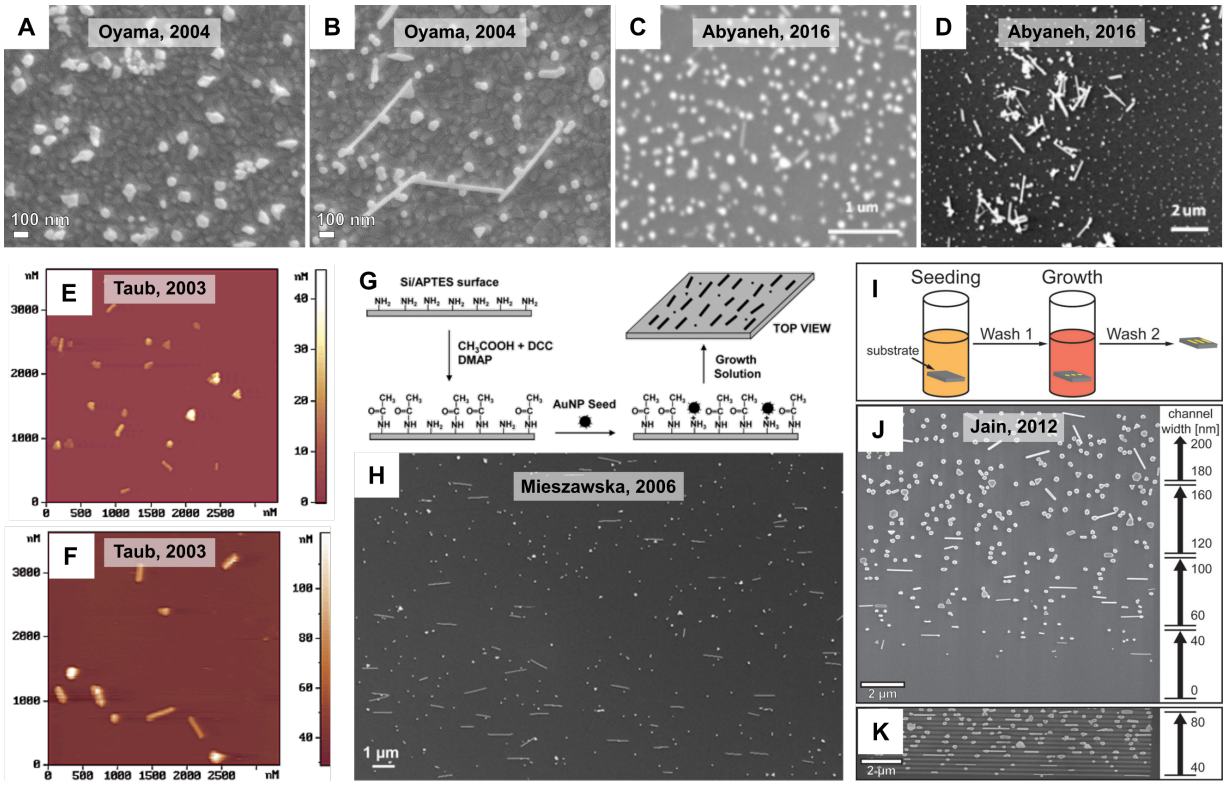

Figure 3.7. Scanning electron microscopy (SEM) images of gold nanoparticles prepared by Oyama on indium tin oxide functionalized with **A:** thiol and **B:** amine groups [reprinted from ref. 27. with permission from Elsevier]. Nanorod SEM images by Abyaneh on **C:** high- and **D:** low-molecular weight polymethylmethacrylate (PMMA) substrates [reproduced from ref. 28]. Atomic force microscopy images of nanorods obtained by Taub after **E:** one and **F:** three rounds of growth [reproduced with permission from ref. 92. Copyright 2003 American Chemical Society]. **G:** Schematic of the surface amidation and aligned nanorod growth on Si(100) by Mieszawska. **H:** SEM image of the aligned rods [reproduced with permission from ref. 23. Copyright 2006 American Chemical Society]. **I:** Schematic of the growth procedure for aligned rods on a Si substrate patterned with PMMA nanochannels prepared *via* electron beam lithography. **J,K:** SEM images of the aligned rods in channels with different dimensions [reproduced with permission from ref. 87. Copyright 2012 American Chemical Society].

In colloidal nanorod syntheses, it is common to apply multiple growth steps to increase the aspect ratio of the nanostructures.[33,91,93] Multiple growth steps are straightforward to apply *in situ* since growth can be stopped by simply removing the growth solution from the substrate. Taub and colleagues explored the multi-step growth of nanorods *in situ*, where citrate seeds 3.5 nm in diameter were anchored to mica substrates with APTMS.[92] Applying synthetic parameters from Murphy,[94] the growth time was varied to optimize the yield of structures with aspect ratio >2,

giving a final yield of 15% after multiple steps, where with only one step the obtained shape yield was 4% (**Figure 3.7E-F**). Overall, the limited improvement in yield was in part attributed to the affinity for CTAB for the mica substrate, preventing gold precursor from reaching the surface-bound seeds. Despite the nearly 4 times improvement in yield of high aspect ratio rods, a disadvantage of *in situ* growth can be highlighted: in colloidal synthesis centrifugation can be used to isolate certain products and to improve overall yield (common for rods[91,94] and triangles[95]), in contrast, it is not possible to isolate the desired shapes in this way for substrate-anchored products. It was also postulated that the seeds may have developed fewer twin defects caused by binding to the substrate, although, because the seeds were prepared colloidally, this explanation is unlikely.

Mieszawska *et al.*'s work further highlighted the importance of substrate-particle interactions, demonstrating that amide-functionalized Si(100) substrate could be used to grow rods aligned in the same direction (**Figure 3.7G-H**).[23] Although the mechanism for aligned growth is not clearly understood, aligned rods were not observed on glass or on Si(100) functionalized with amine or thiol groups, suggesting that both the substrate crystal structure and functionalization play a role influencing particle orientation. Aligned rods can also be prepared with the assistance of top-down fabrication of PMMA nanochannels on Si substrates (**Figure 3.7I-K**).[87] Lastly, for all of the abovementioned syntheses, although some works report synthesis of rods aligned in the same direction with their longitudinal axes parallel to the substrate, no standing rods were formed.

3.3.2. Triangles and other platelets

Kumar and co-workers reported good yield of nanotriangles *in situ* (~70%) from overgrowth of 3-4 nm seeds fabricated in hexagonal arrays with BCML (**Section 3.2.2.3**) .[20] They

found that applying synthetic conditions reported by Sau and Murphy[96] that mainly produced "square" particles (cubes or tetrahedra) in colloidal conditions instead mainly yielded triangular shapes 40-60 nm (**Figure 3.8A**). The authors proposed that the difference in results could be due to the structure of the seeds prepared by BCML, presenting different defects than those prepared in solution. Furthermore, diffusion of reagents to substrate-bound seeds may have an effect. As is the case with nanorods, the nanostructures presented here were oriented with their high-surface area faces parallel to the substrate. Another disadvantage of *in situ* growth is that in many cases, SEM characterization must be used in place of transmission electron microscopy (TEM), with TEM providing better resolution. In the case of *in situ* growth on non-conductive substrates, characterization by electron microscopy becomes even more difficult. In the work of Kumar, the growth procedure was innovatively performed directly on TEM grids coated with a thin Si_3N_4 membrane so that the shapes of the particles could be easily evaluated.

Neretina's group used dynamic templating (**Section 3.2.3.2**) to fabricate seeds and perform epitaxial overgrowth of nanotriangles (**Figure 3.8B**) and *in situ* plasmon-assisted growth of hexagonal nanoplate arrays (**Figure 3.8C-J**). The seeds mainly presented the [111] crystal facet oriented normal to the surface with stacking defects parallel to the substrate.[24] In this case, the seed orientation results from epitaxial formation on the underlying sapphire substrate. In addition, the yield of platelets *in situ* was significantly higher than in solution (78% *vs.* 21%, respectively). Here, TEM analysis was performed on samples prepared by focused ion beam cross-sectioning, leading to the observation that seeds containing defects supporting platelet growth oriented perpendicular to the substrate surface only produced truncated 3D structures. In fact, as with triangles by Kumar and rods, no standing or non-substrate parallel platelets were observed (**Figure 3.8D-G**).

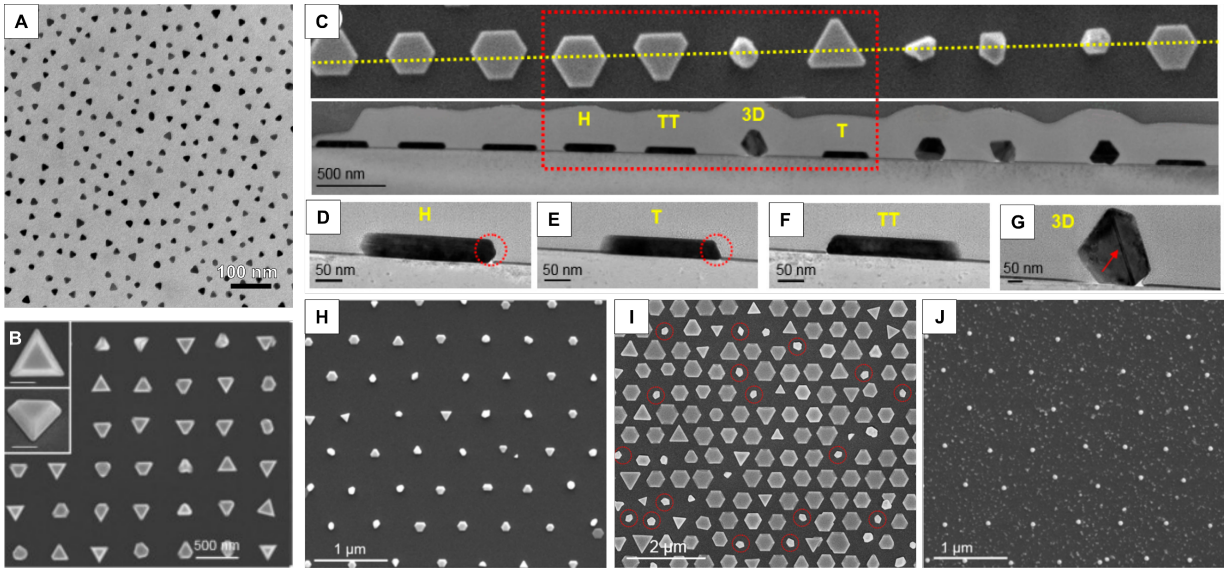

Figure 3.8. A-B: Nanotriangles synthesized by (**A**) Kumar *et al.* [reproduced with permission from ref. 20. Copyright 2007 American Chemical Society] and (**B**) Preston *et al.* [reproduced from ref. 97 with permission from Elsevier] **C:** (*Top*) Scanning electron microscopy image of particles and (*bottom*) cross-sectional transmission electron microscopy (TEM) images of nanoplates. **D:** Higher magnification cross-section TEM images of **D:** hexagonal (H), **E:** triangular (T) **F:** truncated triangular (TT) and **G:** three-dimensional (3D) morphologies. **H-J:** Scanning electron micrographs of nanoplates grown at (**H**) pH = 2.0, (**I**) 3.0, and (**J**) 5.5. [reproduced with permission from ref. 81. Copyright 2019 American Chemical Society].

Furthermore, as for colloidal systems,[98,99] pH is an important component affecting the yield, with low pH conditions giving more triangular platelets and higher pH giving poorly-defined geometries (**Figure 3.8H-J**). This observation hints towards the kinetics of the growth being an important factor in controlling *in situ* overgrowth into anisotropic shapes, because PVP becomes a weaker capping agent at higher pH, causing the growth to occur more quickly. As mentioned in the previous section, centrifugation cannot be used to select for the desired products in a substrate growth format. However, recently, Neretina and co-workers applied sonication to remove byproducts from the platelet synthesis, improving the yield from 78% to 95%.[81] Thus, the sonication approach can potentially serve as the analogue to purification *via* centrifugation for *in situ* systems.

3.3.3. Branched gold nanostructures

Branched gold nanostructures have been synthesized *in situ* by the mid-2000s,[84] around the same time that early colloidal nanostars syntheses were being developed.[100,101] For instance, in 2006, Metz *et al.* reported the synthesis of 50-400 nm long gold spikes on vertically aligned silver-coated carbon nanotubes (**Figure 3.9**).[84] More recent demonstrations of *in situ* growth of branched nanostructures take inspiration from colloidal recipes, by applying growth solutions based on established protocols like those from Kumar[100] and Xie,[101] that use (4-(2-hydroxyethyl)-1-piperazineethanesulfonic acid) (HEPES), PVP/dimethylformamide (DMF), CTAB, or $AgNO_3$ to direct anisotropic growth.

Overgrowth into branched structures driven by ascorbic acid (AA) has been explored extensively, by combining AA with shape directing agents like $AgNO_3$ and CTAB (**Figure 3.9B-D**). In one demonstration of AA-directed synthesis, Osinkina and co-workers used BCML to create hexagonal seed arrays, which were overgrown into stars (**Figure 3.9B**).[19] Later, Giner-Casares and colleagues used a similar method to prepare the arrays, but performed the overgrowth step in a silver-free solution producing structures with branches 40-60 nm long and 30 nm wide (**Figure 3.9C**).[86] Demille and co-workers fabricated seeds with NIL and dynamic templating, and tested overgrowth in a surfactant-free solution (**Figure 3.9D**).[39] Although the final concentrations of added reagents are similar in the aforementioned examples of AA-driven synthesis, in the latter case, it was exceedingly difficult to obtain branched structures directly unless the growth solution was flowed over the substrate, as depicted in **Figure 3.9F**. Demille and coworkers also tested *in situ* growth by following the colloidal protocol established by Xie, which uses HEPES and proved to be unfavorable for branching. However, modification of the protocol by adding a small amount

of $AgNO_3$ produced more roughened morphologies (**Figure 3.9E**). The $AgNO_3$ likely plays a similar role as a shape-directing agent as it does in colloidal systems.

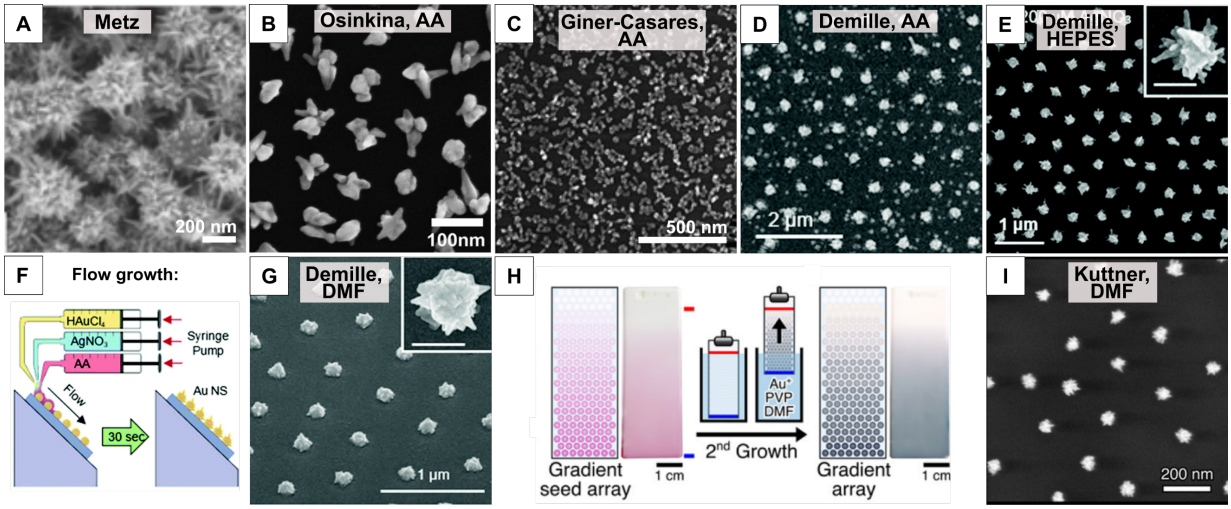

Figure 3.9. Scanning electron microscopy images of branched nanostructures prepared by **A:** Metz [reproduced with permission from ref. 84. Copyright 2006 American Chemical Society], **B:** Osinkina [reproduced with permission from ref. 19. Copyright 2013 American Chemical Society], **C:** Giner-Casares [reproduced with permission from ref. 86], **D,E,G:** Demille [reproduced with permission from ref. 39], and **I:** Kuttner [reproduced with permission from ref. 25. Copyright 2021 American Chemical Society]. **F:** Schematic of flow growth performed by the group of Neretina. **H:** Schematic of nanostars grown using seed size gradients, and **K:** the resulting nanostars present near the end of the substrate. AA = Ascorbic acid, HEPES = (4-(2-hydroxyethyl)-1-piperazineethanesulfonic acid), DMF = Dimethylformamide.

Demille and Kuttner (**Figure 3.9D-I**) both tested *in situ* overgrowth of nanostars using a recipe based on the PVP/DMF colloidal synthesis of Kumar.[100] Although both applied similar overgrowth solution recipes, Kuttner used smaller seeds that were stabilized with a PNIPAm coating, which may contribute to the differences in the results obtained. Furthermore, in the work of Kuttner, instead of incubating the seed substrate in the growth solution, the substrate was pulled out of the solution at a rate of 1 mm/min to fabricate nanostar gradients with spherical nanoparticles at the top and larger, more highly branched particles at the bottom (**Figure 3.9H**). As with multi-

step nanorod overgrowth, Demille and Kuttner also commented on the capability to stop the growth quickly by physically separating the substrate from solution at the desired time point.

In the work of Demille, although seeds were present only on the substrate, the occurrence of significant secondary nucleation in the growth solution, as illustrated in **Figure 3.10**, appeared to inhibit anisotropic growth *in situ*.

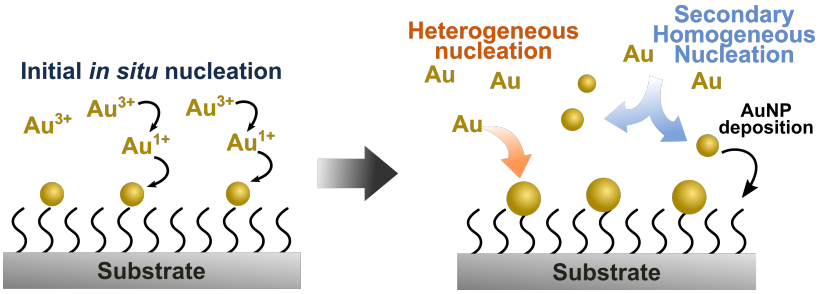

Figure 3.10. Schematic depicting heterogeneous and homogeneous nucleation in *in situ* growth systems that incorporate strong reductants on the substrate.

The competition between the surface-bound nuclei and colloidal nuclei for growth reagents has been noted as a barrier for controlled *in situ* growth by others.[38] In a solution favoring more rapid growth, fast secondary nucleation occurs (this is why colloidal nanostar synthesis involves the rapid addition of the seeds to the growth solution following the reducing agent).[102,103] It is expected, then, that the DMF-driven synthesis was most successful, since it produces less secondary nucleation in the same amount of time as the more rapid AA- and HEPES-driven syntheses. Another aspect to consider is that Demille used large seeds, which would have a slower growth rate compared to the small nuclei spontaneously forming in the solution.

Additional evidence supporting the role of secondary nucleation includes the observation of improved isolation of branched structures by "flowing" the growth solution over the substrate in the AA-driven case (**Figure 3.9F**). The authors attribute this effect to differences caused by the no-slip condition, similar to the rationalizations regarding reagent diffusion suggested in the rod

synthesis by Taub[92] and the nanotriangle synthesis by Kumar.[20] However, between the stationary solution and the applied flowing solution, mass transfer should still be dominated by diffusion rather than convection (see **Chapter 1.2.3** and **Chapter 5**). Thus, significant differences in stationary liquid vs. no flow should not be expected if the differences in the products are due primarily to diffusion. Alternatively, the growth in flow could be reducing the effects of secondary nucleation by replenishing freshly mixed reagents and carrying away colloidal nuclei throughout the synthesis. Even for flow growth, evidence of secondary nucleation can still be observed *via* the population of particles outside of the areas containing seeds (**Figure 3.9D**). Looking back at the work on platelets by the same group, accelerating the reaction by increasing pH likewise increases the appearance of particles outside the patterned regions (**Figure 3.6J**). Overall, these observations are evidence that, even when nuclei are created and/or formed only on the substrate either by *in situ* or hybrid methods, secondary nucleation is vital to consider (**Figure 3.10**).

3.3.4. Vertical growth: Nanowires

Although shape control *in situ* is still greatly understudied compared to colloidal synthesis, there are opportunities for synthesizing shape-controlled plasmonic structures and even fabricating plasmonic substrates that are not routine to produce with colloidal self-assembly. One striking benefit of *in situ* growth is the possibility to synthesize standing nanorods or wires with extremely high yield, which is prohibitively difficult to fabricate with the self-assembly of colloids.[12] The synthetic studies of these structures provide interesting insights into the mechanistic differences of *in situ* growth compared to colloidal systems.

In **Section 3.3.1,2**, we predominantly saw examples of horizontal growth *in situ*. However, there are certain conditions that can instead promote vertical growth from the substrate, showing

that *in situ* growth provides opportunities for controlling the orientation of the particle. He and co-workers were able to synthesize standing nanowires from substrate immobilized seeds in high yield (**Figure 3.11,** following the hybrid *in situ* overgrowth method from **Section 3.2.3.1**).[26] The authors proposed that the vertical growth was due to the presence of a strongly binding thiol ligands (mercaptobenzoic acid, MBA) that only permitted addition of the gold atoms at the interface between the seed and the substrate, where the ligand shell is most disordered (**Figure 3.11A,B**). The sides and tip of the nanowires, on the other hand, are quickly passivated by MBA, making it unfavorable for gold atoms to be added in those regions. The role of the density of the ligand was supported by the execution of the synthesis with different ligand concentrations during the growth. The wires exhibited thicker tails and thinner heads when the MBA concentration was reduced during the synthesis. Conversely, when the ligand concentration was increased, thinner heads and thicker tails were produced (**Figure 3.11C-E**). In a later study, gold nanowires were instead grown by promoting growth selectively at the nanowire tips, as shown in **Figure 3.11F,G**.[88] The wires exhibit curves and changes in diameter along the longitudinal direction, which are proposed to result from changes in the growth direction as addition of gold atoms is occurring at the wire tips (**Figure 3.11H,I**). Overall, these results show that the substrate can be used to influence the direction of the growth, a feature that is unique to *in situ* methods.

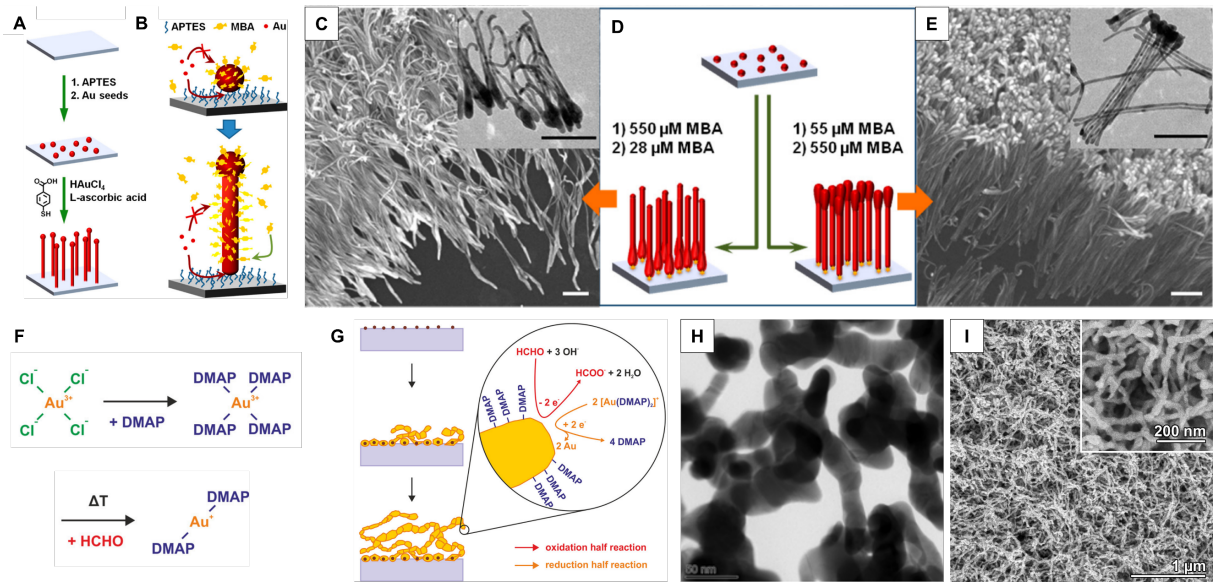

Figure 3.11. A: Schematic showing colloidal seed attachment to silica with (3-aminopropyl)triethoxysilane (APTES) and subsequent growth into nanowires with mercaptobenzoic acid (MBA), ascorbic acid, and gold salt. **B:** Depiction of the fast passivation of MBA at the nanowire sides and selective growth via attachment of gold atoms at the substrate interface. **C-E:** Scanning electron microscopy image showing the result when MBA concentration is (**C**) decreased and (**E**) increased in the latter growth stage as shown in the schematic in panel **D** [reproduced with permission from ref. 26. Copyright 2013 American Chemical Society]. **F:** Reactions occurring in the growth solution and **G:** schematic of Au nanowire growth by Muench *et al.*: Pd seeds were made by electroless plating, then a solution containing 4-dimethylaminopyridine (DMAP) as a capping ligand, gold salt, and formaldehyde as a mild reducing agent is added to produce nanowires with high yield. As depicted in panel **G**, continuous growth occurs at the wire tips **H-I:** Electron microscopy images of the products [reproduced with permission from ref. 88. Copyright 2017 American Chemical Society].

Section 3.4. Summary and Prospects

Several examples that employ *in situ* growth and overgrowth of gold nanoparticles on substrates such as polymers, oxides, and semiconductors have been discussed. Overall, additional synthetic studies are needed to elevate this class of approaches to the same relevance as colloidal techniques for manufacturing plasmonic materials and devices. We can consolidate a few important factors that should be considered for *in situ* growth schemes:

1. The chemical environment (constituents of the growth solution, pH and temperature, *etc.*)
2. Seed size, crystal structure, orientation on the substrate

3. Interaction strength between the nanoparticles/seeds and the substrate
4. Surface density of seeds or nucleation sites
5. Competition between spontaneous colloidal nucleation and substrate growth (secondary homogeneous nucleation)

Of these factors, precisely controlling the location and density of nucleation sites (analogous to controlling the seed concentration in colloidal synthesis), as is done with BCML and other patterning techniques, is especially important for performing synthetic investigations. Moreover, preventing the formation of nuclei in the growth solution away from the substrate or from intended nucleation/growth sites appears to be vital. Competition between *in situ* growth and colloidal nucleation unpredictably consumes reagents and creates nuclei that can deposit in unintended locations. Some strategies for preventing or reducing homogeneous or secondary nucleation could include:

1. Implementing only weak reductants in the growth solution and using substrate bound or native strong reductants.
2. Using overgrowth solutions with slower growth kinetics
3. Applying a clean water source
4. Reducing interaction of the growth solution with other surfaces (*e.g.*, glass)
5. Performing overgrowth from smaller (higher surface energy) seeds

With colloidal synthesis, TEM characterization (including tomography scanning, and high-resolution TEM) provide key insights into the growth by providing crystallographic and morphological information.[104] Instead, *in situ* growth characterization relies mainly on SEM and AFM since the nanoparticles are fixed on the substrate. Consequently, obtaining the detailed crystallographic and structural information necessary for understanding the growth (especially

when working with nanoparticles having few nm diameters) is difficult. Some of the crucial contributions to *in situ* synthesis that I have highlighted were able to acquire high-resolution TEM to provide important insight. For example, Kumar's sample preparation directly on custom-made TEM grids coated with a thin film of silicon nitride enabled sufficient characterization of gold nanoparticles down to ~5 nm.[20] Focused ion beam milling can also be used to prepare samples for high-resolution TEM.[24,26] Characterization can also be obtained by physically removing the nanostructures from the substrate, as was done for the synthesis of standing nanowires.[26]

Overall, there is immense opportunity to explore nanoparticle growth and shape control *in situ* further. Forming particles directly on the substrate potentially enables modification of the particle geometry in all directions relative to the surface, where control in the x-y directions are normally difficult to achieve with traditional self-assembly. Arranged standing nanowires, oriented anisotropic structures (*e.g.,* triangles, platelets, nanostars, and chiral nanohooks[105]), truncated particles,[18] and oriented dimers,[106] are some examples of unique arrangements that could be prepared *in situ*. As for colloidal synthesis, the components of the growth solution can be modified to optimize the yield of a desired structure.

The next generation of *in situ* synthetic protocols should take advantage of the factors that set *in situ* growth apart from colloidal synthesis. For instance, a major opportunity of *in situ* growth lies in the fact that the particles are fixed or bound to the substrate and colloidal stability and solvent compatibility do not need to be considered. This opportunity paves the way for exploring growth in extreme conditions: high temperature, high concentration of salts, testing extremely low or high pH, surfactant-free synthesis, *etc*. Even simply pursuing the development of surfactant-free synthesis offers a major contribution to this class of techniques, enabling facile integration with other materials (*e.g.,* graphene or other two-dimensional materials) for energy and catalysis

applications.[107] Furthermore, nanoparticle-substrate interactions offer another solution for modifying nanoparticle morphology and can offer more flexibility for accessing new structures in the future. Thus far, *in situ* growth has produced a wide breadth of plasmonic materials that can find applications in sensing,[19,21,47,63] cell culture,[86] cancer diagnostics,[37] and optoelectronics,[72] highlighting the potential broad impact to different fields.

Section 3.5. References

[1] M. Mayer, M. Tebbe, C. Kuttner, M. J. Schnepf, T. A. F. König, A. Fery, *Faraday Discuss.* **2016**, *191*, 159.

[2] C. Hamon, S. M. Novikov, L. Scarabelli, D. M. Solís, T. Altantzis, S. Bals, J. M. Taboada, F. Obelleiro, L. M. Liz-Marzán, *ACS Photonics* **2015**, *2*, 1482.

[3] H. Zhang, Y. Liu, M. F. S. Shahidan, C. Kinnear, F. Maasoumi, J. Cadusch, E. M. Akinoglu, T. D. James, A. Widmer-Cooper, A. Roberts, P. Mulvaney, *Adv. Funct. Mater.* **2021**, *31*, 2006753.

[4] Y. Zhou, X. Zhou, D. J. Park, K. Torabi, K. A. Brown, M. R. Jones, C. Zhang, G. C. Schatz, C. A. Mirkin, *Nano Lett.* **2014**, *14*, 2157.

[5] V. Santhanam, R. P. Andres, *Nano Lett.* **2004**, *4*, 41.

[6] J. Chen, P. Mela, M. Möller, M. C. Lensen, *ACS Nano* **2009**, *3*, 1451.

[7] L. Scarabelli, D. Vila-Liarte, A. Mihi, L. M. Liz-Marzán, *Acc. Mater. Res.* **2021**, *2*, 816.

[8] Liao Wei-Ssu, Cheunkar Sarawut, Cao Huan H., Bednar Heidi R., Weiss Paul S., Andrews Anne M., *Science* **2012**, *337*, 1517.

[9] N. Chiang, L. Scarabelli, G. A. Vinnacombe-Willson, L. A. Pérez, C. Dore, A. Mihi, S. J. Jonas, P. S. Weiss, *ACS Mater. Lett.* **2021**, *3*, 282.

[10] C. Zhao, Q. Liu, K. M. Cheung, W. Liu, Q. Yang, X. Xu, T. Man, P. S. Weiss, C. Zhou, A. M. Andrews, *ACS Nano* **2021**, *15*, 904.

[11] K. Sugano, Y. Uchida, O. Ichihashi, H. Yamada, T. Tsuchiya, O. Tabata, *Microfluid. Nanofluidics* **2010**, *9*, 1165.

[12] C. Hanske, E. H. Hill, D. Vila-Liarte, G. González-Rubio, C. Matricardi, A. Mihi, L. M. Liz-Marzán, *ACS Appl. Mater. Interfaces* **2019**, *11*, 11763.

[13] F. Muench, *ChemElectroChem* **2021**, *8*, 2993.

[14] Y. Shacham-Diamand, T. Osaka, Y. Okinaka, A. Sugiyama, V. Dubin, *Micro Nanofabrication Breakthr. Electron. MEMS Life Sci.* **2015**, *132*, 35.

[15] C. Louis, *Gold Nanoparticles for Physics, Chemistry and Biology*, World Scientific, **2017**.

[16] I. Freestone, N. Meeks, M. Sax, C. Higgitt, *Gold Bull.* **2007**, *40*, 270.

[17] M. Kracker, C. Thieme, K. Thieme, C. Patzig, L. Berthold, T. Höche, C. Rüssel, *RSC Adv.* **2018**, *8*, 6267.

[18] T. B. Demille, R. A. Hughes, S. Neretina, *J. Phys. Chem. C* **2019**, *123*, 19879.

[19] L. Osinkina, T. Lohmüller, F. Jäckel, J. Feldmann, *J. Phys. Chem. C* **2013**, *117*, 22198.

[20] S. Kumar, H. Yang, S. Zou, *J. Phys. Chem. C* **2007**, *111*, 12933.

[21] M. J. Ashley, M. R. Bourgeois, R. R. Murthy, C. R. Laramy, M. B. Ross, R. R. Naik, G. C. Schatz, C. A. Mirkin, *J. Phys. Chem. C* **2018**, *122*, 2307.

[22] G. Liu, C. Zhang, J. Wu, C. A. Mirkin, *ACS Nano* **2015**, *9*, 12137.

[23] A. J. Mieszawska, G. W. Slawinski, F. P. Zamborini, *J. Am. Chem. Soc.* **2006**, *128*, 5622.

[24] S. D. Golze, R. A. Hughes, S. Rouvimov, R. D. Neal, T. B. Demille, S. Neretina, *Nano Lett.* **2019**, *19*, 5653.

[25] C. Kuttner, V. Piotto, L. M. Liz-Marzán, *Chem. Mater.* **2021**, *33*, 8904.

[26] J. He, Y. Wang, Y. Feng, X. Qi, Z. Zeng, Q. Liu, W. S. Teo, C. L. Gan, H. Zhang, H. Chen, *ACS Nano* **2013**, *7*, 2733.

[27] J. Zhang, M. Kambayashi, M. Oyama, *Electrochem. Commun.* **2004**, *6*, 683.

[28] M. K. Abyaneh, P. Parisse, L. Casalis, *Beilstein J. Nanotechnol.* **2016**, *7*, 809.

[29] L. Liz-Marzán, *Colloidal Synthesis of Plasmonic Nanometals*, CRC Press, **2020**.

[30] N. G. Bastús, J. Comenge, V. Puntes, *Langmuir* **2011**, *27*, 11098.

[31] I. Ojea-Jiménez, N. G. Bastús, V. Puntes, *J. Phys. Chem. C* **2011**, *115*, 15752.

[32] G. Muralidharan, L. Subramanian, S. K. Nallamuthu, V. Santhanam, S. Kumar, *Ind. Eng. Chem. Res.* **2011**, *50*, 8786.

[33] L. Scarabelli, A. Sánchez-Iglesias, J. Pérez-Juste, L. M. Liz-Marzán, *J. Phys. Chem. Lett.* **2015**, *6*, 4270.

[34] A. Sánchez-Iglesias, K. Jenkinson, S. Bals, L. M. Liz-Marzán, *J. Phys. Chem. C* **2021**, *125*, 23937.

[35] J. N. de Freitas, M. A. Mamo, M. Maubane, W. A. L. van Otterlo, N. J. Coville, A. F. Nogueira, *J. Power Sources* **2012**, *215*, 99.

[36] C. Wang, N. T. Flynn, R. Langer, *Adv. Mater.* **2004**, *16*, 1074.

[37] G. A. Vinnacombe-Willson, N. Chiang, L. Scarabelli, Y. Hu, L. K. Heidenreich, X. Li, Y. Gong, D. T. Inouye, T. S. Fisher, P. S. Weiss, S. J. Jonas, *ACS Cent. Sci.* **2020**, *6*, 2105.

[38] B. Landeke-Wilsmark, L. Nyholm, C. Hägglund, *Langmuir* **2020**, *36*, 6848.

[39] T. B. Demille, R. A. Hughes, N. Dominique, J. E. Olson, S. Rouvimov, J. P. Camden, S. Neretina, *Nanoscale* **2020**, *12*, 16489.

[40] Y.-K. Kim, H.-K. Na, Y. W. Lee, H. Jang, S. W. Han, D.-H. Min, *Chem. Commun.* **2010**, *46*, 3185.

[41] Y.-K. Kim, H.-K. Na, D.-H. Min, *Langmuir* **2010**, *26*, 13065.

[42] B. Song, K. He, Y. Yuan, S. Sharifi-Asl, M. Cheng, J. Lu, W. A. Saidi, R. Shahbazian-Yassar, *Nanoscale* **2018**, *10*, 15809.

[43] J. Kim, S. Byun, A. J. Smith, J. Yu, J. Huang, *J. Phys. Chem. Lett.* **2013**, *4*, 1227.

[44] E. S. Abdel-Halim, S. S. Al-Deyab, *Carbohydr. Polym.* **2011**, *86*, 1615.

[45] X. Wu, C. Lu, Z. Zhou, G. Yuan, R. Xiong, X. Zhang, *Environ. Sci. Nano* **2014**, *1*, 71.

[46] S. B. Ulapane, N. J. B. Kamathewatta, A. K. Borkowski, S. J. Steuart, C. L. Berrie, *J. Phys. Chem. C* **2020**, *124*, 15646.

[47] B. Fortuni, T. Inose, S. Uezono, S. Toyouchi, K. Umemoto, S. Sekine, Y. Fujita, M. Ricci, G. Lu, A. Masuhara, J. A. Hutchison, L. Latterini, H. Uji-i, *Chem. Commun.* **2017**, *53*, 11298.

[48] Q. Zhang, J.-J. Xu, Y. Liu, H.-Y. Chen, *Lab. Chip* **2008**, *8*, 352.

[49] D. J. Campbell, R. B. Villarreal, T. J. Fitzjarrald, *J. Chem. Educ.* **2012**, *89*, 1312.

[50] M.-C. Lim, S.-H. Kim, K. Park, Y.-R. Kim, J.-H. Kim, G. Ok, S.-W. Choi, *RSC Adv.* **2017**, *7*, 13228.

[51] K. Park, M.-A. Woo, J.-A. Lim, Y.-R. Kim, S.-W. Choi, M.-C. Lim, *Colloids Surf. Physicochem. Eng. Asp.* **2018**, *558*, 186.

[52] X. Shi, M. Shen, H. Mohwald, *Prog. Polym. Sci.* **2004**, *29*, 987.

[53] Y.-C. Liu, T. C. Chuang, *J. Phys. Chem. B* **2003**, *107*, 12383.

[54] J. Han, L. Li, R. Guo, *Macromolecules* **2010**, *43*, 10636.

[55] Y. Tsuge, T. Moriya, Y. Moriyama, Y. Tokura, S. Shiratori, *ACS Appl. Mater. Interfaces* **2017**, *9*, 15122.

[56] Ö. Dag, E. J. Henderson, W. Wang, J. E. Lofgreen, S. Petrov, P. M. Brodersen, G. A. Ozin, *J. Am. Chem. Soc.* **2011**, *133*, 17454.

[57] S.-R. Zhai, X. Shao, D. Zhou, B. Zhai, Q.-D. An, *J. Sol-Gel Sci. Technol.* **2012**, *62*, 281.

[58] A. S. Cruz-Félix, A. Santiago-Alvarado, J. Márquez-García, J. González-García, *Heliyon* **2019**, *5*, e03064.

[59] R. Seghir, S. Arscott, *Sens. Actuators Phys.* **2015**, *230*, 33.

[60] I. Miranda, A. Souza, P. Sousa, J. Ribeiro, E. M. S. Castanheira, R. Lima, G. Minas, *J. Funct. Biomater.* **2021**, *13*, 2.

[61] A. Bonyár, Z. Izsold, L. Himics, M. Veres, I. Csarnovics, in *2017 IEEE 23rd Int. Symp. Des. Technol. Electron. Packag. SIITME*, **2017**, pp. 25–28.

[62] K. R. Brown, D. G. Walter, M. J. Natan, *Chem. Mater.* **2000**, *12*, 306.

[63] B. Fortuni, Y. Fujita, M. Ricci, T. Inose, R. Aubert, G. Lu, J. A. Hutchison, J. Hofkens, L. Latterini, H. Uji-i, *Chem. Commun.* **2017**, *53*, 5121.

[64] J. Xu, X. Li, Y. Zhong, J. Qi, Z. Wang, Z. Chai, W. Li, C. Jing, Y. Cheng, *Adv. Mater. Technol.* **2018**, *3*, 1800372.

[65] C. V. Navin, K. S. Krishna, C. S. Theegala, C. S. S. R. Kumar, *Nanotechnol. Rev.* **2014**, *3*, 39.

[66] L. Jibril, P.-C. Chen, J. Hu, T. W. Odom, C. A. Mirkin, *ACS Nano* **2019**, *13*, 12408.

[67] B. Wang, K. Chen, S. Jiang, F. Reincke, W. Tong, D. Wang, C. Gao, *Biomacromolecules* **2006**, *7*, 1203.

[68] A. A. Ellsworth, A. V. Walker, *Langmuir* **2016**, *32*, 2668.

[69] R. Glass, M. M ller, J. P. Spatz, *Nanotechnology* **2003**, *14*, 1153.

[70] T. Lohmüller, D. Aydin, M. Schwieder, C. Morhard, I. Louban, C. Pacholski, J. P. Spatz, *Biointerphases* **2011**, *6*, MR1.

[71] M. Stefik, S. Guldin, S. Vignolini, U. Wiesner, U. Steiner, *Chem. Soc. Rev.* **2015**, *44*, 5076.

[72] A. Alvarez-Fernandez, C. Cummins, M. Saba, U. Steiner, G. Fleury, V. Ponsinet, S. Guldin, *Adv. Opt. Mater.* **2021**, *9*, 2100175.

[73] J. Chai, F. Huo, Z. Zheng, L. R. Giam, W. Shim, C. A. Mirkin, *Proc. Natl. Acad. Sci.* **2010**, *107*, 20202.

[74] A. A. Mewe, E. S. Kooij, B. Poelsema, *Langmuir* **2006**, *22*, 5584.

[75] J. Tang, Q. Ou, H. Zhou, L. Qi, S. Man, *Nanomater. Basel Switz.* **2019**, *9*, 185.

[76] Y. Jin, X. Kang, Y. Song, B. Zhang, G. Cheng, S. Dong, *Anal. Chem.* **2001**, *73*, 2843.

[77] M. Ben Haddada, J. Blanchard, S. Casale, J.-M. Krafft, A. Vallée, C. Méthivier, S. Boujday, *Gold Bull.* **2013**, *46*, 335.

[78] P. Farzinpour, A. Sundar, K. D. Gilroy, Z. E. Eskin, R. A. Hughes, S. Neretina, *Nanoscale* **2013**, *5*, 1929.

[79] S. Y. Chou, P. R. Krauss, P. J. Renstrom, *J. Vac. Sci. Technol. B Microelectron. Nanometer Struct. Process. Meas. Phenom.* **1996**, *14*, 4129.

[80] E. Menumerov, S. D. Golze, R. A. Hughes, S. Neretina, *Nanoscale* **2018**, *10*, 18186.

[81] T. B. Demille, R. D. Neal, A. S. Preston, Z. Liang, A. G. Oliver, R. A. Hughes, S. Neretina, *Nano Res.* **2022**, *15*, 296.

[82] S. D. Golze, S. Porcu, C. Zhu, E. Sutter, P. C. Ricci, E. C. Kinzel, R. A. Hughes, S. Neretina, *Nano Lett.* **2021**, *21*, 2919.

[83] M. Hajfathalian, K. D. Gilroy, S. D. Golze, A. Yaghoubzade, E. Menumerov, R. A. Hughes, S. Neretina, *ACS Nano* **2016**, *10*, 6354.

[84] K. M. Metz, K.-Y. Tse, S. E. Baker, E. C. Landis, R. J. Hamers, *Chem. Mater.* **2006**, *18*, 5398.

[85] T. Lohmueller, E. Bock, J. P. Spatz, *Adv. Mater.* **2008**, *20*, 2297.

[86] J. J. Giner-Casares, M. Henriksen-Lacey, I. García, L. M. Liz-Marzán, *Angew. Chem. Int. Ed.* **2016**, *55*, 974.

[87] T. Jain, S. Lara-Avila, Y.-V. Kervennic, K. Moth-Poulsen, K. Nørgaard, S. Kubatkin, T. Bjørnholm, *ACS Nano* **2012**, *6*, 3861.

[88] F. Muench, S. Schaefer, L. Hagelüken, L. Molina-Luna, M. Duerrschnabel, H.-J. Kleebe, J. Brötz, A. Vaskevich, I. Rubinstein, W. Ensinger, *ACS Appl. Mater. Interfaces* **2017**, *9*, 31142.

[89] C. Fernández-López, L. Polavarapu, D. M. Solís, J. M. Taboada, F. Obelleiro, R. Contreras-Cáceres, I. Pastoriza-Santos, J. Pérez-Juste, *ACS Appl. Mater. Interfaces* **2015**, *7*, 12530.

[90] X. Huang, S. Neretina, M. A. El-Sayed, *Adv. Mater.* **2009**, *21*, 4880.

[91] B. D. Busbee, S. O. Obare, C. J. Murphy, *Adv. Mater.* **2003**, *15*, 414.

[92] N. Taub, O. Krichevski, G. Markovich, *J. Phys. Chem. B* **2003**, *107*, 11579.

[93] C. J. Murphy, L. B. Thompson, D. J. Chernak, J. A. Yang, S. T. Sivapalan, S. P. Boulos, J. Huang, A. M. Alkilany, P. N. Sisco, *Curr. Opin. Colloid Interface Sci.* **2011**, *16*, 128.

[94] N. R. Jana, L. Gearheart, C. J. Murphy, *Adv. Mater.* **2001**, *13*, 1389.

[95] L. Scarabelli, L. M. Liz-Marzán, *ACS Nano* **2021**, *15*, 18600.

[96] T. K. Sau, C. J. Murphy, *J. Am. Chem. Soc.* **2004**, *126*, 8648.

[97] A. S. Preston, R. A. Hughes, T. B. Demille, V. M. Rey Davila, S. Neretina, *Acta Mater.* **2019**, *165*, 15.

[98] K. Chandra, K. S. B. Culver, S. E. Werner, R. C. Lee, T. W. Odom, *Chem. Mater.* **2016**, *28*, 6763.

[99] R. M. Pallares, T. Stilson, P. Choo, J. Hu, T. W. Odom, *ACS Appl. Nano Mater.* **2019**, *2*, 5266.

[100] P. S. Kumar, I. Pastoriza-Santos, B. Rodríguez-González, F. J. G. de Abajo, L. M. Liz-Marzán, *Nanotechnology* **2007**, *19*, 015606.

[101] J. Xie, J. Y. Lee, D. I. C. Wang, *Chem. Mater.* **2007**, *19*, 2823.

[102] P. Pallavicini, A. Donà, A. Casu, G. Chirico, M. Collini, G. Dacarro, A. Falqui, C. Milanese, L. Sironi, A. Taglietti, *Chem. Commun.* **2013**, *49*, 6265.

[103] A. Casu, E. Cabrini, A. Donà, A. Falqui, Y. Diaz-Fernandez, C. Milanese, A. Taglietti, P. Pallavicini, *Chem. - Eur. J.* **2012**, *18*, 9381.

[104] S. Bals, B. Goris, L. M. Liz-Marzán, G. Van Tendeloo, *Angew. Chem. Int. Ed.* **2014**, *53*, 10600.

[105] A. G. Mark, J. G. Gibbs, T.-C. Lee, P. Fischer, *Nat. Mater.* **2013**, *12*, 802.

[106] H.-H. Jeong, M. C. Adams, J.-P. Günther, M. Alarcón-Correa, I. Kim, E. Choi, C. Miksch, A. F. Mark, A. G. Mark, P. Fischer, *ACS Nano* **2019**, *13*, 11453.

[107] E. Cortés, P. H. Camargo, *Plasmonic Catalysis: From Fundamentals to Applications*, John Wiley & Sons, **2021**.

Chapter 4. Surface Lattice Plasmon Resonances by *in Situ* Growth of Gold Nanoparticle Arrays

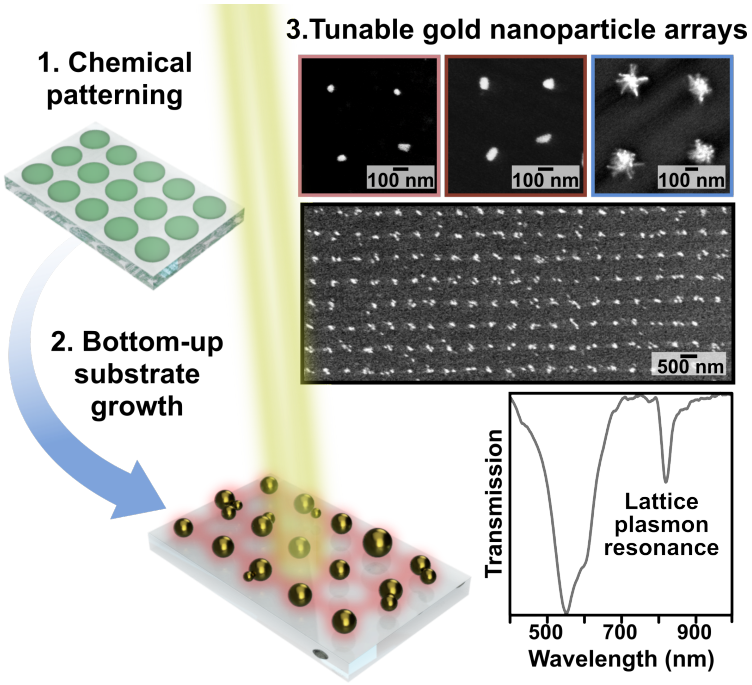

Gold nanoparticle plasmonic ordered arrays were fabricated by an unconventional *in situ* approach where gold precursors are reduced directly at specific pre-patterned locations on the substrate. Nanoparticle morphology and array periodicity are easily tuned using this method. The substrates exhibit far-field plasmonic coupling *via* the emergence of lattice plasmon resonances, constituting a major step forward for *in situ* growth techniques.

Section 4.1. Introduction

Although the localized surface plasmon resonance (LSPR) effect can confine light in subwavelength volumes,[1] these resonances are typically short lived due to intrinsic high radiative optical losses that limit the associated quality factors (< 10).[2] Nonetheless, from **Chapter 1**, recall that arranging plasmonic nanoparticles into ordered arrays is a convenient strategy to overcome this limitation and to boost the quality factors of the system. In this configuration, the optical losses associated with LSPRs can be compensated under Bragg conditions by hybridization with the scattered waves in the plane of the array close to the position of the Rayleigh-Wood anomalies.[2] This compensation generates lattice plasmon resonances (LPRs), and offers an additional possibility for tuning the optical properties, depending on the angle of illumination and the geometrical parameters of the array.[2] Due to their narrow bandwidth (<2 nm) and long lifetimes,[2–4] lattice plasmon resonances already impact the enhancement and manipulation of light-matter interactions,[5–7] sensing,[8–10] displays,[11] information storage[12] and anti-reflective materials.[13]

In **Chapter 3**, recent developments on the *in situ* growth fabrication of plasmonic substrates were comprehensively reviewed. Overall, the possibility of guiding the growth of plasmonic nanoparticles directly into patterns and on the substrate of choice has been proposed several times in the past decades. Probably the best results so far have been achieved using block-copolymer micelle lithography[14–17] (**Section 3.2.2.3**) and dynamic templating (**Section 3.2.3.2**).[18–20] Despite these being concrete solutions, the former suffers from limited pattern tunability (mainly hexagonal arrays) and spacing (typically 30-300 nm), preventing realization of LPRs in the visible and near infrared, while the latter still relies on several evaporation and sublimation steps that require advanced instrumentation and are limited to certain materials.

In this chapter, we establish and demonstrate an alternative straightforward *in situ* growth approach that incorporates spatially selective growth on the substrate. Namely, we target the tunable plasmonic lattices following rapid bottom-up growth of gold nanoparticles (AuNPs) onto chemically patterned reactive areas created by soft lithography. To fabricate these structures, water-soluble hydroxypropyl cellulose (HPC) sacrificial hole masks (or stencils), were applied to create patterned regions containing AuNP growth-active chemical ink. Subsequent site-selective growth of AuNPs was performed with the addition of a droplet of growth solution onto the chemically patterned substrates in one rapid (<10 min), single synthetic step. We demonstrate that the composition of the growth solution can be modulated to alter the size and shape of the AuNPs as they grow on the substrate. We also showed that one-step direct surface growth can be used to generate LPRs, constituting a major development for this class of *in situ* growth techniques for engineering plasmonic materials with low optical losses. The benefits of plasmonic nanoparticle patterning and direct engineering of LPRs by *in situ* growth can contribute to the development of more efficient quantitative chemical and biological sensors,[8–10,21] plasmonic catalytic substrates,[22–24] and biomedical platforms,[25–28] offering far-reaching impacts in broad fields.

Section 4.2. Results and Discussion

4.2.1. Stencil fabrication with thermal nanoimprint lithography

The AuNP arrays were fabricated on polydimethylsiloxane (PDMS) substrates following the creation of nanometric chemical patterns following a scalable and versatile soft lithographic method. Specifically, water-processable HPC stencils were prepared *via* thermal nanoimprint lithography (tNIL) as shown in **Figure 4.1A** and applied to direct AuNP growth to specific areas containing a strong chemical reductant.[29–32] Briefly, in the tNIL process, aqueous solutions of

HPC were spin-coated onto the substrate, then the film was placed in contact with a hard PDMS (hPDMS) mold. Pressure was applied to the mold as the substrate was heated above the HPC glass transition temperature (140 °C), generating patterned holes shaped by the mold. UV-ozone treatment of the underlying PDMS substrate was required to facilitate the adhesion of the HPC film, and it was found that a 10 min treatment time gave optimal results (**Figure 4.1 B-D**). The pressure applied to the hPDMS mold was also optimized and the minimum required pressure for uniform imprinting was determined to be 1.0 bar (**Figure 4.1 E-H**).

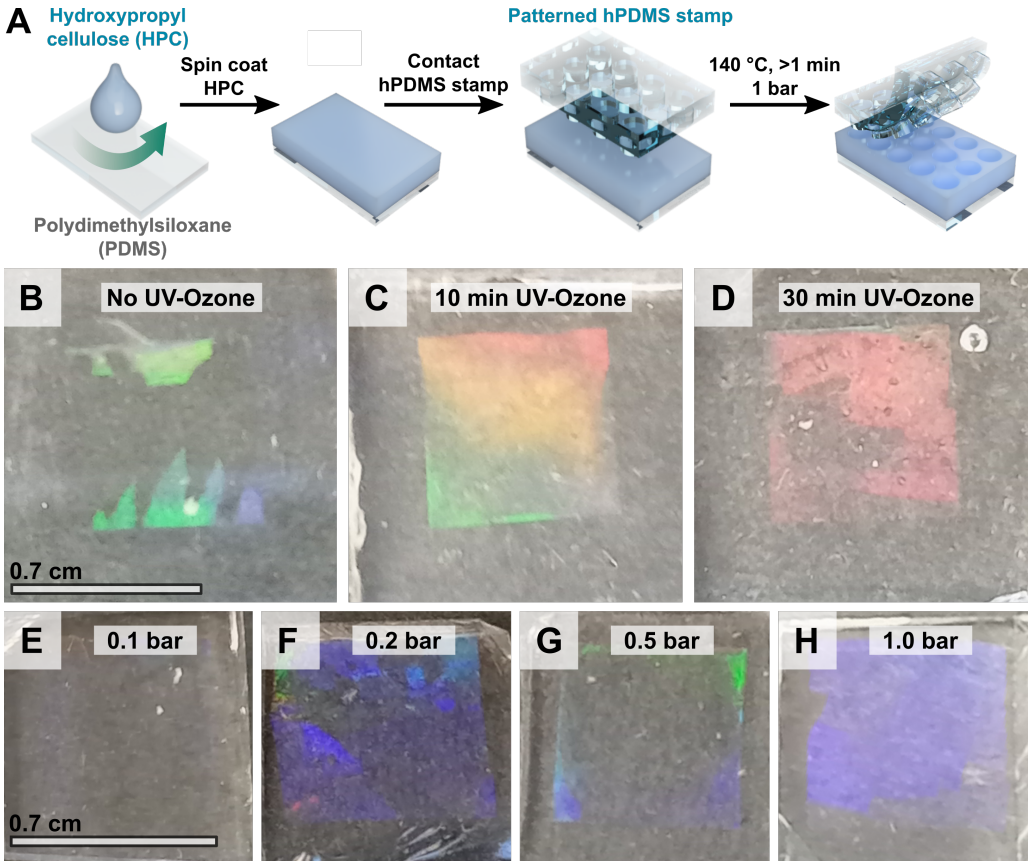

Figure 4.1. A: Schematic of hydroxypropyl cellulose (HPC) thermal nanoimprint lithography on polydimethylsiloxane (PDMS). **B-D:** Digital photographs of patterned HPC films on PDMS with different UV-ozone treatment times. **E-H:** Digital photographs of HPC films patterned using different applied pressures.

The film heights were estimated by comparing the measured and simulated differential refraction spectra for HPC thin films prepared with identical procedures on silicon (**Figure 4.2A**). Overall, high-fidelity patterning of films ranging in height from tens to a few hundred nm (~30-330 nm) was demonstrated (**Figure 4.2B-E**). After t-NIL, the imprinted photonic structures confer iridescence to the patterned films. Successful array transfer was confirmed *via* scanning electron microscopy (SEM) in films as low as ~30 nm (**Figure 4.2F-H**).

This result seems counterintuitive, because normally with t-NIL, uniform patterns are not attainable with HPC volumes that do not match the negative volume of the stamp. The minimum volume requirement is evident when the same HPC formulations were used on a rigid silicon substrate, which gave poor film uniformity apparent by electron microscopy and by visible inspection for films thinner than 330 nm (**Figure 4.2I-N**). The minimum required HPC film height to match the negative volume of the stamps used here were calculated as described in the following section, as corresponding to 250 nm. Electron microscopy analysis shows that the PDMS substrate is imprinted following the t-NIL process (**Figure 4.2O,P**). Therefore, we hypothesize that the key to patterning films nearly an order of magnitude lower in height than the normally required minimum is the implementation of the deformable receiving substrate, which helps to push the HPC into the vacant features as shown in **Figure 4.2Q**.[33–36]

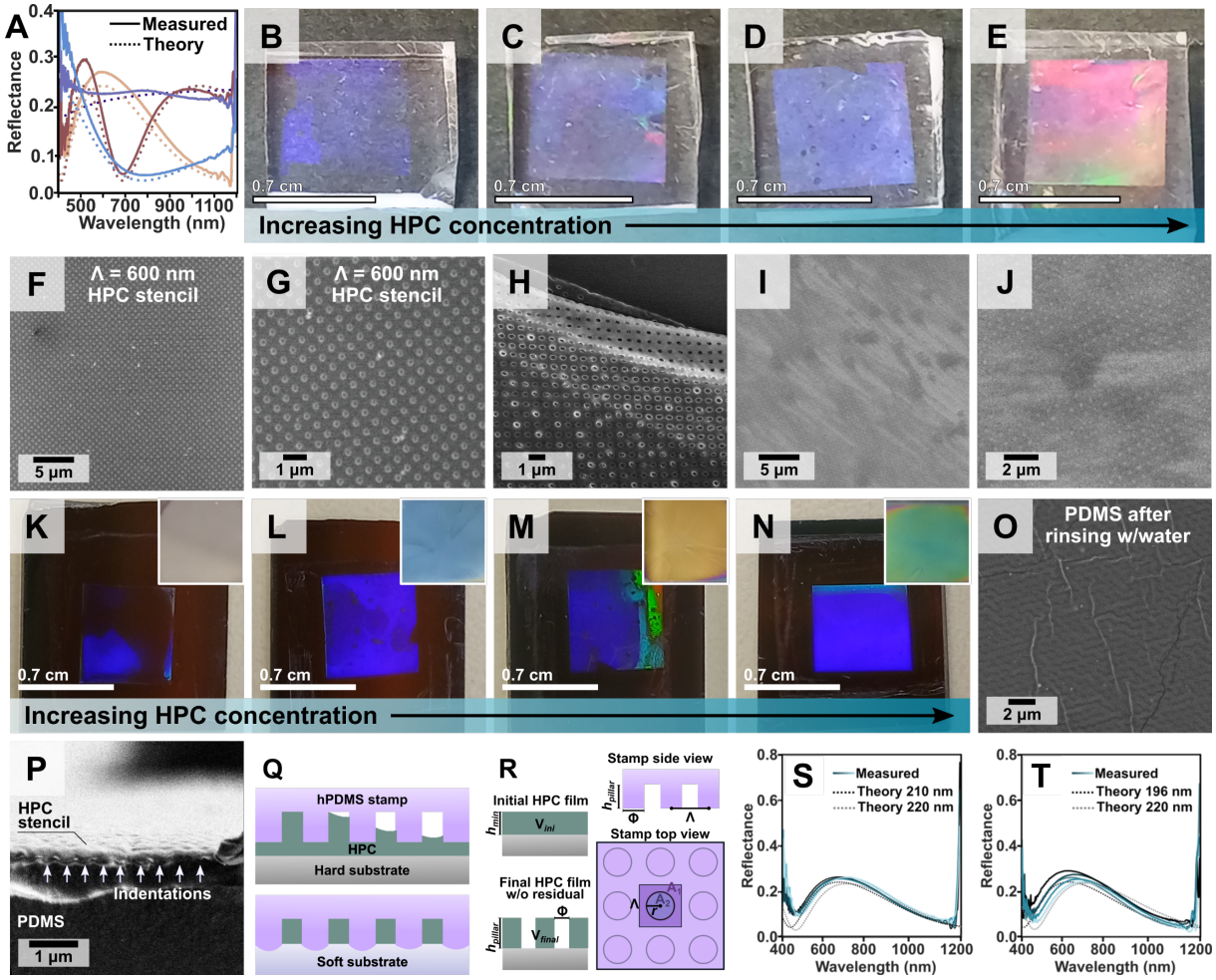

Figure 4.2. A: Reflectance spectra giving the estimated thickness of the films on silicon: 30 nm (solid purple), 125 nm (solid blue), 192 nm (solid orange) and 330 nm (solid red) for the HPC aqueous solutions at different concentrations. The dotted lines are the corresponding simulated interference generated by differential refraction for thin films with heights of 30 nm (dotted purple), 125 nm (dotted blue), 192 nm (dotted orange), and 330 nm (dotted red). **B-E:** Digital photographs of hydroxypropylcellulose (HPC) films on polydimethylsiloxane (PDMS) following patterning of HPC films with (**B**) 30 nm, (**C**) 125 nm, (**D**) 192 nm, and (**E**) 330 nm height. **F-H:** Scanning electron microscopy images of different areas of the thinnest (30 nm) patterned HPC layer, with **H** showing a region at the edge of the film where holes are clearly visible. **I,J:** Scanning electron microscopy images of the patterned films corresponding to 21 mg/mL, 30 nm on silicon. **K-N:** Digital photographs of HPC films on silicon following patterning of HPC films with (**K**) 30 nm, (**L**) 125 nm, (**M**) 192 nm, and (**N**) 330 nm heights. Inset shows the coloration of the HPC layers on silicon pre-patterning (patterned area is 0.49 cm^2). **S,T:** Reflectance spectra showing height ~5% height variation spot-to-spot on one substrate and ~15% variation sample-to-sample, respectively.

4.2.2. Minimum hydroxypropylcellulose film height calculations

In order to estimate the minimum required height of the HPC film to achieve a volume matching the negative volume of the mold, we will consider different geometrical patterns of the square array hPDMS molds applied here as shown in **Figure 4.2R**. The cavity dimension (Φ) represents the diameter of the pillar feature and the lattice parameter (Λ) indicates the center-to-center distance of the pillars.

Table 4.1 Square pillar array hard polydimethylsiloxane (hPDMS) stamp dimensions and calculated minimum hydroxypropylcellulose (HPC) film thicknesses to meet the volume conservation requirements for the hPDMS stamps used in the manuscript.

Lattice parameter (Λ)	Cavity dimension (Φ)	Feature radius (*r*)	Pillar height (h_{pillar})	Minimum HPC film height (h_{min})
400	230 nm	115 nm	350 nm	259 nm
400	230 nm	115 nm	390 nm	289 nm
500	277 nm	138.5 nm	350 nm	266 nm
500	277 nm	138.5 nm	390 nm	296 nm
600	338 nm	169 nm	350 nm	263 nm
600	338 nm	169 nm	390 nm	293 nm

Therefore, the pillar-to-pillar spacings for the 400, 500, and 600 nm lattices are 170 nm, 223 nm, and 262 nm, respectively. All pillar heights (h_{pillar}) are 390 nm. **Table 4.1** summarizes the features for the silicon masters used to fabricate the hPDMS stamps.

The minimum HPC thickness required to fill the stamp features was estimated here using a previously described method.[32] To meet the volume conservation requirement, the volume of the initial HPC layer ($V_{initial}$) is equal to the final volume of the patterned HPC film (V_{final}). In this case, since the volumes are equal, there should be no excess HPC in the holes as shown in **Figure 4.2R**. The final volume (V_{final}) corresponds to the volume of the negative space surrounding the pillar (or the total volume of the patterned HPC film) which can be calculated as:

$$V_{final} = (V_1 - V_2) = A_1(h_{pillar}) = (\Lambda^2 - A_2)\,(h_{pillar}) = (\Lambda^2 - \pi r^2)\,(h_{pillar}) \qquad \textbf{[Eq. 4.1]}$$

Where V_1 is the volume corresponding to the square area A_1, V_2 is the pillar volume corresponding to area A_2, and r is equal to half the cavity dimension (Φ). The initial volume ($V_{initial}$) of film with minimum starting height (h_{min}) of an unpatterned area equivalent to the square area A_1 indicated in **Figure 4.2R**, is:

$$V_{initial} = \Lambda^2 \cdot h_{min} \qquad \textbf{[Eq. 4.2]}$$

since $V_{initial}$ and V_{final} of the HPC film must be equal, h_{min} can be written as:

$$h_{min} = [(\Lambda^2 - \pi r^2)\,(h_{pillar})]/\Lambda^2 \qquad \textbf{[Eq. 4.3]}$$

Although the height of the hole features in the silicon master giving the pillar hPDMS stamp is 390 nm, the actual pillar height is usually lower. Therefore, minimum film heights were calculated for 390 nm and 350 nm, representing the upper limit and estimated lower limit pillar height values, respectively. The final calculated values for h_{min} are summarized in **Table 4.1**. The minimum required film heights range from ~250 to 295 nm, which matches well with the data in **Figure 4.2**, which show that films with estimated height of 330 nm are uniformly patternable on silicon where the other film heights tested (with estimated thicknesses of 190 nm and below) are not.

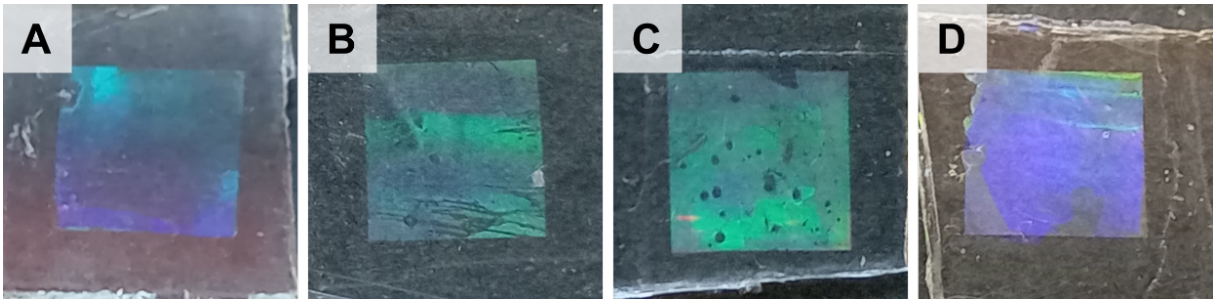

Figure 4.3. A-D: Digital photographs of the hydroxypropylcellulose (HPC) film on glass-supported polydimethylsiloxane (PDMS) patterned with aqueous solutions of HPC giving (**A**) 30 nm, (**B**) 125 nm, (**C**) 192 nm, and (**D**) 330 nm films (patterned area is 0.49 cm^2).

Overall, the spin-coated films gave good reproducibility (**Figure 4.2S,T**). The t-NIL method was used to create patterned HPC films on glass-supported PDMS (**Figure 4.3**). These substrates enabled easier substrate handling during the processing steps required for patterned AuNP growth. Although these substrates cannot undergo extraction of polymethylhydrosiloxane like the free-standing soft PDMS due to delamination from the glass caused by the swelling, an alternative cleaning method was used, and the use of these substrates did not appear to prevent the site-directed growth of the nanoparticles.

The capability to pattern such thin films of HPC has important implications for the thickness of the residual layer. Since ~20 nm of material remains in the imprinted features when performing standard t-NIL on rigid substrates, the removal of the excess material necessitates anisotropic reactive ion etching and cleanroom processing.[31,32] Since we can pattern significantly thinner films, we estimate that the residual layer is accordingly greatly reduced. Consequently, an isotropic UV-ozone etch was used to remove the excess HPC remaining in the holes. The etching procedure was optimized by testing different etch times from 5 s to 2 min (**Figure 4.4,5**). Electron microscopy characterization showed that the films retained the hole patterns after 30 s of etching (**Figure 4.4A-C**). The rate of etching shown in **Figure 4.4D** was estimated by comparing reflectance measurements before and after UV-ozone treatments performed for different durations (**Figure 4.5**). The estimated change in height was around 8 nm/min, and the decreasing film height with increasing etch time can be observed in **Figure 4.4E**. In **Figure 4.4F-I**, we can see that after rinsing with water, the sample etched for 1 min gives reflectance spectra matching the non-UV-ozone treated sample following HPC removal (black and purple line respectively). After 2 min or more of UV-ozone treatment, it was found that a non-water soluble byproduct remained on the silicon (**Figure 4.4G-I**).

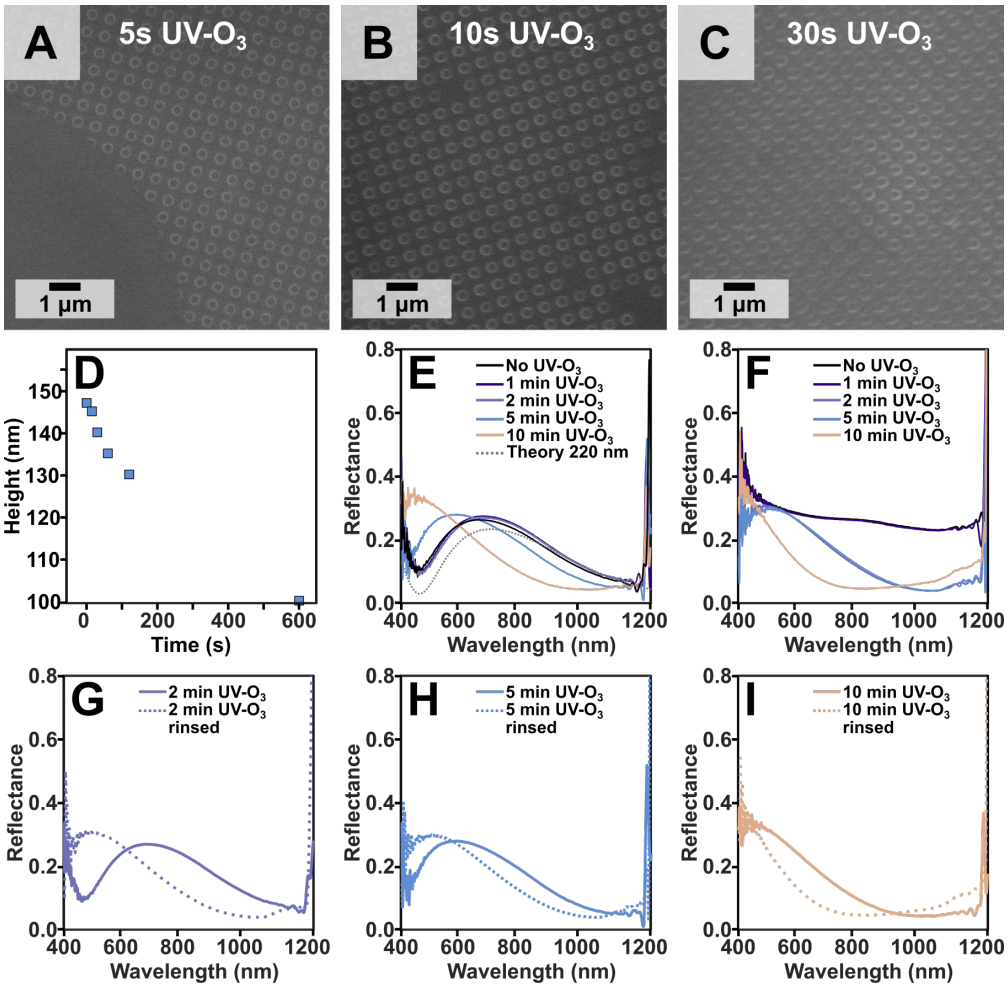

Figure 4.4. A-C: Scanning electron microscopy images of hydroxypropylcellulose (HPC) films on polydimethylsiloxane (PDMS) after (**A**) 5 s, (**B**) 10 s, and (**C**) 30 s ultraviolet (UV)-ozone treatment. **D:** Estimated film height on silicon with increasing UV-ozone treatment time. **E-F**: Reflectance spectra of HPC films on silicon following (**E**) UV-ozone treatment and the substrates following (**F**) rinsing with water. **G-I:** Comparison of the reflectance spectra for UV-ozone-treated films before and after rinsing. The dotted lines in panels **E-I** are the corresponding simulated differential refraction spectra.

The appearance of this non-water soluble byproduct further supports the need for a thin film of HPC. A 20 nm residual would require over 2 min of etch time based on our estimation. Therefore, it is still likely not possible to prepare a stencil from a thick film using a longer UV-ozone etch, even disregarding the effect a longer etching time might have on the pattern features, due to the formation of insoluble byproducts that prevent complete removal of the stencil. Overall, the described procedure enables the reliable fabrication of HPC stencils with nanoscale hole features

(lattice parameter, Λ = 600 nm) without the use of any specialized or costly equipment or cleanroom fabrication.

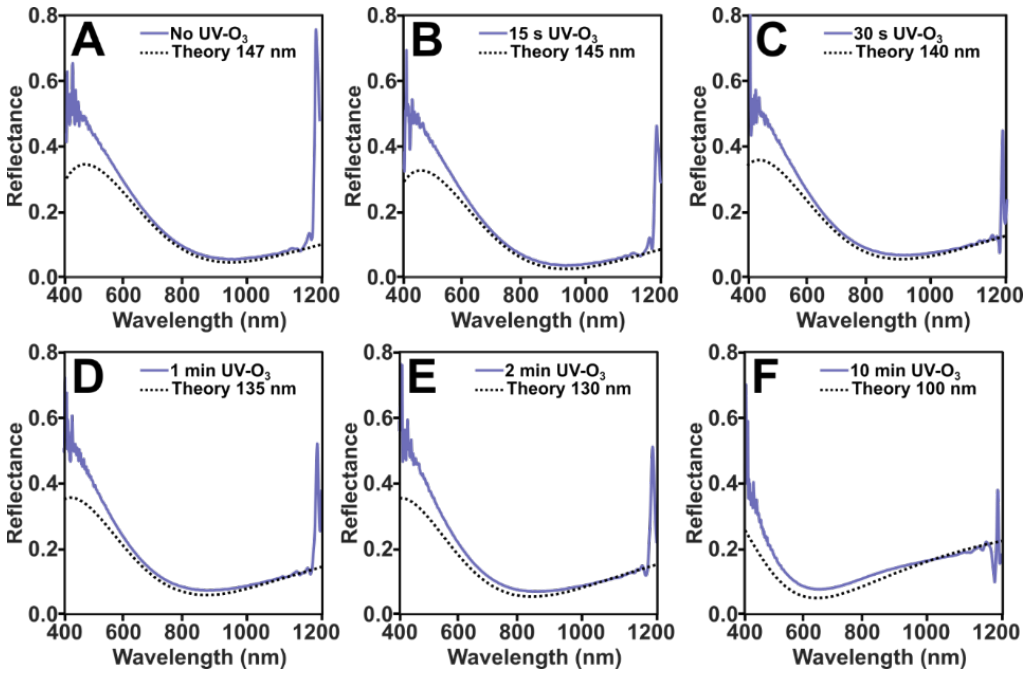

Figure 4.5. Reflectance spectra of a hydroxypropylcellulose (HPC) film on silicon corresponding to the data in panel **D** of **Figure 4.4**. The dotted lines are the corresponding simulated differential refraction spectra.

4.2.3. Ink application and minimization of secondary nucleation

In the next step, the HPC stencils were used for the *in situ* growth of AuNPs into ordered plasmonic arrays as shown in **Figure 4.6A**: following the 30 s UV-ozone etch, the polymethylhydrosiloxane chemical ink was applied on top of the stencil (**Figure 4.6A**). Then, the HPC stencil was dissolved in water, and the chemically patterned substrate was dried with an air gun. Finally, a fixed volume (150 μL) of AuNP growth solution containing capping ligands, a mild reducing agent, and a gold inorganic precursor (tetrachloroauric acid, $HAuCl_4$) was spread on the surface and was allowed to react for 10 min with the physisorbed ink.

Reducing the competition between nuclei formation on the substrate and nucleation in the growth solution is crucial for successful *in situ* growth into patterns and for fundamental *in situ* size- and shape-control.[18,20,37–39] In standard colloidal AuNP seed-mediated synthesis, the nucleation and growth steps are spatiotemporally separated to control the final particle morphology.[40,41] First, small gold nuclei (also known as seeds) are uniformly grown and later added to a separate solution where they grow in a controlled manner into desired sizes and geometries. The nucleation step normally incorporates a strong reductant such as sodium borohydride for the fast, uniform formation of seeds from the gold precursor. The following growth step instead includes weaker reductants, such as ascorbic acid, capable of reducing Au^{3+} to Au^{1+}, but confining the final reduction to Au^{0} to the seed surface, promoting controlled growth. The seed-mediated synthesis scheme ensures suppression of later secondary nucleation events from occurring in the growth solution that would negatively affect size distribution and shape yield.[40,42]

One of the most important aspects explored here is the limitation and control of secondary nucleation, which has proven to be a particularly difficult challenge for *in situ* growth systems.[18,20,28,43] Here, the strong reductant ink is applied only on the substrate to mimic the spatially selective nucleation and growth processes used in colloidal synthesis, while the mild reductant ascorbic acid is added to the growth medium to facilitate the first reduction step of the gold salt from Au^{3+} to Au^{1+}. Although in our *in situ* growth scheme, we are only providing strong reductants on the surface of the substrate, colloidal AuNPs can still spontaneously form from the precursors in the growth solution. Thus, secondary nucleation for *in situ* systems can be described as the uncontrolled formation of nuclei away from sites explicitly containing the strong reductant,

which contributes to irreproducible consumption of reagents and solution-deposited AuNPs outside the pattern (**Figure 4.6B**).

Even though nucleation can be achieved with the sole use of the physisorbed ink, our motivation behind adding ascorbic acid is to reduce the growth time and to use lower concentrations of gold precursor.[37,44,45] In fact, works using only a surface-bound strong reductant usually require ~5 times more gold salt and hours- to days-long incubation.[46–48] Continuing with the goal of limiting secondary nucleation, we identified factors that could lead to the undesired spontaneous formation of colloids: (i) the presence of impurities in the growth solution, (ii) growth rate, and (iii) excess ink leeching into solution. Regarding impurities, the water source is known to play an important role in colloidal synthesis, especially for the synthesis of anisotropic particles.[49,50] Recent work shows that faster growth kinetics can favor colloidal nucleation over nucleation on the substrate.[20] Therefore, we modulated the rate of the reaction by changing the type and concentration of the surfactant (*i.e.,* cetyltrimethylammonium chloride or bromide, CTAC or CTAB, respectively). Lastly, we tested different inking methods and ink concentrations.The appearance of LSPR peaks evaluated by ultraviolet-visible spectroscopy indicated the occurrence of secondary nucleation, and the maximum intensity of the peaks was monitored over 15 min to track the severity of unwanted nuclei formation under different growth conditions (**Figure 4.6C-S**). Overall, growth solutions containing high-performance liquid chromatography (HPLC) grade water, and 25-50 mM CTAB gave the least secondary nucleation (**Figure 4.6R**).

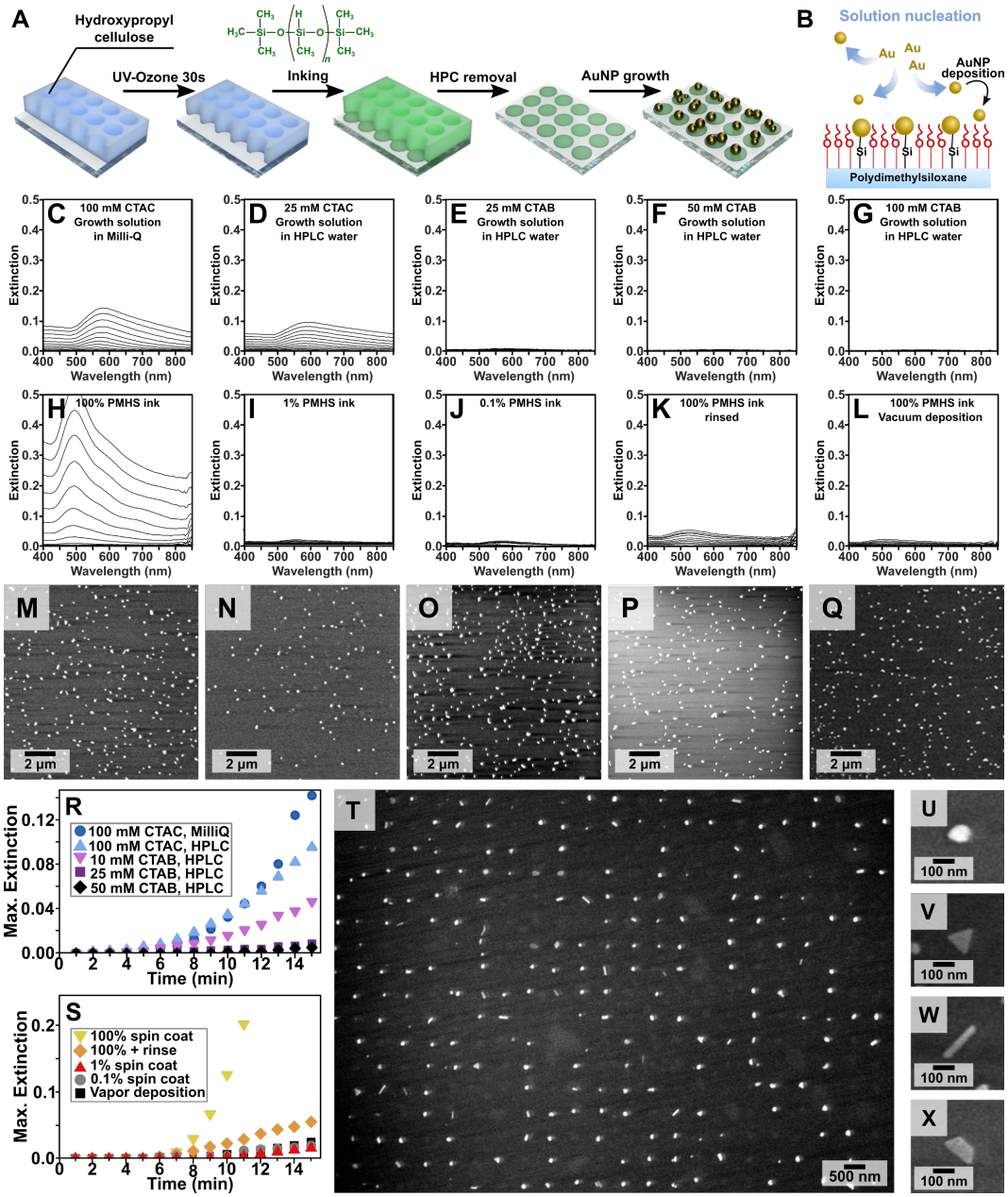

Figure 4.6. A: Schematic of the etching of the residual layer with ultraviolet (UV)-ozone, inking with polymethylhydrosiloxane (PMHS), removal of the hydroxypropyl cellulose (HPC) with water, and introduction of the growth solution to form gold nanoparticles (AuNPs). **B**: Schematic depicting competition between secondary solution nucleation and surface growth. **C-L:** Extinction spectra of the growth solutions over 15 min under different conditions. **M-Q**: Scanning electron microscopy (SEM) images of the substrate showing the formation of AuNPs following the corresponding inking strategies in panels **H-L**. **R,S:** Maximum extinction of growth solutions containing different (**R**) water sources (Milli-Q or high-performance liquid chromatography (HPLC) water) and surfactant conditions and (**S**) with different inking conditions. **T:** SEM image showing the patterned array after 10 min growth. **U-X:** SEM images showing common products: (**U**) spheres, (**V**) triangles, (**W**) rods, and (**X**) platelets/truncated triangles. CTAB/C = cetrimonium bromide/chloride.

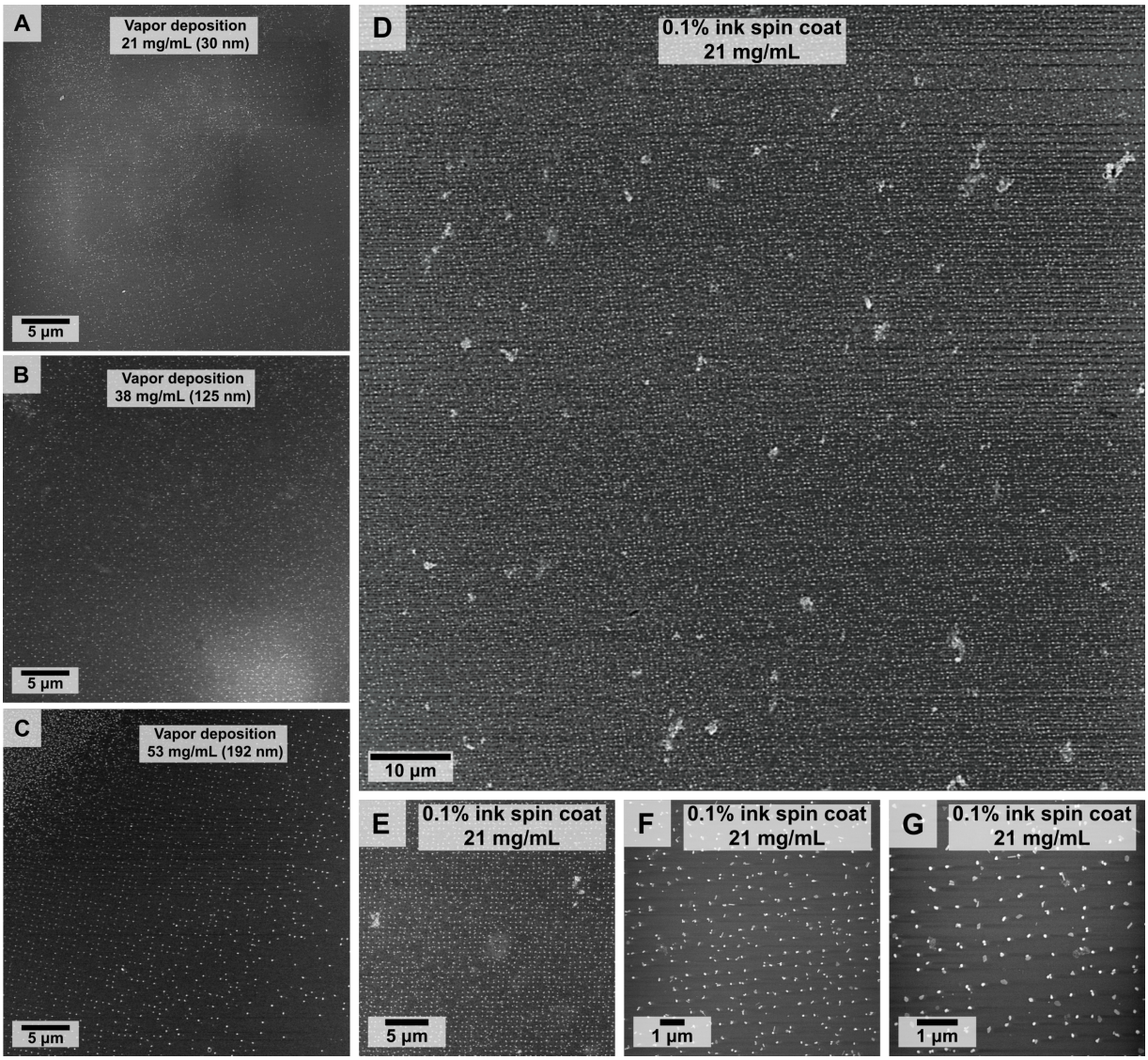

Figure 4.7. A-C: Additional scanning electron microscopy images at lower magnification for arrays prepared from hydroxypropylcellulose (HPC) films on polydimethylsiloxane made with (**A**) 21 mg/mL, (**B**) 38 mg/mL and (**C**) 53 mg/mL. **D-G:** Additional scanning electron microscopy images of gold nanoparticles patterned using the 38 mg/mL solution and spin coat of 0.1% of polymethylhydrosiloxane ink in hexane.

This optimized growth formulation was fixed and the application of chemical ink *via* different routes was tested. Aside from vapor deposition, the least amount of secondary nucleation was observed when dilute (1% or 0.1%) solutions of the ink were spin coated onto the substrate (**Figure 4.6S**). Spin coating dependably produced patterns, and all conditions appeared to give similar nucleation site densities (**Figure 4.6T, Figure 4.7**). Therefore, the 0.1% solution was selected for

the following sections. After 10 min of growth, the products appeared to give variable morphologies, including spheres, triangles, rods, and other platelets as shown in **Figure 4.6U-X**.

Control experiments showed that the HPC stencil retains its features after application of the ink (**Figure 4.8A**). Negative controls of films that were treated with 10 s UV-ozone etch prior to application of the ink did not reliably give patterned AuNP arrays (**Figure 4.8B**). This observation substantiates the assumption that the residual layer, although minimized, is not necessarily completely avoided. If the ink is applied while a residual layer is still present, the removal of the HPC will completely remove the ink as well. Moreover, when ink was not applied to the HPC stencils, patterned growth did not occur as shown in (**Figure 4.8C**), but some large particles are observed on the substrate, probably resulting from secondary nucleation**.**

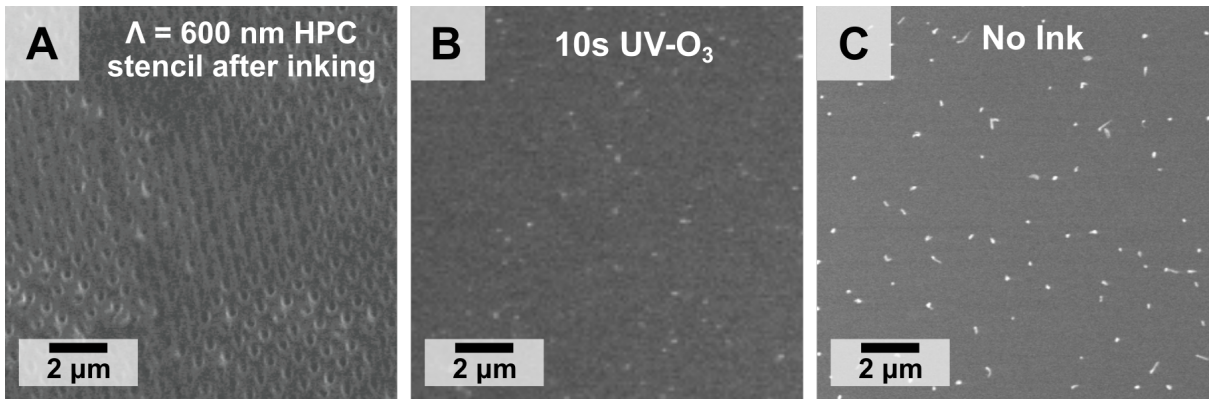

Figure 4.8. Scanning electron microscopy images of the patterned hydroxypropylcellulose (HPC) film (1g HPC stock + 10 mL water) (**A**) after inking, the polydimethylsiloxane PDMS following the *in situ* nanoparticle growth procedure with (**B**) only 10 s of ultraviolet (UV)-ozone treatment and (**C**) following the procedure without applying any chemical ink.

The requirement of HPC films with volume lower than the negative volume of the stamp for successful patterning is further supported by the observation that only films ranging from 30-192 nm gave successfully patterned gold nanoparticle arrays (**Figure 4.9**). The 330 nm film with volume higher than the negative volume of the stamp did not produce arrays, suggesting that

the 30 s UV-ozone etch was insufficient at removing the residual material in the hole features. Ultimately, following optimization, patterned AuNP growth into patterned arrays (~0.5 mm^2 area) was achieved and the grown AuNPs are mechanically stable and remain on the substrate after thorough rinsing and drying steps. In the next section, we explore size and shape-modification of the products.

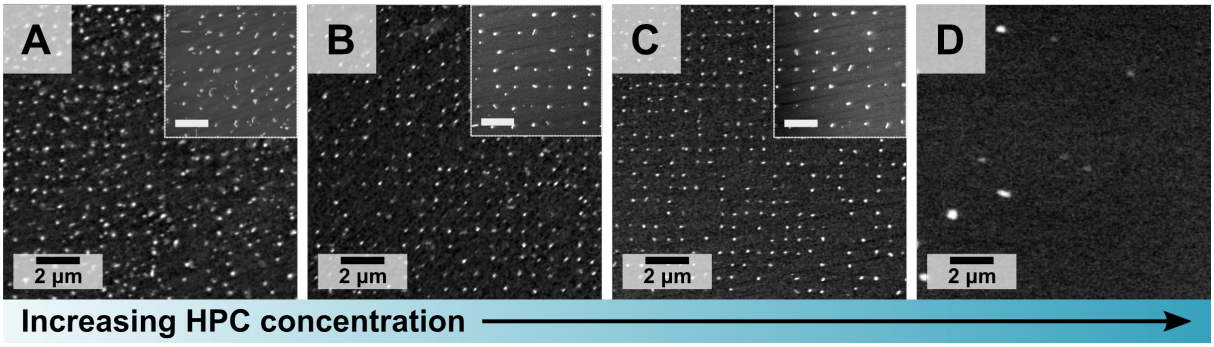

Figure 4.9. A-D: Scanning electron microscope images of the substrates following removal of the hydroxypropylcellulose (HPC) stencil and nanoparticle growth for stencils made from (**B**) 30 nm, (**C**) 125 nm, (**D**) 192 nm, and (**E**) 330 nm initial thickness HPC films (inset scale bar: 500 nm). Brightness and contrast were adjusted to the same levels to facilitate comparison.

4.2.4. *In situ* size and shape modification

Although few prior works have studied mechanistic aspects of substrate-grown particles,[18–20,39,51–53] fundamentals of *in situ* growth remain vastly unexplored compared to colloidal batch systems.[44] Limiting the growth-active areas to diameters < 100 nm has the potential to enable much tighter control over both nucleation and growth conditions. The level of control we achieve over the patterning was leveraged to demonstrate the modulation of size and morphology of the synthesized AuNPs by modifying the growth medium parameters using concepts derived from colloidal synthesis.

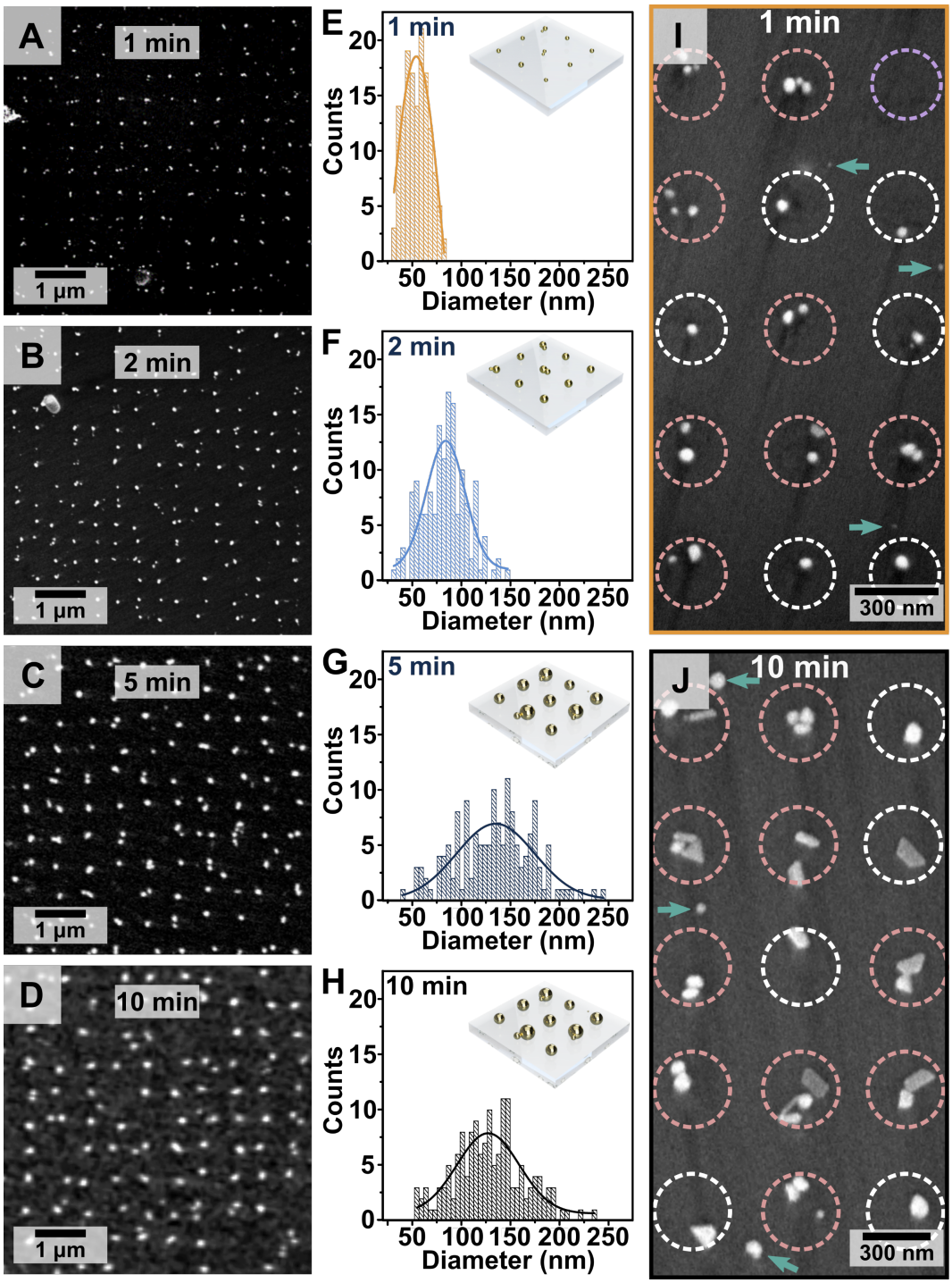

Figure 4.10. A-D: Scanning electron microscopy (SEM) images of patterned nanoparticle substrates after (**A**) 1 min, (**B**) 2 min, (**C**) 5 min, and (**D**) 10 min. **E-H:** Size distributions for the (**E**) 1 min, (**F**) 2 min, (**G**) 5 min, and (**H**) 10 min samples (150 nanoparticles each). **I-J:** Representative SEM images showing pattern yield and common defects: multiple particles per area (*pink circles*), vacancies (*purple circles*) and particles outside the pattern (*green areas*). Patterned regions with single particles are indicated with a white circle.

One unique opportunity for *in situ* growth schemes is the ability to straightforwardly adjust growth time by removing the solution containing nanoparticle precursors from the substrate, therefore arresting growth and regulating AuNP size.[53] Here, the growth times were tuned from 1 min to 10 min using an optimized growth solution (**Figure 4.10A-D**, see Materials and Methods section for details). After 1 min of growth, the average AuNP size already reaches 40 ± 14 nm (**Figure 4.10E**), which is relatively fast compared to colloidal synthesis.[54–56] At 2 min, the products nearly double in size to 70 ± 30 nm (**Figure 4.10F**). Growth times of 5 and 10 min result in similar diameters (120 ± 40 nm and 110 ± 40 nm, respectively, **Figure 4.10G,H**). This behavior is consistent with other *in situ* growth studies.[43,57-59] Along with a change in the average diameter, longer growth times were associated with the appearance of higher percentages of anisotropic products (estimated at ~40% at 10 min vs. 10% at 1 min, **Table 4.2, Figure 4.11**). After 5 min, the AuNPs formed at the specified nucleation sites no longer increase in size, possibly due to the onset of secondary nucleation effects.

Table 4.2. Summary of products observed at different growth times.

Growth time (min)	**1**	**2**	**5**	**10**
Total # of particles counted	255	328	329	201
% platelet	3.9	2.7	2.7	24.4
% sphere	88.2	82.0	82.4	57.2
% rod	6.3	11.3	12.5	15.9
% unclear	1.6	4.0	2.4	2.5
% total anisotropic	10.2	14.0	15.2	40.3
% total platelets and spheres	92.2	84.8	85.1	81.6

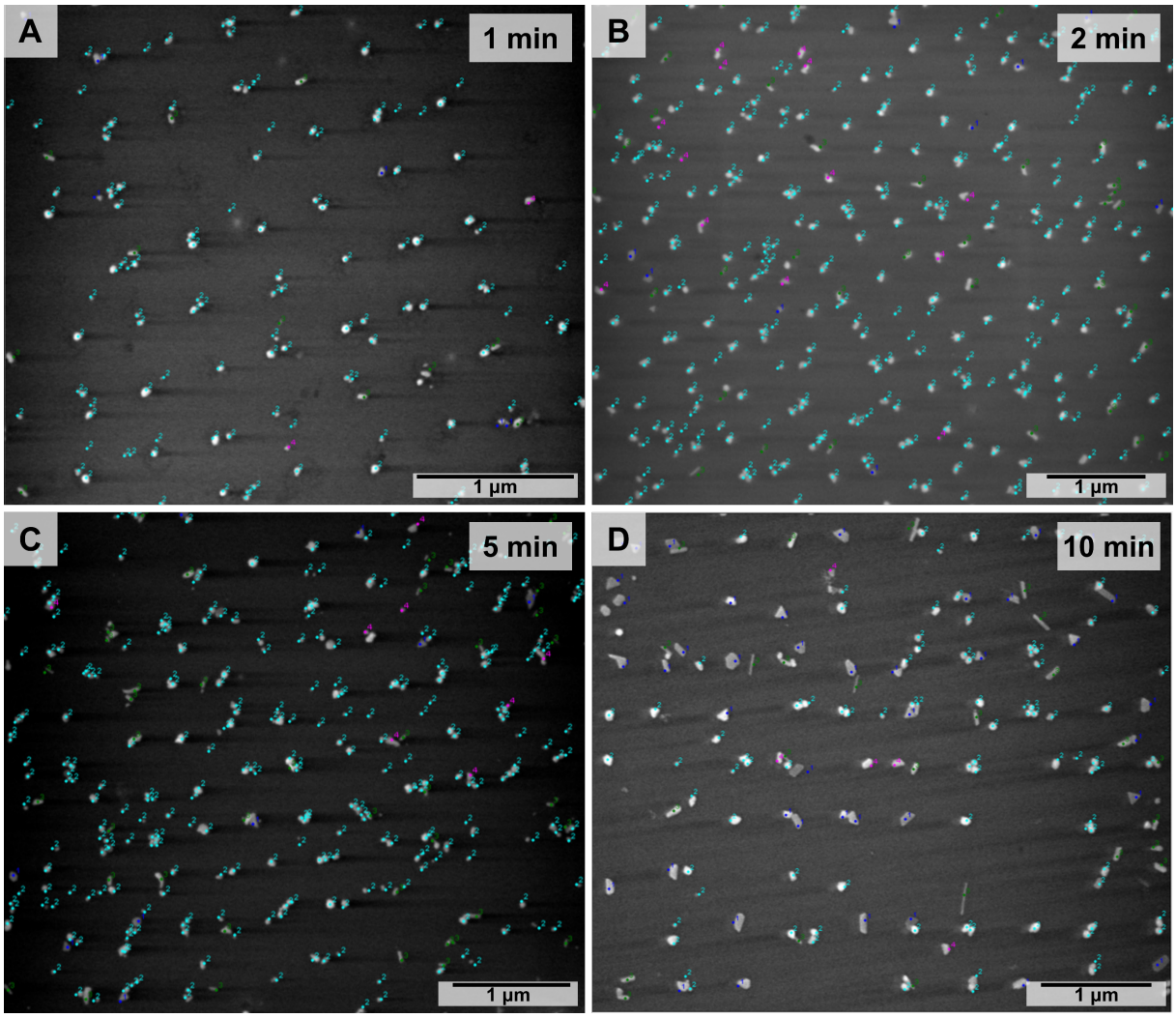

Figure 4.11. Scanning electron microscopy images showing how the number of platelets (dark blue, 1), spheres (light blue, 2), and rods (green, 3) were estimated. Particles with morphologies that could not be determined are indicated in pink (4).

4.2.4.1. Evaluation of patterning yield

Regarding patterning evaluation, various kinds of defects in the arrays can be observed (**Figure 4.10I-J, 4.12**). Standard defects include vacancies (*purple circles*), multiple AuNPs per region (*pink circles*), and AuNPs outside the patterned region (*green arrows*). The patterning yield was evaluated as the percentage of ink-containing regions that produced nanoparticles across all growth times as ~80% (n=5, detailed evaluation summarized in **Figure 4.12, Table 4.3**).

Table 4.3. Characterization of patterning yield across growth times

Growth time (min)	1	2	5	10	TOTAL
Total # of particles counted (including outside pattern)	247	212	279	203	**941**
% pattern yield (% non-empty)	89.6	61.7	97.4	83.8	**83 ± 15**
% single	19.4	35.4	10.3	23.0	**22 ± 10**
% multiple	76.1	54.4	78.9	63.2	**68 ± 12**
% nanoparticles in pattern	95.5	87.7	89.2	86.2	**90 ± 4**
Average # of particles/region	2.0 ± 1.0	1.5 ± 0.6	2.2 ± 1.0	1.8 ± 0.9	**1.8 ± 0.9**

Interestingly, the total percentage of nanoparticles located within the growth active regions was estimated to be ~90%, indicating a strong preference for nucleation and growth within the pattern features due to the chemical contrast created by the presence and absence of the ink . Although the patterned features are much larger than the grown AuNPs, the average number of nuclei per patterned area is similar across all growth times and corresponds to 1.8 ± 0.9 AuNPs per area (not counting vacancies). This is an important observation because it shows that once the initial nuclei are formed, their growth is favored over the later formation of new nuclei. Moreover, this statistic gives us an estimate of the number of particles on each substrate as approximately ~$2x10^8$ particles/substrate, or ~$2x10^9$ AuNPs/mL of growth solution (assuming 100% yield of the t-NIL and ink patterning). The seed concentration in colloidal synthesis is usually 2-4 orders of magnitude higher (typical values for colloidal synthesis range between 10^{11} and 10^{13} seeds/mL of growth solution), giving us a much higher $HAuCl_4$ to AuNP ratio.[49,56] This result provides an explanation for the speed of growth and offers possible improvements to target smaller nanoparticles and/or slower kinetics. Evaluation of patterning yield in **Table 4.3**, indicates that the percentage of AuNPs outside the pattern increases between 5 and 10 min, supporting our earlier hypothesis that the effects of secondary nucleation increase after 5 min.

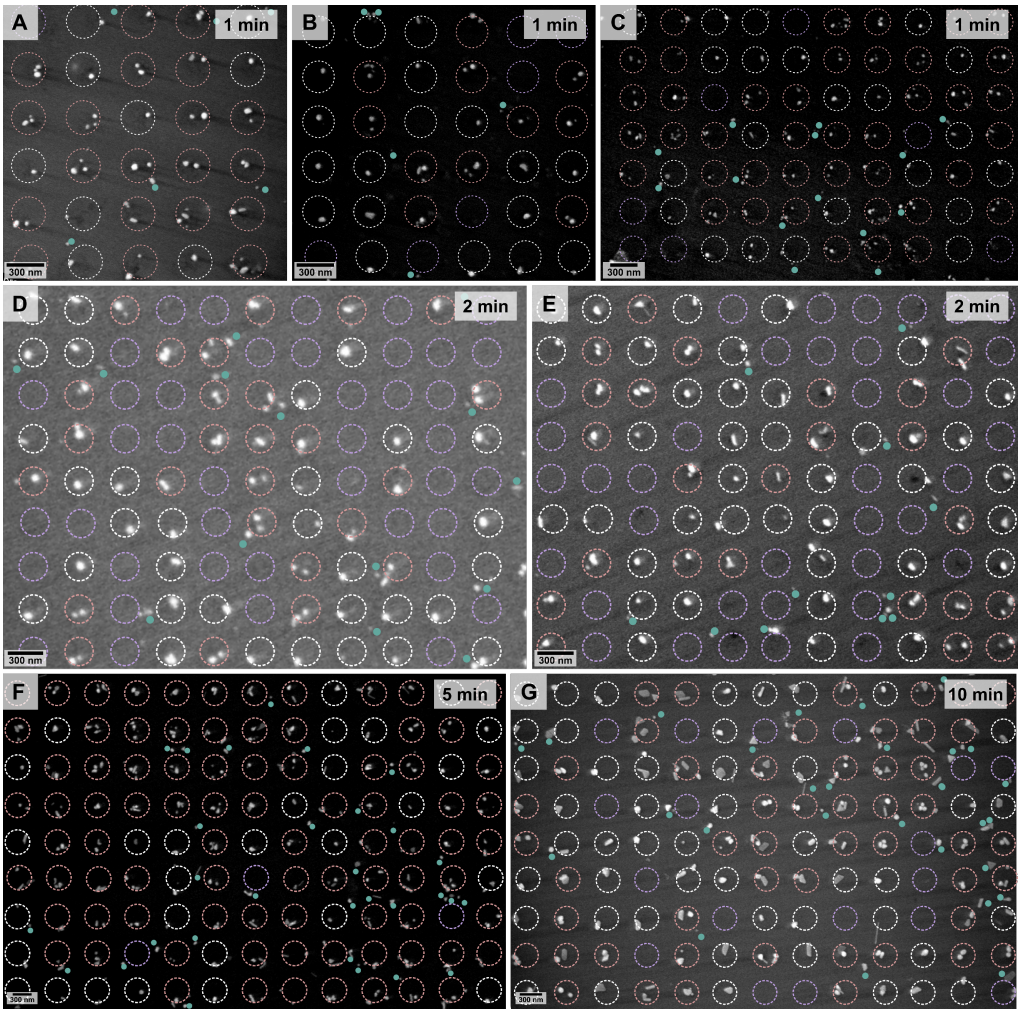

Figure 4.12. A-G: Scanning electron microscopy images from which patterning yield was calculated. For each time condition, enough images were analyzed so that at least 150 gold nanoparticles were counted (n=5). Pink circles represent regions with multiple nanoparticles, white circles represent areas with single particles, purple circles indicate vacancies, and green dots are used to indicate out-of-pattern nanoparticles.

4.2.4.2. Shape modification

Next, we modify the chemical environment so that the AuNP morphology is modulated directly on the substrate. Here, we target overgrowth into branched nanostars, which are attractive due to high localization of electromagnetic fields present at their sharp tips, their high extinction in the near-infrared biological window, and their capability for thermoplasmonic heating.[28,60] Nanosphere arrays were overgrown by subsequent incubation in a nanostar growth solution

containing additional gold precursor and shape-directing reagents (silver nitrate, laurylsulfobetaine, hydrochloric acid, and ascorbic acid, **Figure 4.13A**). Similar to the first growth step, synthetic conditions were optimized to minimize secondary nucleation away from the substrate within the 5 min overgrowth time by lowering the pH of the growth medium, which limits the reducing strength of ascorbic acid.[28] Following the overgrowth step, the substrate exhibited a change in color from red to dark blue. The extinction spectra after 5 min of nanosphere growth gives one dominant LSPR dip at 575 nm, and the samples following 5 min of nanostar overgrowth exhibit high extinction in the near infrared region at 985 nm, matching the expected plasmonic response **Figure 4.13B**.[28] The corresponding colloid recipe for the one used here generally results in three main products: spheres, and low and high aspect ratio nanostars.[28,60] However, electron microscopy characterization interestingly showed a high yield of one major, highly branched product (**Figure 4.13C,D**). The yield of the nanostar arrays over a larger area (measuring a *ca.* 2000 μm^2) can be appreciated in **Figure 4.13E**. Altogether, the data presented in **Figure 4.13** indicate that although certain concepts might transfer from colloidal to substrate growth (*e.g.,* applying shape-directing reagents to promote anisotropic growth), important differences remain between the two environments that can significantly affect the shapes of the final products. The *in situ* surface growth strategy reported here represents an ideal platform for the exploration of such effects.[28]

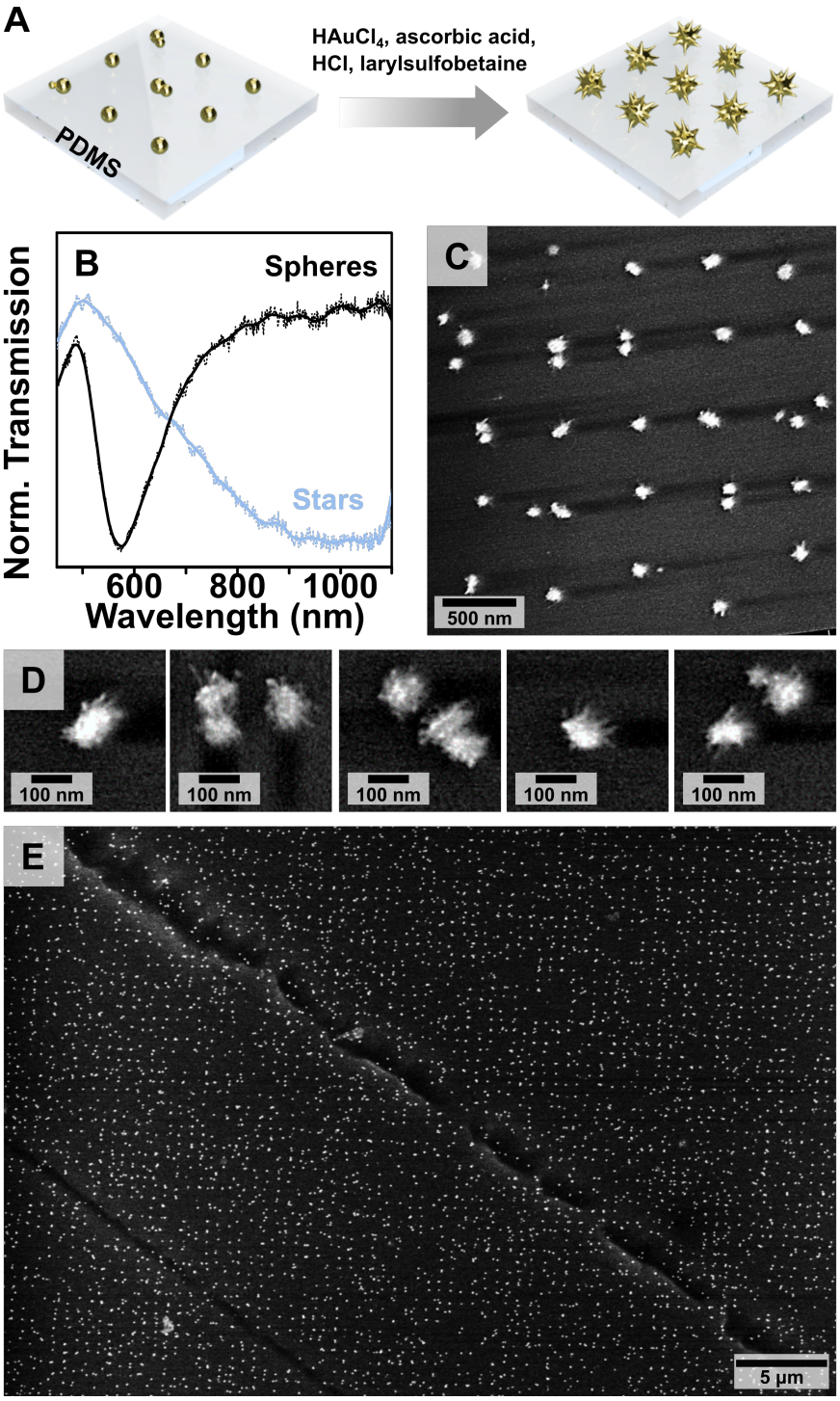

Figure 4.13. A: Schematic of overgrowth process into nanostars on polydimethylsiloxane (PDMS). **B:** Normalized transmission spectra comparing the plasmon band position before (spheres) and after (stars) overgrowth. **C-E:** Scanning electron microscopy images of the nanostar arrays at different magnifications.

4.2.5. Lattice plasmon resonance characterization

Perhaps the most striking advantage of combining t-NIL and *in situ* growth resides in the preparation of ordered plasmonic arrays with arbitrary geometries, achieving control at the same time over both LSPRs and LPRs.[29–32] Although past and recent work proposed this possibility in relation to other *in situ* growth schemes, LPRs have not previously been demonstrated experimentally using only direct surface growth.[14–17] The spatial and geometrical constraints of the state-of-the-art methods prevent engineering LPRs (as well as more complex light-matter interactions),[61–63] limiting the application of *in situ* growth for the design of metasurfaces and intricate plasmonic systems. Our *in situ* growth approach overcomes two major barriers, namely the requirement for lengthy self-assembly steps and the flexibility in array periodicity by modifying the hPDMS stamp.[32] Here, we measure LPRs for arrays with lattice parameters (Λ) of 400 and 500 nm, in addition to the Λ=600 nm samples (**Figures 4.14,15,** and **16**, respectively). Patterned *in situ* growth was achieved in all cases.

With the intention of maximizing the generation of lattice resonances through far-field coupling between the plasmonic units of the array, the AuNPs were covered with a thin layer of soft PDMS after growth was complete. This step ensures a uniform refractive index environment around the plasmonic lattices, facilitating the propagation of the scattered field within the lattice plane.[2] Sharp LPRs were observed in the transmission profile under this refractive index matching condition (**Figure 4.17G-J**),[2,64] giving, to the best of our knowledge, the first demonstration of LPRs *via* a purely *in situ* synthetic route, all without batch synthesis, self-assembly, top-down fabrication, nor costly and specialized equipment. Overall, this promising result shows that further developments in *in situ* growth offers an inexpensive, simple, and rapid alternative for accessing plasmonic responses on par with those engineered by top-down methodologies.

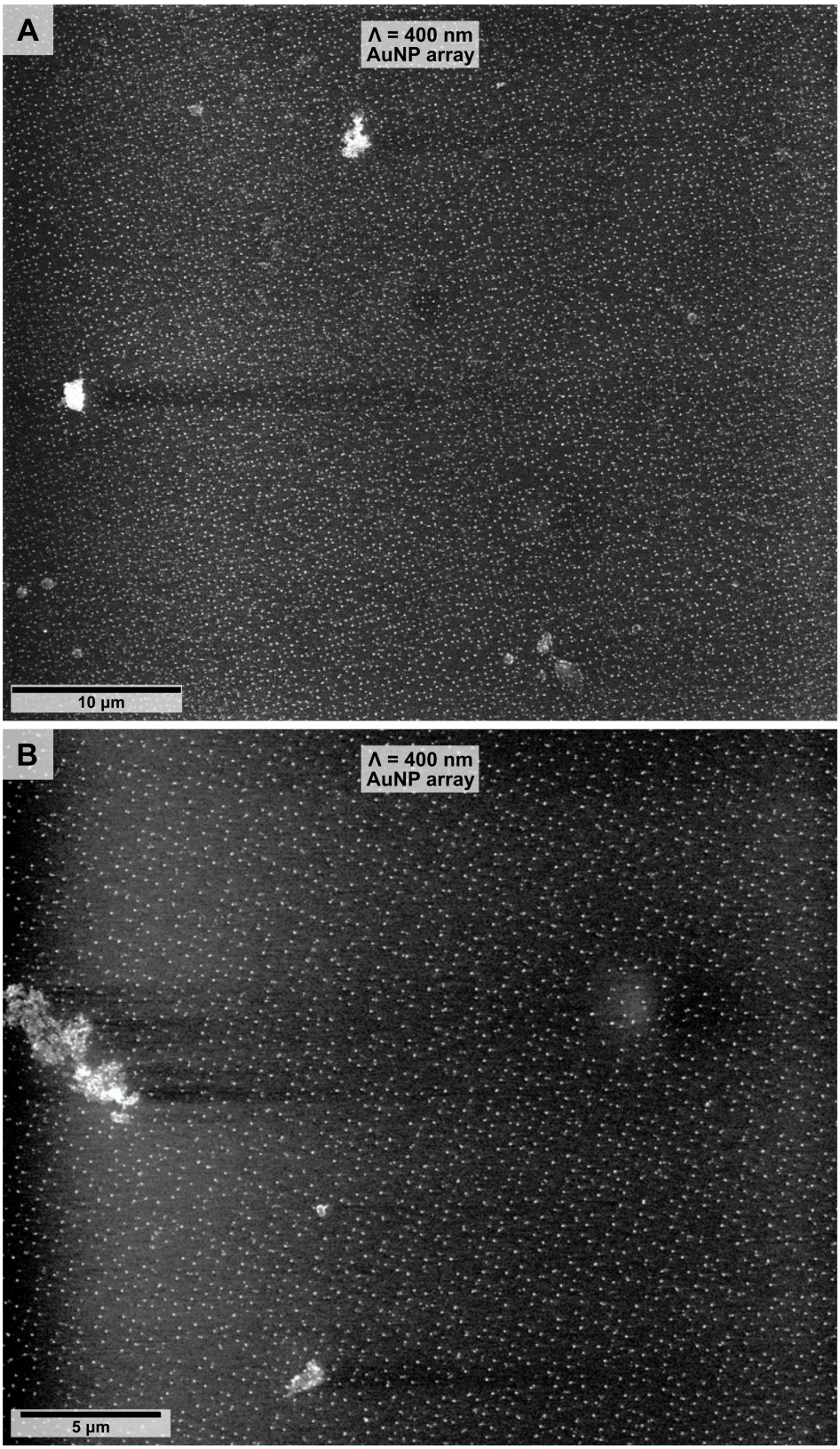

Figure 4.14. Scanning electron microscopy images of the Λ = 400 nm array.

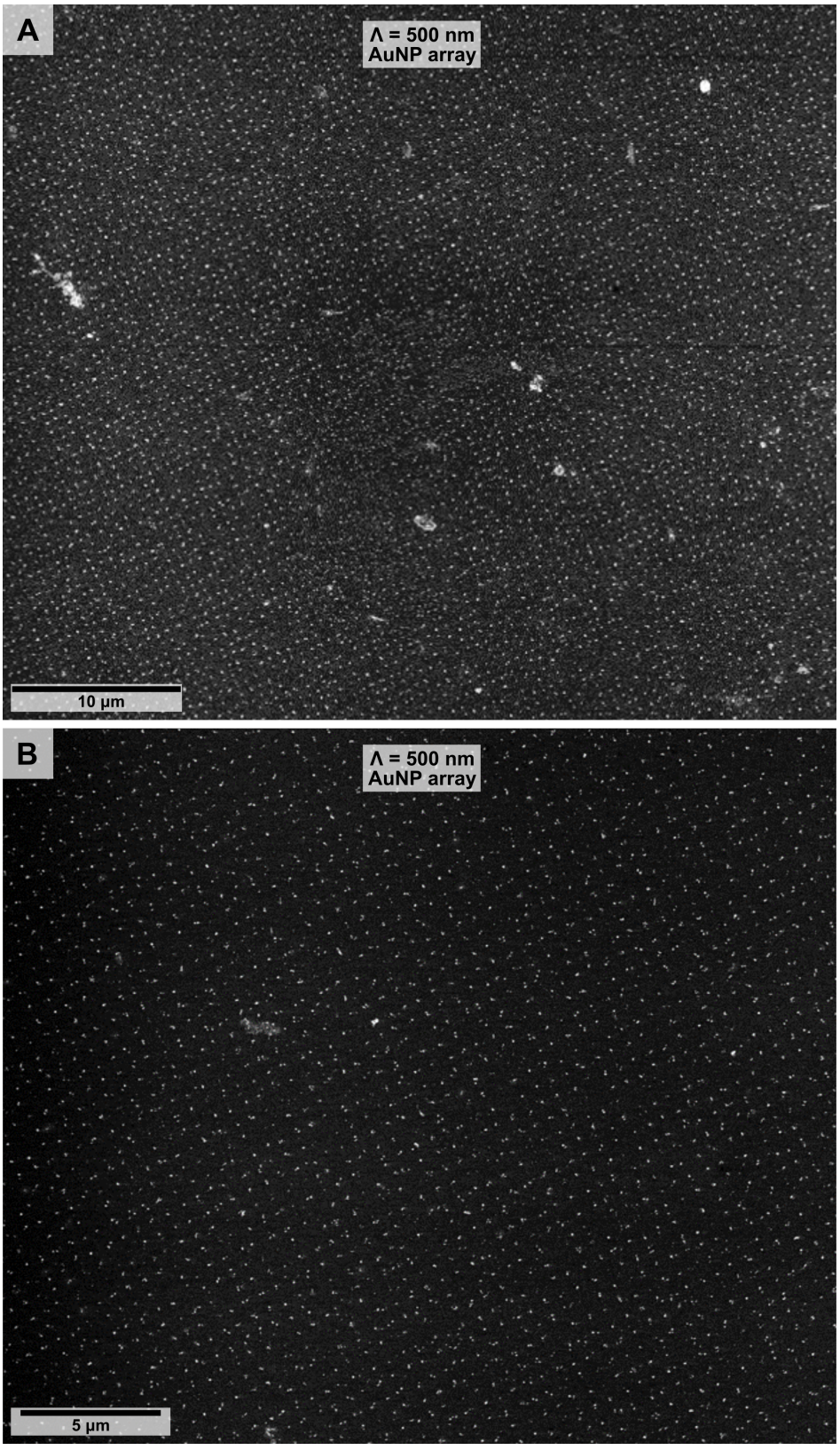

Figure 4.15. Scanning electron microscopy images of the Λ = 500 nm array.

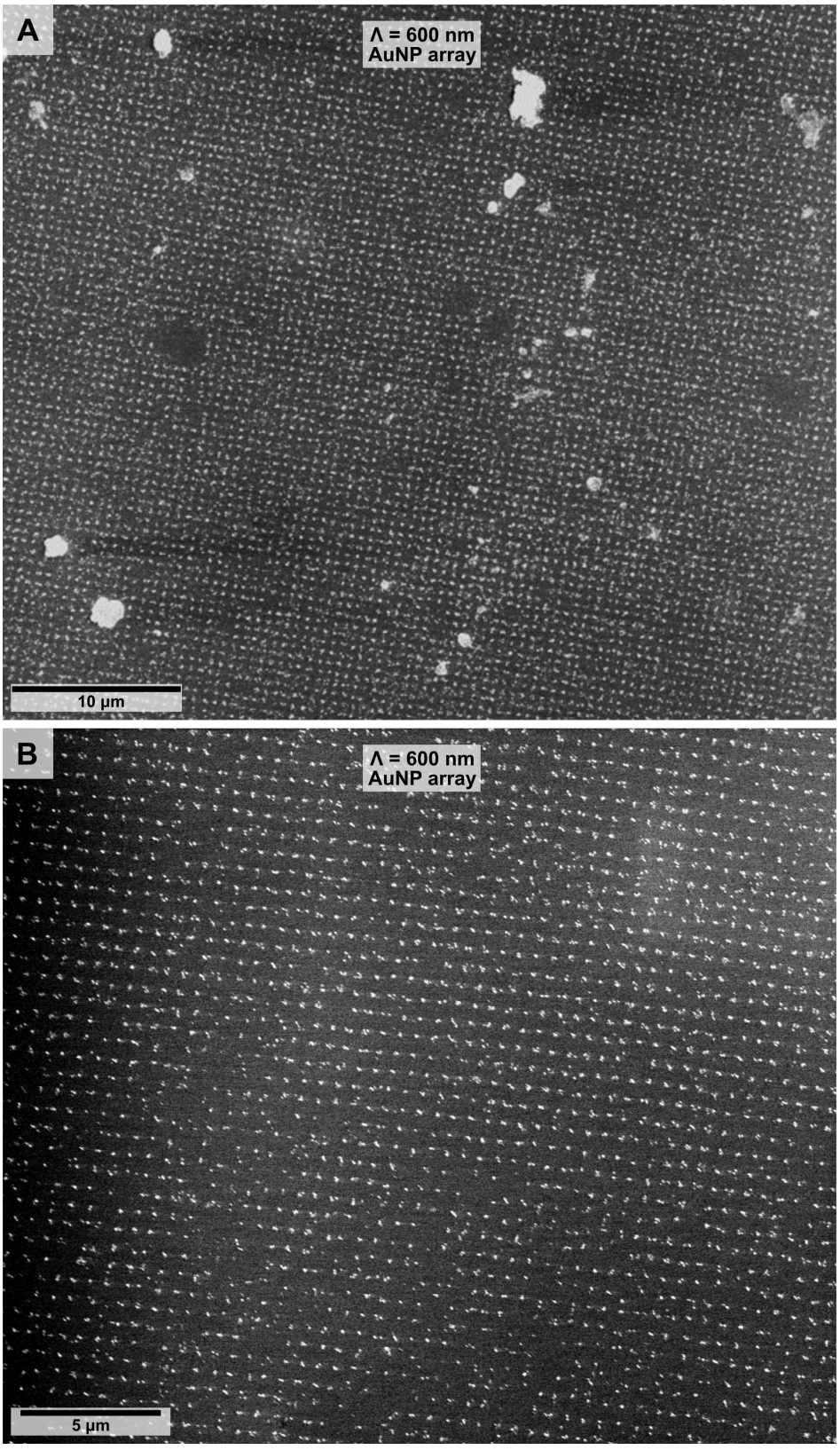

Figure 4.16. Scanning electron microscopy images of the Λ = 600 nm array.

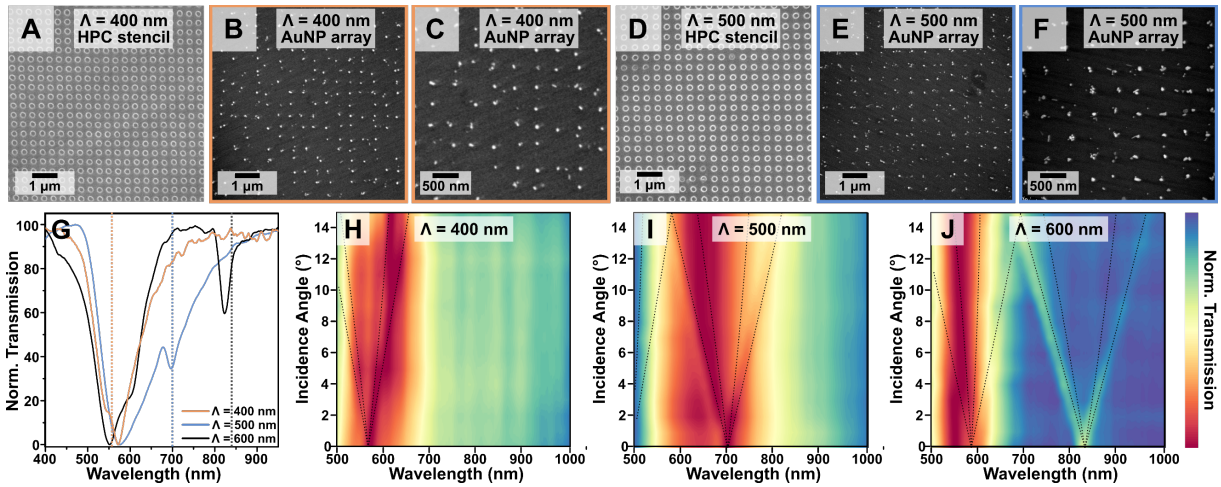

Figure 4.17. Scanning electron microscope (SEM) images showing **A:** patterned hydroxypropyl cellulose (HPC) films with lattice parameter Λ = 400 nm and **B,C:** the resulting patterned nanoparticle substrates. Images showing the **D:** an Λ = 500 nm stencil and **E,F:** the corresponding patterned nanoparticles (SEM data for the Λ = 600 nm HPC stencils and resulting AuNP arrays are shown in **Figure 4.2,6**). **G:** Smoothed and normalized transmission spectra of the substrates following refractive index matching. Dashed lines represent the theoretical position of Rayleigh-Wood anomalies (n_{PDMS}=1.4). **H-J:** Contour plots showing measured angular dependence of the optical response optima for the (**H**) Λ = 400 nm, (**I**) Λ = 500 nm, and (**J**) Λ = 600 nm lattices. Dashed lines represent the predicted positions of the Rayleigh anomalies using n_{PDMS} = 1.4.

As expected, the wavelengths of the LPRs depend on the lattice parameters used for the preparation of the HPC masks (**Figure 4.17G**). Specifically, the most intense LPRs are expected to emerge in proximity to the first-order diffraction line, the spectral position of which can be predicted using the following simplified equation:[64]

$$\lambda = \Lambda_{x,y}\,(n \pm sin\theta) \quad \textbf{[Eq. 4.4]}$$

where $\Lambda_{x,y}$ represents the lattice parameters in the two orthogonal in-plane directions, n is the refractive index of the surrounding medium, and θ is the illumination incidence angle. Under normal incidence, where θ is defined as zero, for a square lattice where $x = y$, and with n_{PDMS} estimated to be 1.4, the predicted wavelengths can be calculated as: 560 nm for Λ = 400 nm, 700 nm for Λ = 500 nm, and 840 nm for Λ = 600 nm. In the 400 nm lattice parameter samples, the predicted LPR overlaps with the LSPR of the AuNPs and can be identified as a shoulder at

560 nm in the transmission spectrum. For the 500 nm lattice, a clear dip is observed at 698 nm, close to the predicted LPR position. In the 600 nm lattice sample, the LPR can be appreciated at 826 nm (**Figure 4.17G**). The minor discrepancies compared to the predicted positions are common and can be attributed to various factors, including the effects of the CTAB AuNP coating, and/or the differences in PDMS refractive index as a function of composition and curing conditions.[65]

The identification of the aforementioned dips as lattice resonances is confirmed by measuring their spectral variation with illumination incidence angle (**Figure 4.17H-J**).[65] The dashed lines in **Figure 4.17H-J** are analytical calculations of the angular dependence of the Rayleigh-Wood anomalies. Apart from refractive index and lattice parameter, this dependence will also be modulated by the azimuthal angle of the array relative to the illumination (see discussion in Materials and Methods). Additionally, the quality of the Λ = 600 nm array is also confirmed by the appearance of a second-order diffraction line (**Figure 4.17J**). Overall, excellent matching between the experimental data and the predicted behavior was observed, confirming the presence of lattice resonances prepared by patterned *in situ* growth of AuNPs. We note that the array periodicities used here to produce LPRs in the visible and near infrared cannot be routinely accessed with block copolymer micelle lithography due to technical limitations for spacings greater than a few hundred nm.[14–17] Ultimately, the experimental realization of LPRs *via* bottom-up surface growth offers a new route towards plasmonic materials engineering with clear advantages compared to self-assembly and top-down methods.

Section 4.3. Conclusions and Prospects

A modified t-NIL protocol was used to pattern HPC thin films on soft polymeric substrates**.** This technique produced periodic structures with minimal residual layers such that water-

processable sacrificial stencils can be created in a standard laboratory environment without special equipment. The sacrificial HPC masks were used for chemical patterning and subsequent site-selective bottom-up AuNP growth. The AuNP size and shape were controlled directly on the substrate by altering the growth time and growth medium composition, respectively. The use of t-NIL provides improved flexibility for modifying the pattern increments by over a wide range by changing the mask features without adjusting the patterning process or increasing processing time. Following optimization of the chemical inking method and the nanoparticle growth solution, LPRs were demonstrated for arrays with periodicities of 400, 500, and 600 nm, giving tunable LPRs from the visible to the near infrared. The versatility in tuning the array geometry can be applied for potentially targeting lattice geometries giving collective responses beyond the near infrared, into the mid- or even far-infrared regions. The developed method overcomes limitations that have, until now, prevented the realization of LPRs using solely *in situ* growth, constituting significant progress for this class of approaches.

Understanding how the chemical environment, substrate wettability, AuNP-substrate interaction, secondary nucleation, and the balance of reducing agents on the substrate and in solution can help to create more reliable protocols achieving AuNP arrays and pave the way for new synthetic possibilities in the future.[17,43,66] Shape control for *in situ*-grown particles has only been briefly studied compared to colloidally synthesized AuNPs and the need to probe various aspects of the growth thoroughly remains. In this regard, the *in situ* growth method presented here is versatile for future investigations studying wet-chemical shape control and selective surface growth. Furthermore, because the AuNPs are fixed on the substrate, colloidal stability no longer represents a barrier to be considered, providing greater opportunities for testing unconventional growth conditions (*e.g.,* surfactant-free synthesis) or facile tailoring of the ligands.[17,66] We

anticipate that the nanoparticle-substrate interactions will represent important aspects to explore, which can potentially be tuned *via* the selected ink. The chosen substrate represents even more opportunities, *i.e.*, replacement of PDMS with different soft polymers, conductive polymers, hydrogels and two-dimensional materials. Ultimately, the presented methodology can bring a new perspective for the development of innovative synthetic paradigms for the growth of plasmonic nanoparticles and can impact the fabrication of solid-state platforms that take full advantage of their catalytic, optical, and magnetic properties.

Section 4.4. Materials and Methods

4.4.1. Materials

1H,1H,2H,2H-perfluorooctyltrichlorosilane (97%, CAS: 78560-45-9) was purchased from Alfa Aesar (Thermo Fisher GmbH, Karlsruhe, Germany). Hydroxypropyl cellulose (HPC; average Mw ~80,000, average Mn ~10,000, powder, 20 mesh particle size (99% through); CAS: 9004-64-2) was purchased from Sigma-Aldrich Quimica SL (Madrid, Spain). Polydimethylsiloxane (PDMS, Sylgard 184) was purchased from Dow Corning (Michigan, USA). The hard PDMS (hPDMS) mixture components were purchased from Gelest (CymitQuimica, Spain): (7.0-8.0% vinylmethylsiloxane)-dimethylsiloxane copolymer, trimethylsiloxy terminated (CAS: 67762-94-1), 1,3,5,7-tetramethylcyclotetrasiloxane (95%, CAS: 2370-88-9), platinum-divinyltetramethyldisiloxane complex (2% in Pt in xylene, CAS: 68478-92-2), and (25-35% methylhydrosiloxane)-dimethylsiloxane copolymer, trimethylsiloxane terminated (CAS: 68037-59-2). All chemicals were used as received. The polymethylhydrosiloxane (average molecular weight 1,700-3,200, CAS: 63148-57-2) used as a chemical ink was purchased from Merck. Piranha solution (3:1 95-98% w/w sulfuric acid, CAS: 7664-93-9, and 30% hydrogen peroxide, CAS:

7722-84-1; Fisher Scientific) was used for cleaning glass slides. *Warning:* Piranha mixture is dangerous as it reacts violently with organics and should be handled with caution.

4.4.2. Solvents

Toluene (≥ 99.5%, CAS: 108-88-3), hexane (≥ 99%, CAS: 92112-69-1), acetone (99.7%, CAS: 67-64-1), high-performance liquid chromatography (HPLC)-grade sub-micron filtered water (CAS: 67-63-0) and 200 proof ethanol (≥ 99.8%, CAS: 64-17-5) were obtained from Fisher Scientific. All solvents were used as received.

4.4.3. Synthesis reagents

All analytical grade reagents, silver nitrate ($AgNO_3$; 99%, CAS: 7761-88-8), $HAuCl_4 \cdot 3H_2O$ (99%, CAS: 16961-25-4) L-ascorbic acid (AA, 99%, CAS: 50-81-7), *N*-dodecyl-*N,N*-dimethyl-3-ammonio-1-propanesulfonate (LSB; 99%, CAS: D0431), hydrochloric acid (HCl; ACS Reagent 37%, CAS: 7647-01-0), cetyltrimethylammonium chloride (CTAC; 25 wt % in H_2O, CAS: 112-02-7) and cetyltrimethylammonium bromide (CTAB 99%, CAS: 200-311-3), were purchased from Merck. All glassware and magnetic stir bars used for synthesis were cleaned thoroughly with *aqua regia* (3:1 concentrated HCl (37%, Millipore Sigma) to HNO_3 (68%, Millipore Sigma)) and rinsed with HPLC grade water before use. *Warning: Aqua regia* is extremely corrosive and causes severe burns. Care is needed in its preparation and usage.

4.4.4. Methods

4.4.4.1. Characterization of hydroxypropylcellulose layer thickness on silicon

All reflectance spectra were collected with an FTIR spectrometer (Vertex 70, Bruker) coupled with an optical microscope (Hyperion, Bruker). Spectra were collected with a pair of 4× objectives with a numerical aperture (N.A.) of 0.10 and a spatial mask. The aperture was fixed at 600 × 600 μm^2.

4.4.4.2. Silanization with perfluorooctyltrichlorosilane

Functionalization with perfluorooctyltrichlorosilane was performed to create hydrophobic non-stick surfaces. The functionalization was performed as follows: 4 µL of the silane was placed in a reservoir in a glass desiccator with the substrates (placed vertically on the side walls) and was placed under vacuum for 20 min using a benchtop vacuum pump. The substrates were rinsed with isopropyl alcohol and completely dried with compressed air.

4.4.4.3. Patterned hard polydimethylsiloxane stamp preparation

The fabrication of the stamps using hard PDMS (hPDMS) is needed to avoid collapse of the pillars due to their small features and high aspect ratio. Composite stamps containing few microns of hPDMS (replicating the master features) and a thicker layer of soft PDMS (millimeters) were fabricated following a published procedure:[65,67] The hPDMS mixture was prepared by thoroughly mixing, 1.7 g of 7-8% vinylmethylsiloxane and 0.05 g of 1,3,5,7-tetracetylcyclosilane. Then, 4 µL of Pt catalyst, 0.5 g of 25-35% hydroxyl siloxane, and 1.5 g of toluene were rapidly added in this order under vigorous stirring. After the reagents are adequately mixed, the hPDMS

mixture can be used for approximately 20 min before the toluene evaporation causes the solution to become too viscous. Within this time frame, the mixture is drop cast onto a perfluorooctyltrichlorosilane-functionalized silicon master and spread over the surface using an air gun to ensure uniform coverage and removal of microbubbles. Drop casting of the hPDMS mixture was repeated three times for each master, and the substrates were subsequently left at room temperature for 1 h to ensure complete evaporation of the toluene. Following this step, the masters were placed for an additional 1 h at 60 °C to cure the hPDMS.

Next, the fabrication of soft PDMS is performed by mixing ~20-30 g of 10:1 PDMS. The PDMS was placed in a centrifuge at 3500 rpm for 2 min to remove trapped air. The mixture was then cast onto a petri dish containing the master with a layer of cured hPDMS and left at 60 °C for at least 4 h to ensure complete curing. Finally, the hPDMS composite stamps were carefully demolded from the master and functionalized with perfluorooctyltrichlorosilane *via* vapor deposition.

4.4.4.4. Preparation of soft polydimethylsiloxane substrates

Flat soft PDMS was prepared by first mixing ~1 mL 10:1 PDMS and centrifuging the mixture at 3500 rpm for 2 min to remove bubbles. The mixture was cast into a petri dish containing a perflorooctyltrichlorosilane-treated silicon wafer. This was cured at 80-85 ºC on a hot plate for 1 h. The PDMS was carefully removed from the petri dish and heated on a hotplate to 120 ºC for 1 h. This is done to oxidize/react excess oligomer which can cause nucleation of particles. Although baking removes some oligomer, additional cleaning steps are needed to ensure minimal nucleation on the PDMS. To extract the oligomer, the PDMS is sonicated in ethanol 5 min, then in hexane for 30 min.[37,45,47,48,68,69] The PDMS should swell with hexane, and then de-swell upon

drying for 30 min at 60 ºC in the oven. This swelling and de-swelling process should be repeated three times. The last drying step should be done for ~60 min to ensure that the PDMS is completely de-swelled prior to coating with HPC.

Glass-supported flat PDMS was prepared by first mixing ~1mL 10:1 PDMS and centrifuging the mixture at 3500 rpm for 2 min to remove bubbles. A drop of PDMS was placed on perfluorooctyltrichlorosilane-functionalized silicon, then a piece of piranha-cleaned glass (cut to be ~1.5 cm^2) was placed on top of the PDMS drop. The glass-PDMS-silicon sandwich was then degassed for 10 min and subsequently placed on a hotplate at 120 ºC for 1 h. After curing, the glass-PDMS was carefully separated from the silicon by carefully wedging a razor blade between the glass and the silicon. Unlike the non-supported PDMS, extraction in hexane cannot be performed for these samples since it will cause delamination of the PDMS from the glass. Therefore, the PDMS was instead cleaned by sonication in ethanol for 5 min, followed by sonication in acetone 60 min. The samples were dried for 1 h in an oven at 60 °C, then allowed to cool to room temperature before use.

4.4.4.5. Fabrication of hydroxypropyl cellulose stencils

The HPC stock solution (usable for ~1 month) was prepared by adding 23 g of HPC to every 100 mL of water under stirring at room temperature (HPC is less soluble in warm water). Within 5 min, the solution will become a paste. At this point, the solution was left to dissolve over ~48 h at room temperature until it appeared clear/uniform. Aqueous HPC working solutions at 21 mg/mL, 38 mg/mL, 53 mg/mL, and 66 mg/mL were prepared by adding 1.0 g, 2.0 g, 3.0 g, and 4.0 g of concentrated HPC stock solution to 10 mL of water and stirring for at least 1 h prior to use. The HPC stock solution and film spin-coating processes can vary depending on the individual

and the conditions and equipment of the laboratory, thus, note that the final spin-coated thickness of the HPC film should be checked either using reflectance spectra, atomic force microscopy, or profilometry. The final height of the film being lower than the negative volume of the stamp is the most important aspect for ensuring successful pattern transfer, rather than the concentration of the working solutions.

The PDMS substrates were first UV-ozone (Jelight Model 42) activated for 10 min to promote coating with HPC. The HPC was then spin coated onto the PDMS at 3000 rpm (accel. 500 rpm/s) for 60 s within 1 h of the UV-ozone treatment. A silane-functionalized hPDMS stamp was contacted with the HPC-coated PDMS substrate. Then, a pressure of 1 bar was applied, and the substrate was brought to 140 ºC using a compact nanoimprint tool (CNI v 2.0 by NIL Technology ApS, NILT, DK. This procedure can be performed manually on a hotplate, simply applying a weight that can simulate the necessary pressure (~1 kg/1 cm^2 substrate). A dwell time of at least 1 min when a temperature of 140 ºC was reached was applied until the substrate was allowed to cool below 75 ºC. The hPDMS is then carefully and slowly removed from the substrate. The hPDMS stamp can be used 3-5 times before the silane functionalization needs to be repeated, and the stamps were re-used a total of 10-15 times to ensure that possible contamination or degradation of the surface would not affect the t-NIL step. The removal of any residual in the holes of the stencil was done *via* a short 30 s UV-ozone treatment. It is important to note that UV-ozone treatments of the stencil any longer than ~2 min will produce a hard-to-dissolve byproduct (**Figure 4.4,5**).

4.4.4.6. Chemical ink application and stencil removal

Polymethylhydrosiloxane was applied using the same vapor deposition process as perfluorooctyltrichlorosilane or by spin coating a 0.1% (v/v) polymethylhydrosiloxane solution in hexane at 5000 rpm for 60 s (accel. 2500 rpm/s). The 0.1% polymethylhydrosiloxane solution in hexane must be stirred for ~1 h prior to use to ensure even distribution of the ink. A drop of Milli-Q water (resistivity 18.2 MOhm) was then placed on the sample and allowed to rest for 30 min. This step is done to swell the HPC and facilitate its removal. After 30 min, the sample is dried, then rinsed and dried very thoroughly with Milli-Q water two more times. *N.B.* It is very important to remove the residual completely as HPC can also act as a reductant for AuNP formation.[70–72]

Although polymethylhydrosiloxane is naturally present in PDMS due to native unreacted oligomer remaining after the preparation of the elastomer, and it was previously demonstrated to reduce gold salts effectively and to lead to particle formation both on the surface and within the polymer matrix.[37,44,47,73] However, the quantity of excess polymethylhydrosiloxane fluctuates with the curing agent and base ratio, curing conditions,[74] and substrate age, making its concentration and distribution difficult to control.[75] To regulate the nucleation sites of the nanoparticles on the substrate more precisely, the native polymethylhydrosiloxane was removed from the bulk material using high curing temperature and solvent extraction[76] and subsequently reapplied to the surface as a chemical ink in a controlled manner.

4.4.4.7. *In situ* gold nanoparticle growth

Growth solution was placed as a 150 µL drop on the substrate. This approach was chosen instead of immersing the substrate in the solution to minimize contamination from the back of the substrate that can induce secondary nucleation. Moreover, particular attention was taken to prepare

samples with consistent surface areas, in order to maximize the reproducibility and consistency of the results. In the optimized growth solution 12 µL of 50 mM aqueous $HAuCl_4$ gold stock solution was added to 1 mL of 25 mM CTAB. Then, 12 µL of 100 mM aqueous AA was added, the solution was rapidly stirred by hand, and within 5 s the solution changes color from orange to clear. Immediately after the solution turns clear it was added to the substrates and allowed to react for 1, 2, 5, or 10 min, then the growth solution was removed by thorough rinsing with Milli-Q water and dried with compressed air.

Overgrowth of gold nanostars was carried out on substrates grown by the previously published method for 5 min by drop casting 150 µL drop of growth solution containing 1 mL of 100 mM LSB solution, 15 µL of 50 mM $HAuCl_4$, 6 µL 10 mM $AgNO_3$, and 10 µL HCl and 50 µL of 100 mM AA. All other reagents are mixed prior to addition of AA which was rapidly added, rapidly mixed, and immediately introduced to the substrate. Like what was done in prior work, the HCl was added to prevent significant secondary nucleation for the 10 min growth time.[28]

4.4.4.8. Scanning electron microscopy characterization

Scanning electron microscopy (SEM) images were collected with a FEI QUANTA 200 Field Emission Gun, operating between 5 and 15 kV under low vacuum (60 Pa). Samples for cross section imaging were prepared by sputtering 5-10 nm of Au/Pd onto the patterned HPC film (the 30 nm film was used for **Figure 1K**) to improve conductivity, then scoring the back of the substrate with a razor and placing it in liquid nitrogen for 5 min. Upon the removal of the substrate from the nitrogen, the sample was snapped in two using pliers.

4.4.4.9. Optical characterization and data analysis

The far-field transmission optical response of the plasmonic ordered arrays was characterized on a custom-built optical setup with a dedicated software (Labview NXG). A tungsten halogen lamp (Ocean Optics, HL-2000-HP) was used as light source and was corrected by two separated filters (Edmund Optics, SCHOTT BG64, and Thorlabs, SRF11) to increase count rate in the UV and near infrared regions of the spectra. The light is focused on the sample and collected using two achromatic doublet lenses with a NA < 0.1 (Thorlabs, AC254-100-AB and AC254-50-AB, respectively), and finally coupled to an optical fiber (Thorlabs, RC08SMA-P01), and analyzed by a spectrophotometer (Ocean Optics, QEPro-FL). The samples were mounted on a software-controlled rotational stage (Thorlabs, ELL18K/M) that allows varying the illumination angle θ with a precision of 0.1º, while a custom-made sample holder enables control of the azimuthal angle φ (± 3º). The reference for the spectra was collected on the same sample, outside the patterned area, to eliminate eventual Fabri-Perot interference created by air trapped between the glass supports and the PDMS layers.

Transmission spectra were collected with an illumination angle varying between 0º (normal incidence) and 15º. The collected data were baseline-corrected with an exponential curve to eliminate the distortions generated by the substrate, and, where indicated in the main text, smoothed with a Savitzky–Golay filter and normalized.

4.4.4.10. Expected processing time for each step

1. PDMS/Supported PDMS fabrication: 1.5 h
2. Cleaning: 2h
3. PDMS UV-ozone activation: 10 min

4. HPC stencil spin coating and t-NIL: 10-15 min
5. UV-Ozone etch: 30 s
6. Inking (*via* optimized spin coating): 1 min

wait 1 h to overnight between these steps for best results*

7. HPC removal: 30-35 min
8. gold nanoparticle growth: 2-10 min

Total: ~6 working hours, including ***all*** sample preparation steps, or if waiting overnight between steps #6-7, ~16 h for all sample preparation. Multiple samples can be run in parallel.

Section 4.5. References

[1] K. A. Willets, R. P. Van Duyne, *Annu. Rev. Phys. Chem.* **2007**, *58*, 267.

[2] V. G. Kravets, A. V. Kabashin, W. L. Barnes, A. N. Grigorenko, *Chem. Rev.* **2018**, *118*, 5912.

[3] R. Adato, A. A. Yanik, C.-H. Wu, G. Shvets, H. Altug, *Opt. Express* **2010**, *18*, 4526.

[4] D. Wang, A. Yang, A. J. Hryn, G. C. Schatz, T. W. Odom, *ACS Photonics* **2015**, *2*, 1789.

[5] W. Zhou, M. Dridi, J. Y. Suh, C. H. Kim, D. T. Co, M. R. Wasielewski, G. C. Schatz, T. W. Odom, *Nat. Nanotechnol.* **2013**, *8*, 506.

[6] A. M. Berghuis, V. Serpenti, M. Ramezani, S. Wang, J. Gómez Rivas, *J. Phys. Chem. C* **2020**, *124*, 12030.

[7] T. S. Heiderscheit, S. Oikawa, S. Sanders, H. Minamimoto, E. K. Searles, C. F. Landes, K. Murakoshi, A. Manjavacas, S. Link, *J. Phys. Chem. Lett.* **2021**, *12*, 2516.

[8] C. Matricardi, C. Hanske, J. L. Garcia-Pomar, J. Langer, A. Mihi, L. M. Liz-Marzán, *ACS Nano* **2018**, *12*, 8531.

[9] D. G. Montjoy, J. H. Bahng, A. Eskafi, H. Hou, N. A. Kotov, *J. Am. Chem. Soc.* **2018**, *140*, 7835.

[10] G. Palermo, M. Rippa, Y. Conti, A. Vestri, R. Castagna, G. Fusco, E. Suffredini, J. Zhou, J. Zyss, A. De Luca, L. Petti, *ACS Appl. Mater. Interfaces* **2021**, *13*, 43715.

[11] J. Olson, A. Manjavacas, T. Basu, D. Huang, A. E. Schlather, B. Zheng, N. J. Halas, P. Nordlander, S. Link, *ACS Nano* **2016**, *10*, 1108.

[12] F. Yang, S. Ye, W. Dong, D. Zheng, Y. Xia, C. Yi, J. Tao, C. Sun, L. Zhang, L. Wang, Q. Chen, Y. Wang, Z. Nie, *Adv. Mater.* **2021**, *33*, 2100325.

[13] J. Jeon, K. Bhattarai, D.-K. Kim, J. O. Kim, A. Urbas, S. J. Lee, Z. Ku, J. Zhou, *Sci. Rep.* **2016**, *6*, 36190.

[14] T. Lohmüller, D. Aydin, M. Schwieder, C. Morhard, I. Louban, C. Pacholski, J. P. Spatz, *Biointerphases* **2011**, *6*, MR1.

[15] M. Stefik, S. Guldin, S. Vignolini, U. Wiesner, U. Steiner, *Chem. Soc. Rev.* **2015**, *44*, 5076.

[16] A. Alvarez-Fernandez, C. Cummins, M. Saba, U. Steiner, G. Fleury, V. Ponsinet, S. Guldin, *Adv. Opt. Mater.* **2021**, *9*, 2100175.

[17] H.-H. Jeong, M. C. Adams, J.-P. Günther, M. Alarcón-Correa, I. Kim, E. Choi, C. Miksch, A. F. Mark, A. G. Mark, P. Fischer, *ACS Nano* **2019**, *13*, 11453.

[18] S. D. Golze, R. A. Hughes, S. Rouvimov, R. D. Neal, T. B. Demille, S. Neretina, *Nano Lett.* **2019**, *19*, 5653.

[19] T. B. Demille, R. A. Hughes, S. Neretina, *J. Phys. Chem. C* **2019**, *123*, 19879.

[20] T. B. Demille, R. A. Hughes, N. Dominique, J. E. Olson, S. Rouvimov, J. P. Camden, S. Neretina, *Nanoscale* **2020**, *12*, 16489.

[21] F. Zang, Z. Su, L. Zhou, K. Konduru, G. Kaplan, S. Y. Chou, *Adv. Mater.* **2019**, *31*, 1902331.

[22] L. Huang, P.-C. Chen, M. Liu, X. Fu, P. Gordiichuk, Y. Yu, C. Wolverton, Y. Kang, C. A. Mirkin, *Proc. Natl. Acad. Sci.* **2018**, *115*, 3764.

[23] E. Cortés, P. H. Camargo, *Plasmonic Catalysis: From Fundamentals to Applications*, John Wiley & Sons, **2021**.

[24] S. Ezendam, M. Herran, L. Nan, C. Gruber, Y. Kang, F. Gröbmeyer, R. Lin, J. Gargiulo, A. Sousa-Castillo, E. Cortés, *ACS Energy Lett.* **2022**, *7*, 778.

[25] Z. Ao, E. Parasido, S. Rawal, A. Williams, R. Schlegel, S. Liu, C. Albanese, R. J. Cote, A. Agarwal, R. H. Datar, *Lab. Chip* **2015**, *15*, 4277.

[26] S.-W. Lv, Y. Liu, M. Xie, J. Wang, X.-W. Yan, Z. Li, W.-G. Dong, W.-H. Huang, *ACS Nano* **2016**, *10*, 6201.

[27] M.-H. Park, E. Reátegui, W. Li, S. N. Tessier, K. H. K. Wong, A. E. Jensen, V. Thapar, D. Ting, M. Toner, S. L. Stott, P. T. Hammond, *J. Am. Chem. Soc.* **2017**, *139*, 2741.

[28] G. A. Vinnacombe-Willson, N. Chiang, L. Scarabelli, Y. Hu, L. K. Heidenreich, X. Li, Y. Gong, D. T. Inouye, T. S. Fisher, P. S. Weiss, S. J. Jonas, *ACS Cent. Sci.* **2020**, *6*, 2105.

[29] M. Colburn, S. C. Johnson, M. D. Stewart, S. Damle, T. C. Bailey, B. Choi, M. Wedlake, T. B. Michaelson, S. V. Sreenivasan, J. G. Ekerdt, C. G. Willson, in (Ed.: Y. Vladimirsky), Santa Clara, CA, **1999**, p. 379.

[30] S. Y. Chou, P. R. Krauss, P. J. Renstrom, *J. Vac. Sci. Technol. B Microelectron. Nanometer Struct. Process. Meas. Phenom.* **1996**, *14*, 4129.

[31] A. Espinha, C. Dore, C. Matricardi, M. I. Alonso, A. R. Goñi, A. Mihi, *Nat. Photonics* **2018**, *12*, 343.

[32] C. Dore, J. Osmond, A. Mihi, *Nanoscale* **2018**, *10*, 17884.

[33] J. Dumond, H. Y. Low, *Adv. Mater.* **2008**, *20*, 1291.

[34] J. L. Perry, K. P. Herlihy, M. E. Napier, J. M. DeSimone, *Acc. Chem. Res.* **2011**, *44*, 990.

[35] T. Lee, C. Lee, D. K. Oh, T. Badloe, J. G. Ok, J. Rho, *Sensors* **2020**, *20*, 4108.

[36] T. J. Merkel, K. P. Herlihy, J. Nunes, R. M. Orgel, J. P. Rolland, J. M. DeSimone, *Langmuir* **2010**, *26*, 13086.

[37] B. Fortuni, T. Inose, S. Uezono, S. Toyouchi, K. Umemoto, S. Sekine, Y. Fujita, M. Ricci, G. Lu, A. Masuhara, J. A. Hutchison, L. Latterini, H. Uji-i, *Chem. Commun.* **2017**, *53*, 11298.

[38] B. Fortuni, Y. Fujita, M. Ricci, T. Inose, R. Aubert, G. Lu, J. A. Hutchison, J. Hofkens, L. Latterini, H. Uji-i, *Chem. Commun.* **2017**, *53*, 5121.

[39] S. Kumar, H. Yang, S. Zou, *J. Phys. Chem. C* **2007**, *111*, 12933.

[40] L. Liz-Marzán, *Colloidal Synthesis of Plasmonic Nanometals*, CRC Press, **2020**.

[41] L. Scarabelli, *Pure Appl. Chem.* **2018**, *90*, 1393.

[42] N. G. Bastús, J. Comenge, V. Puntes, *Langmuir* **2011**, *27*, 11098.

[43] B. Landeke-Wilsmark, L. Nyholm, C. Hägglund, *Langmuir* **2020**, *36*, 6848.

[44] J. R. Dunklin, G. T. Forcherio, K. R. Berry, D. K. Roper, *J. Phys. Chem. C* **2014**, *118*, 7523.

[45] D. J. Campbell, R. B. Villarreal, T. J. Fitzjarrald, *J. Chem. Educ.* **2012**, *89*, 1312.

[46] M.-C. Lim, S.-H. Kim, K. Park, Y.-R. Kim, J.-H. Kim, G. Ok, S.-W. Choi, *RSC Adv* **2017**, *7*, 13228.

[47] K. Park, M.-A. Woo, J.-A. Lim, Y.-R. Kim, S.-W. Choi, M.-C. Lim, *Colloids Surf. Physicochem. Eng. Asp.* **2018**, *558*, 186.

[48] Q. Zhang, J.-J. Xu, Y. Liu, H.-Y. Chen, *Lab Chip* **2008**, *8*, 352.

[49] L. Scarabelli, A. Sánchez-Iglesias, J. Pérez-Juste, L. M. Liz-Marzán, *J. Phys. Chem. Lett.* **2015**, *6*, 4270.

[50] L. M. Liz-Marzán, C. R. Kagan, J. E. Millstone, *ACS Nano* **2020**, *14*, 6359.

[51] G. Liu, C. Zhang, J. Wu, C. A. Mirkin, *ACS Nano* **2015**, *9*, 12137.

[52] M. J. Ashley, M. R. Bourgeois, R. R. Murthy, C. R. Laramy, M. B. Ross, R. R. Naik, G. C. Schatz, C. A. Mirkin, *J. Phys. Chem. C* **2018**, *122*, 2307.

[53] C. Kuttner, V. Piotto, L. M. Liz-Marzán, *Chem. Mater.* **2021**, *33*, 8904.

[54] N. Chiang, L. Scarabelli, G. A. Vinnacombe-Willson, L. A. Pérez, C. Dore, A. Mihi, S. J. Jonas, P. S. Weiss, *ACS Mater. Lett.* **2021**, *3*, 282.

[55] C. Hanske, G. González-Rubio, C. Hamon, P. Formentín, E. Modin, A. Chuvilin, A. Guerrero-Martínez, L. F. Marsal, L. M. Liz-Marzán, *J. Phys. Chem. C* **2017**, *121*, 10899.

[56] P. Chhour, J. Kim, B. Benardo, A. Tovar, S. Mian, H. I. Litt, V. A. Ferrari, D. P. Cormode, *Bioconjug. Chem.* **2017**, *28*, 260.

[57] F. Muench, S. Schaefer, L. Hagelüken, L. Molina-Luna, M. Duerrschnabel, H.-J. Kleebe, J. Brötz, A. Vaskevich, I. Rubinstein, W. Ensinger, *ACS Appl. Mater. Interfaces* **2017**, *9*, 31142.

[58] Y. Sun, *Chem. Mater.* **2007**, *19*, 5845.

[59] T. Lohmueller, E. Bock, J. P. Spatz, *Adv. Mater.* **2008**, *20*, 2297.

[60] A. Casu, E. Cabrini, A. Donà, A. Falqui, Y. Diaz-Fernandez, C. Milanese, A. Taglietti, P. Pallavicini, *Chem. - Eur. J.* **2012**, *18*, 9381.

[61] J.-Y. Kim, J. Yeom, G. Zhao, H. Calcaterra, J. Munn, P. Zhang, N. Kotov, *J. Am. Chem. Soc.* **2019**, *141*, 11739.

[62] E. S. A. Goerlitzer, R. Mohammadi, S. Nechayev, K. Volk, M. Rey, P. Banzer, M. Karg, N. Vogel, *Adv. Mater.* **2020**, *32*, 2001330.

[63] P. T. Probst, M. Mayer, V. Gupta, A. M. Steiner, Z. Zhou, G. K. Auernhammer, T. A. F. König, A. Fery, *Nat. Mater.* **2021**, *20*, 1024.

[64] L. Scarabelli, D. Vila-Liarte, A. Mihi, L. M. Liz-Marzán, *Acc. Mater. Res.* **2021**, *2*, 816.

[65] P. Molet, N. Passarelli, L. A. Pérez, L. Scarabelli, A. Mihi, *Adv. Opt. Mater.* **2021**, *9*, 2100761.

[66] A. G. Mark, J. G. Gibbs, T.-C. Lee, P. Fischer, *Nat. Mater.* **2013**, *12*, 802.

[67] T. W. Odom, J. C. Love, D. B. Wolfe, K. E. Paul, G. M. Whitesides, *Langmuir* **2002**, *18*, 5314.

[68] A. Goyal, A. Kumar, P. K. Patra, S. Mahendra, S. Tabatabaei, P. J. J. Alvarez, G. John, P. M. Ajayan, *Macromol. Rapid Commun.* **2009**, *30*, 1116.

[69] J. H. Kim, H. Park, S. W. Seo, *Nano Converg.* **2017**, *4*, 33.

[70] W. Hao, W. Yang, W. Huang, G. Zhang, Q. Wu, *Mater. Lett.* **2008**, *62*, 3106.

[71] E. S. Abdel-Halim, S. S. Al-Deyab, *Carbohydr. Polym.* **2011**, *86*, 1615.

[72] X. Wu, C. Lu, Z. Zhou, G. Yuan, R. Xiong, X. Zhang, *Environ. Sci. Nano* **2014**, *1*, 71.

[73] Y. Tsuge, T. Moriya, Y. Moriyama, Y. Tokura, S. Shiratori, *ACS Appl. Mater. Interfaces* **2017**, *9*, 15122.

[74] A. Karlsson, S. K. Singh, A.-C. Albertsson, *J. Appl. Polym. Sci.* **2002**, *84*, 2254.

[75] I.-J. Chen, E. Lindner, *Langmuir* **2007**, *23*, 3118.

[76] J. N. Lee, C. Park, G. M. Whitesides, *Anal. Chem.* **2003**, *75*, 6544.

Chapter 5. Gold Nanostars *in Situ* Shape Control on Oxide Substrates and in Microfluidic Channels

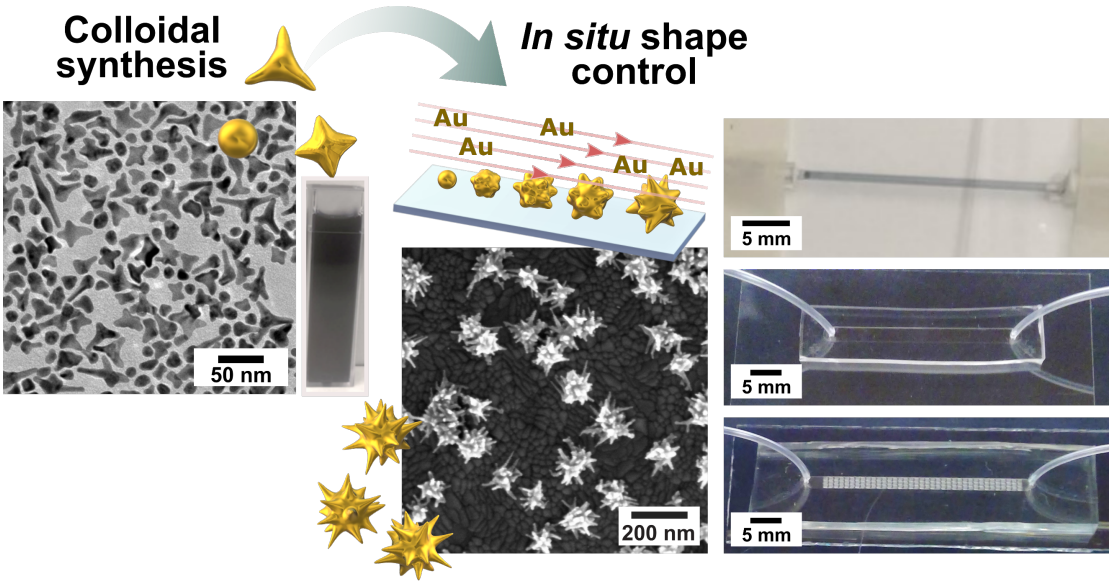

***In situ* seed-mediated synthesis was applied to grow thermoplasmonic branched gold nanoparticles** directly onto oxide substrates and on the internal walls of microfluidic channels. The effects of various synthetic parameters on the nanostructure geometry, including reagent concentrations, growth time, flow rate, and flow profile, were interrogated. Ultimately, the plasmonic microfluidic systems developed herein may find applications in sensing and biology.

Section 5.1. Introduction

Like many other anisotropic shapes, gold nanostars (AuNSTs) are accessible *via* bottom-up seed-mediated growth. In terms of incorporating AuNSTs in plasmonic devices, functionalization with pre-synthesized nanoparticles (*i.e.,* applying self-assembly, lithography, or combinations of the two)[1–5] and direct nanoparticle synthesis[6–12] on the desired substrates offer common approaches towards achieving surface decoration with crystalline products. However, the development of robust methods for generating substrates functionalized with size- and shape-controlled nanoparticles at high density remains an active area of research.[13]

Here, we report a facile method for the generation of AuNSTs on oxide substrates. Protocols for the synthesis of AuNSTs in colloidal suspensions were adapted by first grafting colloidally synthesized seeds and performing subsequent shape control *in situ* by simply submerging the functionalized surface in a growth solution. We also adapted this growth methodology to various microfluidic devices, including glass capillaries, and polydimethylsiloxane (PDMS) channels bound to both glass and indium tin oxide (ITO) substrates. Previously, microfluidic systems for precisely synthesizing colloidal nanoparticles have been explored.[14–18] Here, we take an unconventional approach by creating the plasmonic structures on the internal walls of microfluidic channels. This approach enables us to probe the effects of flow rate, flow profile, and the growth time on the geometry of the nanostructures while also modulating the chemical environment through the growth solution. Systematically varying flow and growth solution parameters, we achieved dense coatings of highly branched nanostructures with configurable aspect ratios in various microfluidic device configurations. These thermoplasmonic-nanostructure-integrated microfluidic platforms offer new solutions for small-molecule sensing,[19–23] intracellular delivery *via* poration,[24,25] and/or the targeted retrieval of single cells

in adherent cultures, representing a starting point for the development of devices capable of cell capture and targeted, selective light-triggered release.[26,27]

Section 5.2. Results and Discussion

5.2.1. Growth solution optimization for *in situ* shape control

Gold nanostars with high aspect ratios and numbers of branches efficiently produce intense localized heat in response to near-infrared light.[28,29] Of the various bottom-up wet-chemical approaches for synthesizing branched nanoparticles, the seed-mediated growth method, where the nucleation and growth steps are performed separately and sequentially, is one of the most promising approaches for precise nanoparticle shape control.[30–35] However, the immobilization of pre-synthetized nanoparticles on substrates can result in low surface density and inhomogeneous distributions.[13] To address this limitation, we developed a seed-mediated synthetic method that enables direct growth of shape-controlled AuNPs uniformly on oxide substrates using *in situ* shape control designed to prepare branched structures on surfaces.[26,36]

We modified a previously established batch seed-mediated growth protocol from Pallavicini and co-workers,[37] improving product reproducibility and reducing the impact of secondary nucleation (*i.e.,* uncontrolled formation of new nuclei after particle growth has already begun). In the original approach, the zwitterionic surfactant laurylsulfobetaine (LSB) yields rapid growth of nanostars through kinetic control to achieve sharp tips. The seeds were also capped with LSB, resulting in the requirement for the reagents to be kept at low temperatures to avoid rapid aging and batch-to-batch variation in the positions and intensities of the localized surface plasmon resonance (LSPR) peaks. In our synthesis, we opted to use cetyltrimethylammonium chloride

(CTAC)-capped seeds, which age more slowly and yield products with reproducible ultraviolet (UV)-visible spectra (**Figure 5.1**).

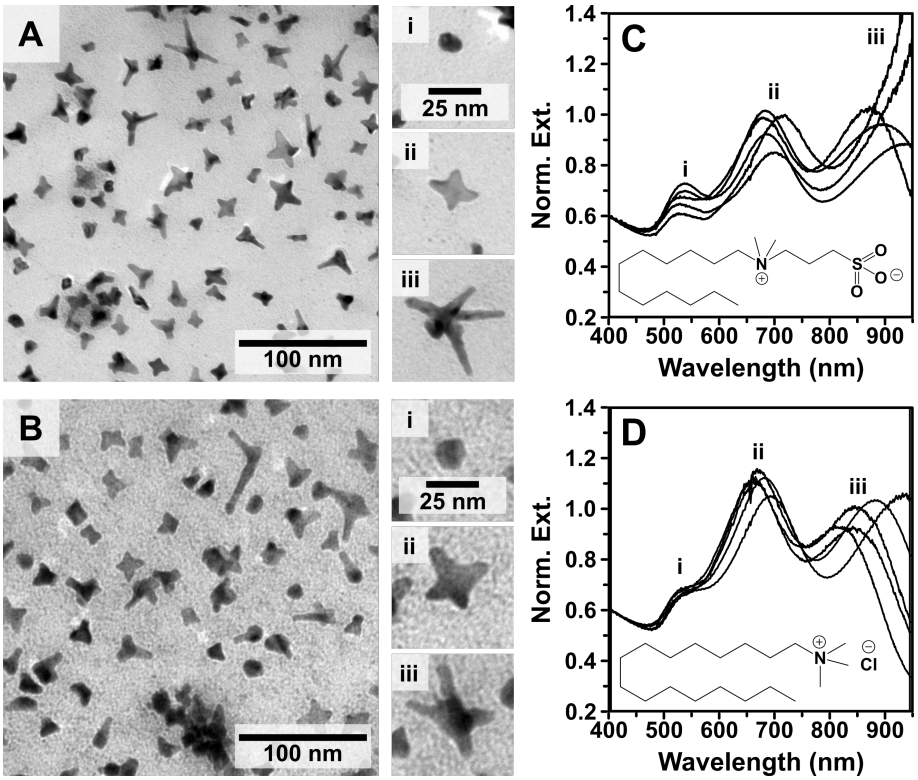

Figure 5.1. A,B: Transmission electron microscopy images showing gold nanostar (AuNST) products synthesized using (**A**) seeds capped with laurylsulfobetaine (LSB) and (**B**) cetyltrimethylammonium chloride (CTAC). **C,D:** Ultraviolet-visible spectra showing three repetitions of each synthesis, performed with (**C**) LSB-capped seeds and (**D**) CTAC-capped seeds.

The addition of ascorbic acid (reducing agent) in the absence of the seeds results in rapid secondary nucleation, leading to the uncontrolled growth of sub-optimal morphologies. Secondary nucleation is especially undesired if our intention is to apply this synthesis in microfluidic channels, where the growth solution is required to flow through tubing for some time prior to reaching the channel containing the substrate-anchored seeds. In order to slow secondary nanoparticle nucleation, we further modified the growth solution through addition of HCl to reduce

the pH and effectively decrease the reduction strength of ascorbic acid (**Figure 5.2**). Spectroscopic analysis of the growth kinetics in **Figure 5.2** indicate that significant nucleation does not occur for at least 20-40 min following the addition of ascorbic acid, unless the gold seeds are added to the growth medium.

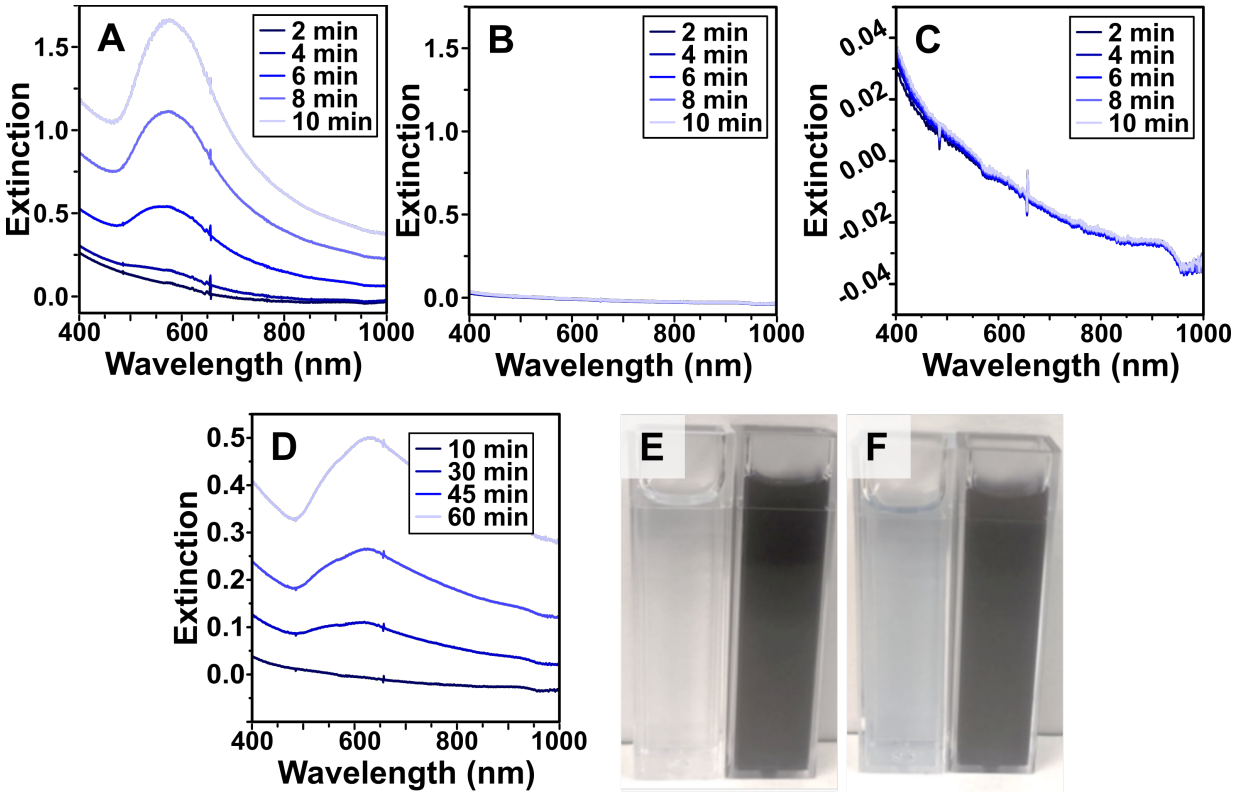

Figure 5.2. A-D: Ultraviolet-visible spectra of (**A**) nucleation of nanoparticles in growth solution without HCl and **(B)** with 10 µL/mL 1 M HCl over 10 min without the addition of any seeds. **C:** Scaled view of graph **B** and **D:** spectra of solution with HCl addition from 10 min to 60 min. **E:** Digital photographs of solutions after 30 min and **F:** 1 h. The solution with HCl is on the left in both pictures.

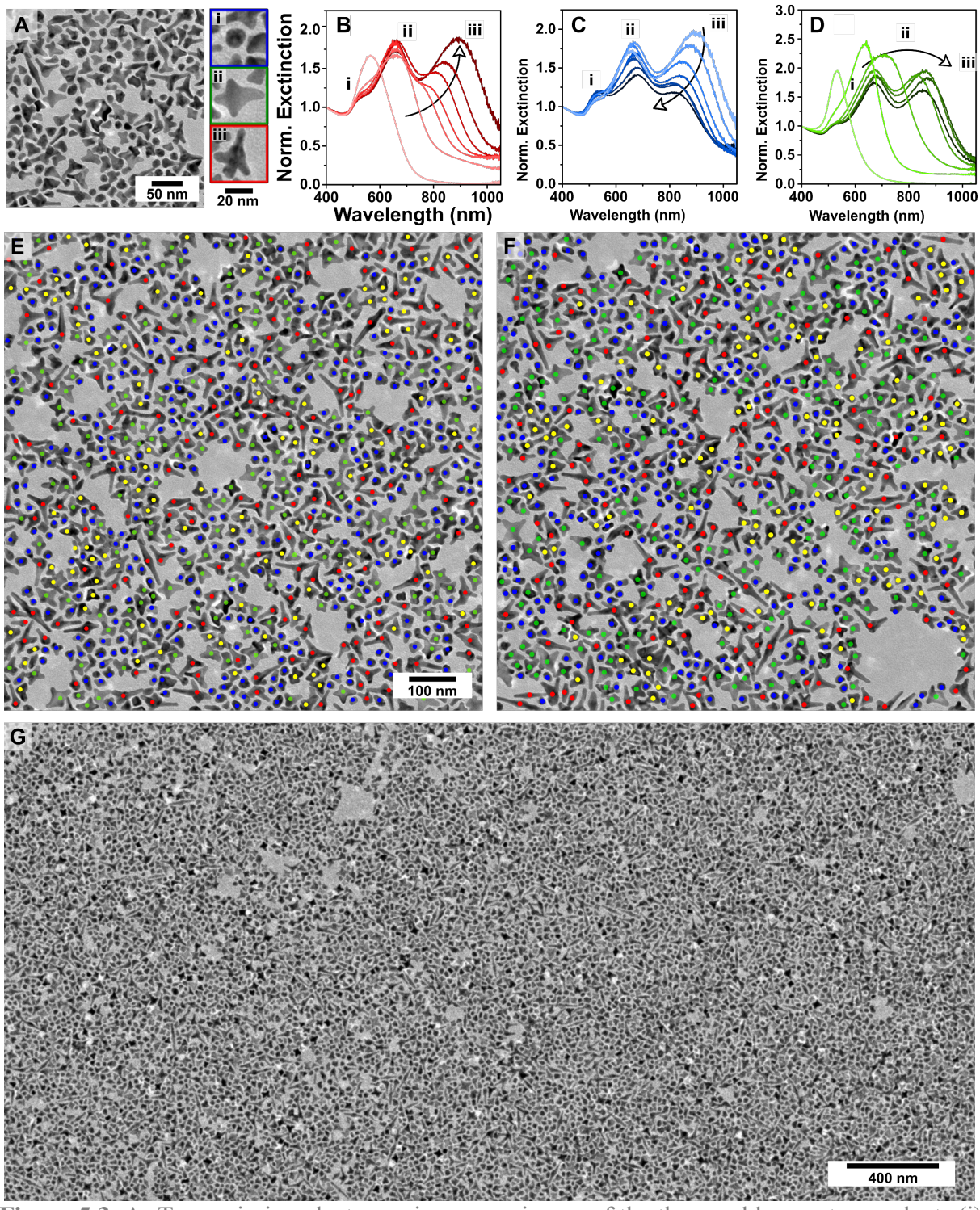

Figure 5.3. A: Transmission electron microscopy image of the three gold nanostar products (i) anisotropic spheroids, (ii) low aspect-ratio products, and (iii) high aspect-ratio products. Ultraviolet-visible spectra showing the effect of increasing **B:** ascorbic acid, **C:** hydrochloric acid, and **D:** silver nitrate in the growth solution. Transmission electron microscopy images **E,F:** showing product identification for yield determination, and **G:** large-scale view of final products yield: 42% spheroids (i), 24% low aspect ratio (ii), 20% high aspect ratio (iii), 14% unidentified.

The final adjusted colloidal protocol produced three major products, as observed by transmission electron microscopy (TEM) and UV-vis spectroscopy: anisotropic spheroids, low-aspect ratio AuNSTs, and high-aspect ratio AuNSTs (**Figure 5.3A-D**), exhibiting LSPR peaks at *ca.* 525 nm, 650 nm, and 875 nm, respectively. The corresponding yield of high-aspect ratio products was 20% (**Figure 5.3E-G**). Addition of HCl slows the growth process and therefore could disfavor formation of highly branched and high aspect ratio products.[32] However, even without HCl addition, three different products are observed, indicating that the low yield of the desired products is likely due to inevitable secondary nucleation in solution. As discussed below, the low yield of high aspect ratio products is ultimately resolved when the growth is translated *in situ* on slides and within the microfluidic channels.

5.2.2. *In situ* nanostars overgrowth on slides and in capillaries

The *in situ* seed-mediated AuNST growth and shape control strategy developed here takes advantage of the size of pre-synthesized seeds, which can be grafted easily onto a variety of oxide materials. Our *in situ* growth strategy is summarized in detail in **Figure 5.4A**: (i) substrate chemical modification with (3-aminopropyl)triethoxysilane (APTES), (ii) grafting pre-synthesized gold seeds onto the APTES chemical anchor to serve as catalytic surfaces for the growth of AuNSTs, and (iii) subsequent introduction of a growth solution *via* incubation or flow. Attaching the smaller seed particles prior to AuNST growth, rather than tethering larger pre-synthesized nanostructures to the substrates, improves product density and limits the formation of byproducts resulting from secondary nucleation events that normally occur during the colloidal growth step. Moreover, our methodology can be applied to a variety of substrate geometries, including glass microcapillaries, enabling straightforward integration with microfluidic systems.[38–41]

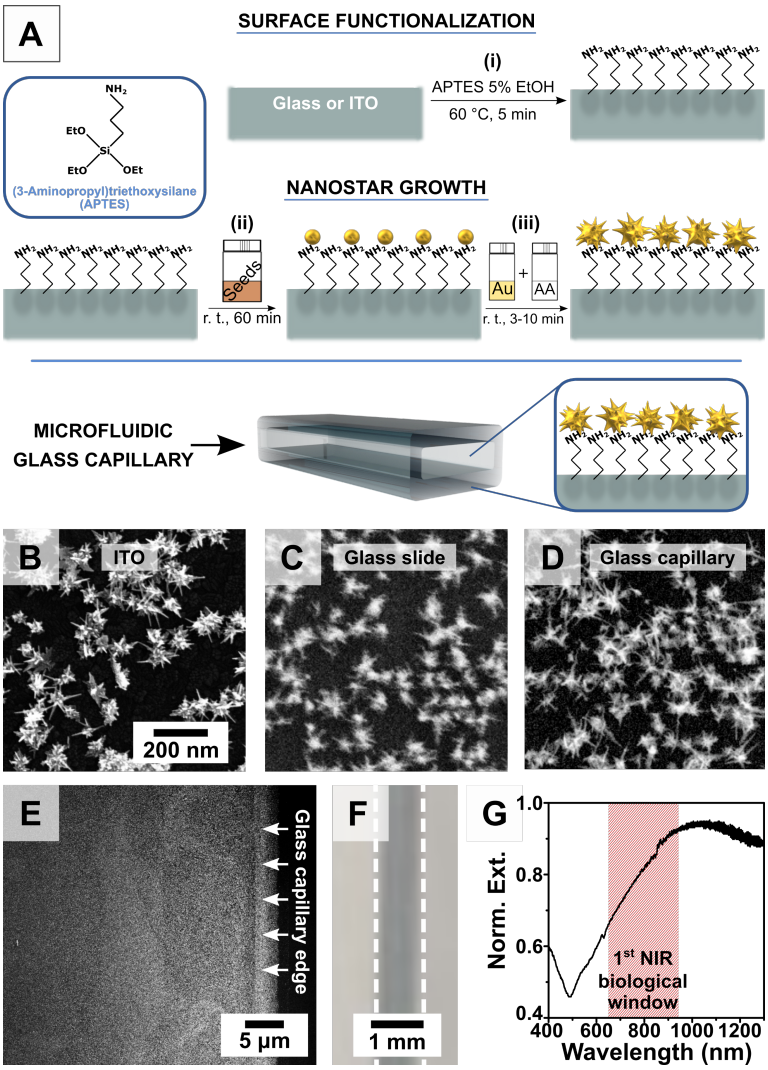

Figure 5.4. (**A**) Schematic of *in situ* seed-mediated gold nanostar growth: (*i*) indium tin oxide (ITO) and glass surface functionalization with (3-aminopropyl)triethoxysilane (APTES), (*ii*) tethering of catalytic seeds, and (*iii*) incubation (*top*) or flow (for microfluidic capillaries, *bottom*) of growth solution containing tetrachloroauric acid, silver nitrate, laurylsulfobetaine, and ascorbic acid (AA). Scanning electron microscopy images of gold nanostars on (**B**) ITO and (**C**) glass slides, and (**D, E**) within glass microcapillaries (all shown at the same scale). (**F**) Digital photograph showing blue capillary coloration following flow of growth solution and (**G**) ultraviolet–visible spectrum of the nanostar-coated capillary. The red area indicates the first near-infrared biological window.

We achieved uniform AuNST coatings on ITO (**Figure 5.4B**), glass slides (**Figure 5.4C**), and along the internal walls of glass microcapillaries (**Figure 5.4D,E**). The final products yield

films that appear blue in color with a broad LSPR peak at *ca.* 975 nm after flowing growth solution for 3 min (**Figure 5.4F,G**). Silver nitrate is known to play an important role in the shape control of anisotropic nanoparticles.[31] Recalibration of the silver concentration in the growth solution confirmed that nanostructures with the highest near-infrared extinction were produced with the same concentration used for conducting the synthesis in a colloidal suspension (**Figure 5.5**). This observation suggests that the optimal colloidal shape-directing reagent concentrations are directly translatable to growth in flow.

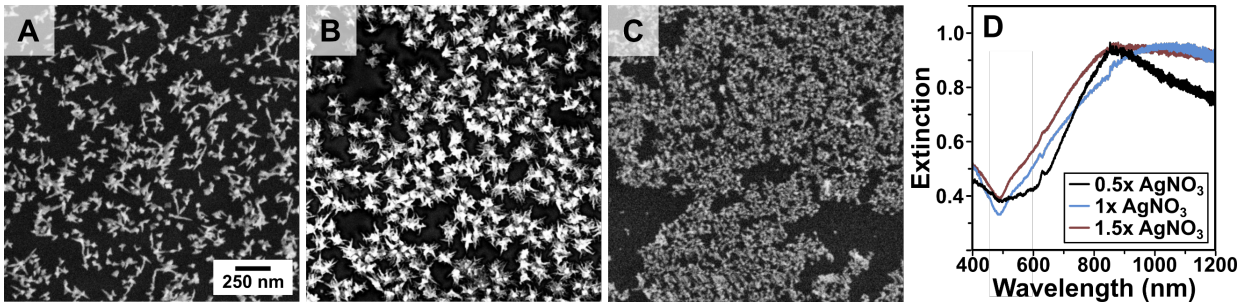

Figure 5.5. Scanning electron microscopy images showing products with **A:** 33 µM (0.5×), **B:** 75 µM (1.0×), and **C:** 108 µM (1.5×) $AgNO_3$ in the growth solution, and **D:** the corresponding ultraviolet-visible spectra.

The AuNSTs grown *in situ* were characterized by scanning electron microscopy (SEM) and were found to have branches with average aspect ratio of 3 ± 1, and an average of 7 ± 2 branches per AuNST without accounting for hyperbranching (n=3, 150 nanoparticles each). Moreover, flow can increase the rate at which the gold precursor is delivered to the surface-bound seeds, requiring shorter growth times (3 min) to achieve branched products in flow compared to the 10 min growth time necessary for slides or wafers. The AuNSTs grown *in situ* on flat substrates and in rectangular microcapillaries had 2.4× higher average aspect ratio and nearly twice the branching of those synthesized in solution (**Figure 5.6** and **Table 5.1**).

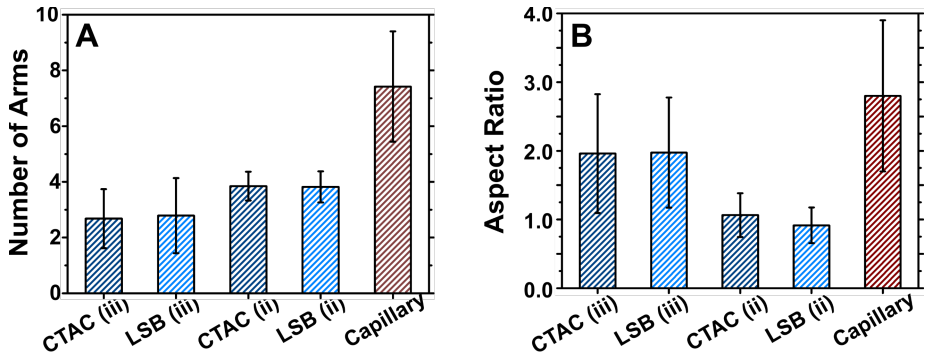

Figure 5.6. A: The average number of arms obtained by analyzing 150 particles of each type. Low aspect ratio (AR) corresponds to product **Figure 5.3A**(ii) and **Figure 5.3B**(ii) for LSB- and CTAC-capped seeds, respectively. High AR corresponds to products shown in **Figure 5.3A**(iii) and **Figure 5.3B**(iii) for LSB- and CTAC-capped seeds, respectively. **B:** The average aspect ratio (arm length/arm base width) for 150 of each product.

Table 5. 1. Comparison of colloidal and in situ products. CTAC: cetyltrimethylammonium chloride; LSB: laurylsulfobetaine

Particle	Growth Method	Seed Capping Ligand	Core (nm)	Aspect Ratio (arm length/base)	Branches
Spheroids	Colloid	LSB	13 ± 2	--	--
Low aspect ratio	Colloid	LSB	13 ± 3	0.9 ± 0.3	3.8 ± 0.6
High aspect ratio	Colloid	LSB	14 ± 3	2.0 ± 0.8	3 ± 1
Spheroids	Colloid	CTAC	12 ± 2	--	--
Low aspect ratio	Colloid	CTAC	16 ± 3	1.1 ± 0.3	3.8 ± 0.5
High aspect ratio	Colloid	CTAC	16 ± 3	2.2 ± 0.9	3 ± 1
High aspect ratio	Microfluidic	CTAC	40 ± 10	3 ± 1	7 ± 2

On the substrate, the effective ratio of gold precursor to the seeds depends on factors absent in standard colloidal growth, including the yield of APTES functionalization and seed deposition. In the case of the microfluidic capillary, the flow profile and rate must also be considered. Given

these factors, the higher yield of high aspect ratio products on both the flat substrates and the capillary can be attributed to the spatial restrictions for growth from the surface-bound seeds. Furthermore, byproduct deposition is prevented by removal of the substrates from the growth solution or by flowing the growth solution out of the capillary prior to significant secondary nucleation. More detailed analysis of the products *in situ* are shown in **Figure 5.7**.

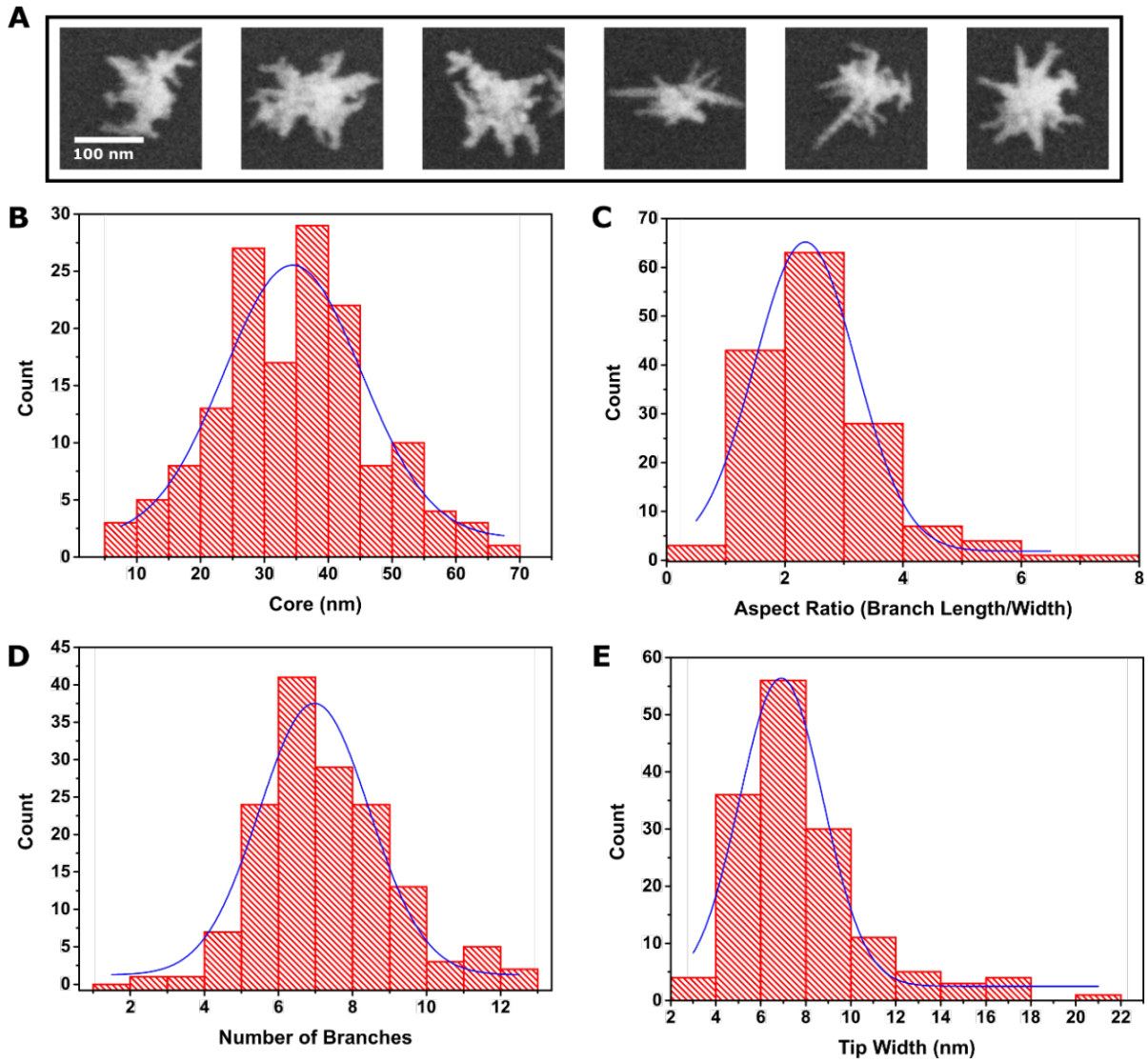

Figure 5.7. A: Scanning electron microscopy images of representative gold nanostars grown *in situ* on a glass capillary. Histograms showing measurements (150 nanoparticles for each) of the nanostars' **B:** core diameter, **C:** aspect ratio, **D:** number of branches, and **E:** tip width.

When the synthesis is performed under flow, there are several factors affecting nanoparticle morphology, such as the volume of growth solution passed through the microfluidic channel, *i.e.*, the "growth time" (**Figure 5.8A-E**), and the flow rate used (**Figure 5.8F-J**).

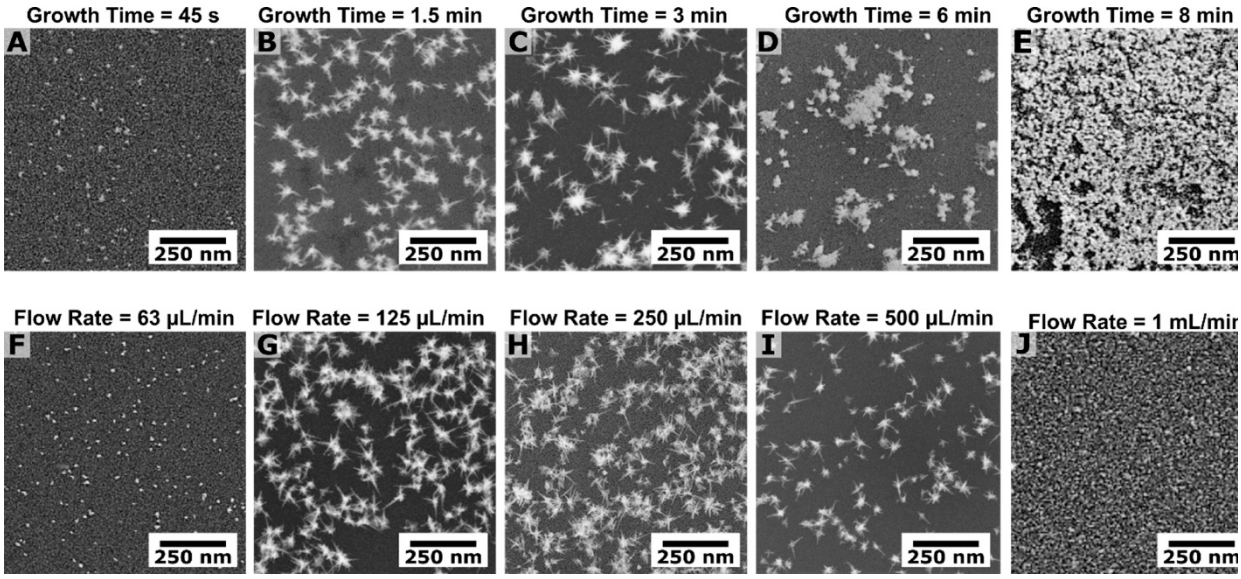

Figure 5.8. A-E: Gold nanostars grown at the various growth times shown, all with flow rate 250 µL/min and **F-J:** flow rates, all with 3 min growth times. Products shown in panel **C** and **H** represent the standard growth conditions.

Nanostars grown over short time periods lacked branching, likely due to insufficient quantities of growth solution within the microcapillary (**Figure 5.8A**). Nanostructures grown for greater than 6 min at the same flow rate produced overgrown nanoparticle films, consistent with the introduction of excess gold precursor (**Figure 5.8E**). Conditions generating products shown in **Figure 5.8C,H** have 3 min growth times, which ensured that enough growth solution passed through the microfluidic system without leading to significant secondary nucleation (**Figure 5.2**) and appear to yield the desired highly branched, high aspect ratio products more reproducibly than those grown at different flow rates (**Figure 5.9**). Assuming lateral diffusion was negligible, the flow rate should dictate the deposition of gold atoms onto the seeds, where faster flow rates are expected

to produce structures with the highest anisotropy and branching. However, both the lowest and highest flow rates yielded particles with minimal branching and low aspect ratio (**Figure 5.8F,J**).

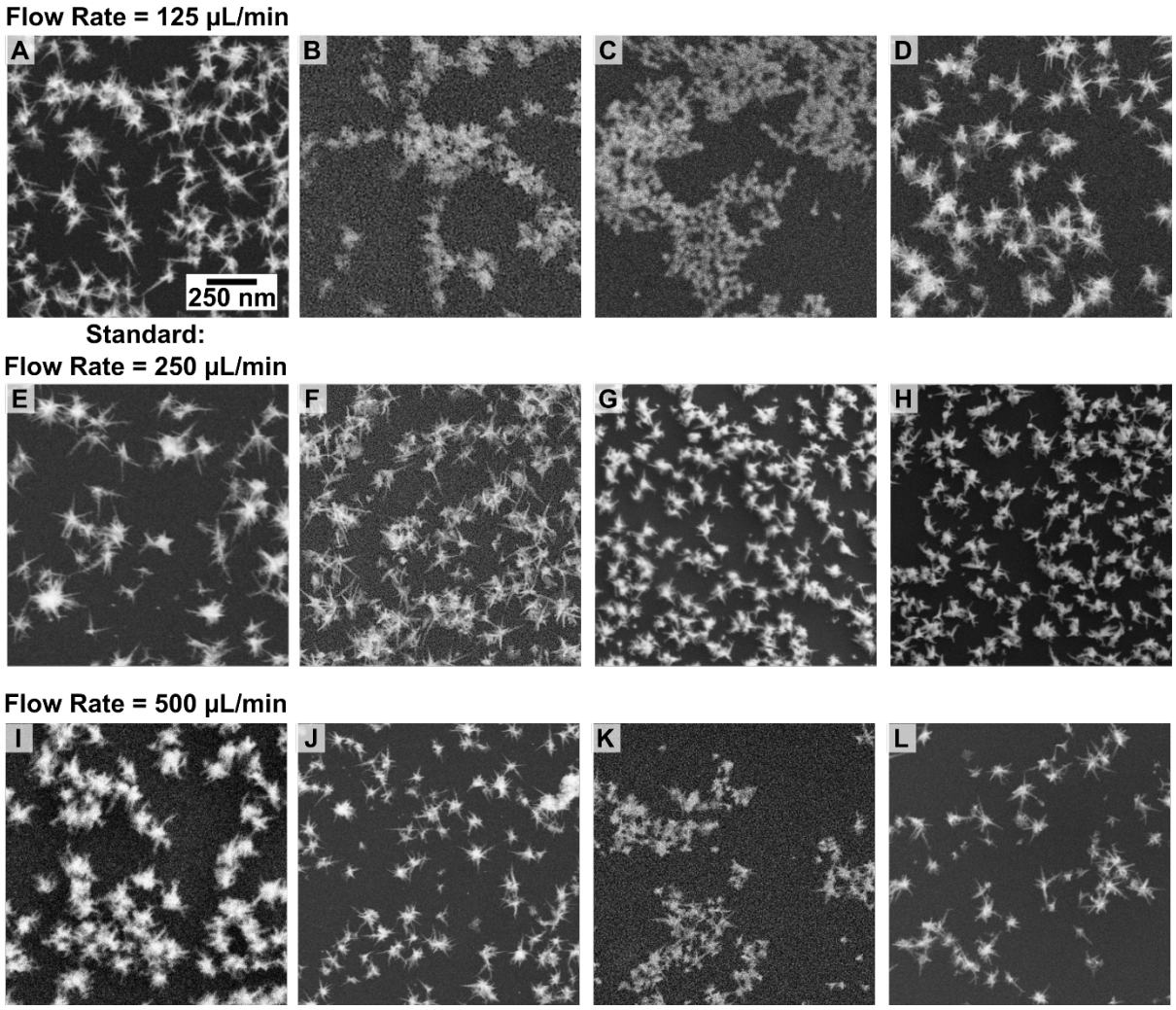

Figure 5.9. Scanning electron microscopy images showing the products grown in four different capillaries for each flow rate shown: **A-D:** Samples grown at half the standard rate, **E-H:** samples prepared under "standard" flow conditions, and **I-L:** samples prepared using double the standard flow rate. Growth solution was flowed through the capillary for ~3 min (± 30 s) for each sample. All images are shown at the same magnification.

We expect that several factors affect the spatial distributions of the nanostructures, including variabilities in the flow rate and profile within the capillaries due to sample-to-sample differences in capillary positioning within the tubing, the yield of APTES functionalization, and

seed anchoring. The branched particles were synthesized under laminar conditions (Reynold's number, $R_e \sim 8.5$), and we infer that the flow has profound effects on AuNST morphology, since the products found at the outlet of the capillary have much less branching than those present at the inlet and center (**Figure 5.10**). Ultimately, the optimized *in situ* synthetic parameters provide a useful method for functionalizing oxide substrates of arbitrary geometries with dense coatings of shape-controlled products (additional images shown in **Figure 5.11**) and demonstrate the potential for accessing different nanoparticle morphologies through the careful design and incorporation of fluid flow into the synthesis.

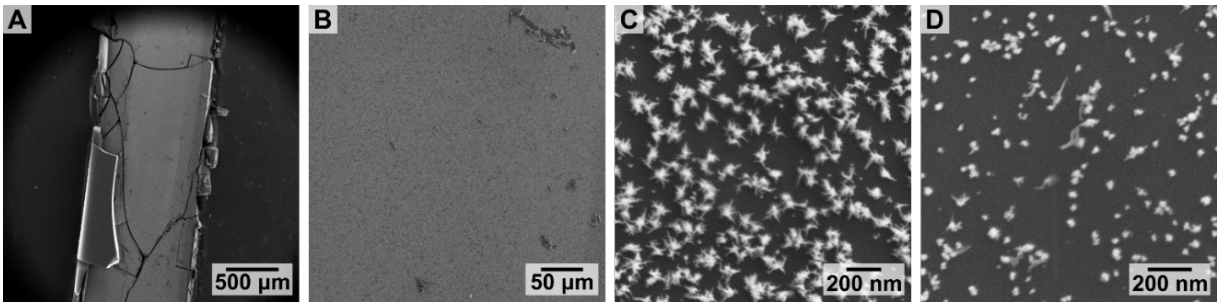

Figure 5.10. Scanning electron microscopy images of a split capillary at **A-B:** lower magnification, and at higher magnification **C:** showing products in the first *ca*. two-thirds of the capillary and **D:** products near the outlet of the same capillary.

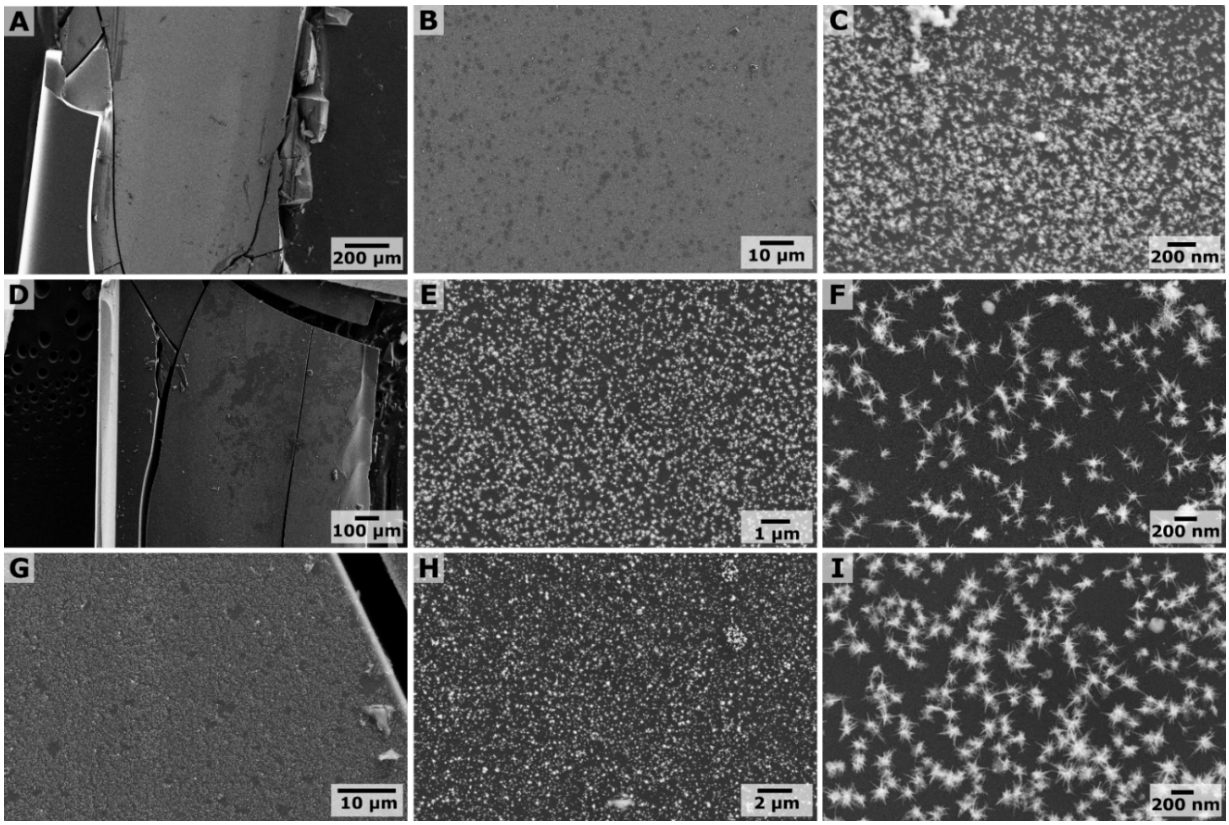

Figure 5.11. Scanning electron microscopy images showing three different capillaries prepared under standard growth conditions (3 min, 250 µL/min flow; one row=one sample) at different magnifications.

5.2.3. *In situ* nanostars overgrowth in polydimethylsiloxane-microfluidics

Microfluidic channels made of PDMS are commonly used in devices that implement different flow profiles, such as embedded barrier, herringbone, and other micromixers (**Section 1.2.3**).[17,42,43] The introduction of vertical mixing in these devices is useful for applications like particle or cell sorting, can facilitate exchange of reagents within the channel,[14,17,44–46] and can be useful for developing novel diagnostic tools or sensors that take advantage of the size-related properties of plasmonic AuNSTs.[27,47,48] Our unconventional synthetic strategy enables us to test the effects of fluid flow profile on the *in situ* shape control of the plasmonic structures. Here, we probe how these factors can be controlled to optimize AuNST growth in channels with three-

dimensional (3D) features and under different flow environments. Specifically, we fabricate and compare "featureless" microfluidic channels with a laminar flow profile and "herringbone" micromixers that have 3D staggered herringbone features that promote vertical mass exchange (**Figure 5.12**).[43,47,49]

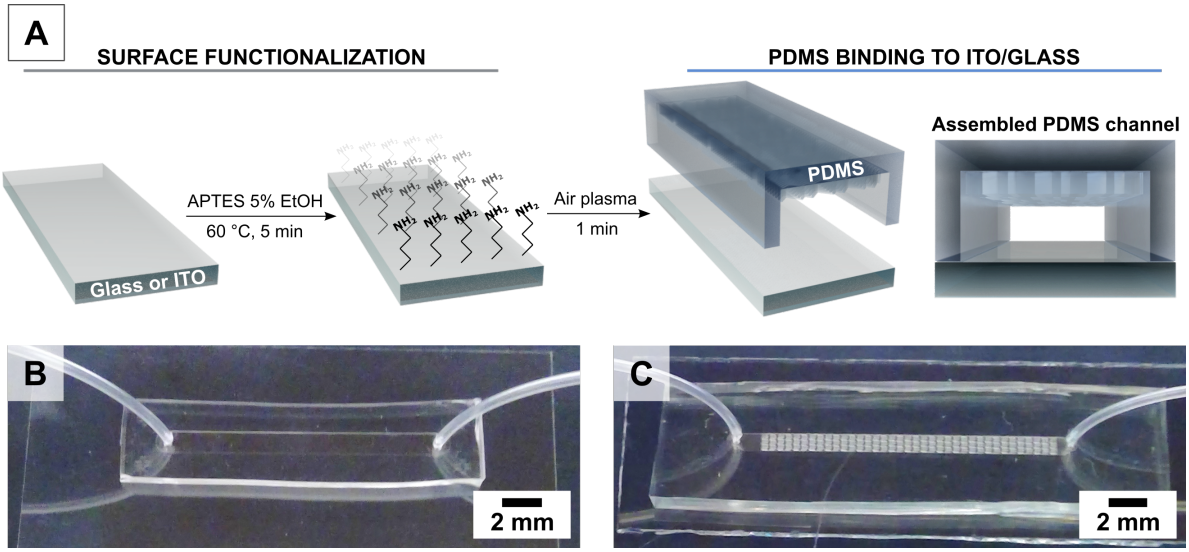

Figure 5.12. A: Schematic of substrate surface functionalization and binding of polydimethyl siloxane (PDMS) microchannels. For indium tin oxide (ITO) substrates, (3-aminopropyl)triethoxy silane is used to facilitate binding during the device assembly step. **B,C:** Digital photographs of a (**B**) featureless and (**C**) herringbone PDMS channel.

Although the PDMS channels readily bind to air or oxygen plasma treated glass *via* condensation reaction, we observed that PDMS could not be strongly bound to ITO with this same method. Therefore, in order to facilitate binding of the PDMS channel with ITO, we first functionalized the ITO-coated glass with APTES as an adhesion layer. The air plasma treatment of the APTES-functionalized ITO and the PDMS channel resulted in the activation of both surfaces so that strong binding and a liquid-tight seal could be achieved (**Figure 5.12A, Figure 5.13**). The control experiments presented in **Figure 5.13** show that leakage occurs within 5 min after flowing

solutions with different viscosities between 150 and 500 µL/min in channels that did not have both an APTES coating and air plasma treatment.

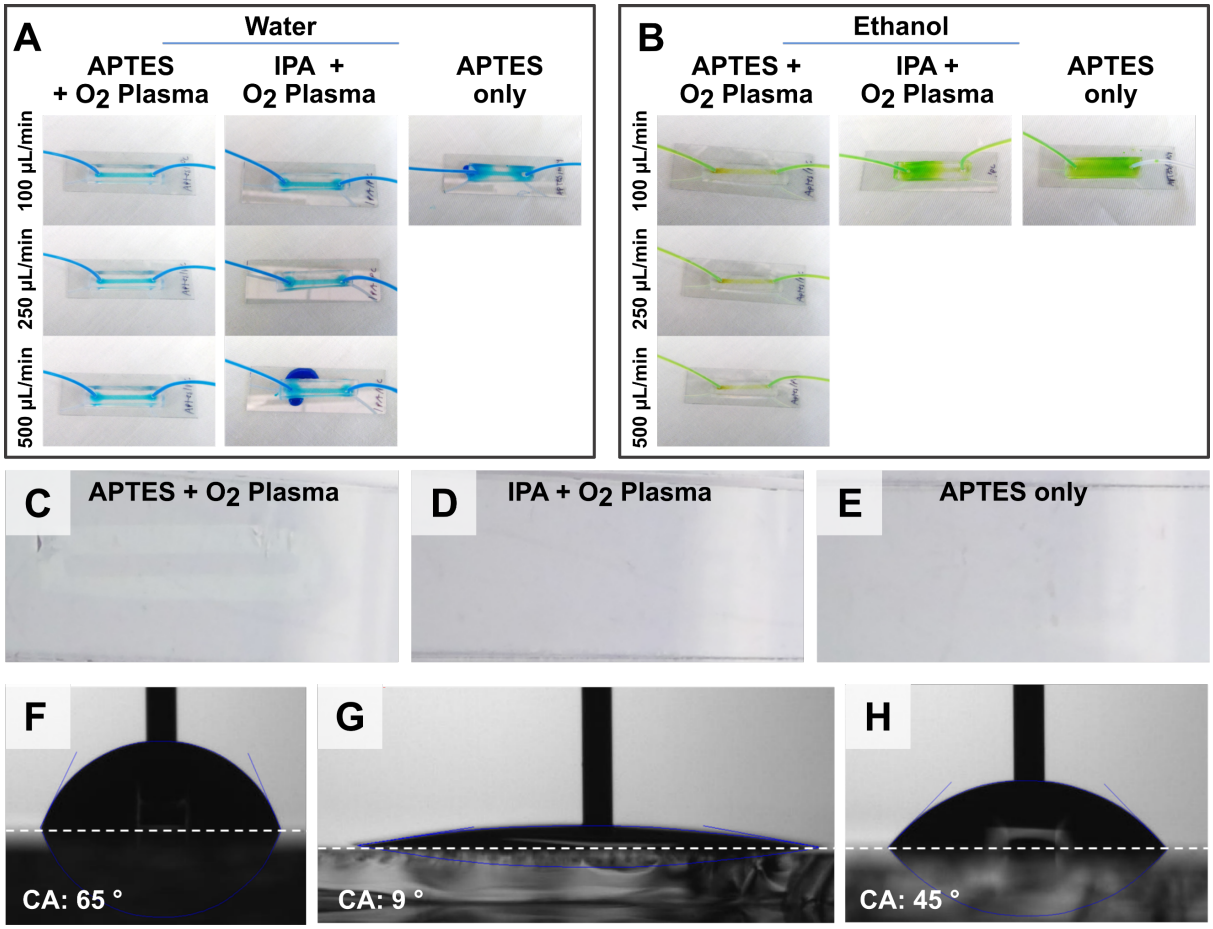

Figure 5.13. A: Digital photographs of polydimethylsiloxane (PDMS) channels bound to indium tin oxide (ITO) substrates under different conditions after flowing (**A**) water and (**B**) ethanol**.** *Left to right:* after (3-aminopropyl)triethoxysilane (APTES) functionalization and air plasma activation, after rinsing with isopropyl alcohol (IPA) and air plasma treatment, and after only the APTES functionalization. Each row represents a different rate of flow tested over a 5 min period. Absent photographs indicate conditions where device failure occurred within the first 30s of testing. **C-E:** Digital photographs of the underlying ITO-coated substrate after removal of the channel assembled with different surface treatments. **F-H:** Contact angle goniometry measurements of water on the ITO substrate after (**F**) the first APTES functionalization step, (**G**) after air plasma activation, and (**H**) after the second APTES functionalization step.

In **Figure 5.13C-E**, the strength of the PDMS-ITO binding can be further appreciated, where the subsequent removal of the PDMS channel leads to removal of the ITO coating from the

underlying glass substrate. This effect is observed when the complete binding protocol is followed. In order to attach the gold seeds and perform *in situ* AuNST overgrowth, as described in the previous sections, the channels need to be re-functionalized with APTES. We used water contact angle goniometry to test how the surface chemistry of the ITO changed following an initial coating with APTES, then air plasma treatment, and finally, the second APTES functionalization step (**Figure 5.13F-H**).

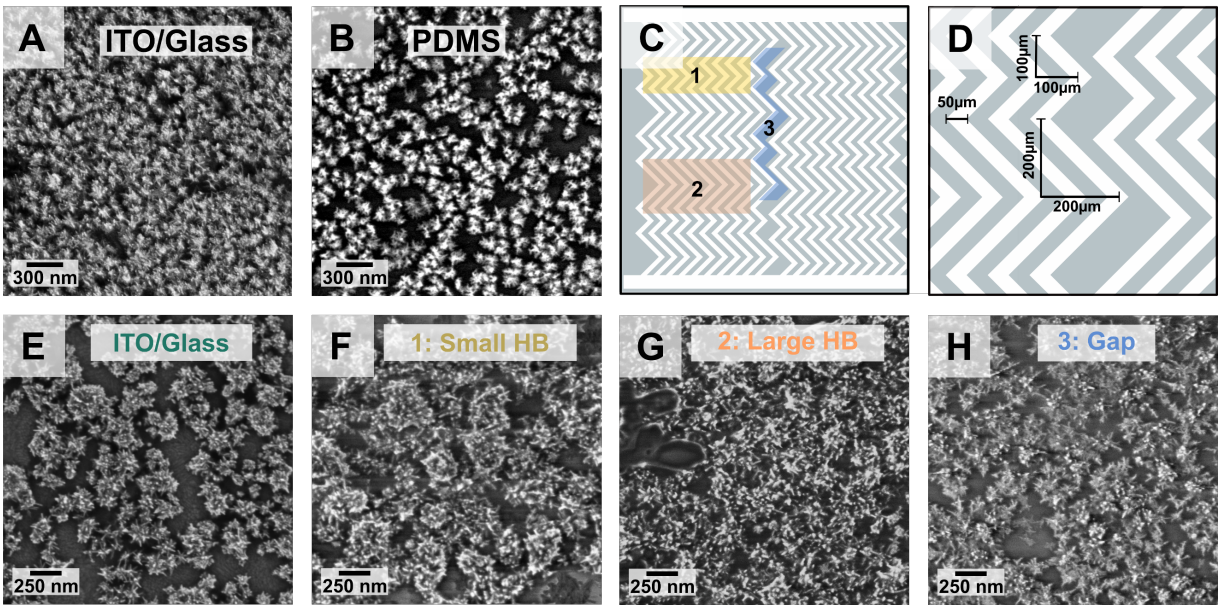

Figure 5.14. A,B: Scanning electron microscopy images of the branched products grown on (**A**) indium tin oxide (ITO)/glass and (**B**) polydimethylsiloxane (PDMS) in a featureless channel. **C,D:** Schematics showing different areas and dimensions of the herringbone PDMS channel. **E-H:** Scanning electron microscopy images of gold nanostars grown on the (**E**) substrate (ITO or glass), (**F**) the small herringbone (HB) feature (*area 1*), (**G**) the large HB feature (*area 2*) and (**H**) the gap between the HB repeats (*area 3*).

Although the second APTES layer yielded a lower contact angle than the initial one, it appeared that the second functionalization led to changes in surface hydrophilicity, indicating that the functionalization was at least partially successful. Moving forward, although the difference in contact angle potentially suggests that the density or organization of the APTES on the surface

does change between the initial and latter functionalization steps, we show that overall the formation of dense AuNST layers on the ITO was achieved (**Figure 5.14**). With the optimized fabrication method and growth solution recipe described in the previous section, environmental SEM revealed branched structures on the PDMS channel and the ITO and glass substrates. In herringbone channels, AuNSTs were present at all areas within the 3D features, namely the "small herringbone," "large herringbone," and "gap" features indicated in **Figure 5.14E-H**. Because PDMS is naturally hydrophobic, the assembled channels were exposed to air plasma treatment for 1 min to assist in wetting and the removal of trapped air bubbles, which could be especially problematic for the herringbone channels with 3D features (**Figure 5.15**). When the second air plasma treatment is not performed, it is common to observe growth defects like those shown in **Figure 5.16A**, where the gap areas have non-uniform AuNST coverage due to poor wetting. Interestingly, by visual inspection, the density of the particles matches the modeled flow profile. Simulations show that the simulated trajectories of 10 nm objects is concentrated away from the "peaks" of the herringbones as indicated by the dotted red lines (COMSOL Multiphysics package, **Figure 5.16A,C,D**). Overall, this observation indicates that the reaction occurs in the flow-limited regime, where the kinetics of the reaction is determined by the flow rate more so than the rate of precursor reduction on the gold seeds. Compared to the glass capillaries, the PDMS-ITO channels enable us to more easily and directly perform high vacuum electron microscopy characterization. Therefore, we are able to carry out more detailed studies on the products observed at different locations within the channel (inlet, center, outlet) and under different flow conditions using this channel configuration.

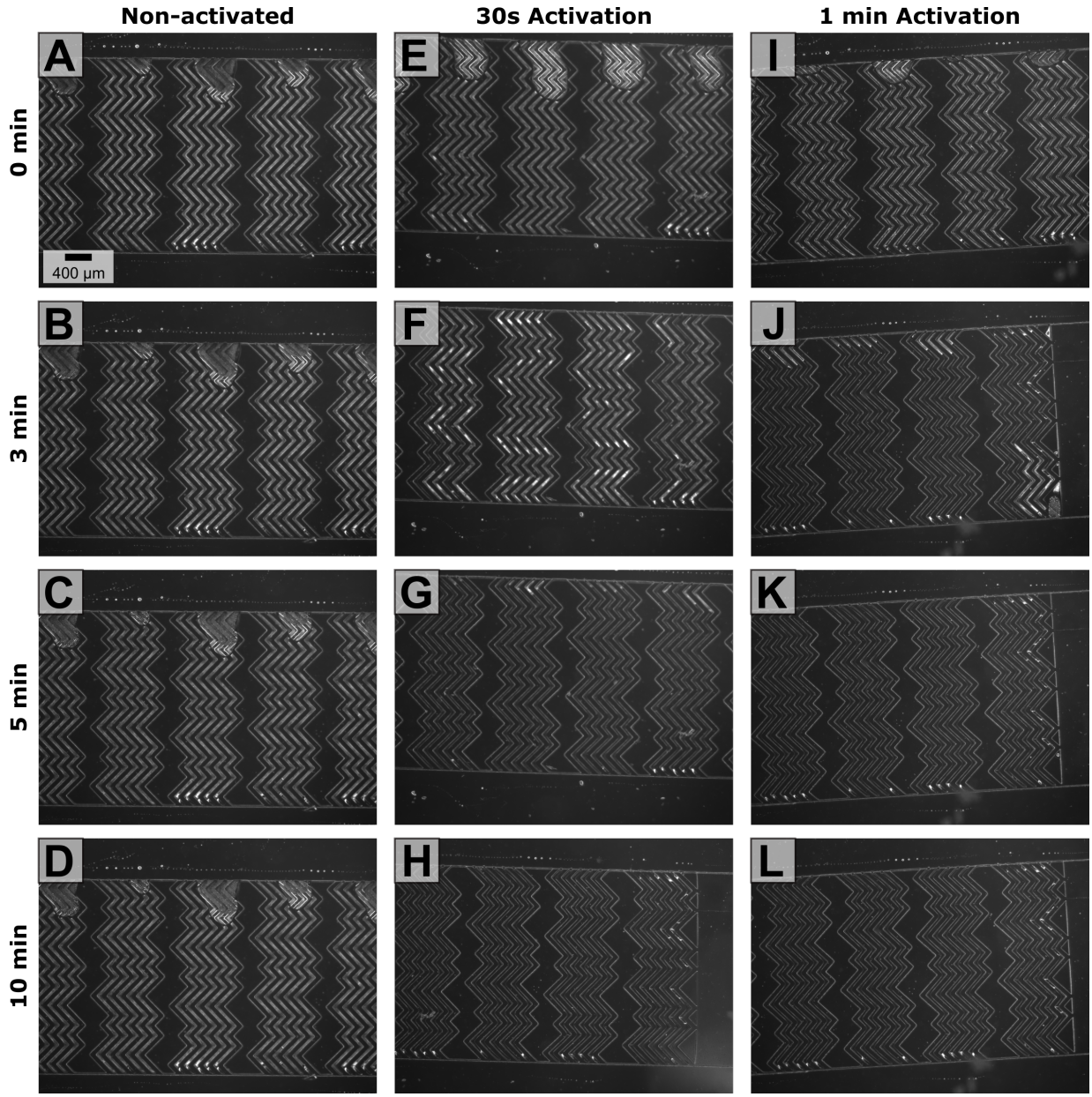

Figure 5.15. A-L: Optical microscope images of water flowing at 250 µL/min for the indicated time (*left*) through polydimethylsiloxane – indium tin oxide channels after (**A-D**) 0 s, (**E-H**) 30 s, and (**I-L**) 1 min air plasma activation.

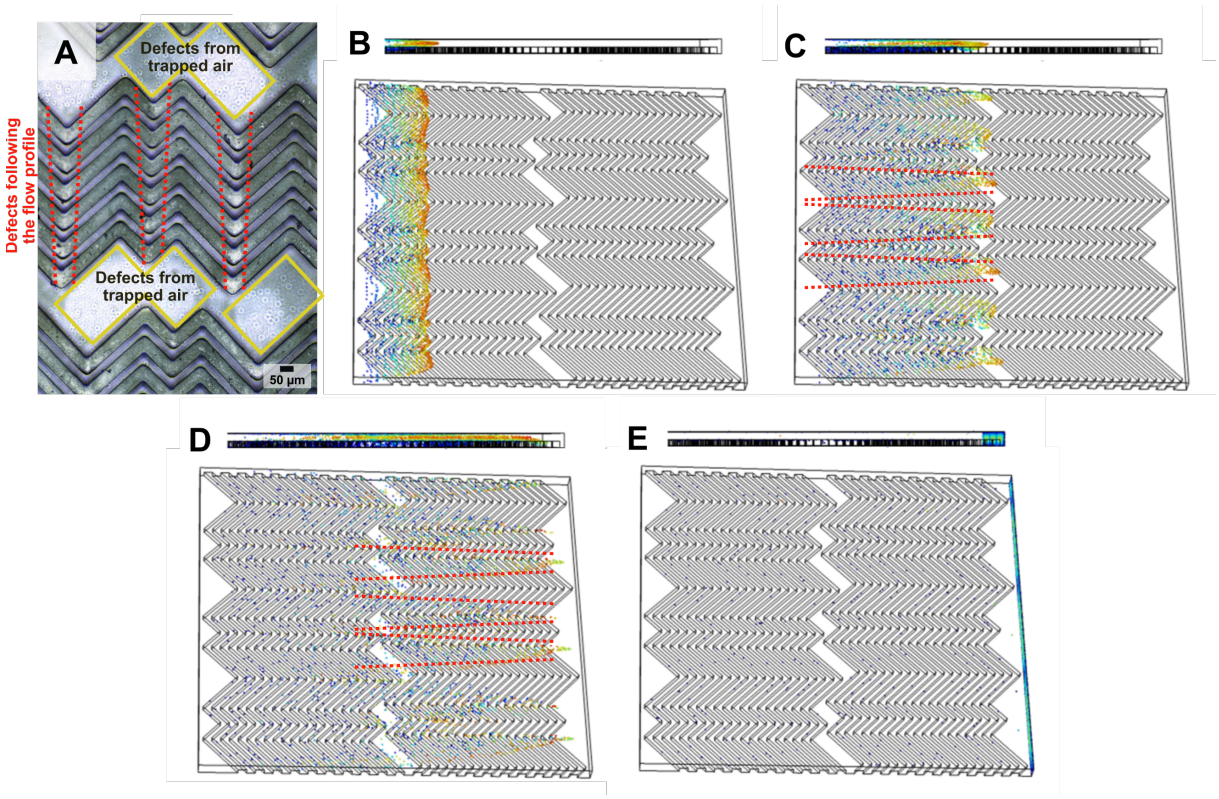

Figure 5.16. A: Bright-field microscope image of the PDMS of the herringbone (HB) channel after growth showing potential effect of bubbles (yellow outlined regions) due to presence of three-dimensional features. **B-E:** Snapshots of simulated particle tracing in the HB channel with time (increasing time in order from **B-E**), showing the trajectories of 10 nm sized objects at 250 µL/min. The red lines are guides for the eye showing how the flow appears to be directed away from the "peaks" of the herringbones, matching the low-density areas observed at the peaks in panel **A**.

Recently, *in situ* growth schemes have been applied to create substrates with gradient colloid arrays where the nanostructures exhibit decreasing degrees of branching along the substrate.[50] These "plasmonic libraries" are useful for rapidly screening the SERS efficiencies of different AuNST morphologies. However, these prior studies use time-consuming self-assembly processes to establish these gradients. Here, we directly create AuNST gradients within 3 min by leveraging the depletion of reagents in laminar flow. The formation of gradients is caused by consumption of reagents near the surface as the solution flows through the channel (there is no significant vertical mass transfer **Figure 5.16**). In the featureless channels, the observation of a

product gradient is consistent with the previously discussed results from *in situ* overgrowth in glass capillaries (see **Section 5.2.2**).

Gradient formation was also seen in herringbone channels. This observation is somewhat surprising considering that one could hypothesize that the introduction of vertical mixing would help replenish the reagents at the substrate walls with reagents from the "bulk" of the flowing growth solution. The electron microscopy images of AuNSTs at the inlet, center, and outlet (**Figure 5.17B-D**) of the channels were converted to black and white images and the percentages of white pixels were determined using MATLAB to evaluate the surface coverages of gold (**Figure 5.17E**). Using these analyses, the gold coverage in the featureless and herringbone channels was observed to decrease significantly from the inlet to the outlet, by ~20 % for samples grown close to the optimal flow rate for achieving highly branched structures (50-100 μL/min). Here, we find that although there is vertical mixing in the herringbone channel, the gold precursor still appears to be consumed quickly when reaching the substrate-bound seeds, significantly reducing the overall concentration of the growth solution at the outlet. Thus, we hypothesize that this result is another indication that the synthesis is flow limited and the reduction of the gold precursor onto the seed does not appear to be the rate-determining step.

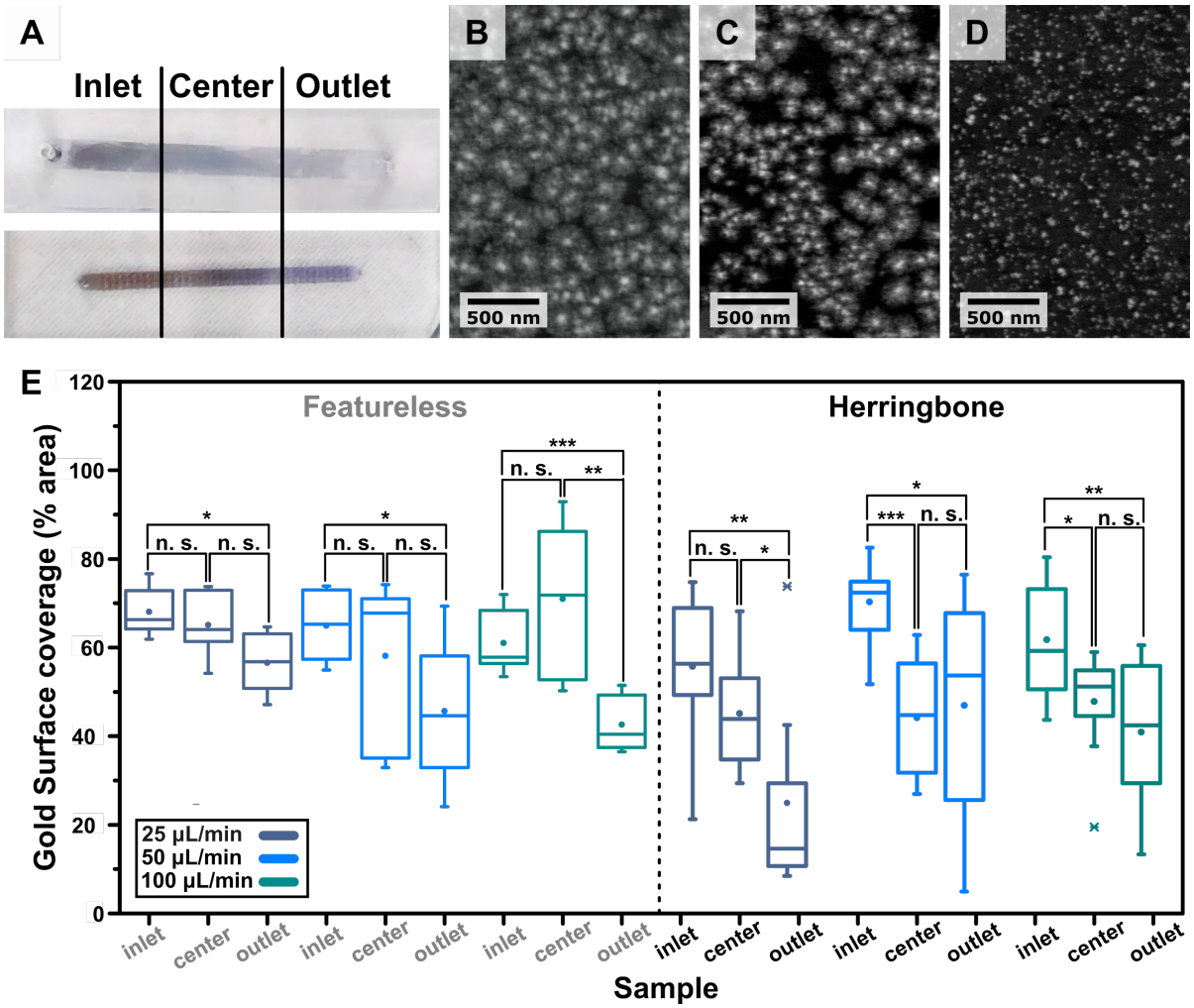

Figure 5.17. A: Digital photographs showing the gradient from inlet to outlet (*left to right*) for nanostars grown in the featureless (*top*) and herringbone (HB, *bottom*) channels. **B-D:** Scanning electron microscopy images of the products at the (**B**) inlet, (**C**) center, and (**D**) outlet of a herringbone channel grown at 150 µL/min flow rate. **E:** Box graph showing differences in gold coverage between the inlet, center, and outlet regions of the products grown in featureless (*left*) and HB channels (*right*) at different flow rates.

If the growth is flow limited, then the products should change when different flow rates are applied. For example, one could predict that lower flow rates would produce smaller or less developed structures compared to higher flow rates over the same growth time (resulting in different total flow volumes). To test this hypothesis, we examined growth at flow rates at a wider range, from 25 to 1000 µL/min, in both featureless (**Figure 5.18**) and herringbone channels (**Figure 5.19**) and performed analyses on obtained SEM images. The highest rate value was

selected since it is the maximum flow rate that PDMS-ITO microchannels can usually withstand without delamination. The density and size of the AuNSTs were quantified *via* SEM along with the percentage of surface gold coverage as described earlier (**Figure 5.20**). For featureless channels, changing the flow rate between 25 and 500 µL/min still does not significantly affect the size (~100 nm), density (~60 AuNSTs/µm^2), nor percentage of gold coverage (~50%) (**Figure 5.20A,C,E**) until 1 mL/min is applied and the structures start to overgrow into films. In the herringbone channel, a similar trend is observed where the average size (~60 nm), density (~100 AuNSTs/µm^2), and gold coverage (~50%) remain relatively unchanged until films are fabricated at 250 µL/min after excessive growth (**Figure 5.20B,D,F**).

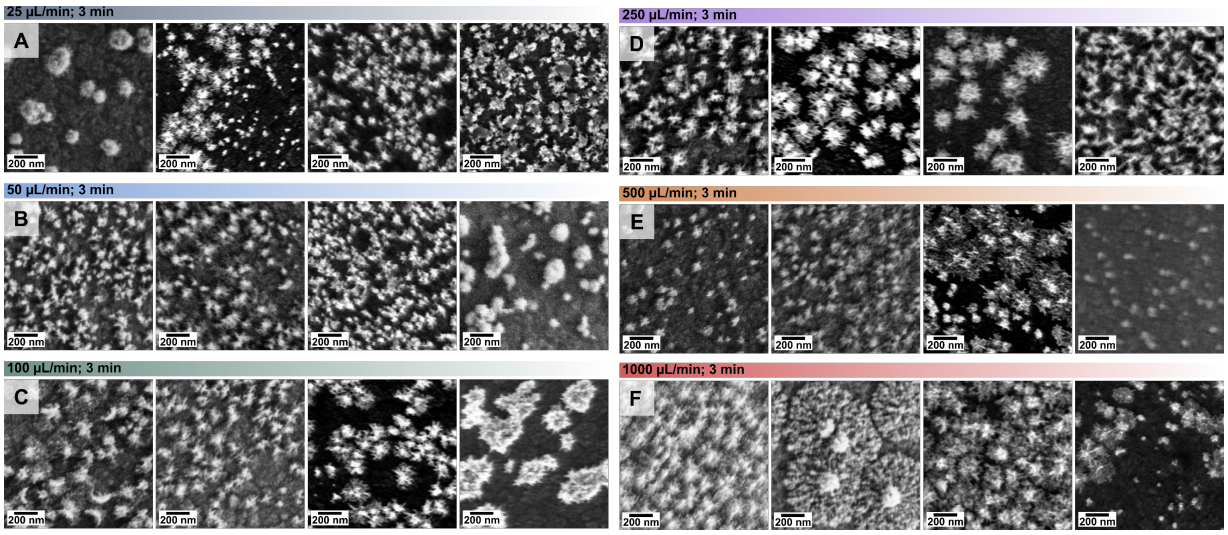

Figure 5.18. Scanning electron microscopy images of branched products on the indium tin oxide substrate after flowing growth solution for 3 min at the indicated flow rate in the featureless channels. Each image in the row for each tested flow rate corresponds to a separate sample. Excessive growth into films is increasingly observed at 1 mL/min, and the device begins to fail at higher flow rates.

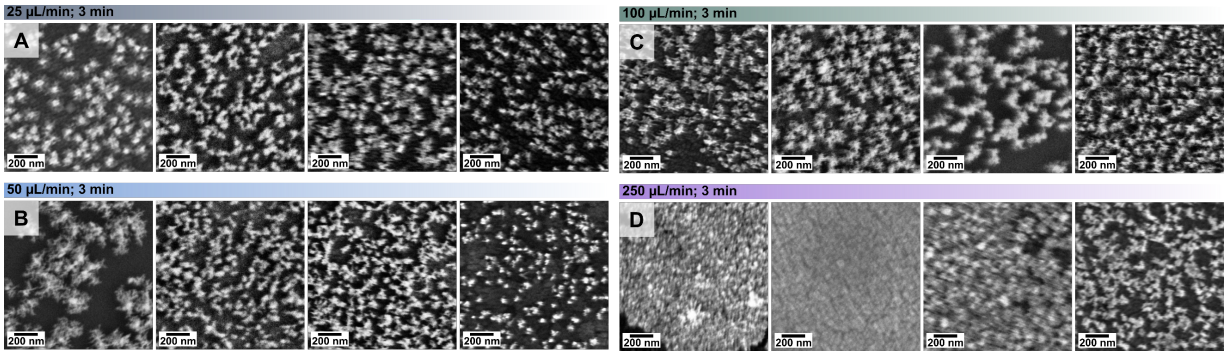

Figure 5.19. Scanning electron microscopy images of branched products on the indium tin oxide substrate after flowing growth solution for 3 min at the indicated flow rate in the herringbone (HB) channels. Each image in the row for each tested flow rate corresponds to a separate sample. For the HB channels, flow rates above 250 µL/min are not shown because this is the point at which the appearance of gold films dominates.

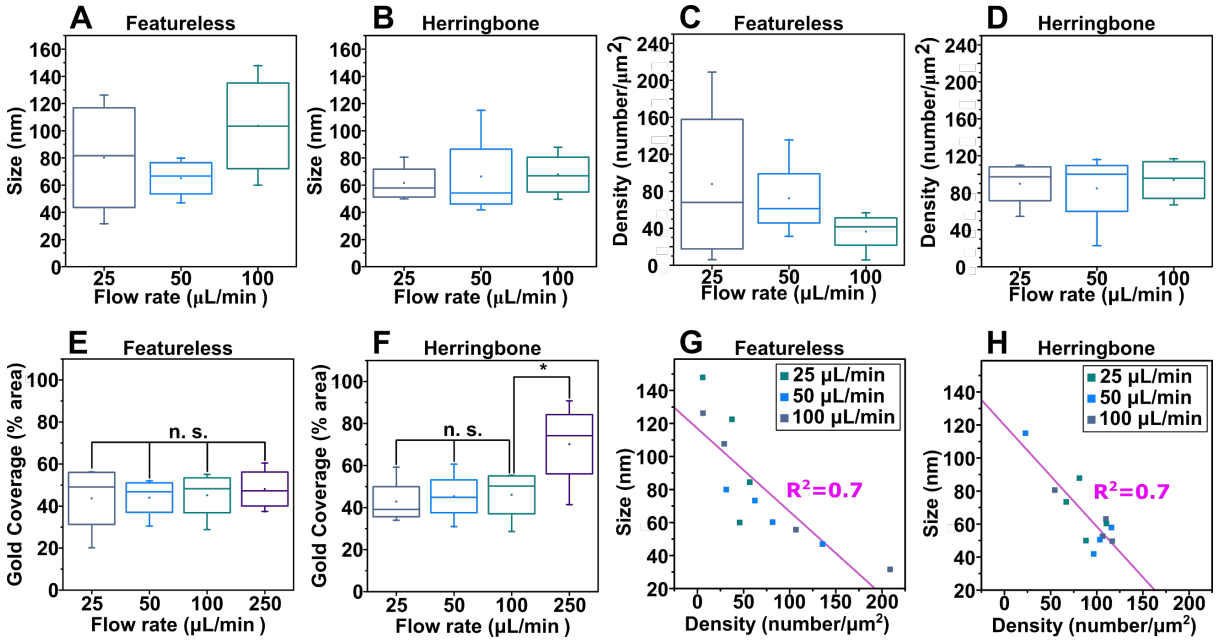

Figure 5.20. A-F: Box graphs of measured nanostar (**A,B**) size, (**C,D**) density, and (**E,F**) overall percent surface coverage of gold for featureless and herringbone devices. Relationship of particle size to density for (**G**) featureless and (**H**) herringbone channels.

These evaluations show that herringbone channels reach the point of excessive growth into gold films at lower flow rates than featureless channels, indicating that vertical mixing leads to more efficient consumption of the growth reagents. Although a difference in products at flow rates from 25-100 µL/min is not significant, comparing the product density to the nanoparticle size

provides some insight into this result. In both the featureless and herringbone channels, the size and density have weak negative correlations at all flow rates tested. Even though there is evidence that the growth is flow limited (growth in the herringbone following the simulated flow profile, product gradients from the inlet to outlet, excessive growth at high flow rate), it appears that at low flow rates the density of the nanostructures, resulting from the yield of the APTES coating and seed attachment, has a greater effect on the product size than the flow rate. Thus, high reproducibility in nuclei density in *in situ* growth schemes appears to be important for performing more detailed studies focused on understanding how flow parameters can be modulated to alter substrate-grown nanostructures. It was found that the herringbone channels generally result in products that are smaller and denser than the featureless channels, while also giving more reproducible density values. Therefore, the mixing in the channel possibly facilitates better uniformity of the APTES coating and seeding steps. Thus, selecting a microfluidic geometry with more efficient mixing could be used to improve the seeding uniformity. This result provides significant observations that can inform future advancements of *in situ* growth in microfluidic channels.

Next, we performed spectroscopic analyses of the growth solution exiting the microfluidic channel in order to understand the observation of excessive growth in the herringbone channel at 250 µL/min further (**Figure 5.21A**). Even without the addition of seeds, the gold precursor in the growth solution will eventually be spontaneously reduced and particles will be formed. The absorbance at 400 nm is dominated by interband transitions in metallic gold.[51,52] Therefore, the intensity of the absorbance at 400 nm can be used to compare the amount of reduced gold present in the sample regardless of particle size or shape.[53,54] From our spectroscopic measurements, the

reduction of gold precursor in the growth solution at the outlet is complete after 2 h (at this point the spectra stop changing, **Figure 5.21B**).

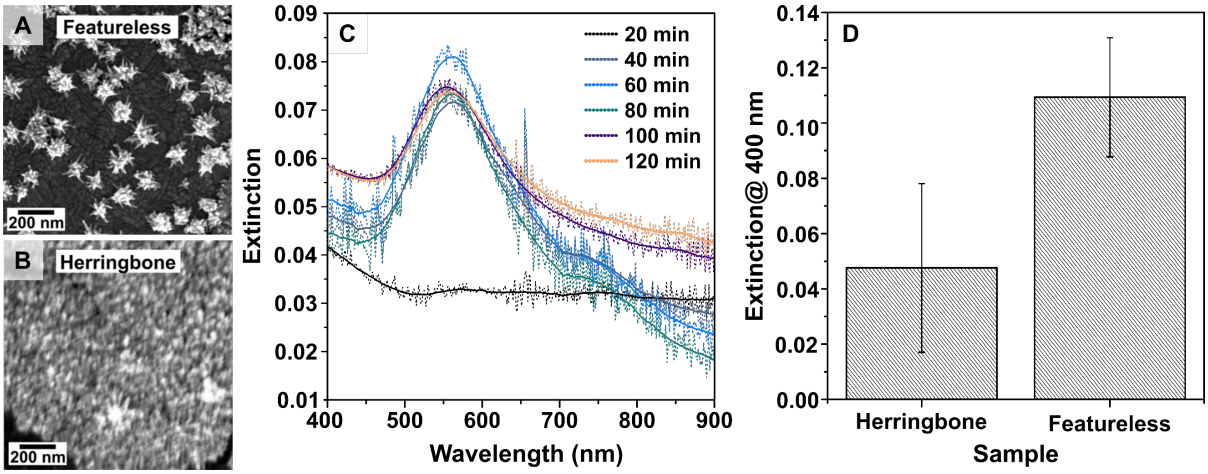

Figure 5.21. A: Products at 250 µL/min in a featureless channel and **B:** a herringbone channel. **C:** Extinction at 400 nm of the growth solution collected at the outlet, comparing herringbone and featureless channels at 250 µL/min.

We collected the aged outlet solution and obtained UV-visible spectra to compare the amount of gold that remained in the growth solution after the synthesis.[53,54] Overall, we find that at 250 µL/min, the extinction at 400 nm of the herringbone outlet solution is roughly half that of the featureless channels. This result is consistent with our hypothesis that gold precursor consumption is more efficient in herringbone channels.

Section 5.3. Conclusions and Prospects

We developed a seeded method for AuNST growth *in situ* on substrates with arbitrary geometries, including microfluidic devices. Our optimized synthesis applies temperature-stable CTAC-capped seeds and utilizes HCl as a handle for reducing secondary nucleation, which is a common issue for *in situ* syntheses. We applied our optimized protocol to grow AuNSTs in flow

within microcapillaries and PDMS microchannels, where growth time, flow rate, and flow profile can be tuned to manipulate AuNST morphology. A detailed electron microscopy study enabled by the implementation of semiconductor ITO as the channel substrate revealed that although the growth appears to be flow-limited, the density of the nuclei on the substrate plays a dominant role compared to flow rate in influencing the final size of the particles. However, at high flow rates, the effect of the flow limited growth is observed when densely overgrown gold films are produced. In the case of the herringbone channels, the vertical mixing leads to more efficient and rapid consumption of the growth reagents than what is achieved with channels exhibiting a laminar flow profile. Overall, with the optimized device fabrication and synthesis protocols, dense coatings of highly branched anisotropic nanostructures were rapidly formed on complex substrates, including those containing 3D features. Ultimately, our optimization of the AuNSTs in flow indicates that microreactors can be rationally designed to fabricate microfluidic devices decorated with anisotropic plasmonic nanoparticles. This work ultimately lays the groundwork for additional exploration into flow-controlled growth of shaped nanoparticles on substrates.

Section 5.4. Materials and Methods

5.4.1. Materials

All analytical grade reagents, silver nitrate ($AgNO_3$; 99%, CAS: 7761-88-8), $HAuCl_4 \cdot 3H_2O$ (99%, CAS: 16961-25-4) L-ascorbic acid (99%, CAS: 50-81-7), *N*-dodecyl-*N*,*N*-dimethyl-3-ammonio-1-propanesulfonate (LSB; 99%, CAS: D0431), hydrochloric acid (HCl; ACS Reagent 37%, CAS: 7647-01-0), (3-aminopropyl)triethoxysilane (APTES, 99%, CAS: 919-30-2), cetyltimethylammonium chloride (CTAC; 25 wt % in H_2O, CAS: 112-02-7), and thiophenol (99%, CAS: 108-98-5) were purchased from Millipore Sigma. Piranha solution (3:1 98% sulfuric

acid, CAS: 7664-93-9, and 30% hydrogen peroxide, CAS: 7722-84-1; Fisher Scientific) was used for cleaning glass capillaries. *Warning:* Piranha mixture is dangerous as it violently reacts with organics and should be handled with caution. High performance liquid chromatography (HPLC)-grade sub-micron filtered water (CAS: 67-63-0) and 200 proof ethanol (CAS: 64-17-5) were obtained from Fisher Scientific. All glassware and magnetic stir bars used for synthesis were cleaned thoroughly with *aqua regia* (3:1 concentrated HCl to HNO_3, Millipore Sigma) and rinsed with HPLC-grade water before use (nitric acid: 15.8 M, Fisher Scientific, CAS: 7697-37-2). *Warning: Aqua regia* solution is extremely corrosive and reactive. Care is needed in its preparation and usage. Polydimethylsiloxane (PDMS, Sylgard 184) was purchased from Dow Corning (Michigan, USA). Indium tin oxide (ITO) coated glass slides were purchased from MSE supplies (0.7 mm 7-10 Ohm/Sq ITO Coated Glass Substrate, 50 mm x 50 mm x 0.7 mm).

5.4.2. Colloidal gold nanostar synthesis

The AuNST synthesis was carried out using a seed-mediated growth method.[37] First, CTAC-capped seeds were prepared by adding 4.7 mL of 0.1 M CTAC with 25 μL $HAuCl_4$, followed by injection of 300 μL of 10 mM $NaBH_4$ under vigorous magnetic stirring, yielding a light brown product. A separate growth solution containing 4 mL 0.1 M LSB, 60 μL of 50 mM $HAuCl_4 \cdot 3H_2O$, and 60 μL of 10 mM $AgNO_3$ and 40 μL 1 M HCl was prepared. An aliquot of 200 μL of 100 mM ascorbic acid was added to the solution and stirred by hand until the solution turned clear. This step is immediately followed by the addition of 8 μL of the seed solution and stirred by hand. The growth solution then turned from a clear color, to pink, purple, and finally a dark blue color.

5.4.3. Preparation of functionalized glass capillaries

Glass capillaries (VitroCom, Product No.: 5010-050) 1 mm × 100 μm were cleaned with piranha solution for 30 min, sonicated 4 times with HPLC-grade water, sonicated 3 × 5 min in water, 1 × 5 min in ethanol, and oven-dried. Due to the size of the capillaries, there is a chance that residual piranha solution might remain following the rinsing step;, to ensure that all piranha solution is completely inactivated, the capillaries should be carefully dried at 60-120 °C for 1-5 d. Once completely dried, the capillaries were functionalized with APTES. The capillaries were placed in a vial containing APTES (5% v/v in ethanol), where the functionalization was performed at 60 °C for 5 min. Following functionalization, the capillaries were sonicated in ethanol three times for 5 min each and stored in ethanol (*N.B.,*– the capillaries, if stored in air, will degrade over time). Due to the small internal diameter of the capillaries, it is important to ensure that the solutions wet the entire length of the capillaries for each step, brief sonication can be used to remove bubbles. Moreover, the capillaries must be completely dry and free of any water prior to silane functionalization; otherwise, the APTES will polymerize (leading to cloudy residue in the capillary). For best results, it should be handled/stored under inert gas because APTES is air sensitive.

The APTES-functionalized capillaries were dried with nitrogen before use, and 5-min epoxy (Devcon, No. 14240) was used to secure tubing ~6 cm in length (Cole Parmer, Tygon S3-B-44-4X) onto each end of the capillary. The capillary was inserted ~1-2 mm into the tubing, to prevent the epoxy from sealing the capillary. This assembly was secured to four glass slides to prevent the capillary from breaking during handling. The epoxy was allowed to dry overnight, and the capillary was rinsed twice by hand with a 5 mL syringe of HPLC water before the growth step.

5.4.4. Preparation of polydimethylsiloxane channels

The PDMS was thoroughly mixed at a standard 10:1 base to curing agent ratio by weight. After mixing, the solution was degassed by centrifuge at 3500 rpm for 2 min. Then, the PDMS mixture was poured onto a silicon master that was treated with an anti-stick coating of perfluorooctyltrichlorosilane. The functionalization with perfluorooctyltrichlorosilane was performed as follows: 4 µL of the silane was placed in a reservoir in a glass desiccator with the masters (placed vertically on the side walls) and was placed under vacuum for 20 min using a benchtop vacuum pump. The substrates were rinsed with isopropyl alcohol and completely dried with compressed air. The masters could be re-used ~5 times before the non-stick coating had to be reapplied. The PDMS was cured for 1 h at 80 °C.

The PDMS-glass channels were fabricated by simultaneously treating both the glass substrate and the PDMS channel to 30 s of air plasma activation (8 sccm, 100 W, Henniker Plasma HPT200). The channel and substrate were immediately placed in contact after plasma treatment, then placed in a 60 °C oven to facilitate binding for at least 1 h before use, but they can also be kept in the oven overnight. ITO-coated glass was functionalized with APTES following the same procedure detailed for the capillaries, then the APTES functionalized ITO and the PDMS channels were air plasma treated and bound in the same way as the PDMS-glass devices.

After the channels were successfully bound and cooled to room temperature, the devices (with inlet and outlet holes already created) were placed in the air plasma cleaner for 1 min to increase the hydrophilicity of the internal channel walls. The channels were then pre-wetted with 200 proof ethanol at 250-500 µL/min for ~2 min. When herringbone channels were used, extra care was taken during this step to ensure that bubbles did not remain trapped in the 3D features. Difficult to remove bubbles could be released by tapping the channel either by hand or with the

back of a pair of tweezers while the wetting ethanol solution was flowing through the channel. Then, an APTES solution (for facilitating binding of the colloidal seeds) was introduced into the channels and allowed to flow into the channel for 2 min at 250-500 μL/min. Then, the channels were quickly placed in a 60 °C oven for 8 min with tubing attached. (*N.B.,*– without the tubing the APTES solution will evaporate, if this appears to be happening, the tubing should be plugged with a syringe so that the solution is able to warm to 60 °C without evaporating).

5.4.5. Microfluidic synthesis

A solution of CTAC-coated seeds was flowed into the capillary or channel at 0.1 mL/min using a syringe pump (Harvard, Chemyx 400) for 1 h. Here, it is again important for the herringbone channels that bubbles are not trapped in the 3D features, otherwise the growth will not be uniform. The devices were then gently hand-rinsed with water using a syringe. (*N.B.*- Other brands of syringe pumps were tested and, with other models, the pump would significantly heat up over a long period of use, negatively affecting the synthesis reproducibility, so, one must verify that the brand of pump used does not heat). The 4 mL growth solution (without seeds or ascorbic acid) was prepared, as described in the **Colloidal AuNST Synthesis** section. The ascorbic acid was added quickly and mixed well (*N.B.,*– the solution should appear clear rather than yellow following the addition), immediately taken into a syringe and flowed through the capillary at the specified flow rate (0.63 mL/min – 1 mL/min; standard: 0.125 mL/min). The growth was continued for 3 min after which the pump was stopped, and the channels were immediately rinsed with MilliQ water by hand two times using a syringe to remove any residual growth solution. During the flow step, the start of the growth time is recorded when the growth solution reaches the capillary, which can take 15–30 s depending on tubing length. During flow, the solution coming from the outlet

was checked by visual inspection to confirm that it is clear immediately upon exiting the device, rather than red/blue, which would indicate nucleation inside the solution due to insufficient rinsing of the seed solution out of the channel. The final products appeared dark blue in color.

5.4.6. Gold nanostar characterization

An ultraviolet (UV)-visible spectrophotometer (Agilent, Cary 8454) was used for spectroscopic characterization. Transmission electron microscopy (TEM; 120 kV, Technai T12) was used to determine the aspect ratio and distribution of products synthesized in solution. Samples were prepared by centrifuging 10 mL of the final solution at 15,000 rpm for 20 min, followed by removal of the supernatant. Functionalization with thiolated 2000 MW polyethylene glycol (PEG-SH) was performed as previously reported[37] for TEM grid preparation so that the nanoparticles could be washed multiple times without aggregating. The sample was redispersed in 10 mL of water and 1.0-1.1 mg of PEG-SH was added. The solution was left to stir on an orbital shaker for 2 h. Afterwards, the solution was washed by centrifuging 4 mL at 15,000 rpm for 20 min, removing the supernatant, and redispersing in 4 mL in milliQ water. After the final rinsing step, the particles were redispersed in 5 μL of milliQ water. A 400-mesh Cu grid with carbon support (Ted Pella, Inc., Part No.: 01844-F) was placed in a petri dish lined with parafilm, and a 5 μL drop of the washed AuNSTs was placed on the grid. The petri dish was closed and covered with parafilm to allow slow evaporation of the drop over 4 h.

Scanning electron microscopy (SEM) was utilized to characterize the morphology and uniformity for the AuNSTs grown on glass and ITO (ZEISS Supra 40VP SEM, 3-10 kV). The AuNST on glass slides and microcapillaries were coated with an iridium thin film (~3 nm) using an Ion Beam Sputtering/Etching System (South Bay Technology, model number). Carbon tape

was used to secure the sample to the sample holder, along with copper tape to reduce charging. The AuNSTs on the PDMS channels was characterized with environmental SEM (FEI QUANTA 200 Field Emission Gun) operating between 5 and 15 kV under low vacuum (60 Pa).

Section 5.5. References

[1] D. Wang, M. R. Bourgeois, J. Guan, A. K. Fumani, G. C. Schatz, T. W. Odom, *ACS Photonics* **2020**, *7*, 630.

[2] N. Gisbert Quilis, M. Lequeux, P. Venugopalan, I. Khan, W. Knoll, S. Boujday, M. Lamy de la Chapelle, J. Dostalek, *Nanoscale* **2018**, *10*, 10268.

[3] S. Khabbaz Abkenar, A. Tufani, G. Ozaydin Ince, H. Kurt, A. Turak, C. W. Ow-Yang, *Nanoscale* **2017**, *9*, 2969.

[4] L. Velleman, D. Sikdar, V. A. Turek, A. R. Kucernak, S. J. Roser, A. A. Kornyshev, J. B. Edel, *Nanoscale* **2016**, *8*, 19229.

[5] C. Hamon, S. Novikov, L. Scarabelli, L. Basabe-Desmonts, L. M. Liz-Marzán, *ACS Nano* **2014**, *8*, 10694.

[6] A. Ali Umar, M. Oyama, *Cryst. Growth Des.* **2005**, *5*, 599.

[7] M. Kambayashi, J. Zhang, M. Oyama, *Cryst. Growth Des.* **2005**, *5*, 81.

[8] L. Osinkina, T. Lohmüller, F. Jäckel, J. Feldmann, *J. Phys. Chem. C* **2013**, *117*, 22198.

[9] S. Kumar, H. Yang, S. Zou, *J. Phys. Chem. C* **2007**, *111*, 12933.

[10] B. Fortuni, Y. Fujita, M. Ricci, T. Inose, R. Aubert, G. Lu, J. A. Hutchison, J. Hofkens, L. Latterini, H. Uji-i, *Chem. Commun.* **2017**, *53*, 5121.

[11] U. Cataldi, R. Caputo, Y. Kurylyak, G. Klein, M. Chekini, C. Umeton, T. Bürgi, *J Mater Chem C* **2014**, *2*, 7927.

[12] Q. Zhang, J.-J. Xu, Y. Liu, H.-Y. Chen, *Lab Chip* **2008**, *8*, 352.

[13] Z. Li, X. Huang, G. Lu, *J. Mater. Chem. C* **2020**, *8*, 3956.

[14] J. Boleininger, A. Kurz, V. Reuss, C. Sönnichsen, *Phys. Chem. Chem. Phys.* **2006**, *8*, 3824.

[15] G. Tofighi, H. Lichtenberg, J. Pesek, T. L. Sheppard, W. Wang, L. Schöttner, G. Rinke, R. Dittmeyer, J.-D. Grunwaldt, *React. Chem. Eng.* **2017**, *2*, 876.

[16] H. Huang, H. du Toit, M. O. Besenhard, S. Ben-Jaber, P. Dobson, I. Parkin, A. Gavriilidis, *Chem. Eng. Sci.* **2018**, *189*, 422.

[17] S. Abalde-Cela, P. Taladriz-Blanco, M. G. de Oliveira, C. Abell, *Sci. Rep.* **2018**, *8*, 2440.

[18] M. Sarsfield, A. Roberts, K. A. Streletzky, P. S. Fodor, C. R. Kothapalli, *Chem. Eng. Technol.* **2021**, *44*, 622.

[19] M. Bhamidipati, H.-Y. Cho, K.-B. Lee, L. Fabris, *Bioconjug. Chem.* **2018**, *29*, 2970.

[20] T. Vo-Dinh, *J. Immunol. Sci.* **2018**, *2*, 1.

[21] D. Jimenez de Aberasturi, A. B. Serrano-Montes, J. Langer, M. Henriksen-Lacey, W. J. Parak, L. M. Liz-Marzán, *Chem. Mater.* **2016**, *28*, 6779.

[22] E. Lenzi, D. Jimenez de Aberasturi, L. M. Liz-Marzán, *ACS Sens.* **2019**, *4*, 1126.

[23] E. Lenzi, D. Jimenez de Aberasturi, M. Henriksen-Lacey, P. Piñeiro, A. J. Muniz, J. Lahann, L. M. Liz-Marzán, *ACS Appl. Mater. Interfaces* **2022**, *14*, 20708.

[24] T. Man, X. Zhu, Y. T. Chow, E. R. Dawson, X. Wen, A. N. Patananan, T. L. Liu, C. Zhao, C. Wu, J. S. Hong, P.-S. Chung, D. L. Clemens, B.-Y. Lee, P. S. Weiss, M. A. Teitell, P.-Y. Chiou, *ACS Nano* **2019**, *13*, 10835.

[25] R. Xiong, K. Raemdonck, K. Peynshaert, I. Lentacker, I. De Cock, J. Demeester, S. C. De Smedt, A. G. Skirtach, K. Braeckmans, *ACS Nano* **2014**, *8*, 6288.

[26] J. J. Giner-Casares, M. Henriksen-Lacey, I. García, L. M. Liz-Marzán, *Angew. Chem. Int. Ed.* **2016**, *55*, 974.

[27] S.-W. Lv, Y. Liu, M. Xie, J. Wang, X.-W. Yan, Z. Li, W.-G. Dong, W.-H. Huang, *ACS Nano* **2016**, *10*, 6201.

[28] H. Vanrompay, E. Bladt, W. Albrecht, A. Béché, M. Zakhozheva, A. Sánchez-Iglesias, L. M. Liz-Marzán, S. Bals, *Nanoscale* **2018**, *10*, 22792.

[29] L. M. Maestro, P. Haro-González, A. Sánchez-Iglesias, L. M. Liz-Marzán, J. García Solé, D. Jaque, *Langmuir* **2014**, *30*, 1650.

[30] W. Niu, L. Zhang, G. Xu, *Nanoscale* **2013**, *5*, 3172.

[31] M. L. Personick, M. R. Langille, J. Zhang, C. A. Mirkin, *Nano Lett.* **2011**, *11*, 3394.

[32] Y. Xia, X. Xia, H.-C. Peng, *J. Am. Chem. Soc.* **2015**, *137*, 7947.

[33] Y. Xia, K. D. Gilroy, H.-C. Peng, X. Xia, *Angew. Chem. Int. Ed.* **2017**, *56*, 60.

[34] L. Scarabelli, *Pure Appl. Chem.* **2018**, *90*, 1393.

[35] M. Grzelczak, J. Pérez-Juste, P. Mulvaney, L. M. Liz-Marzán, *Chem. Soc. Rev.* **2008**, *37*, 1783.

[36] Q. Su, X. Ma, J. Dong, C. Jiang, W. Qian, *ACS Appl. Mater. Interfaces* **2011**, *3*, 1873.

[37] A. Casu, E. Cabrini, A. Donà, A. Falqui, Y. Diaz-Fernandez, C. Milanese, A. Taglietti, P. Pallavicini, *Chem. - Eur. J.* **2012**, *18*, 9381.

[38] M. Dhar, J. N. Lam, T. Walser, S. M. Dubinett, M. B. Rettig, D. Di Carlo, *Proc. Natl. Acad. Sci.* **2018**, *115*, 9986.

[39] J. Che, V. Yu, M. Dhar, C. Renier, M. Matsumoto, K. Heirich, E. B. Garon, J. Goldman, J. Rao, G. W. Sledge, M. D. Pegram, S. Sheth, S. S. Jeffrey, R. P. Kulkarni, E. Sollier, D. D. Carlo, *Oncotarget* **2016**, *7*, 12748.

[40] L. Zhao, P. Cheng, J. Li, Y. Zhang, M. Gu, J. Liu, J. Zhang, J.-J. Zhu, *Anal. Chem.* **2009**, *81*, 7075.

[41] J. Komen, F. Wolbers, H. R. Franke, H. Andersson, I. Vermes, A. van den Berg, *Biomed. Microdevices* **2008**, *10*, 727.

[42] P. Tabeling, *Introduction to Microfluidics*, Oxford University Press Inc., New York, **2005**.

[43] A. D. Stroock, S. K. W. Dertinger, A. Ajdari, I. Mezić, H. A. Stone, G. M. Whitesides, *Science* **2002**, *295*, 647.

[44] D. Anggraini, N. Ota, Y. Shen, T. Tang, Y. Tanaka, Y. Hosokawa, M. Li, Y. Yalikun, *Lab. Chip* **2022**, *22*, 1438.

[45] M. Antognoli, D. Stoecklein, C. Galletti, E. Brunazzi, D. Di Carlo, *Lab. Chip* **2021**, *21*, 3910.

[46] D. J. Beebe, G. A. Mensing, G. M. Walker, *Annu. Rev. Biomed. Eng.* **2002**, *4*, 261.

[47] M.-H. Park, E. Reátegui, W. Li, S. N. Tessier, K. H. K. Wong, A. E. Jensen, V. Thapar, D. Ting, M. Toner, S. L. Stott, P. T. Hammond, *J. Am. Chem. Soc.* **2017**, *139*, 2741.

[48] J. Langer, D. Jimenez de Aberasturi, J. Aizpurua, R. A. Alvarez-Puebla, B. Auguié, J. J. Baumberg, G. C. Bazan, S. E. J. Bell, A. Boisen, A. G. Brolo, J. Choo, D. Cialla-May, V. Deckert, L. Fabris, K. Faulds, F. J. García de Abajo, R. Goodacre, D. Graham, A. J. Haes, C. L. Haynes, C. Huck, T. Itoh, M. Käll, J. Kneipp, N. A. Kotov, H. Kuang, E. C. Le Ru, H. K. Lee, J.-F. Li, X. Y. Ling, S. A. Maier, T. Mayerhöfer, M. Moskovits, K. Murakoshi, J.-M. Nam, S. Nie, Y. Ozaki, I. Pastoriza-Santos, J. Perez-Juste, J. Popp, A. Pucci, S. Reich, B. Ren, G. C. Schatz, T. Shegai, S. Schlücker, L.-L. Tay, K. G. Thomas, Z.-Q. Tian, R. P. Van Duyne, T. Vo-Dinh, Y. Wang, K. A. Willets, C. Xu, H. Xu, Y. Xu, Y. S. Yamamoto, B. Zhao, L. M. Liz-Marzán, *ACS Nano* **2020**, *14*, 28.

[49] S. L. Stott, C.-H. Hsu, D. I. Tsukrov, M. Yu, D. T. Miyamoto, B. A. Waltman, S. M. Rothenberg, A. M. Shah, M. E. Smas, G. K. Korir, F. P. Floyd, A. J. Gilman, J. B. Lord, D. Winokur, S. Springer, D. Irimia, S. Nagrath, L. V. Sequist, R. J. Lee, K. J. Isselbacher, S. Maheswaran, D. A. Haber, M. Toner, *Proc. Natl. Acad. Sci.* **2010**, *107*, 18392.

[50] C. Kuttner, V. Piotto, L. M. Liz-Marzán, *Chem. Mater.* **2021**, *33*, 8904.

[51] P. Rao, R. Doremus, *Opt. Electr. Prop. Glas.* **1996**, *203*, 202.

[52] T. K. Sau, C. J. Murphy, *J. Am. Chem. Soc.* **2004**, *126*, 8648.

[53] T. Hendel, M. Wuithschick, F. Kettemann, A. Birnbaum, K. Rademann, J. Polte, *Anal. Chem.* **2014**, *86*, 11115.

[54] J. Rodríguez-Fernández, J. Pérez-Juste, P. Mulvaney, L. M. Liz-Marzán, *J. Phys. Chem. B* **2005**, *109*, 14257.

Chapter 6. Plasmonic Response of *in Situ* Gold Nanostars and Hyperthermia-Mediated Cell Removal

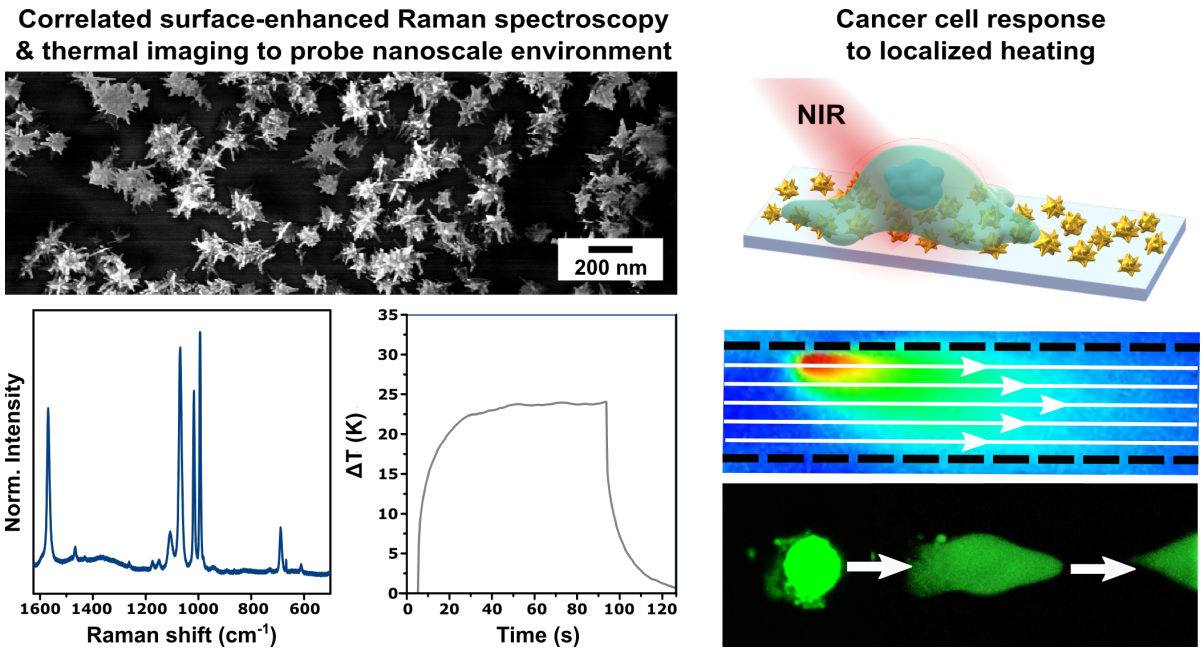

Branched gold nanoparticles convert light to heat and exhibit intense localized fields near their sharp tips. Thermoplasmonic nanostars synthesized on the internal walls of microfluidic channels efficiently produce heat in response to light in the near-infrared biological window. The application of these structures for hyperthermia-mediated cell removal was evaluated, paving the way to applications in cell isolation and sorting.

Section 6.1. Introduction

6.1.1. Localized heating in gold nanostars

Gold nanostars (AuNSTs) fall into a class of plasmonic materials called "thermoplasmonic nanoparticles" capable of efficiently converting light into heat.[1] Thermoplasmonic rods,[2] shells/cages,[3] and stars[4] produce heat *via* non-radiative plasmon-phonon coupling in response to light in the near-infrared (NIR) biological window. Thanks to their stability and biocompatibility, thermoplasmonic gold nanoparticles have been popularly leveraged for numerous studies focused on tissue-nanoparticle interactions,[5–8] cargo delivery platforms,[9,10] substrates for light-responsive cell retrieval,[11,12] materials for combined cancer cell hyperthermia/chemotherapies,[2,5,13] and studies on phenomena resulting from plasmonic heating (*e.g.,* bubble generation).[14–16] Among these NIR-responsive morphologies, AuNSTs have gained particular interest due to the significant electromagnetic field enhancement at their sharp points,[17] high NIR extinction, and large surface areas.[4,18] Another popular application of AuNSTs is its implementation in sensors, since plasmonic structures are capable of enhancing the Raman scattering cross sections for molecules adsorbed on their surface (*via* surface-enhanced Raman scattering, SERS).[19–22] The SERS phenomenon is described in the following section.

6.1.2. Surface-enhanced Raman scattering

A small portion of scattered light (~1 in 10 million photons) will have a different energy than the incoming light. As shown in the Jablonski diagrams in **Figure 1.5**, scattered light with lower or higher energy than the incoming light is called Stokes or anti-Stokes Raman scattering, respectively. Probing the scattered light results in a chemically specific "fingerprint," however, because so few photons are inelastically scattered, the Raman signal is relatively weak. Despite

this, there are many benefits to Raman vibrational spectroscopy, because unlike IR spectroscopy, it is based in probing changes in the polarizability of the molecule, rather than the dipole moment.[19] So, often times molecules or functional groups that give intense Raman signals are observed relatively weakly in IR. For example, the O-H stretch in water gives a weak Raman signal, meaning that it is possible to probe molecules in aqueous solutions, which is much more challenging to do with IR spectroscopy. Furthermore, because Raman spectroscopy does not rely on absorption of light corresponding to the vibrational energies of the molecule, one does not need to use an infrared lamp as a source, and instead different wavelength lasers can be used. Experimentally, this capability can be more convenient because the use of fiber optic cables offer more versatility instrumentally.

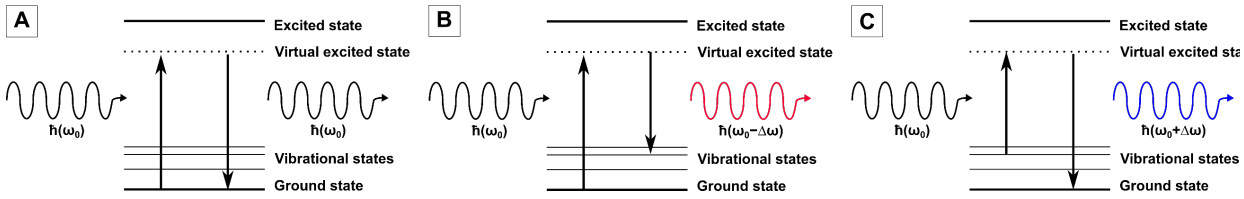

Figure 6.1. A-C: Jablonski diagrams showing (**A**) elastic scattering, (**B**) inelastic Stokes Raman scattering, and (**C**) anti-Stokes Raman scattering.

In 1977, Jeanmaire and Van Duyne[23] and Albrecht and Creighton[24] discovered that corrugated metal surfaces can greatly enhance the Raman scattering, and it was later established that the enhancement in signal depended upon the enhanced fields created by localized surface plasmons. The SERS intensity (I_{SERS}) depends on the size of the localized fields, and therefore the average size of the field-enhancing features on the surface (a) and the distance of the adsorbate from the feature surface (r):

$$I_{SERS} = \left(\frac{a+r}{a}\right)^{-10} \qquad \textbf{[Eq. 6.1]}$$

With current systems, a SERS enhancement of 10^5-10^6 is routine, and even single-molecule detection is possible, with SERS enhancement factors as high as ~10^{14}.[25]

Plasmonic structures can be engineered to enhance the local field, like with the hotspots in nanosphere dimers discussed in **Chapter 1**, improving the SERS enhancement. In this regard, gold nanostars are especially useful for SERS-based sensing because, even without the formation of dimers, individual nanostars present intense localized fields near their sharp tips.[26] The field localization in these regions have been demonstrated with electron energy loss spectroscopy as shown in **Figure 6.2A-C**.

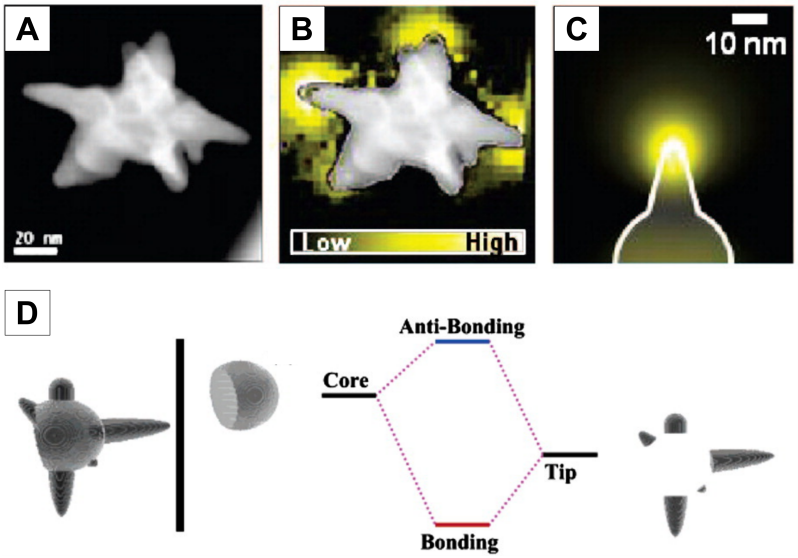

Figure 6.2. A: Electron microscopy image of an individual nanostar, and **B,C:** the electron energy loss spectra showing field enhancements localized to the nanostar's sharp tips. **D:** The plasmon hybridization diagram illustrating coupling between the core and tip plasmon modes [reproduced with permission from ref. 26,28. Ref. 26: Copyright 2007 American Chemical Society. Ref. 28: Copyright 2009 American Chemical Society].

Overall, the plasmon response of AuNSTs can be described similarly to the plasmon hybridization theory discussed for dimers in **Chapter 1**, but this time, instead of the hybridization

of the plasmon modes of individual particles, the plasmonic response of AuNSTs is described by the hybridization of their tip and core plasmons.[26–28] As illustrated in **Figure 6.2C**, although the plasmonic response of the AuNSTs is dominated by the lower energy tip plasmons, the mixing with the higher energy core plasmons leads to increased extinction and local field enhancements observed with electron energy loss spectroscopy.[27] Overall, the enhancement in extinction is ~4 times greater than the individual tip plasmons as calculated by finite-difference time-domain simulations). The physical description of this result is that the higher frequency core plasmon oscillations are able to adiabatically follow the lower frequency tip plasmon oscillations, increasing the effective dipole moment at the tips, leading to an antenna effect.[26–28] Nowadays, SERS with AuNSTs is used for sensitive detection of environmental pollutants, biomolecules, and for monitoring complex biological systems.[21,22,29,30]

6.1.3. Application of nanostars grown in microfluidic channels

Here, we characterize the plasmonic properties of the glass microfluidic capillaries fabricated in **Chapter 5** and explore their applications in the isolation and light-triggered release of grafted cells. Although AuNSTs are commonly used in photothermal cancer therapy to kill cancer cells by localized heating, recent work by Giner-Casares explores the utility of AuNST heating for fabricating cell culture substrates capable of light-triggered retrieval of viable cells.[31] In this scheme, the cultured adherent cancer cells are gently removed from the substrate thanks to a ~2-3 °C increase in temperature at the substrate upon irradiation with light in the first NIR biological window. Implementing this light-retrieval mechanism in a microfluidic device can be useful for creating new diagnostic tools for monitoring circulating tumor cells in the blood of patients with metastatic diseases (**Figure 6.3**). [32–34]

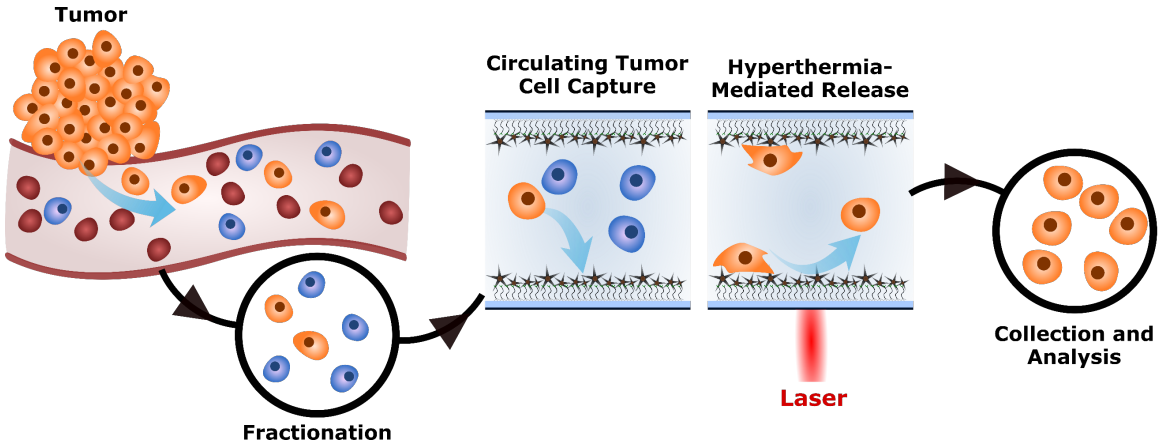

Figure 6.3. Schematic showing circulating tumor cell capture and release with gold nanostars in a microfluidic channel.

Recent works focuses on implementing microfluidic devices for the enumeration and genetic characterization of circulating tumor cells released in to the blood stream from primary metastatic sites to inform patient treatment strategies.[12,33–35] In our scheme, the implementation of AuNSTs has various benefits: (i) selective capture of target cells can be achieved by attaching antibodies to the AuNST surface taking advantage of strong gold-thiol binding,[36] (ii) the localized heating can enable either the release of viable cells or the recollection of the internal contents of the cell that contain its genetic information without having to dismantle the device,[12,31,32,34] and (iii) the capability for the AuNSTs to enable SERS measurements can be useful for performing drug screening studies,[37] or monitoring the cell response to localized heating.[38,39]

In this work, we show that the mesoscale heating of the microcapillary can be controlled by adjusting the laser power, as well as by flowing water into AuNST-decorated microcapillaries at different rates. Changes in the overall mesoscale temperature were correlated with phenomena at the local nanoscale environment through simultaneous thermal and SERS measurements. Moreover, we applied this system to interrogate the response of adhered glioblastoma cells to AuNST localized heating and identified conditions that facilitate the systematic detachment of single cells from the capillary walls. Cellular responses, such as cell reshaping, necrosis/membrane

permeabilization, and rapid cell ablation were dependent on local heating and flow conditions. Our results suggest that this plasmonic-nanostructure-integrated microfluidic platform has potential for new solutions in small-molecule sensing,[40,41] intracellular delivery *via* poration,[10,42] or the targeted retrieval of single cells in adherent cultures, representing a starting point for the development of devices capable of cell capture and targeted, selective light-triggered release.[11,39]

Section 6.2. Results and Discussion

6.2.1. Nanostar plasmonic and photothermal response

Cell hyperthermia can be broken down into temperature regimes giving rise to different biological phenomena: 37-41 °C is the diathermia range, where cells are able to maintain homeostasis and do not undergo significant damage due to heating; for 41-48 °C, cell death can be achieved and protein unfolding and aggregation occurs; 48-60 °C constitutes the ablation regime where thermalization yields DNA damage and rapid, irreversible protein denaturation.[1] Plasmonic heating is a near-field effect that can be detected by far-field temperature changes as heat is transferred from the nanoparticle to the surroundings.[43] We characterized the photothermal performance of the prepared substrates by measuring the mesoscale temperature using a thermal camera as the AuNST-coated microcapillary was irradiated at different laser power densities with a continuous wave laser and under different flow conditions. The thermal camera measures the temperature of the outer capillary surface, because the infrared radiation inside the capillary does not transmit through the capillary wall. However, because the capillary wall is thin, the temperature gradient through the wall can be neglected, and the capillary surface temperatures are used to approximate the fluid temperatures inside the capillary. Temperature changes (ΔT) of *ca.* 40 °C were observed in "no flow" (stationary liquid) conditions (**Figure 6.4A**).

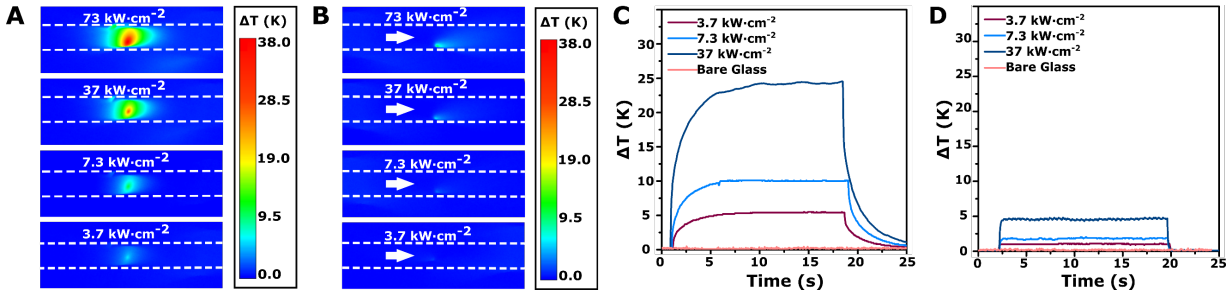

Figure 6.4. Thermal camera images of gold-nanostar-coated capillaries irradiated at different laser power in **A:** no flow and **B:** 50 µL/min flow. The dotted line indicates the edges of the capillary (width: 1 mm) Heating curves in **C:** no flow and **D:** 50 µL/min flow.

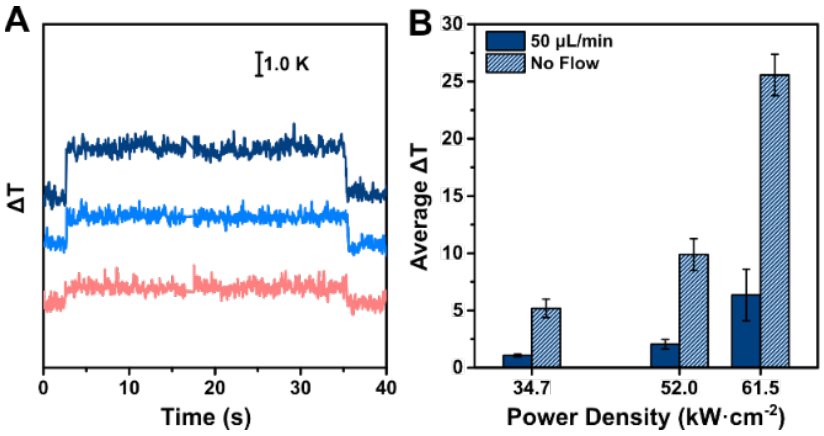

Figure 6.5. A: Heating curves obtained at different spots in the capillary under 50 µL/min flow at the same power density (34.7 kW·cm^{-2}). **B:** Average temperature between three different capillaries prepared with standard growth conditions (3 min, 250 µL/min flow).

When cooling (*via* flowing liquid) was applied at the same power density, temperature changes of 10 °C were observed (**Figure 6.4B**). Without flow, equilibrium temperature was reached after ~10 s of irradiation, compared to less than 1 s with flow. Rapid cooling occurred once laser irradiation was discontinued (**Figure 6.4C,D**). Negligible changes in temperature were measured when an unfunctionalized capillary was irradiated, consistent with the heating being due to the plasmonic response of the AuNSTs (**Figure 6.4C,D**). Moreover, characterization comparing sample-to-sample and spot-to-spot variations in localized heating showed that the photothermal response of the *in situ* synthesized AuNSTs gave good reproducibility (**Figure 6.5**).

Because nanophotothermolysis is a near-field phenomenon, the measured macroscale or mesoscale temperatures are much lower than the temperature at the nanoparticle surface, which can exceed hundreds of degrees Celsius.[14] Rapid local thermalization can result in a number of events, including damage to molecules bound to the nanostructures, nanoparticle reshaping, and vaporization/cavitation of fluid immediately surrounding the nanoparticles to produce nano- and micro-bubbles.[14–16,44–46] The plasmonic activity of the nanoparticles should not be affected by the presence of flowing water. Consequently, although the reported mesoscale temperatures in flow are lower than those seen under static conditions, we hypothesized that the nanoscale temperatures are comparable regardless of the flow. To test this hypothesis, we probed the near-field environment by measuring the SERS signal for AuNST-bound thiolated ligands using the setup shown in **Figure 6.6**.

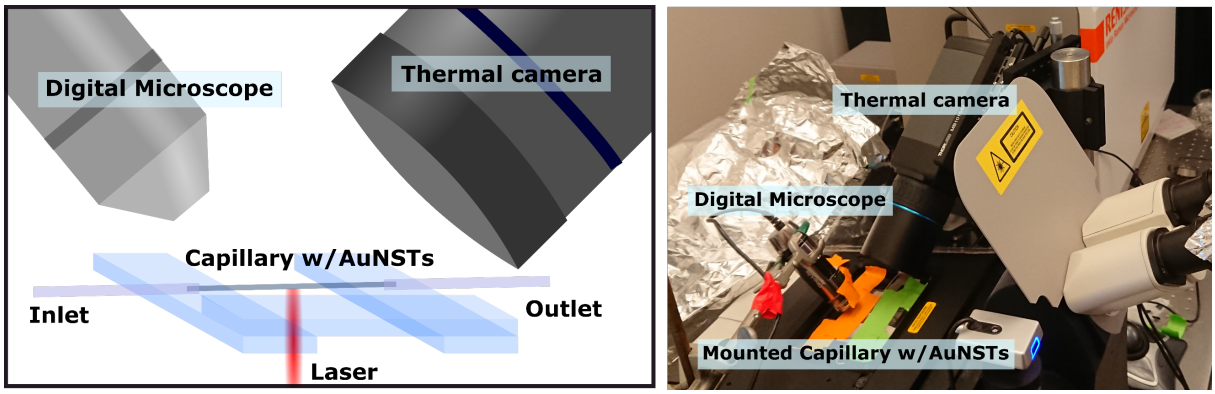

Figure 6.6. Schematic of instrumentation setup for the simultaneous thermal camera/surface enhanced Raman scattering (SERS) measurements. The camera and digital microscope are placed at an angle to prevent damage from the laser and a digital photograph of the setup.

In fact, both the high SERS enhancement and the heat generation in branched AuNPs results from high electric field localization at sharp points.[17,47,48] Additionally, phenomena such as tip rounding and reshaping of the nanostructures, as well as damage to the ligand coating can occur at high temperatures, reducing both light-to-heat conversion and SERS intensity. Therefore, the

combination of near-field and far-field optical measurements leads to better assessment and understanding of the nanoscale effects of flow over the photothermal process.

Experimentally, the LSB coating on the AuNSTs was displaced by thiophenol, a common non-resonant model system for SERS studies, taking advantage of the gold-thiol bond. We show the surface-enhanced Raman scattering spectra of thiophenol over 20 min at 55 W/cm^2 (**Figure 6.7A**). Thus, the device should be operable for long periods of time at 55 W/cm^2 power density or lower, which addresses the temperature changes of interest required for cell-removal in our system. With the spectra shown in **Figure 6.7B-D**, we compare water and various solutions of potential interest for biological applications, including phosphate-buffered saline and Dulbecco's Modified Eagle's Medium (DMEM) cell culture medium. Spectra in **Figure 6.7B-D** were obtained with irradiation at 28 kW/cm^2, representing a laser power applied within the range 37-0.7 kW/cm^2, achieving relevant temperature changes for cell removal. Moreover, as dilute aqueous solutions containing salts, vitamins and amino acids, phosphate-buffered saline and DMEM are thermally similar to water. Therefore, we also do not expect the localized heating effect to differ significantly between the three environments.

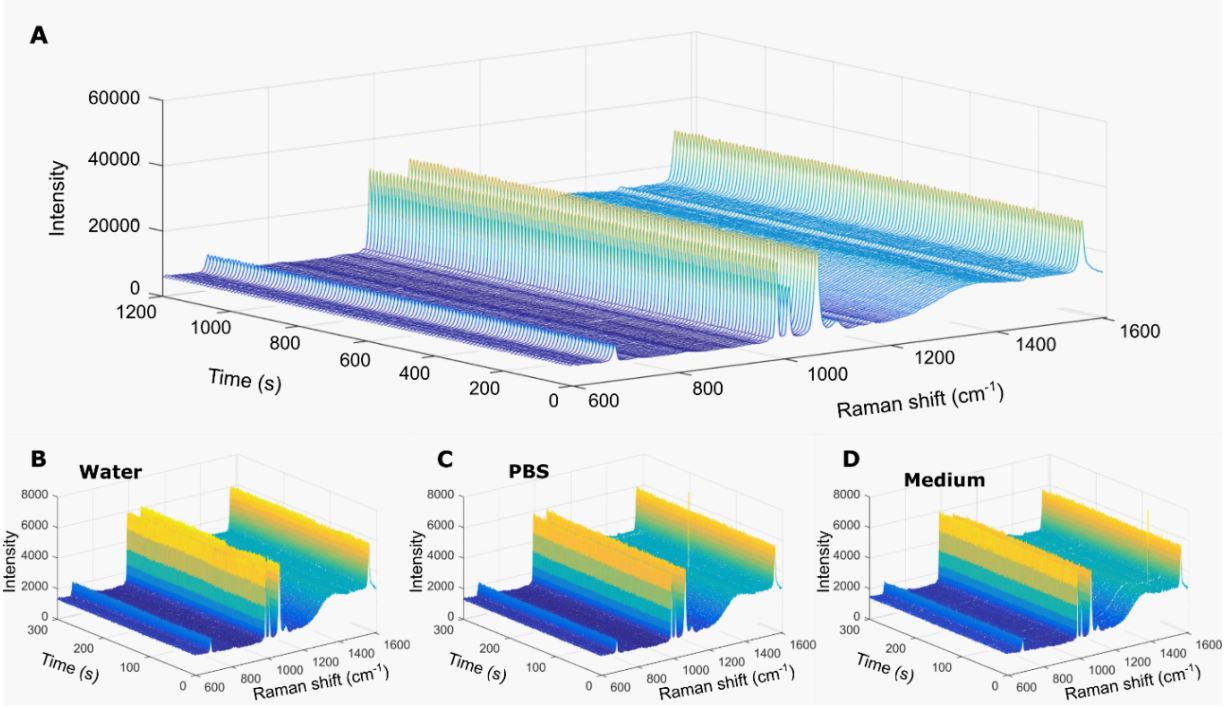

Figure 6.7. A: Surface-enhanced Raman spectra for thiophenol measured in a gold nanostar capillary at 55 W/cm^2 over 20 min. **B-D:** Comparison of surface-enhanced Raman spectra measured in flowing water, phosphate-buffered saline, and cell culture medium (Dulbecco's Modified Eagle's Medium; used to culture U-87-GFP cells) over 5 min.

To track both the mesoscale temperature of the capillary (*i.e,* probing the far field) and the SERS signal of the thiols bound to the nanostructures (*i.e.,* probing the near field), we incorporated concurrent thermal camera measurements along with the collection of SERS spectra. As expected, both temperature and SERS intensity increase with laser power (**Figure 6.6,8**). Although the mesoscale temperature decreases significantly under flow, the SERS intensity remains comparable at flow rates ranging between 0-50 µL/min and at laser fluences up to the highest power density tested (73 kW·cm^{-2}; **Figure 6.8A,B**). However, under stationary conditions, we observed the disappearance of the thiophenol fingerprints at the highest power density tested (73 kW·cm^{-2}) together with the appearance of the Raman spectra for amorphous carbon (*ca*. 1400 cm^{-1}, **Figure 6.8A,B**). Furthermore, at the same power density (73 kW·cm^{-2}, **Figure 6.8C**), we observed a

decrease in ΔT over time, indicating that there was reduced light-to-heat conversion. Taken together, these results point towards two phenomena occurring: damage to the thiol ligands and nanoparticle reshaping. Spatially correlated SEM measurements provide further evidence that nanoparticle restructuring occurs under these conditions **Figure 6.9**. We conclude that the cooling effects of the fluid flow protect the nanostructures from thermally induced reshaping. Furthermore, we observed the formation of bubbles large enough (*i.e.,* several microns in diameter based on the microscope images) to result in measurable mesoscale temperature fluctuations of a few degrees as they refill and coalesce with one another (**Figure 6.8C** shows the temperature fluctuations during this process).

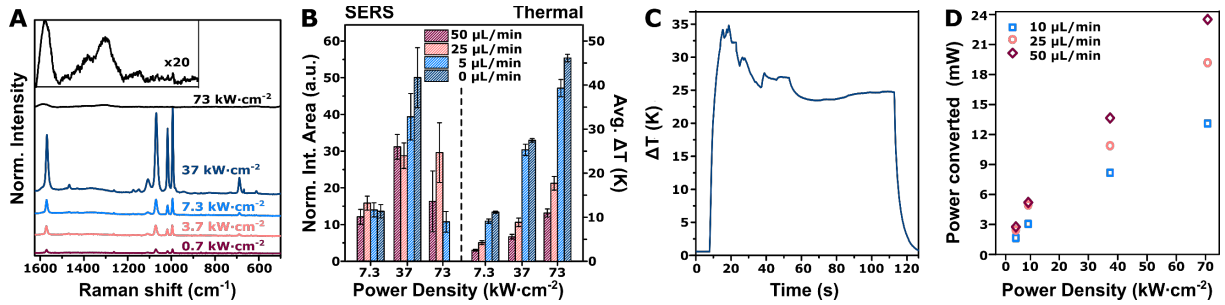

Figure 6.8. A: Surface-enhanced Raman spectra of thiophenol at various laser power (no flow), and the Raman spectra showing amorphous carbon obtained at 73 kW·cm^{-2} at 20× intensity (inset). **B:** Comparison of Raman normalized integrated peak area at 1581 cm^{-1} and measured mesoscale heating at different flow conditions and laser power. **C:** Heating profile of capillary at high power density. **D:** Average power converted to heat at different laser power densities (maximum laser power is 25 mW). Additional data on the thermal performance and scanning electron microscopy images of products before and after reshaping are shown in **Figure 6.9**.

The comparable SERS intensities observed under the various flow conditions indicate that although the presence of flowing liquid alters the mesoscale temperature, and flowing water can thereby reduce ligand damage or AuNST reshaping, it ultimately does not affect the near-field generation of heat.

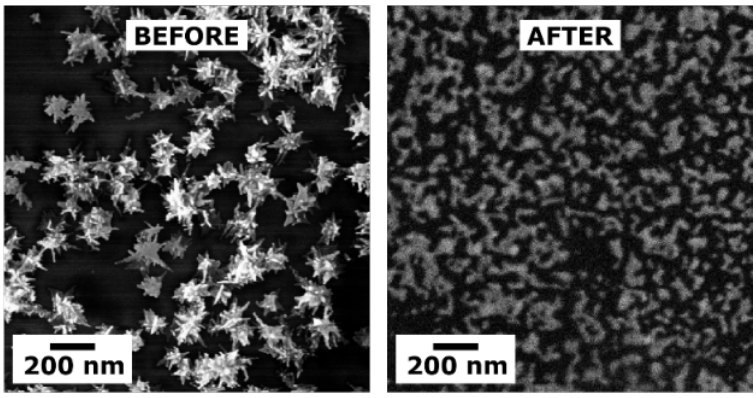

Figure 6.9. Scanning electron microscopy imageof capillary irradiated at high laser power density (73.3 mW/cm^2) before and after irradiation, corresponding to the heating curve shown in **Figure 6.8**.

To test if the light-to-heat conversion is independent of the flow conditions (*i.e.,* when damage to the plasmonic structures does not occur), we estimated the heat q for different flow rates at multiple laser power settings (**Figure 6.10**,**11**).

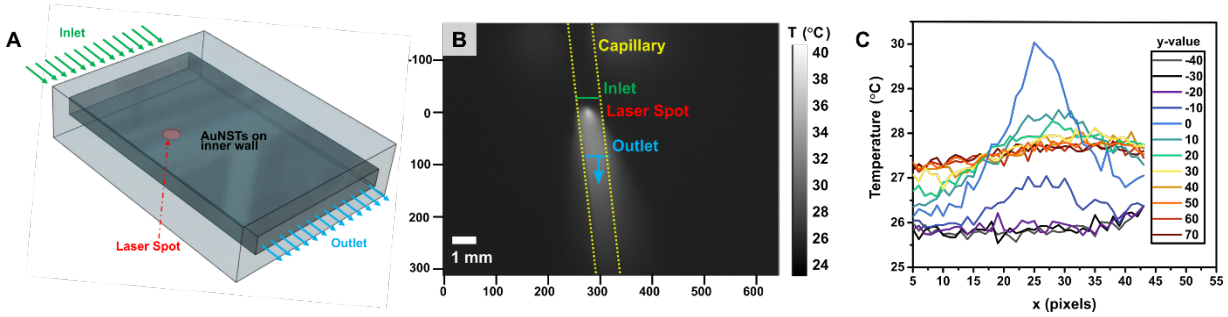

Figure 6.10. A: Schematic of system. **B:** Thermal image showing capillary under irradiation, **C:** Temperature profiles at y-values from -40 to 70 pixels for determination of outlet.

The calculations were performed as follows: consider the control volume shown in **Figure 6.10A**. We denote the volumetric flow rate as $\dot{V}$, and the temperature difference between the inlet and outlet as ΔT. At steady state, the laser power converted into heat q can be estimated using:

$$q = \dot{V}\rho C_p \Delta T \quad \textbf{[Eq. 6.2]}$$

where ρ indicates water density and C_p indicates water specific heat. $\dot{V}$ was controlled by the syringe pump, and ρ and C_p are both known constants. We need to measure ΔT to estimate q and rely on IR thermography to determine the former quantity.

Figure 6.10B shows a temperature field measured by the IR camera (x and y axis units in pixels). We use y = 0 to indicate the plane exposed to the laser. Steady-state temperature distributions at several y locations on the capillary surface are shown in **Figure 6.10C**. Positive y values indicate capillary positions downstream of the laser spot whereas negative y values indicate upstream positions of the laser spot. To determine ΔT, we first determine the inlet and outlet boundaries of the control volume (shown in **Figure 6.10A**), and corresponding temperatures at these boundaries. Based on **Figure 6.10C**, either y = -40 or y = -30 can be used as the boundary for the flow inlet, because the temperatures at these y locations do not vary significantly along the x-direction. Similarly, y = 50, 60, or 70 can be used as the boundary for the flow outlet. The stable temperature profiles at different y locations indicate steady-state flow and also supports the assumption of neglecting heat loss because temperature decreases little in the y direction within the capillary region.

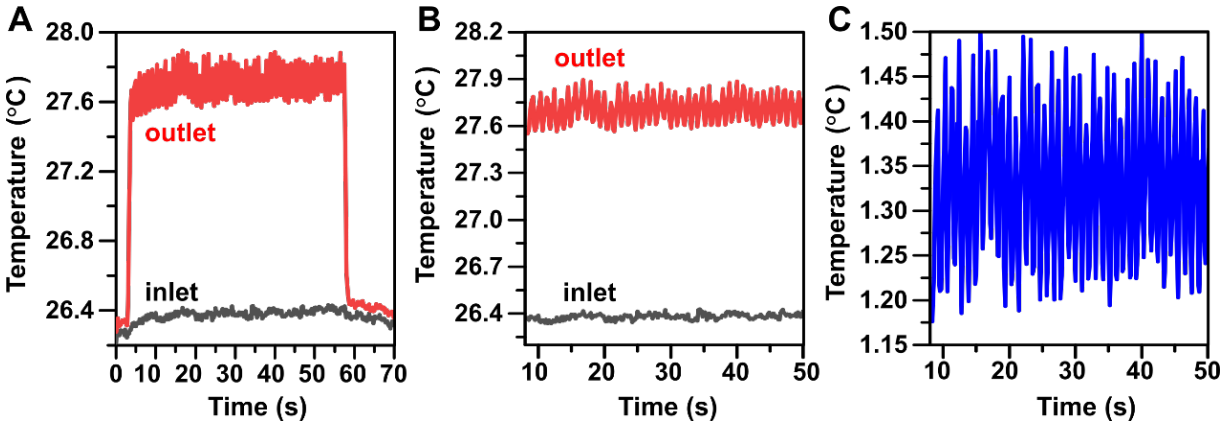

Figure 6.11. A: Mean temperature at the inlet and outlet of the gold nanostar-functionalized capillary as indicated in **Figure 6.10B**. **B:** Isolation of steady-state temperatures. **C:** Temperature difference between the inlet and outlet.

We use the mean value along *x*-axis of the capillary to indicate the temperature at y = -30 and y = 50 respectively (**Figure 6.11A**). We extract the temperatures at steady state as shown in **Figure 6.11B**, and the temperature difference between inlet and outlet is shown in **Figure 6.11C**. ΔT is calculated using the mean value of the temperature differences.

Based on the power of the laser source X (W), the power absorbed as heat is approximately *q*/X%. For different flow rates, the laser power converted into heat increases linearly with the percentage of the laser power and is comparable for the three different flow rates (**Figure 6.8D**). We estimate up to ~90% power conversion (based on the ~24 mW power converted compared to the max laser power of 25 mW) into heat from our estimation of the steady state ΔT at 50 μL/min flow rate, which lies within the expected performance previously reported for branched structures in colloidal suspension.[49,50] These results provide additional support that the flow conditions do not alter the plasmonic activity of the nanostructures within the capillary.

In summary, we demonstrate that these simultaneous SERS-thermal measurements can be correlated to far-field and near-field plasmonic responses of the AuNSTs and can be applied as tools for probing the nanoscale environment. In addition, we find that tuning the microfluidic flow rate enables finer control over total capillary heating without sacrificing plasmonic activity and has potential for protecting the nanostructures from temperature-induced morphological changes.

6.2.2. Nanophotothermolysis of adherent cells

Microfluidic systems have previously been proposed to confine adherent and suspension cells spatially to the same focal plane for performing fluorescence confocal microscopy studies on apoptosis and cell response to chemotherapeutics.[51–53] Fluorescence confocal cell imaging and simultaneous monitoring of the mesoscale temperature change has potential to offer new insight

into the temperature dependence of cellular responses to plasmonic heating as they occur in real-time. Our setup enables us to use laser-scanning fluorescence confocal microscopy to visualize AuNST-cell interactions with adherent cells while irradiating the AuNSTs with a NIR fs-pulsed laser and measuring capillary temperature (**Figure 6.12**).

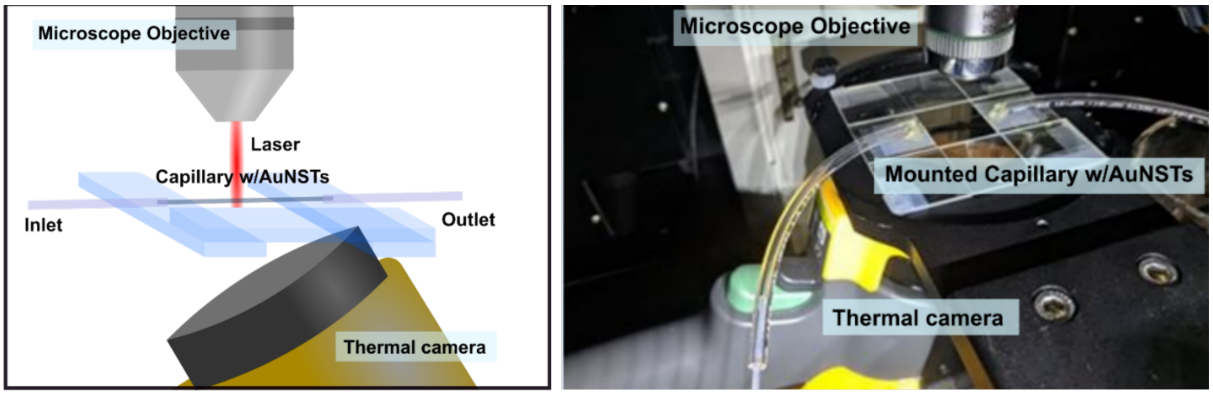

Figure 6.12. Schematic of instrumentation set up for the simultaneous thermal/fluorescence scanning confocal microscopy measurements and a digital photograph of the setup.

Moreover, we demonstrated hyperthermia-mediated single-cell "point-and-shoot" release of grafted adherent cells (**Figure 6.13A**) and observe changes in cell morphology, appearance of necrotic blebs, and microbubble formation, depending on the flow rate and temperature.

First, we evaluated the adhesion of model cells onto AuNSTs by culturing them over a AuNST-coated substrate. Mercaptoundecanol was used to displace LSB and facilitate coating with fibronectin in order to enhance cell interactions with the AuNSTs. After functionalization, the AuNST-capillary was split, and an adherent glioblastoma cell line expressing green fluorescent protein (U-87 GFP) was incubated on the substrate in a well plate for 24 h (at 37 °C, 95% humidity, 5% CO_2). Scanning electron microscopy images and fluorescence confocal microscopy images show that the cells spread over the functionalized substrate (**Figure 6.13B-D**). When cells were administered into the capillary *via* flow, spreading was observed within 60 min (**Figure 6.14**). This

analysis shows that the functionalization procedure enables direct interactions of the cell membrane with the local environment of the plasmonic nanostructures.

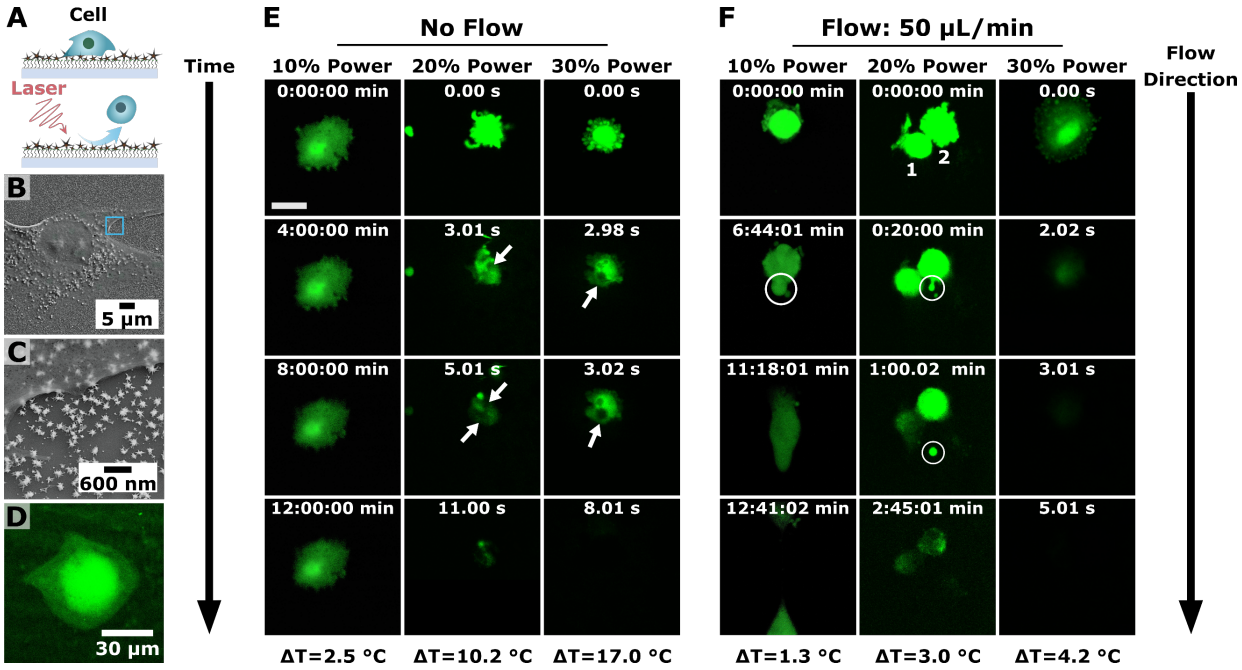

Figure 6.13. A: Schematic of adherent cell attachment and light-activated removal. **B,C:** Scanning electron microscopy images and **D:** scanning fluorescence confocal microscopy image of a green fluorescent protein-expressing U-87 cell on gold nanostars. Scanning fluorescence confocal microscopy images of cell response at different laser fluences in **E:** no flow (white arrows indicate microbubbles) and at **F:** 50 µL/min flow rate (white circles indicate blebs which caused leaking of intracellular contents) (scale bar = 25 µm; E-F shown at the same scale. Maximum fluence = 17 mJ/cm^2, **Table 6.1,2**).

Plasmonic heating has previously been used to detach cells from surfaces.[11,12] Here, we used point-and-shoot selective release of grafted cells to demonstrate the plasmonic activity and possible applications of our structures (**Figure 6.13A**). The cells were flowed into the capillary and incubated within the capillary for 60 min to facilitate attachment (based on the initial SEM/fluorescence confocal microscopy data), then irradiated in the capillary, giving an overall ΔT of ~1-30 ºC depending on the laser power and flow conditions. Without fluid flow, cell removal occurs quickly with increased maximum temperature, where rapid cell ablation is observed within

s as ΔT approaches 20 ºC. Furthermore, if the irradiation area in the capillary temperature is increased by more than *ca.* 10 ºC, we observed the formation of microbubbles (**Figure 6.13E**).

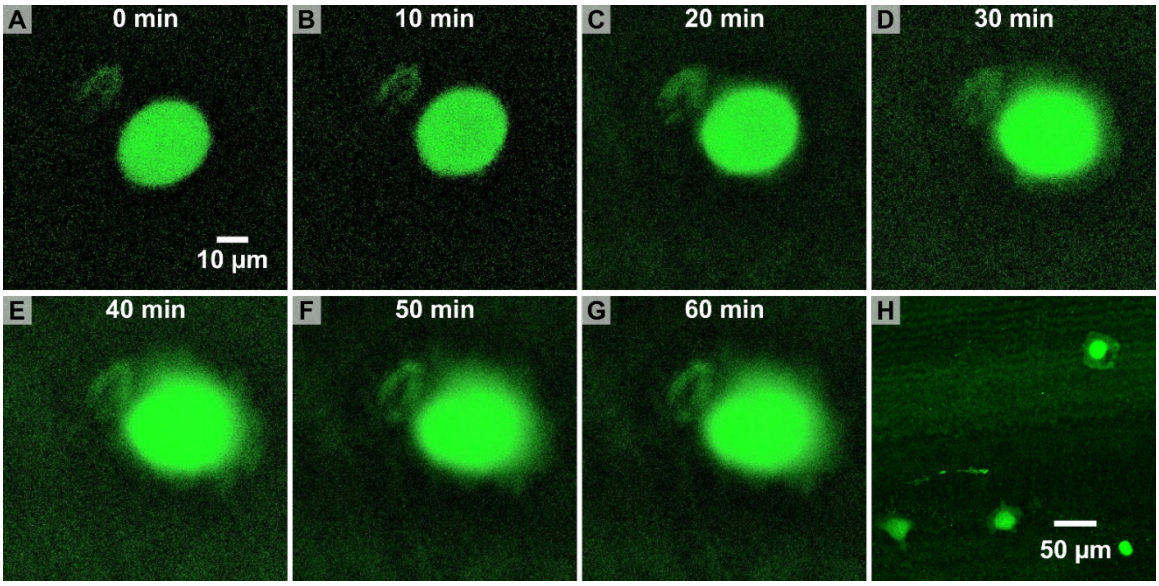

Figure 6.14. Fluorescence scanning confocal microscopy images showing **A-G:** the same green fluorescent protein-expressing U-87 cell spreading over the course of 60 min within a gold nanostar-decorated capillary, and **H:** image of multiple cells following incubation for 60 min.

Steam nanobubble generation and subsequent formation of microbubbles *via* diffusion of dissolved gases has been previously described for substrates (such as glass slides) decorated with thermoplasmonic nanoparticles, and their formation has been shown to play a role in causing mechanical damage to cell membranes.[6] Air bubble formation requires local temperatures near the spinodal temperature of water (277 ºC) and consequently the local heat energy produced in this system is likely to exceed the measured mesoscale capillary heating greatly.[14,46] Bubble formation during nanophotothermolysis of cells induces significant mechanical stress, which likely plays major roles in the mechanism of cell removal under these circumstances.[45,54] As a control experiment, we observe no cell damage, bubble formation, nor significant temperature change for at least 5 min irradiation time up to 30% of the fs-pulsed laser power (17 mJ/cm^2; **Table 6.,2**) when

AuNSTs are not present in the capillary (**Figure 6.15**). The incident laser power from the fs-pulsed laser was measured at low power percentage using a power meter (Thorlabs PM120V; S120UV Sensor, 200-1100 nm). Laser spot size (785 nm) was calculated from the factory reported size at a wavelength of 488 nm (7.48×10^{-13} m^2) as 1.2×10^{-12} m^2.

Table 6.1. Measured power for the continuous wave laser used in the correlated surface-enhanced Raman scattering and thermal imaging measurements.

Percent laser power	Measured Power (mW)	Residual
0	0	--
1	0.027	0.03
1.5	0.068	0.01
2	0.135	0.03

Table 6.2. Extrapolated power for the fs-pulsed laser used for the laser scanning confocal microscopy measurements.

Percent laser power	Power (mW)	Calculated fluence (mJ/cm^2)
10	5.5 ± 0.1	5.7
15	8.3 ± 0.1	8.6
20	11.0 ± 0.1	11
25	13.8 ± 0.1	14
30	16.5 ± 0.1	17

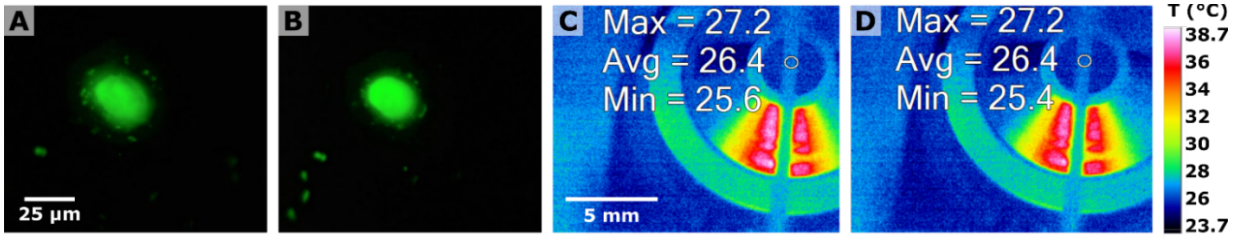

Figure 6.15. Laser scanning confocal microscopy images of green fluorescent protein-expressing U-87 cells **A:** before irradiation and **B:** after 5 min of irradiation at 17 mJ/cm^2 (30% power, no flow). Thermal camera images of capillary **C:** before and **D:** during irradiation with a fs-pulsed laser. Maximum (max), average (avg), and minimum (min) temperatures are shown in °C for the circular region of interest.

Under flow (**Figure 6.13F**), significant cell membrane damage occurs with temperature changes above 4 ºC, and ablation leads to the loss of intracellular materials and near instantaneous removal from the substrate (*i.e.,* similar to what was observed at 17 ºC without flow). At the fluences tested (5.7-17 mJ/cm^2), we do not observe microbubbles, which may be due to the flowing liquid carrying the bubbles downstream. However, even in the absence of microbubbles, cells exhibit membrane damage with changes in temperature of only 1-3 ºC, leading to the rapid formation of protrusions called "blebs," with diameters in the tens of microns, which are precursors to the release of intracellular contents. The formation of blebs indicates rupture of the outer cell membrane and the nature of the blebbing can also indicate different mechanisms of cell death, such as apoptosis or necrosis, which have been observed previously with nanoparticle hyperthermia.[5,55–57] Apoptosis is a biologically controlled process, whereas necrosis is rapid cell death caused by external stimuli (*e.g.,* high local temperature in this case). The size and degree of blebbing indicates necrosis as the primary mechanism of cell removal and damage. Note that without flow, the formation of blebs is harder to detect using confocal microscopy, as the blebs quickly move out of the focal plane and do not move around nor detach from the main body of cells exposed to fluid flow.

The rate of local temperature increase is important to control when studying cell interactions with thermoplasmonic nanoparticles, where selection between apoptosis and necrosis can be achieved through careful control of the heating conditions. Furthermore, we leverage gradual heating to demonstrate controlled release of cultured cells from substrates with branched thermoplasmonic structures.[11] In our system, we are able to tune both the flow and the laser fluence systematically to control the heating experienced by the cells. Although the laser fluences (11 mJ/cm^2) giving ΔT of 10 and 3 ºC without and with flow, respectively, are the same, the

cooling effects of flow mitigate damage to the cell, enabling cells to remain on the substrate substantially longer. With flow, we also do not observe bubble formation, likely because any bubbles generated are rapidly carried downstream. Both with and without flow, the cells exhibit significant membrane disruption, even at low overall capillary temperatures. In these experiments, we used a fs-pulse laser to trigger the plasmonic response, which might result in more aggressive localized heating compared to continuous wave illumination sources, where the energy deposition and generation of heat can be more efficiently controlled.[58–60] The SERS experiments (continuous wave laser) and the cell experiments (fs pulsed laser) exhibit similar photothermal phenomena (*i.e.,* bubble formation, AuNST reshaping), but we note that these systems are not directly comparable in their deposition of energy to the particles and therefore the mechanisms leading to the resulting phenomena likely differ between the two illumination conditions. Thus, building upon what was done here, one interesting avenue to pursue will be to compare temperature measurements, SERS spectra, and fluorescence confocal cell images collected simultaneously in real time with different illumination sources to probe phenomena that result from intense nanoscale heat generation.

Section 6.3. Conclusions and Prospects

Upon illumination, the AuNST coatings in microfluidic capillaries exhibit intense local heating, achieving up to ~40 ºC mesoscale temperature increase, and flowing water acts as a heat sink, mitigating overall capillary heating. Thermal fluctuations and SERS can be used to monitor damage to ligands and heat-induced changes to AuNST morphology occurring at the nanoscale. We have demonstrated light-triggered “point-and-shoot” selective removal of cells from the substrate and were able to observe cell necrosis, ablation, microbubble formation, and intact cell

removal depending on flow conditions and laser fluence. With and without visibly evident microbubble formation, AuNST photothermal response leads to cell membrane damage, causing their rapid removal from the substrate. Although the presented studies on adherent cell interactions with AuNSTs in flow are preliminary, these data indicate that future studies elucidating the interplay between temperature, flow, and cell-AuNST interaction strength can be leveraged to identify conditions that support controlled removal of intact, viable cells. Later designs of the platform will target soft-release of viable cells and incorporate systems for cell collection and viability analysis.

Section 6.4. Materials and Methods

6.4.1. Materials

See previous chapter for details on the chemicals used for microfluidic channel fabrication.

6.4.2. Thermal imaging and surface-enhanced Raman scattering

The SERS spectra were obtained using a Renishaw InVia micro-Raman spectrometer (Renishaw PLC, Wotton-under-Edge, Gloucestershire, UK) with an 1800 grooves mm^{-1} grating, Rayleigh line rejection edge filter, Peltier-cooled deep depletion CCD array detector (576 × 384 pixels). All SERS spectra were acquired with a 40× air objective and 785 nm continuous wave laser excitation with an approximate irradiation spot area of 34 μm^2 and maximum output power of about 25.0 mW. Simultaneous temperature measurements were obtained with a thermal camera (Flir A655sc, equipped with a 25 μm Close-up Infrared Lens, 25 frames per second). A 5 mM solution of thiophenol in ethanol was flowed into the capillary at 0.1 mL/min over the course of

1 h to displace LSB. It is important to wait at least 8-24 h after the nanostar *in situ* growth prior to adding the thiophenol. If it is performed immediately after the growth, the nanostars may not have sufficient time to interact strongly with the APTES, causing it to be displaced by the thiol and resulting in washing the nanostars out of the capillary. The source code for the absorption calculations has been published online at: https://github.com/yuanyuansjtu/Nanostar/

6.4.3. Imaging cells on the gold nanostar films

The cell grafting on the AuNSTs was characterized by SEM. First, the cells were fixed and stained following an established procedure.[61] Critical point drying of the cells was performed with a Tousimis Autosamdri-810 Critical Point Dryer and an iridium thin film was sputtered on the sample. Copper tape and carbon tape were again used to secure the sample to the substrate to improve conductivity.

6.4.4. Proof-of-concept cell release studies

The LSB on the AuNSTs was displaced by flowing an ethanolic solution of 1-5 mM 11-mercapto-1-undecanol (MUD, 99%, CAS: 73768-94-2, Millipore Sigma) for 1 h into the capillary, followed by hand rinsing with Milli-Q water three times. Then, 1 μg/mL fibronectin (0.1% solution, BioReagent, for cell culture, Millipore Sigma) in phosphate-buffered saline (no calcium or magnesium, Gibco™ 14190250, Fisher Scientific) was flowed into the capillary under the same flow conditions for 1 h, followed by three additional rinses with Milli-Q water. Cell response to nanoscale heating was performed with the setup with a Leica SP8 DIVE/FLIM laser scanning fluorescence confocal microscope (1.2×10^{-8} cm^2 spot area at 785 nm, 80 MHz rep rate, 35 fs pulse width) and simultaneous temperature measurements with a thermal camera (Fluke Ti450 infrared

camera). Green fluorescent protein-expressing U-87 glioblastoma cells were cultured as per protocols from ATCC and following trypsinization were immediately introduced into the capillary (at ~10^3-10^5 cells/mL at a flow rate of 50 μL/min). The cells were allowed to incubate for at least 1 h prior to irradiation of the nanostructures. During cell release experiments under 50 μL/min flow, a bubble trap Fluigent, CTQ-006BT) was used to prevent air bubbles from entering the capillary and removing the cells.

Section 6.5. References

[1] G. Baffou, *Thermoplasmonics: Heating Metal Nanoparticles Using Light*, Cambridge University Press, Cambridge, **2017**.

[2] X. Huang, I. H. El-Sayed, W. Qian, M. A. El-Sayed, *J. Am. Chem. Soc.* **2006**, *128*, 2115.

[3] A. M. Gobin, M. H. Lee, N. J. Halas, W. D. James, R. A. Drezek, J. L. West, *Nano Lett.* **2007**, *7*, 1929.

[4] R. Rodríguez-Oliveros, J. A. Sánchez-Gil, *Opt. Express* **2012**, *20*, 621.

[5] M. R. K. Ali, Y. Wu, M. A. El-Sayed, *J. Phys. Chem. C* **2019**, *123*, 15375.

[6] X. Huang, M. A. El-Sayed, *Alex. J. Med.* **2011**, *47*, 1.

[7] D. H. M. Dam, R. C. Lee, T. W. Odom, *Nano Lett.* **2014**, *14*, 2843.

[8] C. Loo, A. Lowery, N. Halas, J. West, R. Drezek, *Nano Lett.* **2005**, *5*, 709.

[9] B. Zhang, Y. Shi, D. Miyamoto, K. Nakazawa, T. Miyake, *Sci. Rep.* **2019**, *9*, 6806.

[10] T. Man, X. Zhu, Y. T. Chow, E. R. Dawson, X. Wen, A. N. Patananan, T. L. Liu, C. Zhao, C. Wu, J. S. Hong, P.-S. Chung, D. L. Clemens, B.-Y. Lee, P. S. Weiss, M. A. Teitell, P.-Y. Chiou, *ACS Nano* **2019**, *13*, 10835.

[11] J. J. Giner-Casares, M. Henriksen-Lacey, I. García, L. M. Liz-Marzán, *Angew. Chem. Int. Ed.* **2016**, *55*, 974.

[12] S.-W. Lv, Y. Liu, M. Xie, J. Wang, X.-W. Yan, Z. Li, W.-G. Dong, W.-H. Huang, *ACS Nano* **2016**, *10*, 6201.

[13] L. R. Hirsch, R. J. Stafford, J. A. Bankson, S. R. Sershen, B. Rivera, R. E. Price, J. D. Hazle, N. J. Halas, J. L. West, *Proc. Natl. Acad. Sci.* **2003**, *100*, 13549.

[14] G. Baffou, J. Polleux, H. Rigneault, S. Monneret, *J. Phys. Chem. C* **2014**, *118*, 4890.

[15] O. Neumann, A. S. Urban, J. Day, S. Lal, P. Nordlander, N. J. Halas, *ACS Nano* **2013**, *7*, 42.

[16] Z. Fang, Y.-R. Zhen, O. Neumann, A. Polman, F. J. García de Abajo, P. Nordlander, N. J. Halas, *Nano Lett.* **2013**, *13*, 1736.

[17] S. Barbosa, A. Agrawal, L. Rodríguez-Lorenzo, I. Pastoriza-Santos, R. A. Alvarez-Puebla, A. Kornowski, H. Weller, L. M. Liz-Marzán, *Langmuir* **2010**, *26*, 14943.

[18] Y. Hua, K. Chandra, D. H. M. Dam, G. P. Wiederrecht, T. W. Odom, *J. Phys. Chem. Lett.* **2015**, *6*, 4904.

[19] K. A. Willets, R. P. Van Duyne, *Annu. Rev. Phys. Chem.* **2007**, *58*, 267.

[20] D. Jimenez de Aberasturi, A. B. Serrano-Montes, J. Langer, M. Henriksen-Lacey, W. J. Parak, L. M. Liz-Marzán, *Chem. Mater.* **2016**, *28*, 6779.

[21] E. Lenzi, D. Jimenez de Aberasturi, L. M. Liz-Marzán, *ACS Sens.* **2019**, *4*, 1126.

[22] E. Lenzi, D. Jimenez de Aberasturi, M. Henriksen-Lacey, P. Piñeiro, A. J. Muniz, J. Lahann, L. M. Liz-Marzán, *ACS Appl. Mater. Interfaces* **2022**, *14*, 20708.

[23] D. L. Jeanmaire, R. P. Van Duyne, *J. Electroanal. Chem.* **1977**, *84*, 1.

[24] M. G. Albrecht, J. A. Creighton, *J. Am. Chem. Soc.* **1977**, *99*, 5215.

[25] P. G. Etchegoin, E. C. Le Ru, *Phys. Chem. Chem. Phys.* **2008**, *10*, 6079.

[26] F. Hao, C. L. Nehl, J. H. Hafner, P. Nordlander, *Nano Lett.* **2007**, *7*, 729.

[27] A. Guerrero-Martínez, S. Barbosa, I. Pastoriza-Santos, L. M. Liz-Marzán, *Curr. Opin. Colloid Interface Sci.* **2011**, *16*, 118.

[28] L. Rodríguez-Lorenzo, R. A. Álvarez-Puebla, I. Pastoriza-Santos, S. Mazzucco, O. Stéphan, M. Kociak, L. M. Liz-Marzán, F. J. García de Abajo, *J. Am. Chem. Soc.* **2009**, *131*, 4616.

[29] D. Jimenez de Aberasturi, A. B. Serrano-Montes, J. Langer, M. Henriksen-Lacey, W. J. Parak, L. M. Liz-Marzán, *Chem. Mater.* **2016**, *28*, 6779.

[30] Q. T. Lê, N. H. Ly, M.-K. Kim, S. H. Lim, S. J. Son, K.-D. Zoh, S.-W. Joo, *J. Hazard. Mater.* **2021**, *402*, 123499.

[31] J. J. Giner-Casares, M. Henriksen-Lacey, I. García, L. M. Liz-Marzán, *Angew. Chem. Int. Ed.* **2016**, *55*, 974.

[32] M.-H. Park, E. Reátegui, W. Li, S. N. Tessier, K. H. K. Wong, A. E. Jensen, V. Thapar, D. Ting, M. Toner, S. L. Stott, P. T. Hammond, *J. Am. Chem. Soc.* **2017**, *139*, 2741.

[33] Z. Ao, E. Parasido, S. Rawal, A. Williams, R. Schlegel, S. Liu, C. Albanese, R. J. Cote, A. Agarwal, R. H. Datar, *Lab. Chip* **2015**, *15*, 4277.

[34] S. L. Stott, C.-H. Hsu, D. I. Tsukrov, M. Yu, D. T. Miyamoto, B. A. Waltman, S. M. Rothenberg, A. M. Shah, M. E. Smas, G. K. Korir, F. P. Floyd, A. J. Gilman, J. B. Lord, D. Winokur, S. Springer, D. Irimia, S. Nagrath, L. V. Sequist, R. J. Lee, K. J. Isselbacher, S. Maheswaran, D. A. Haber, M. Toner, *Proc. Natl. Acad. Sci.* **2010**, *107*, 18392.

[35] J. Che, V. Yu, M. Dhar, C. Renier, M. Matsumoto, K. Heirich, E. B. Garon, J. Goldman, J. Rao, G. W. Sledge, M. D. Pegram, S. Sheth, S. S. Jeffrey, R. P. Kulkarni, E. Sollier, D. D. Carlo, *Oncotarget* **2016**, *7*, 12748.

[36] J. C. Love, L. A. Estroff, J. K. Kriebel, R. G. Nuzzo, G. M. Whitesides, *Chem. Rev.* **2005**, *105*, 1103.

[37] J. Plou, B. Molina-Martínez, C. García-Astrain, J. Langer, I. García, A. Ercilla, G. Perumal, A. Carracedo, L. M. Liz-Marzán, *Nano Lett.* **2021**, *21*, 8785.

[38] K. Majzner, A. Kaczor, N. Kachamakova-Trojanowska, A. Fedorowicz, S. Chlopicki, M. Baranska, *Analyst* **2013**, *138*, 603.

[39] R. Smith, K. L. Wright, L. Ashton, *Analyst* **2016**, *141*, 3590.

[40] M. Bhamidipati, H.-Y. Cho, K.-B. Lee, L. Fabris, *Bioconjug. Chem.* **2018**, *29*, 2970.

[41] T. Vo-Dinh, *J. Immunol. Sci.* **2018**, *2*, 1.

[42] R. Xiong, K. Raemdonck, K. Peynshaert, I. Lentacker, S. C. D. Smedt, A. G. Skirtach, K. Braeckmans, **2014**, *8*, 9.

[43] L. Jauffred, A. Samadi, H. Klingberg, P. M. Bendix, L. B. Oddershede, *Chem. Rev.* **2019**, *119*, 8087.

[44] G. Baffou, R. Quidant, *Laser Photonics Rev.* **2013**, *7*, 171.

[45] L. Hou, M. Yorulmaz, N. R. Verhart, M. Orrit, *New J. Phys.* **2015**, *17*, 013050.

[46] V. Kotaidis, C. Dahmen, G. von Plessen, F. Springer, A. Plech, *J. Chem. Phys.* **2006**, *124*, 184702.

[47] D. Jimenez de Aberasturi, A. B. Serrano-Montes, J. Langer, M. Henriksen-Lacey, W. J. Parak, L. M. Liz-Marzán, *Chem. Mater.* **2016**, *28*, 6779.

[48] X. Meng, J. Dyer, Y. Huo, C. Jiang, *Langmuir* **2020**, *36*, 3558.

[49] C. Bi, J. Chen, Y. Chen, Y. Song, A. Li, S. Li, Z. Mao, C. Gao, D. Wang, H. Möhwald, H. Xia, *Chem. Mater.* **2018**, *30*, 2709.

[50] A. Espinosa, A. K. A. Silva, A. Sánchez-Iglesias, M. Grzelczak, C. Péchoux, K. Desboeufs, L. M. Liz-Marzán, C. Wilhelm, *Adv. Healthc. Mater.* **2016**, *5*, 1040.

[51] L. Zhao, P. Cheng, J. Li, Y. Zhang, M. Gu, J. Liu, J. Zhang, J.-J. Zhu, *Anal. Chem.* **2009**, *81*, 7075.

[52] J. Komen, F. Wolbers, H. R. Franke, H. Andersson, I. Vermes, A. van den Berg, *Biomed. Microdevices* **2008**, *10*, 727.

[53] C. Muñoz-Pinedo, D. R. Green, A. van den Berg, *Lab. Chip* **2005**, *5*, 628.

[54] V. P. Zharov, K. E. Mercer, E. N. Galitovskaya, M. S. Smeltzer, *Biophys. J.* **2006**, *90*, 619.

[55] T. Vo-Dinh, *J. Immunol. Sci.* **2018**, *2*, 1.

[56] B. Crawford, R. Shammas, A. Fales, D. Brown, S. Hollenbeck, T. Vo-Dinh, G. Devi, *Int. J. Nanomedicine* **2017**, *Volume 12*, 6259.

[57] M. Pérez-Hernández, P. del Pino, S. G. Mitchell, M. Moros, G. Stepien, B. Pelaz, W. J. Parak, E. M. Gálvez, J. Pardo, J. M. de la Fuente, *ACS Nano* **2015**, *9*, 52.

[58] P. Díaz-Núñez, G. González-Rubio, A. Prada, J. González Izquierdo, A. Rivera, L. Bañares, A. Guerrero-Martínez, O. Peña-Rodríguez, *J. Phys. Chem. C* **2018**, *122*, 19816.

[59] J. Yan, D. Zhu, J. Xie, Y. Shao, W. Xiao, *Small* **2020**, 2001101.

[60] G. Baffou, R. Quidant, *Laser Photonics Rev.* **2013**, *7*, 171.

[61] C. Heckman, S. Kanagasundaram, M. Cayer, J. Paige, *Protoc. Exch.* **2007**, DOI 10.1038/nprot.2007.504.

Chapter 7. Conclusions and Prospects

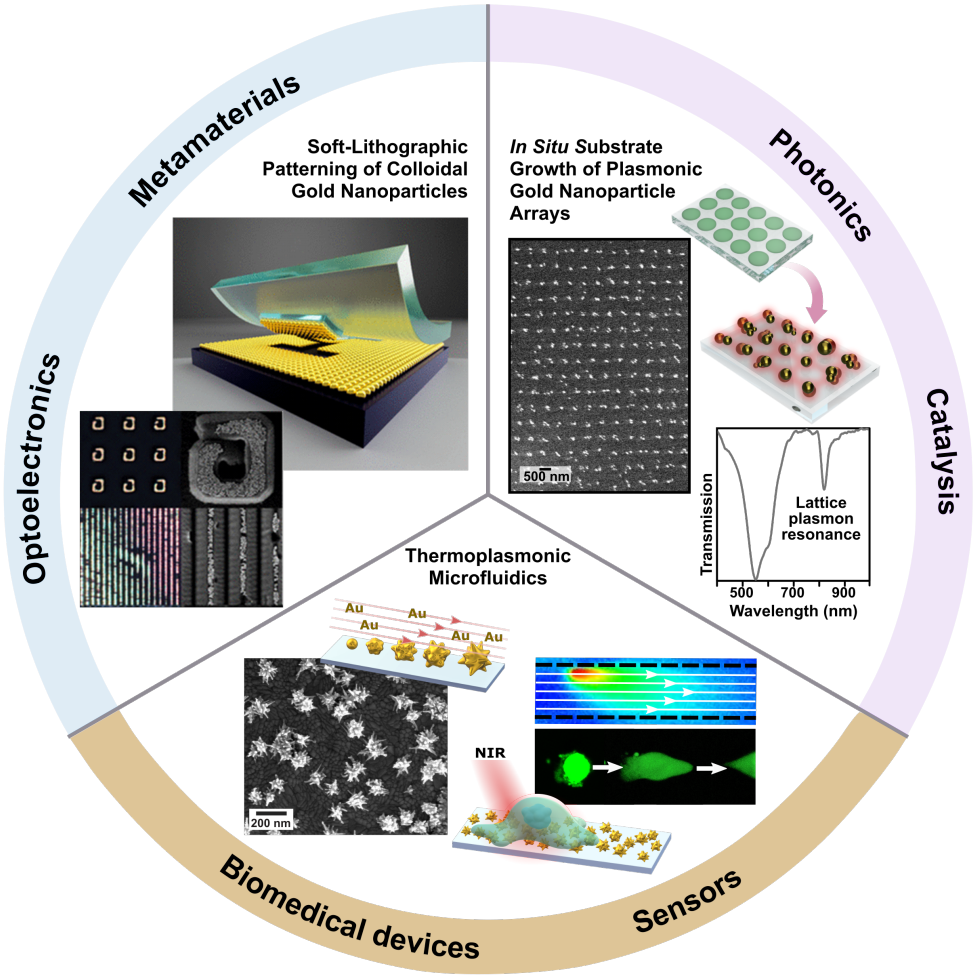

The methodologies for plasmonic substrate fabrication presented in this thesis offer straightforward, versatile, and cost-effective solutions for designing plasmonic materials incorporating gold nanoparticles. Each of the developed techniques take advantage of bottom-up wet-chemical synthesis to produce nanoparticles with selected shape, diameter, and plasmonic response. These plasmonic systems have broad potential applications in metamaterials, optoelectronics, sensors, heterogeneous catalysts, and biomedical devices.

Section 7.1. Conclusions

Overall, the work presented in this thesis involves the development of different approaches for fabricating plasmonic substrates with engineered optical responses.[1,2] These projects take advantage of scalable and affordable techniques, such as soft lithography and bottom-up wet chemical synthesis. Much of the work presented applies unconventional synthetic approaches involving the *in situ* formation of size- and shape-controlled nanoparticles directly on the substrate. Although the conclusions are detailed at the end of each chapter, here I provide a summary of the main contributions from each work.

7.1.1. Nanoparticle chemical lift-off lithography

Combining self-assembly and soft-lithographic patterning in nanoparticle chemical lift-off lithography (NP-CLL) enables micro- and nanoscale arrangement of colloidal nanoparticles into arbitrary patterns on substrates.[1] One can take advantage of subsequent patterning steps, such as performing the NP-CLL process once more on a previously patterned gold nanoparticle monolayer or transferring the lifted-up nanoparticles onto another substrate. The developed patterning method is not only highly versatile in regard to the types of patterned features that can be accessed, but is also translatable to different materials, *e.g.,* silicon, glass, and polymers. The NP-CLL technique has great potential for the fabrication of structures with engineered plasmonic responses, such as chiral plasmonic substrates[3–6] or waveguides.[7,8] Overall, my work has shown that NP-CLL is a facile, scalable, inexpensive, and flexible approach for the fabrication of plasmonic substrates.

7.1.2. *In situ* growth of gold nanoparticle arrays

In **Chapter 3** and **4**, *in situ* substrate growth was discussed, where bottom-up wet-chemical synthetic techniques were applied to fabricate plasmonic nanoparticles with controlled morphology and precise spatial positioning.[9–12] Here, I performed the *in situ* growth of 40-120 nm nanospheres and nanostars directly into arrays using a chemical reductant ink which was patterned with a modified thermal nanoimprint lithography process. Understanding the role of the chemical environment is one of the main focuses of the work presented in **Chapter 4**. Specifically, key synthetic aspects were identified, such as the importance of implementing strong reductants only on the substrate (rather than in the growth solution) to mimic the spatial separation of nucleation and growth in colloidal synthesis and the need for significantly minimizing secondary nucleation in the growth solution. The arrays have tunable spacings and, thanks to the control over the chemical environment, I was able to synthesize plasmonic substrates that exhibit high quality lattice plasmon resonances,[13] which had not yet been previously demonstrated *via* site-directed *in situ* chemical growth.[14,15]

7.1.3. *In situ* overgrowth of gold nanostars in microfluidics

In this work, I used a hybrid method to grow nanostars on slides and within microfluidic channels.[2] Colloidal seeds were grafted onto substrates and within the internal walls of microfluidic devices, and then a growth solution was subsequently introduced to overgrow the substrate-bound seeds into branched structures. These platforms are useful for studying fundamental synthetic aspects of *in situ* growth. One of the unique features of this work is the capability to use flow parameters (*e.g.,* rate, profile, and time) to alter the yield and morphology of the nanostructures. Overall, my work demonstrated that flow-mediated growth in PDMS-based

microchannels occurs in the flow-limited regime. Moreover, growth in micromixers[16,17] led to faster and more efficient consumption of the growth reagents compared to channels with laminar flow, demonstrating that flow profile can have a profound effect on the final products. Ultimately, a dominant factor affecting nanostar size in this synthesis is the density of the surface-bound seeds, and future works pursing *in situ* microfluidic synthesis should take steps to optimize the surface functionalization.

7.1.4. Plasmonic response and point-and-shoot cell release in nanostar-coated microfluidic channels

Here, I investigated the plasmonic properties of the *in situ* synthesized nanostars in the microfluidic capillary.[2] The biocompatibility of the nanostars and their plasmonic response in the biological transparency window indicate their utility for biomedical applications.[18–20] I found that both flow and laser fluence can be tuned to modulate macroscale heating in the capillary. Correlating surface-enhanced Raman spectra and thermal camera measurements enabled us to probe and to monitor phenomena at the nanoscale, such as damage to molecules bound to the nanostars or thermal reshaping of their sharp arms. Furthermore, controlled heating could induce different biological responses in cells grafted to the nanostars, such as ablation, cell deformation, release of intracellular components, and removal of intact cells. Ultimately, this platform has potential applications in biological and chemical sensing,[18–20] hyperthermia-mediated drug delivery,[21] and microfluidic soft-release of grafted cells with single-cell specificity.[22]

Section 7.2. Prospects

Overall, *in situ* synthesis offers a promising route for the fabrication of plasmonic substrates, since it takes advantage of the high degree of chemical control possible with bottom-up synthetic approaches.[23,24] The lack of a comprehensive understanding of the mechanism of *in situ* growth presents a significant knowledge gap that offers countless opportunities for fundamental synthetic studies focused on understanding how different factors, such as the substrate-particle interaction,[25–27] type of chemical reductant ink,[28,29] and the chemical environment in general[10,11] can be modulated to select for certain shapes. Another great challenge in *in situ* growth is the development of robust patterning methods that precisely confine the formation of nuclei on the substrate with single-particle resolution.[30–34] Future developments targeting these aspects can pave the way towards exciting possibilities, such as the direct synthesis of oriented anisotropic structures,[35–37] such as chiral nanoparticle arrays,[3–6] without having to apply any specialized or costly equipment[38] or time-consuming and complex self-assembly processes.[39] Moreover, the *in situ* growth process is especially interesting for the fabrication of sensors[40] and catalytic substrates,[41] since capping ligands are not explicitly required for *in situ* synthesis, unlike most colloidal growth schemes.

Even though it does not follow a purely *in situ* chemical growth scheme and relies on premade colloidal seeds as nuclei, the *in situ* overgrowth of nanostars in microfluidic systems also opens up stimulating possibilities for fundamental synthetic studies. Namely, precisely manipulating the flow profile and the kinetics of the growth solution can be used as a tool to fabricate unique plasmonic structures. In another example, one could also apply this platform to investigate how changing the surface charge and/or the wettability of the surface affects growth

kinetics as well. These kinds of studies would provide important insights that can lead to further development of novel *in situ* growth methods.

Regarding the development of a circulating tumor cell isolation and capture device based on nanostar-decorated microfluidic channels, further experiments testing the functionalization of the nanostars with target cell specific antibodies will be necessary.[2,17,42] Moreover, evaluations of viability in intact released cells are needed to understand and to optimize the soft release of specific cells.[22] This development would showcase the potential for applying this system as a point-of-care diagnostic tool. Thanks to the robustness of the gold-thiol binding, this platform could be applied to target many different kinds of cancers.[17,43,44] Ultimately, my contributions to the synthetic schemes presented herein help identify new opportunities in the growth of plasmonic nanostructures and I look forward to seeing what future possibilities will be unlocked with the continued development of *in situ* approaches.

Section 7.3. References

[1] N. Chiang, L. Scarabelli, G. A. Vinnacombe-Willson, L. A. Pérez, C. Dore, A. Mihi, S. J. Jonas, P. S. Weiss, *ACS Mater. Lett.* **2021**, *3*, 282.

[2] G. A. Vinnacombe-Willson, N. Chiang, L. Scarabelli, Y. Hu, L. K. Heidenreich, X. Li, Y. Gong, D. T. Inouye, T. S. Fisher, P. S. Weiss, S. J. Jonas, *ACS Cent. Sci.* **2020**, *6*, 2105.

[3] E. S. A. Goerlitzer, R. Mohammadi, S. Nechayev, K. Volk, M. Rey, P. Banzer, M. Karg, N. Vogel, *Adv. Mater.* **2020**, *32*, 2001330.

[4] G. Klös, A. Andersen, M. Miola, H. Birkedal, D. S. Sutherland, *Nano Res.* **2019**, *12*, 1635.

[5] G. Klös, M. Miola, D. S. Sutherland, *J. Phys. Chem. C* **2019**, *123*, 7347.

[6] P. T. Probst, M. Mayer, V. Gupta, A. M. Steiner, Z. Zhou, G. K. Auernhammer, T. A. F. König, A. Fery, *Nat. Mater.* **2021**, *20*, 1024.

[7] F. N. Gür, C. P. T. McPolin, S. Raza, M. Mayer, D. J. Roth, A. M. Steiner, M. Löffler, A. Fery, M. L. Brongersma, A. V. Zayats, T. A. F. König, T. L. Schmidt, *Nano Lett.* **2018**, *18*, 7323.

[8] K. Vogele, J. List, G. Pardatscher, N. B. Holland, F. C. Simmel, T. Pirzer, *ACS Nano* **2016**, *10*, 11377.

[9] F. Muench, *ChemElectroChem* **2021**, *8*, 2993.

[10] B. Fortuni, T. Inose, S. Uezono, S. Toyouchi, K. Umemoto, S. Sekine, Y. Fujita, M. Ricci, G. Lu, A. Masuhara, J. A. Hutchison, L. Latterini, H. Uji-i, *Chem. Commun.* **2017**, *53*, 11298.

[11] B. Fortuni, Y. Fujita, M. Ricci, T. Inose, R. Aubert, G. Lu, J. A. Hutchison, J. Hofkens, L. Latterini, H. Uji-i, *Chem. Commun.* **2017**, *53*, 5121.

[12] Q. Zhang, J.-J. Xu, Y. Liu, H.-Y. Chen, *Lab. Chip* **2008**, *8*, 352.

[13] V. G. Kravets, A. V. Kabashin, W. L. Barnes, A. N. Grigorenko, *Chem. Rev.* **2018**, *118*, 5912.

[14] H.-H. Jeong, M. C. Adams, J.-P. Günther, M. Alarcón-Correa, I. Kim, E. Choi, C. Miksch, A. F. Mark, A. G. Mark, P. Fischer, *ACS Nano* **2019**, *13*, 11453.

[15] A. Alvarez-Fernandez, C. Cummins, M. Saba, U. Steiner, G. Fleury, V. Ponsinet, S. Guldin, *Adv. Opt. Mater.* **2021**, *9*, 2100175.

[16] A. D. Stroock, S. K. W. Dertinger, A. Ajdari, I. Mezić, H. A. Stone, G. M. Whitesides, *Science* **2002**, *295*, 647.

[17] S. L. Stott, C.-H. Hsu, D. I. Tsukrov, M. Yu, D. T. Miyamoto, B. A. Waltman, S. M. Rothenberg, A. M. Shah, M. E. Smas, G. K. Korir, F. P. Floyd, A. J. Gilman, J. B. Lord, D. Winokur, S. Springer, D. Irimia, S. Nagrath, L. V. Sequist, R. J. Lee, K. J. Isselbacher, S. Maheswaran, D. A. Haber, M. Toner, *Proc. Natl. Acad. Sci.* **2010**, *107*, 18392.

[18] E. Lenzi, D. Jimenez de Aberasturi, L. M. Liz-Marzán, *ACS Sens.* **2019**, *4*, 1126.

[19] E. Lenzi, D. Jimenez de Aberasturi, M. Henriksen-Lacey, P. Piñeiro, A. J. Muniz, J. Lahann, L. M. Liz-Marzán, *ACS Appl. Mater. Interfaces* **2022**, *14*, 20708.

[20] D. Jimenez de Aberasturi, A. B. Serrano-Montes, J. Langer, M. Henriksen-Lacey, W. J. Parak, L. M. Liz-Marzán, *Chem. Mater.* **2016**, *28*, 6779.

[21] T. Vo-Dinh, *J. Immunol. Sci.* **2018**, *2*, 1.

[22] J. J. Giner-Casares, M. Henriksen-Lacey, I. García, L. M. Liz-Marzán, *Angew. Chem. Int. Ed.* **2016**, *55*, 974.

[23] Y. Xia, K. D. Gilroy, H.-C. Peng, X. Xia, *Angew. Chem. Int. Ed.* **2017**, *56*, 60.

[24] L. Liz-Marzán, *Colloidal Synthesis of Plasmonic Nanometals*, CRC Press, **2020**.

[25] J. Zhang, M. Kambayashi, M. Oyama, *Electrochem. Commun.* **2004**, *6*, 683.

[26] M. K. Abyaneh, P. Parisse, L. Casalis, *Beilstein J. Nanotechnol.* **2016**, *7*, 809.

[27] T. Jain, S. Lara-Avila, Y.-V. Kervennic, K. Moth-Poulsen, K. Nørgaard, S. Kubatkin, T. Bjørnholm, *ACS Nano* **2012**, *6*, 3861.

[28] C. Wang, N. T. Flynn, R. Langer, *Adv. Mater.* **2004**, *16*, 1074.

[29] A. Goyal, A. Kumar, P. K. Patra, S. Mahendra, S. Tabatabaei, P. J. J. Alvarez, G. John, P. M. Ajayan, *Macromol. Rapid Commun.* **2009**, *30*, 1116.

[30] L. Osinkina, T. Lohmüller, F. Jäckel, J. Feldmann, *J. Phys. Chem. C* **2013**, *117*, 22198.

[31] B. Landeke-Wilsmark, L. Nyholm, C. Hägglund, *Langmuir* **2020**, *36*, 6848.

[32] P. Farzinpour, A. Sundar, K. D. Gilroy, Z. E. Eskin, R. A. Hughes, S. Neretina, *Nanoscale* **2013**, *5*, 1929.

[33] T. B. Demille, R. A. Hughes, N. Dominique, J. E. Olson, S. Rouvimov, J. P. Camden, S. Neretina, *Nanoscale* **2020**, *12*, 16489.

[34] T. B. Demille, R. D. Neal, A. S. Preston, Z. Liang, A. G. Oliver, R. A. Hughes, S. Neretina, *Nano Res.* **2022**, *15*, 296.

[35] M. Chekini, U. Cataldi, P. Maroni, L. Guénée, R. Černý, T. Bürgi, *Langmuir* **2015**, *31*, 13221.

[36] H. Zhang, Y. Liu, M. F. S. Shahidan, C. Kinnear, F. Maasoumi, J. Cadusch, E. M. Akinoglu, T. D. James, A. Widmer-Cooper, A. Roberts, P. Mulvaney, *Adv. Funct. Mater.* **2021**, *31*, 2006753.

[37] Y. Zhou, X. Zhou, D. J. Park, K. Torabi, K. A. Brown, M. R. Jones, C. Zhang, G. C. Schatz, C. A. Mirkin, *Nano Lett.* **2014**, *14*, 2157.

[38] T. Lee, C. Lee, D. K. Oh, T. Badloe, J. G. Ok, J. Rho, *Sensors* **2020**, *20*, 4108.

[39] L. Scarabelli, D. Vila-Liarte, A. Mihi, L. M. Liz-Marzán, *Acc. Mater. Res.* **2021**, *2*, 816.

[40] A. Minopoli, A. Acunzo, B. Della Ventura, R. Velotta, *Adv. Mater. Interfaces* **2022**, *9*, 2101133.

[41] E. Cortés, P. H. Camargo, *Plasmonic Catalysis: From Fundamentals to Applications*, John Wiley & Sons, **2021**.

[42] M.-H. Park, E. Reátegui, W. Li, S. N. Tessier, K. H. K. Wong, A. E. Jensen, V. Thapar, D. Ting, M. Toner, S. L. Stott, P. T. Hammond, *J. Am. Chem. Soc.* **2017**, *139*, 2741.

[43] S.-W. Lv, Y. Liu, M. Xie, J. Wang, X.-W. Yan, Z. Li, W.-G. Dong, W.-H. Huang, *ACS Nano* **2016**, *10*, 6201.

[44] Z. Ao, E. Parasido, S. Rawal, A. Williams, R. Schlegel, S. Liu, C. Albanese, R. J. Cote, A.

Agarwal, R. H. Datar, *Lab. Chip* **2**

Appendix A. Seeded-Growth Experiment Demonstrating Size- and Shape-Dependence on Gold Nanoparticle-Light Interactions

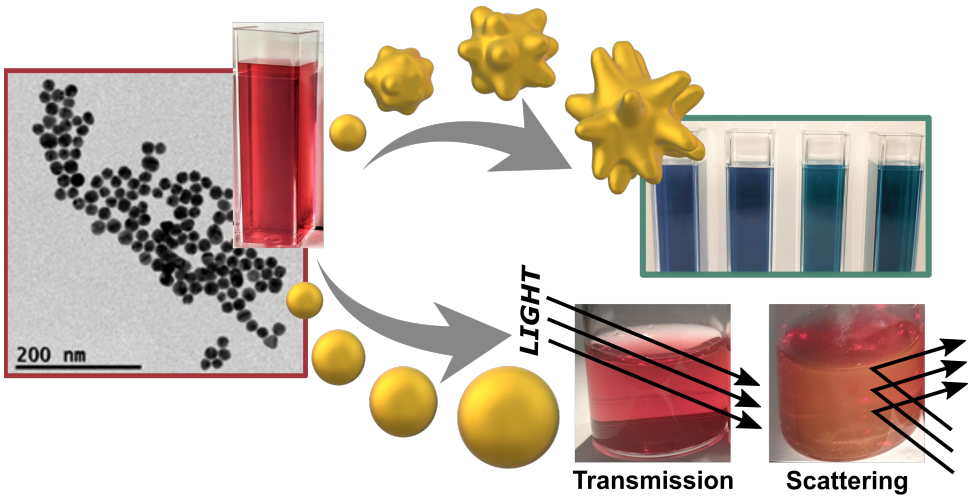

We developed a high school nanoscience laboratory experiment where students apply seed-mediated synthesis to prepare solutions of nanospheres and nanostars. The color difference between nanosphere and nanostar solutions demonstrate the concept of localized surface plasmon resonance. The light scattering intensity of 10 nm and 100 nm colloidal spheres demonstrates the dependence of the plasmonic response on particle size.

Section A.1. Introduction

Nanoparticles are materials that have physical dimensions on the nanometer scale in three dimensions, and possess unique size-related characteristics, such as high surface areas,[1] unique magnetic properties,[2] and interactions with light[3] that differ from their bulk counterparts. In this experiment, students will explore how the sizes and shapes of gold nanoparticles affect their interactions with light, including visible color, the wavelengths of light transmitted/absorbed, and the probability of light scattering. The bright colors observed in gold nanoparticle suspensions are due to plasmons, which are defined as collective oscillations of loosely bound electrons in response to electromagnetic waves (*i.e.*, light). When the frequency of the incident light wave matches the frequency of the plasmon, the oscillating electric field from the light can move the electrons back and forth, causing the light to be absorbed by the nanoparticle. This absorption is called a localized surface plasmon resonance (LSPR). The relationship of nanoparticle shape, composition, and local dielectric environment to their LSPR is well understood and can be used in nanotechnology.[4] In this work, we designed and implemented hands-on experiments introducing nanoscience and plasmonics to high school and early undergraduate-level students, connecting students to this active research topic.

Bottom-up synthetic methods have been used to create nanoparticle suspensions with tailored plasmonic properties for a wide range of applications, including cancer therapies,[5] drug delivery,[6] and chemical detection.[4] Here, we use a method called seed-mediated growth, where small nanoparticles are first synthesized and then grown into large particles in a second step. This strategy enables precise tailoring of nanoparticle sizes and shapes for different applications.[7] During synthesis, small gold nanoparticle clusters (also called nuclei or seeds) form from gold atoms. After the nucleation step, seeds, which are usually below 20 nm in diameter, are injected

into a separate solution containing 'shape-directing reagents', which are molecules that will bind to the growing nanoparticle surface and dictate the shape of the particle as it grows. This approach enables the precise control of the chemical solution for the two separate steps, nucleation and growth, so that the final shape of the nanoparticles is directed and better controlled. The development of this method has led to the uniform synthesis of many different nanoparticle shapes, including rods,[8] wires,[9] stars,[10] cubes,[11] and triangles.[12]

Currently, educational experiments involving gold nanoparticles primarily focus on testing their stability in solution,[13–15] utilizing them as colorimetric sensors,[16–18] and bottom-up synthetic approaches.[15,19–22]Although some educational experiments focusing on nanoparticle shape control[20] and seed-mediated growth[22] have been implemented previously, protocols that allow for the formation of complex shapes are generally not applied in high school level settings due to the use of toxic chemicals and the need for characterization equipment such as ultraviolet (UV)-visible spectroscopy and electron microscopy, which may not be available in most high school settings. The experiments presented here do not require complex instrumentation and involve optimized robust synthetic seed-mediated protocols for preparing gold nanostars and 100 nm nanospheres. Students will visualize the effects of nanoparticle size and shape on their optical properties. Additionally, students will compare different light interactions, such as absorption and scattering, on solutions containing different particle sizes. Overall, this experiment provides an opportunity to introduce students to several topics currently studied in research labs across the globe, including nanomaterials fabrication, surface area and colloidal stability, and the effect of size and shape on nanoparticle-light interactions.

Section A.2. Experimental

Students will learn and use basic concepts and models, such as the wave model of light, physical examples of a resonance, and the color wheel to understand nanoscience concepts, including interactions of plasmonic nanoparticles with light, bottom-up synthetic approaches, and the roles of surface energy in nanoscale objects. The laboratory consists of three experiments, which can be performed in one or multiple sessions. Preparation of reagent stock solutions require at most 1 h by the instructor (to perform dilutions) and can be done up to a week before the experiment. The experiments were designed for groups of 2-5 high school students to complete within 2-3 h (depending on the depth of the explanation). Parts I, II, and III take *ca*. 30 min each to perform. In our workshops, the discussion and explanation of the concepts took an additional 45 min – 1 h in total, but this timing can be adjusted at the discretion of the instructor, based on the backgrounds of the students. All chemical reagents were purchased from Millipore Sigma, and detailed experimental procedures are provided *via* the links in **Section A.8**.

A.2.1. Experimental Turkevich synthesis of gold nanospheres

In this experiment, students use a 'bottom-up approach' to grow small gold nanoparticles (~15 nm), which exhibit bright red coloration due to their plasmonic properties using the Turkevich-Frens method (**Figure A.1A**).[23,24] An aqueous solution of the gold precursor, 25 mL of 0.5 mM $HAuCl_4$ (≥99.9%), is heated to a gentle boil, and sodium citrate (2.5% wt, 0.5 mL) is added as a reducing agent and capping ligand. The high temperature causes the nuclei to grow quickly and uniformly. As the growth progresses, the solution changes color from faint yellow, to clear, then to black/blue, purple, and finally to a deep red. The students will note the color changes

they observe at different times as the particles are formed, and each student should note at least 4 color changes. As an optional activity, once the particle solution has stopped changing color and has cooled to room temperature, two 5 mL aliquots of the solution will be separated into two vials. Liquid dish or hand soap will be added to one of the vials, and subsequently a table salt solution will be added to both aliquots. Students will record the color changes over time and discuss how the addition of soap (surfactant) and salt affect the colloidal stability of the nanoparticles.

A.2.2. Seed-mediated growth of nanostars

The particles from the first part of the experiment are used as seeds to synthesize nanoparticles with different shapes, using seed-mediated growth. The shape-directing agent $AgNO_3$, and reducing agent ascorbic acid, will be used in the growth step to facilitate nanostar formation (**Figure A.1B**, top). Specifically, students prepare a solution containing 5 mL of 0.5 mM $HAuCl_4$, 0.2 mL of 10 mM $AgNO_3$, and 0.4 mL of the Turkevich seeds from Experiment 1 and combine this with 5 mL of a solution containing 1 mM ascorbic acid and 16 mM HCl. The students will record the final color of the solution. This part of the experiment can be combined with UV-visible spectroscopy, if it is available, but it is not necessary for understanding which colors are absorbed and transmitted or interpreting data based on changes in particle shape.

A.2.3. Seed-mediated growth of 100 nm nanospheres

In addition to absorption and transmission, this experiment will enable students to explore the differences between light absorption and scattering. Students will again apply seed-mediated growth by adding 0.120 mL of the seeds synthesized in the first part of the laboratory to a solution containing 6.5 mL 1.92 mM $HAuCl_4$, 0.4 mL 0.75% wt sodium citrate, followed by the addition

of 5 mL of 4 mM ascorbic acid as a reducing agent (**Figure A.1B**, *bottom*). Once the growth is complete (<5 min), the students can observe the difference in scattering intensity between the small and large nanoparticle suspensions by shining a flashlight onto the vial. Students will record their observations and rationalize their results based on the particle size.

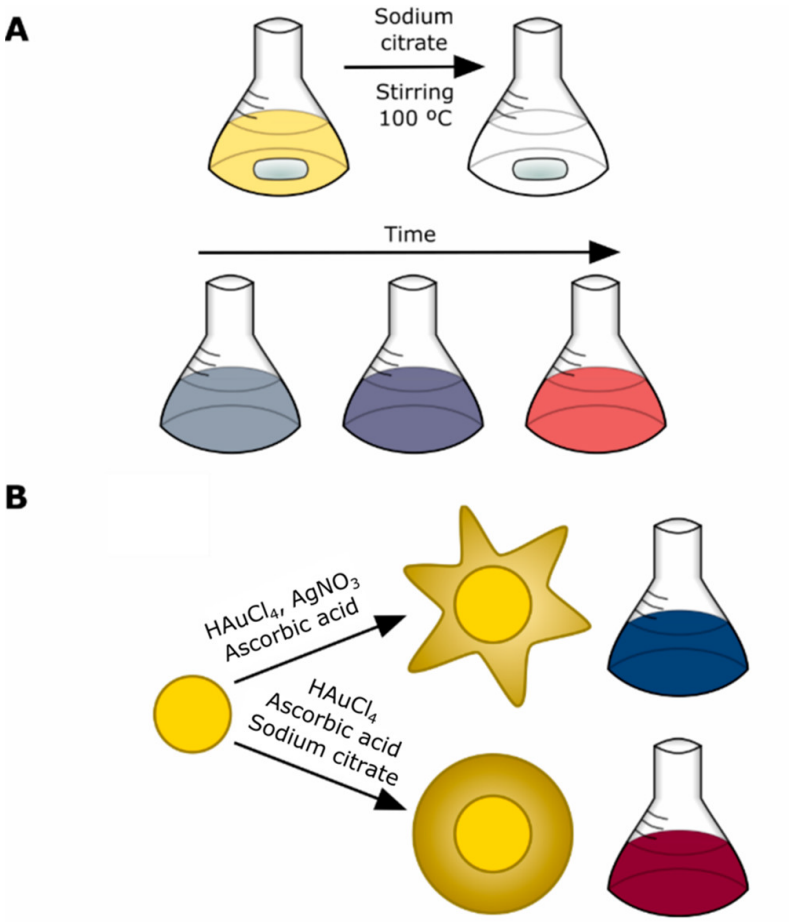

Figure A.1. Schematics of **A:** Turkevich seed synthesis and **B:** subsequent nanostar and large nanosphere growth utilizing the seed-mediated method.

Section A.3. Hazards

Personal protective equipment will be worn by students at all times during the experiment, including lab coats, goggles, and gloves. Although non-toxic materials are used in this experiment,

both tetrachloroauric acid and silver nitrate can cause stains to clothes and skin. The synthesis also uses a small amount of 16 mM HCl, which can cause skin irritation. The HCl should only be handled by the instructor during the pre-laboratory preparation period. When performing the Turkevich synthesis, the solution should be brought to a gentle boil and handled carefully. No fume hoods are necessary, and all reagents are non-toxic.

Section A.4. Results and Discussion

Observations of the synthesis in Experiment I will help students establish the idea that gold nanoparticles, due to their small size, appear brightly colored instead of the metallic yellow color characteristic of bulk gold. These observations will then be used in a discussion led by the instructor, who should then define the key terms 'plasmon' and 'localized surface plasmon resonance.' Following completion of Experiment I, students should have recorded data indicating the color change at different time points of the Turkevich synthesis (example shown in **Figure A.2A**). The observed bright colors that arise as nanoparticles are formed can be explained using the wave electrons in the metal nanoparticle back-and-forth as the electric field oscillates. When the light wave frequency is in resonance with the inherent oscillation frequency of the electrons in the nanoparticle (called the plasmon), the light is absorbed. This absorption is referred to as a localized surface plasmon resonance (LSPR) because the process is localized on a single nano-sized object. Physical models, such as resonant pushing of a swing in motion, can be applied to explain the LSPR phenomena to students. In this model, when a person on a swing is pushed at exactly the right time, their motion can increase, representing absorption of the matching frequency of light (see **Appendix B,C**). If the swing is pushed either too early or too late, however, the force instead slows down the motion of the swing; this off-resonance pushing corresponds to light

with either too low or too high a frequency, which is not absorbed by the nanoparticle. Moreover, students will learn the basic procedure for bottom-up nanoparticle synthesis, which can be expanded to discuss chemical oxidation/reduction and the role of capping molecules to stabilize colloidal nanoparticle suspensions.

Once students have been introduced to the key terminology, color complementarity (using the color wheel) provides a short cut to enable students to predict the position of the LSPR peak, and thus the approximate wavelengths of absorbed and transmitted light. The final ~15 nm particle solution exhibits a red color, due to their LSPR peak at ~512 nm (**Figure A.2B-C**). In this case, the LSPR peak corresponds to green, which is the complement of red (**Figure 2B**). For more advanced students, addressing the color changes (black/blue, purple, to red) throughout the synthesis can reinforce the relationship between size and absorbed wavelengths, as well as the concept of small particles having high surface energies. As particles grow in size, the resonant frequency of their plasmon decreases, leading them to absorb longer wavelengths and shifting the LSPR peak to the red. Therefore, a solution of large particles that absorbs more in the yellow region instead of green would have a more purple coloration to it based on the color wheel. As small particles form, they are unstable due to their high surface-to-volume ratio, meaning that a higher percentage of their total atoms are on the surface (see **Section A.8**). To reduce their high surface energy, the small nanoparticles form clusters. The clusters effectively absorb light as if they were large particles with lower plasmon resonance frequencies, causing absorption at longer wavelengths (**Figure A.2A**: black/blue, purple). As the individual particles grow in size, they become more stable as their surface areas decrease and eventually the clusters separate (**Figure A.2A**: red).

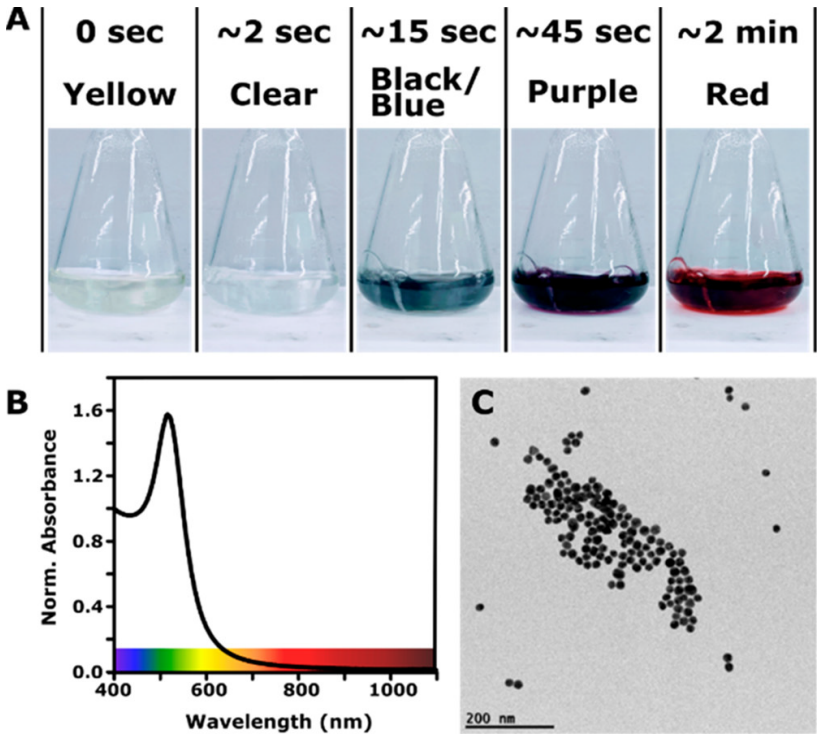

Figure A.2. A: Examples of typical student observations and data for the Turkevich synthesis. **B:** The UV-visible spectra showing maximum absorbance of the final products at ~520 nm. **C:** Transmission electron microscopy imageof a typical seed sample.

In this part of the laboratory, students will also learn about the required components for the bottom-up synthesis of gold nanoparticles: (*i*) gold salt (source of gold ions), (*ii*) a reducing agent (to turn gold cations into Au^0 atoms so nanoparticles can form), and (*iii*) a "capping" molecule that binds to the surface of the nanoparticle, reducing the surface energy and allowing the particle to retain nanoscale dimensions. The initial color change in the Turkevich synthesis from yellow to clear (**Figure A.2A**) is due to the reduction of Au^{3+} following the addition of reducing agent sodium citrate. In this synthesis, sodium citrate also acts as the capping molecule (see links in **Section A.8** for detailed discussion). Expanding upon the idea of surface energy for advanced students, the additional soap/salt colloidal stability activity in Experiment I tests the surface stability of the nanoparticles following addition of surfactants, which acts as a stronger capping ligand for stabilizing the particles and preventing them from aggregating following the addition of

table salt, which causes aggregation due to electrostatic interactions. This concept has been documented in previous educational lab experiments[13–15] and is a general phenomenon of nanomaterials that are stabilized in solution by putting charges on their surfaces.

In Experiment II, students test the effects of nanoparticle shape on the observed color and LSPR peaks. This experiment uses the seed-mediated growth method, where the nucleation step (initial formation of small gold clusters <20 nm in diameter, also called nuclei or seeds, from gold atoms) and the growth step (increased reduction of gold ions onto the seeds) are performed separately. Synthesis of uniform nanoparticle suspensions can be done through the rapid and uniform reduction of gold salt. In the Turkevich synthesis, heat is used to achieve quick, uniform nucleation in solution. Various nanoparticle shapes can be produced through addition of various surfactants, salts, and metal ions, and other shape-directing reagents. However, the presence of these reagents would also affect the nucleation step. So, rather than performing the nanostar synthesis in one single step, we instead perform the nucleation step first, then add the seeds to a separate growth solution where shape-control is performed (**Figure A.1B**). This so-called seed-mediated growth method enables improved control over each synthesis step and is reliable for generating uniform suspensions of different nanoparticle shapes.[7–12] A digital photograph of a typical nanostar solution synthesized via the seed-mediated method is shown in **Figure A.3A**. The difference in color between the gold nanostars and the original seeds is due to the generation of a new LSPR peak at ~650 nm (**Figure A.3B**). The arms/branches of the nanostar have a distinct shape compared the spherical "core" or center of the nanoparticle, and therefore the arms and core will have different plasmon resonance frequencies (**Figure A.3B:** pink = LSPR for the core, blue = LSPR for the arms).[25] Since changing nanoparticle shape leads to the formation of new LSPRs,

shape control can be applied to access LSPRs across the entire visible spectrum, and even into the near-infrared regime.

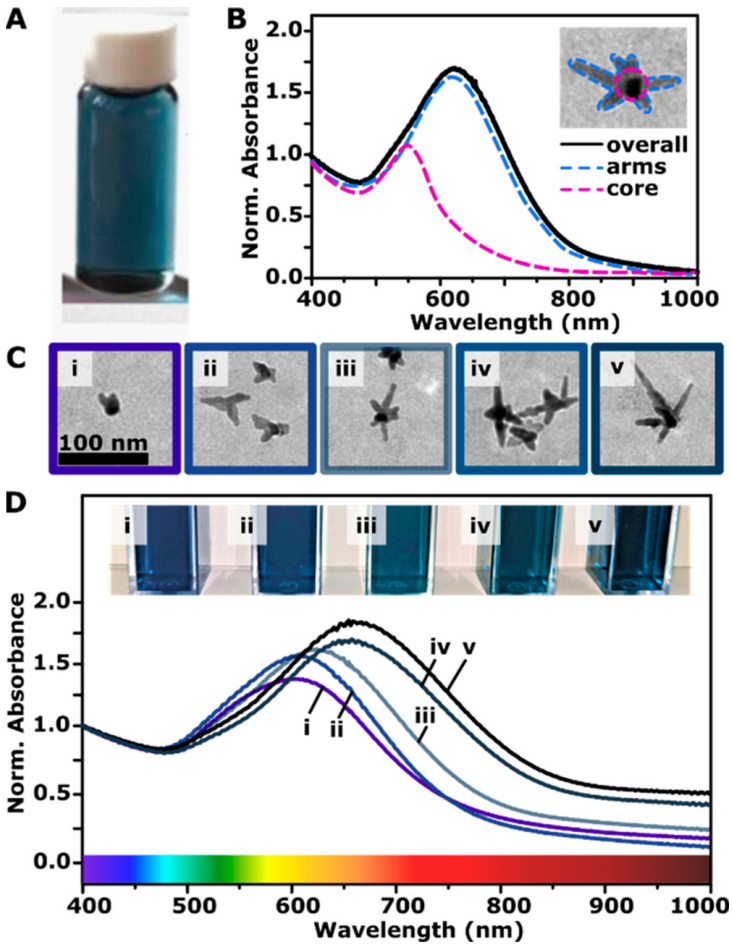

Figure A.3. A: Digital photograph of typical gold nanostar products and **B:** corresponding UV-visible spectrum (inset: diagram showing gold nanostar core and arms). **C:** Transmission electron microscopy images showing variation in nanostar shape with longer and shorter branches, **D:** the color change resulting from the different shapes and their corresponding UV-visible spectra; longer branches cause the peak to shift to the right.

When developing experiments for high school and undergraduate students, it is important to consider aspects in the procedure that may lead to variations in the final products. The size of the arms in the final products depends on the accuracy in timing the addition of growth reagents,

which can vary between student groups. **Figure A.3C** shows transmission electron microscopy (TEM) images of gold nanostars with different arm lengths. In **Figure A.3D**, we show a representative set of final nanostar products that are ordered in color from smallest to largest branches, and their corresponding UV-visible spectra. Due to yield differences, the student samples can range in color from purple (shortest arms) to black (longest arms).[26,27] However, regardless of their yields, students can again use complementary colors to understand the size and shape effects on the optical property: purple color comes from a combination of complement pairs green-red and orange-blue. Particles with a darker blue color can be attributed to longer arms and thus higher absorption in the orange/red region of the spectrum. Thus, this reasoning relating nanostar arm length to the observed color, can be applied to infer particle shape. Student groups can compare and rank the lengths of the arms of their nanostars without UV-visible spectroscopy or TEM analyses, which are generally not available to high school students.

In Experiment I, students discuss the relationship between nanoparticle size and the absorbed wavelength. Here, students will revisit nanoparticle size in the context of evaluating different light-matter interactions, namely transmission (light passing through the sample) and scattering (light bouncing back from a sample). Light transmission can be observed by holding a light source (smartphone light, white light-emitting diode (LED), or flashlight) behind the nanoparticle solution, as shown in **Figure A.4A**. The nanoparticle solution coloration from this viewing angle is a direct result of the color of light that is being absorbed. When the illumination direction is changed so that the light source is moved to the same side as the viewing angle, the effect of nanoparticle light scattering can be observed (**Figure A.4B**). Following the synthesis of large spheres in Experiment III, students will find that although both large and small particles

appear red in the transmission setup (**Figure A.4A,C**), larger nanoparticles will scatter light with a greater intensity than the small particles (**Figure A.4B**).

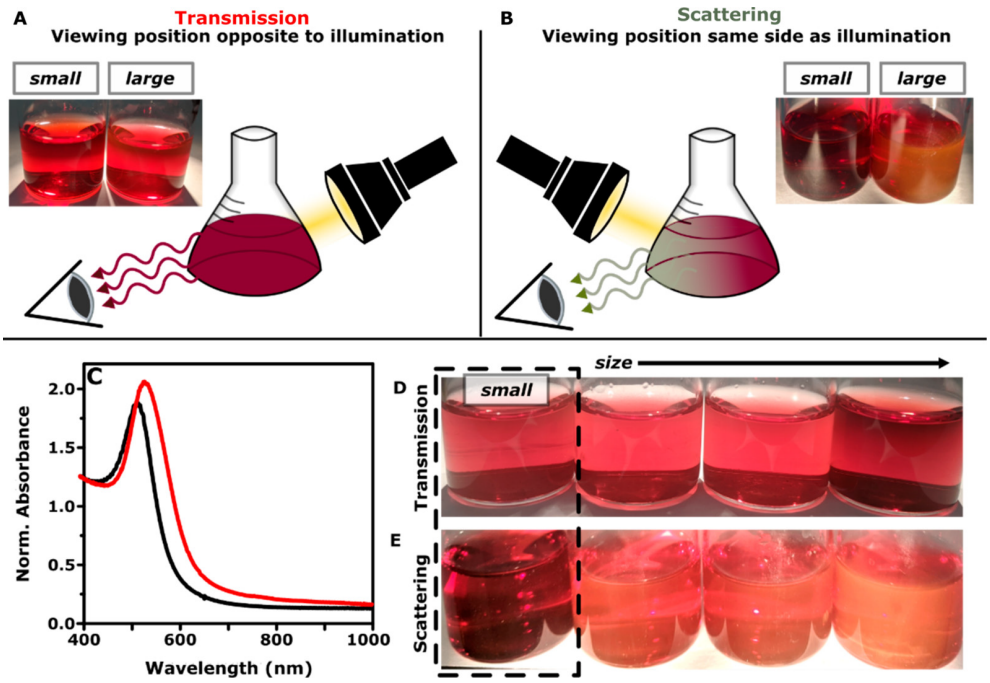

Figure A.4. A: Schematic showing illumination angle to observe color of transmitted light for small and large nanospheres (Flashlight=illumination source; eye=viewing position); inset: photo of large and small samples viewed with transmitted light. **B:** Illumination schematic to evaluate scattering intensity for small and large nanospheres; inset: photo of large and small samples viewed with scattered light. **C:** UV-visible spectra of small nanospheres (black) and large nanospheres (red). Digital photographs comparing nanospheres of different sizes, viewed under transmitted light in part **D** and under scattered light in part **E**. Here, small = the Turkevich seeds.

When the light source and viewing position are in the same direction, the ~100 nm spheres will appear a murky green or brown color, where the ~15 nm seeds will still appear red. This experiment demonstrates the optical effect where particle solutions appear to be completely different colors depending on their viewing direction. From this section, students will understand that there are different ways in which light can interact with nano-objects, and that these interactions depend on nanoparticle size.

As can be seen in the sample data shown in **Figure A.4D**, variations in the color of the final products can arise due to addition of inexact amounts of citrate or poor stirring. These differences also lead to variations in the scattering intensity (**Figure A.4E**). Although particle size differences will affect the scattering yield, students should nonetheless see noticeable differences between the particles synthesized in this step and those synthesized in Experiment I. Moreover, much like with the nanostar synthesis, the scattering variation in products between groups can be used to rank the sizes of each group's particles without the need for UV-visible spectroscopy or TEM (highest scattering intensity = largest particles). The instructor can further apply nanoparticle absorption and scattering concepts to connect to art history through the example of famous Lycurgus cup, which is colored by gold nanoparticles embedded in the glass and exhibits different coloration based on the direction of illumination.[28]

Section A.5. Use and Assessment

This experiment was developed as part of the University of California, Los Angeles (UCLA) California NanoSystems Institute (CNSI) Nanoscience Education Program targeting teachers from schools in the greater Los Angeles area. The experiment has been implemented with high school teachers for the last two years (2018 - 2020). This far, more than 35 teachers have participated in the three-hour workshop. The understanding of the teachers was gauged through a questionnaire following the experiment, focusing on concepts of plasmons/plasmon resonances, light absorption/transmission/scattering, and how these phenomena relate to nanoparticle size and shape (included in **Section A.6**). Based on these assessments, it was determined that concepts requiring the most emphasis include: (1) the electrons in the metal particle are resonantly oscillating, but the particle itself is not moving, and (2) the resonant excitation of the electrons is

due to the light having the same frequency as the inherent plasmon oscillation frequency. Thus, we found that greater understanding was obtained when the workshop leaders and teachers took time to discuss the concepts thoroughly with the teachers and students, respectively, in between each synthesis step, rather than at the end of the laboratory. High school teachers from the workshops have implemented the experiment independently with their classes in 2018 and 2019.

This workshop is easy to implement in high school settings due to the fact that no fume hoods or specialized equipment is required (only a hot plate with magnetic stirring is needed) and no toxic chemicals are used. Although gold and silver salts, and other reagents in the synthesis can be costly, we find that proper storage of the chemicals prevents the cost from becoming prohibitive to performing the experiment in high school settings. Aqueous solutions of tetracholroauric acid in distilled water (distilled water purchasable from any grocery store) can be stored away from light and in a designated chemical refrigerator (4 °C) for at least three years. Teachers additionally found that silver nitrate, sodium citrate, and ascorbic acid have greater longevity (~2-3 years) when kept as solids out of light at 4 °C (aqueous solutions of these last ~3 months under refrigeration). One gram of gold salt costing ~$134 is enough for ~300 repetitions of the entire experiment (enough for performing the laboratory ~10 times for classes of 30 students working in groups of 3, performing 3 repetitions). Furthermore, citrate-capped seeds are stable and can last for years, if kept refrigerated and out of the light (such as in aluminum-foil wrapped containers), and thus can be used to grow stars or large spheres at much later times. We have also found that off-the-shelf hand soap can be added to the synthesized stars and large spheres to preserve them for later demonstrations, if desired (they are then stable for more than 1 year).

This experiment has also been implemented in the 2019 UCLA CNSI High School summer nanoscience workshops (**Section A.7.**). Thus far, two summer workshop sections, with 66 high

school students total, have performed the experiment (3 students per group) over a 2-h period. As mentioned above, the synthesis itself is fairly forgiving, and all groups were able to synthesize seeds, stars, and large spheres. When students made mistakes, such as adding inexact amounts of reagents, adding reagents too slowly, or overheating their solutions, slightly different LSPR peaks in their final products and slight differences in scattering yields resulted, as shown in **Figures A.3** and **A.4**. Following the laboratory, students were evaluated via a drawing assignment where they had to depict two nanoscience concepts they learned from the experiment (prompt in **Section A.7.**). Overall, the feedback from instructors and students was extremely positive, and shows that this experiment is useful for introducing students to complex ideas in nanoscience and plasmonics.

Section A.6. Teacher Workshop Evaluation Sheet

Evaluation for the Color of Nanoscale Gold, Plasmonics Workshop

1. Were the explanations of the scientific concepts and experimental procedures clear and easy to follow? If not, what could be we do to correct the problem?

2. Did the discussions on pedagogy and practice offer any ideas in regard to utilizing this experiment to meet the new science standard requirements: Common Core and/or NGSS (Please elaborate)? If not, what could be we do to correct the problem?

3. Please describe how the Plasmonics experiment might support your existing curriculum. If this workshop offered new ideas to add to your curriculum, please also describe.

4. Of the many science concepts discussed in the Plasmonics lab, list three that highlights how the behaviors/properties at the nano-scale are distinctly different from the macro-scale:

(1)

(2)

(3)

5. What was your overall impression of this workshop (i.e., administration, facilities, location, time, topic, materials, instructors, and instructions)? Would you recommend it to a colleague?

6. Please share with us any suggestions, changes, or additions that would improve our program.

Section A.7. Summer Program Homework Guidelines

Homework Assignment: *Draw a picture(s) to explain one of the key nanoscience concepts you learned today, with the goal of explaining the concept to someone who has never heard of the science topic (e.g., a younger sibling, or perhaps your grandparent, who is not a researcher in nanoscience).*

Guidelines:

1. Only black and white (pencil) on a blank 8.5" x 11" paper
2. Words can be used only as labels (maximum 5 labels) of objects.
3. Use the grading rubric from instructors as guideline on the key nanoscience concepts of the day.
4. Your name on the backside of the paper (NOT on the side of the picture).

Challenges:

1. **Capture the *ESSENCE* of the nanoscience concept in your picture analogy**
2. **Offer a simple analogy a elementary school student can understand**
3. **Explain the nanoscience concept with an original analogy**

Common Q&As

1. Shoot for one whole picture / analogy. The more secondary concepts that you can integrate with the main concept, the better!
2. You can show a process with arrows.
3. Labels should only be for objects, to clarify your drawing, not a science/topic concepts (such as "hydrophobic")
4. Perfect artwork is not expected; emphasis is on good communication, meaning others must be able to understand your effort.

Homework Grading: satisfactory (√), outstanding (√+), or unsatisfactory (√-)

Course Grading: Pass / No pass

1. One third in participation during the week
2. One third in homework (need an average grade of √)
3. One third in final presentation (team grade – teams of three)

Plasmonics Rubric: Summer 2019

50 points possible

1. A plasmon is the collective oscillation of surface electrons in response to an electromagnetic wave. (15 points)
2. Plasmon resonance and the colors they confer depends on a nanoparticle's size and shape. (15 points)
3. Additional concepts: (10 points for including one of the following)
    a. Show the difference between light transmission and light scattering.
    b. Show the photothermal effect.
4. Creative and artistic effort! (10 points)

Section A.8. Link to Student and Teacher Manuals

The .pdf and .docx files for the laboratory manuals can be found free of charge at:
https://pubs.acs.org/doi/full/10.1021/acs.jchemed.0c01150

Section A.9. References

[1] S. Chakraborty, S. M. Ansar, J. G. Stroud, C. L. Kitchens, *J. Phys. Chem. C* **2018**, *122*, 7749.

[2] J. Reguera, D. Jiménez de Aberasturi, M. Henriksen-Lacey, J. Langer, A. Espinosa, B. Szczupak, C. Wilhelm, L. M. Liz-Marzán, *Nanoscale* **2017**, *9*, 9467.

[3] A. Kristensen, J. K. W. Yang, S. I. Bozhevolnyi, S. Link, P. Nordlander, N. J. Halas, N. A. Mortensen, *Nat. Rev. Mater.* **2016**, *2*, 16088.

[4] K. A. Willets, R. P. Van Duyne, *Annu. Rev. Phys. Chem.* **2007**, *58*, 267.

[5] X. Huang, M. A. El-Sayed, *Alex. J. Med.* **2011**, *47*, 1.

[6] C. Wang, Y. Wang, L. Zhang, R. J. Miron, J. Liang, M. Shi, W. Mo, S. Zheng, Y. Zhao, Y. Zhang, *Adv. Mater.* **2018**, *30*, 1804023.

[7] Y. Xia, K. D. Gilroy, H.-C. Peng, X. Xia, *Angew. Chem. Int. Ed.* **2017**, *56*, 60.

[8] N. R. Jana, L. Gearheart, C. J. Murphy, *Adv. Mater.* **2001**, *13*, 1389.

[9] Y.-N. Wang, W.-T. Wei, C.-W. Yang, M. H. Huang, *Langmuir* **2013**, *29*, 10491.

[10] A. Guerrero-Martínez, S. Barbosa, I. Pastoriza-Santos, L. M. Liz-Marzán, *Curr. Opin. Colloid Interface Sci.* **2011**, *16*, 118.

[11] J. Zhang, M. R. Langille, M. L. Personick, K. Zhang, S. Li, C. A. Mirkin, *J. Am. Chem. Soc.* **2010**, *132*, 14012.

[12] L. Scarabelli, M. Coronado-Puchau, J. J. Giner-Casares, J. Langer, L. M. Liz-Marzán, *ACS Nano* **2014**, *8*, 5833.

[13] C. D. Keating, M. D. Musick, M. H. Keefe, M. J. Natan, *J. Chem. Educ.* **1999**, *76*, 949.

[14] A. D. McFarland, C. L. Haynes, C. A. Mirkin, R. P. Van Duyne, H. A. Godwin, *J. Chem. Educ.* **2004**, *81*, 544A.

[15] L. Mulfinger, S. D. Solomon, M. Bahadory, A. V. Jeyarajasingam, S. A. Rutkowsky, C. Boritz, *J. Chem. Educ.* **2007**, *84*, 322.

[16] A. R. Campos, C. M. Knutson, T. R. Knutson, A. R. Mozzetti, C. L. Haynes, R. L. Penn, *J. Chem. Educ.* **2016**, *93*, 318.

[17] F. Zarantonello, F. Mancin, R. Bonomi, *J. Chem. Educ.* **2020**, *97*, 2025.

[18] J. Bai, K. Flowers, S. Benegal, M. Calizo, V. Patel, S. W. Bishnoi, *J. Chem. Educ.* **2009**, *86*, 712.

[19] S. L. A. Paluri, M. L. Edwards, N. H. Lam, E. M. Williams, A. Meyerhoefer, I. E. Pavel Sizemore, *J. Chem. Educ.* **2015**, *92*, 350.

[20] J. A. Jenkins, T. J. Wax, J. Zhao, *J. Chem. Educ.* **2017**, *94*, 1090.

[21] R. K. Sharma, S. Gulati, S. Mehta, *J. Chem. Educ.* **2012**, *89*, 1316.

[22] Á. M. Pérez-Mariño, M. C. Blanco, D. Buceta, M. A. López-Quintela, *J. Chem. Educ.* **2019**, *96*, 558.

[23] J. Turkevich, P. C. Stevenson, J. Hillier, *Discuss. Faraday Soc.* **1951**, *11*, 55.

[24] G. Frens, *Nat. Phys. Sci.* **1973**, *241*, 20.

[25] F. Hao, C. L. Nehl, J. H. Hafner, P. Nordlander, *Nano Lett.* **2007**, *7*, 729.

[26] P. Pallavicini, A. Donà, A. Casu, G. Chirico, M. Collini, G. Dacarro, A. Falqui, C. Milanese, L. Sironi, A. Taglietti, *Chem Commun* **2013**, *49*, 6265.

[27] A. Casu, E. Cabrini, A. Donà, A. Falqui, Y. Diaz-Fernandez, C. Milanese, A. Taglietti, P. Pallavicini, *Chem. - Eur. J.* **2012**, *18*, 9381.

[28] I. Freestone, N. Meeks, M. Sax, C. Higgitt, *Gold Bull.* **2007**, *40*, 270.